STUDIES OF SOME BISMUTH BASED ELECTROLYTES FOR SOLID OXIDE FUEL CELLS

A

Thesis

Submitted for the award of the degree of

DOCTOR OF PHILOSOPHY

BY

RAVI KANT

SCHOOL OF PHYSICS AND MATERIALS SCIENCE

THAPAR UNIVERSITY

PATIALA-147004

INDIA

April/May -2008

Dedicated to my family

Son (Tushar), Daughter (Diksha) and Wife (Anju)

The important thing is not to stop questioning

Albert Einstein (1879-1955)

CERTIFICATE

This is to certify that this thesis entitled **"STUDIES OF SOME BISMUTH BASED ELECTROLYTES FOR SOLID OXIDE FUEL CELLS"** which is being submitted by Ravi Kant in fulfillment of the requirements for the award of the degree of Doctor of Philosophy in the School of Physics and Materials Science, Thapar University, Patiala, Punjab, India is an exclusive record of candidate's own research work under our supervision. The thesis in part or in full has not been submitted in any other university or institute for the award of any degree. The thesis is fit to be considered for the award of degree of Doctor of Philosophy.

Dr. Kulvir Singh
Assistant Professor
School of Physics and Materials Science
Thapar University
Patiala-147 004 (INDIA)

Dr. O.P. Pandey
Professor
School of Physics and Materials Science
Thapar University
Patiala-147 004 (INDIA)

ACKNOWLEDGEMENT

It is a great privilege for me to express my deep gratitude to my supervisors, Dr. Kulvir Singh and Dr. O.P. Pandey at this momentous occasion of completing my research. Both of them encouraged and supported me throughout research work by their fruitful advice, able guidance and expertise. Special thanks for Dr. O.P. Pandey who alongwith Dr. Kulvir Singh managed the adverse situations encountered and made the project a successful event.

It gives me immense pleasure to feel the blessings and constant inspiration by Dr. K.K. Raina (Deputy Director) and Dr. N.K. Verma (Dean, Student Affairs).

My thanks are due to Dr. Manoj Sharma (Assistant Professor) and Dr Sunil Kumar (Lecturer) for their motivated approach.

Help rendered by Dr. A.R. West and Dr. R.N. Vannier by sending their useful research papers is highly appreciated.

Furthermore, I am deep in debt to Mr. Purshotam Kumar for his technical help in various aspects of life during odd hours for the help and without whom it was not possible to carry out my research work. Great cooperation extended by Dr. Parveen Malik and Dr. Pankaj Kumar during the hours of need is highly acknowledged and is placed on my personal record. I am highly obliged to Dr. Sarbjit Singh for getting the pellets gold sputtered for conductivity measurement. I am thankful to Mr. Vishal, Mr. Mohit and other M. Tech. students (2006-08) especially Mr. Ravi Srivastva for their timely help. I am also thankful to Mr. Jant Singh for his kind cooperation.

A sense of apology is due to my loving son Tushar and daughter Diksha who missed many precious moments of fatherly love and care. My wife Anju deserves the special

thanks and great appreciation for her persistent moral support and capability to rejuvenate me during the course of the Ph.D. work.

Above all, hidden force by **Almighty God** steered me in the right direction to achieve the goal.

(Ravi Kant)

PREFACE

Ionic conductivity is the result of ions migration. It pays a key role in the development of electrolyte materials for several electrochemical devices like solid oxide fuel cell (SOFC). Solid electrolytes are the class of materials found to exhibit high ionic conductivity which depends upon different transport mechanism associated with it. Other type of conduction e.g. electrons (electronic conductivity) reduces the efficiency of solid oxide fuel cell due to internal short circuit.

Oxide phases derived from Bi_2O_3 are particularly interesting due to their high ionic conductivity with respect to other solid electrolytes. High conducting δ-phase of Bi_2O_3 can be stabilized down to room temperatures by the substitution with V_2O_5 thus forming $Bi_4V_2O_{11}$ compound. Materials like yittria stabilized zirconia (YSZ), $La_{10-x}Ge_6O_{26.5}$ etc. require high temperatures for their synthesis. Their compatibility and performance with other components of devices show limited applicability. The cost and maintenance of a fuel cell stack makes it mandatory to operate it below 800^oC, but these temperatures are at the technical limit that can not be achieved with YSZ as the electrolyte below 800 ^oC. Moreover, oxygen ion conduction through the YSZ electrolyte membrane is a highly activated process, thus resulting in high voltage losses across the layer at lower temperatures. This fact continues to motivate to search for developing electrolytes with low resistance at intermediate temperatures.

Currently, considerable attention is paid to search solid oxide electrolyte materials which exhibit high ionic conductivity at low temperature. Replacement of YSZ with intermediate temperature oxide ion conductor in solid oxide fuel cell would give a significant reduction in the material cost and fabrication problems together with an

improvement in the efficiency and longevity of the cell. Solid solutions based on γ-$Bi_4V_2O_{11}$ by partial substitution of vanadium with metal cations ($Bi_4V_{2-x}Me_xO_{11}$) exhibit high ionic conductivity and oxygen ion transference numbers close to unity at temperatures below 600^oC. Although, these materials were developed as early as 1986 when Bush and Debreuille-Gresse reported some of the highest oxygen-ion conductivities to date. Since then a large number of systems were developed and investigated. In order to demonstrate the superiority of the bismuth vanadate based compounds as compared to the other commonly used materials, a number of new electrolytes doped on the vanadum and bismuth sites respectively were prepared: (i) $Bi_4V_{2-x}Me_xO_{11-\delta}$ (Me = Cu^{2+}, Mn^{2+}, Ti^{3+}, Al^{3+}, Cr^{3+}, Ga^{3+} and As^{5+}) (ii) $Bi_{4-x}V_2Me_xO_{11-\delta}$ (Me = Pb^{2+}, La^{3+} and Gd^{3+}) and their physical and electrical characterizations were carried out in the present work. In all the systems, the composition selected is x = 0.1, 0.2, 0.3, 0.4 and microstructural study was carried out to correlate it with the ionic conductivity. This was undertaken because of fact that no systematic study up to higher composition range and its correlation with microstructure is reported in the literature. The entire study is described in the following six chapters.

Chapter I

Chapter 1 presents in brief the background of the solid electrolyte. Classification of solid electrolytes has also been presented. Structural aspects of solid electrolytes have been incorporated in context to oxide ion conduction. The fundamental characteristics, principle of defect formation, ions transport mechanism and temperature dependent conductivity behavior of the solid electrolytes is also explained. The concepts of solid

oxide fuel cell based on solid electrolytes have been summarized. Different fabrication and processing techniques of solid electrolytes are mentioned for its application in solid oxide fuel cell. Various applications of solid electrolytes are also given in this chapter.

Chapter II

Chapter II reviews the literature and research findings reported by various research groups in the field of solid electrolytes. Zirconia based solid electrolytes and related systems have been discussed in length for their application in intermediate temperature range [600-800ºC]. Research findings of various other electrolyte materials like $La_{0.8}Sr_{0.2}Ga_{0.83}Mg_{0.17}O_{2.815}$ (LSGM), $GdAlO_3$ etc. are also reported. Emphasis on the literature survey on Bi_2O_3 based electrolyte materials *viz.* $Bi_{0.8}Er_{0.2}O_{1.5}$, $Bi_{0.88}Dy_{0.08}W_{0.04}O_{1.5}$, $Bi_2Sr_2Nb_2GaO_{11.5}$, in general, and doped $Bi_4V_2O_{11}$, in particular, is discussed.

Chapter III

Chapter III gives the experimental techniques and procedures in detail for sample preparation, physical characterization and electrical measurement of the samples. The samples are prepared by solid-state reaction technique by taking appropriate stoichiometric amounts of the required materials. As prepared samples are characterized using X-ray diffraction (XRD), thermal analyses (DSC/DTA) and conductivity measurement techniques. The XRD technique is used to detect the formation of bismuth vanadate based compounds of different (α, β and γ) phases at room temperature and lattice parameter determinations whereas DSC/DTA is used to observe the phase

transitions in the samples. Scanning Electron Microscopy (SEM) analysis of the fractured surfaces of the samples is also carried out to reveal the microstructural features.

Chapter IV

Chapter IV deals with experimental results on bismuth vanadate ($Bi_4V_2O_{11}$) and its derived compounds. These compounds are prepared by substitution of metallic cations on vanadium site represented as $Bi_4V_{2-x}Me_xO_{11-\delta}$, where Me = Cu^{2+}, Mn^{2+}, Ti^{3+}, Al^{3+}, Cr^{3+}, Ga^{3+} and As^{5+}; x = 0.1, 0.2, 0.3 and 0.4. The ionic conductivity was measured from 200-700^oC during cooling cycle. The samples were characterized by XRD, DSC/DTA and SEM to explain the conductivity behaviour of the materials and their correlation with the microstructure. In addition, high conducting samples of $Bi_4V_{1.6}Ti_{0.4}O_{11-\delta}$ and $Bi_4V_{1.8}Al_{0.2}O_{11-\delta}$ were also prepared at different sintering temperatures to understand the conductivity behaviour and its relation with microstructure.

Chapter V

Chapter V describes preparation of various substitutions, such as Gd^{3+}, La^{3+} and Pb^{2+} for Bi^{3+} sites in $Bi_4V_2O_{11}$ for the composition x = 0.1, 0.2, 0.3 and 0.4. The detailed study by XRDs was carried out to find the existing phases and their stability in the sintered samples.The ionic conductivity was measured in the temperature range of 200-700^oC during cooling cycle. DSC/DTA was done to support the conductivity behaviour and its correlation with microstructure. The high conducting samples of $Bi_{3.8}Pb_{0.2}V_2O_{11-\delta}$ and $Bi_{3.9}La_{0.1}V_2O_{11-\delta}$ were prepared and sintered at different temperatures. These samples were also characterized with XRD, SEM and ionic conductivity measurements. The study

was carried out to observe the effect of sintering temperature on order-disorder transitions, ionic conductivity and its microstructural aspects.

Chapter VI

Chapter VI summarizes the results of all the experiments conducted for the doping on both sites viz. $Bi_4V_{2-x}Me_xO_{11-\delta}$ and $Bi_{4-x}Me_xV_2O_{11-\delta}$ (x =0.1, 0.2, 0.3, 0.4) systems. The overall conclusion shows that conductivity and solid solution range is highest for $Bi_4V_{1.6}Ti_{0.4}O_{11-\delta}$ and $Bi_{3.8}Pb_{0.2}V_2O_{11-\delta}$ compounds on vanadium and bismuth sites respectively. The suggestion for future work is also given.

At the end, all the references which have been consulted during the study are given in increasing order. The list of papers published, presented and communicated is also appended.

TABLE OF CONTENTS

List of Tables

List of Figures

Chapter I

INTRODUCTION

Overview

This chapter presents a review of solid electrolytes. Classification of solid electrolytes and their fundamental characteristics are mentioned. Properties including ionic conductivity of various ZrO_2-, CeO_2- and Bi_2O_3 - based electrolytes which are currently in use are discussed. Structures of the various oxygen ion conductors which play an important role for conductivity enhancement have been elaborated in detail. Important parameters and defect formation that govern the properties of solid electrolyte have been discussed. The mechanism of ion conductivity which is the key feature of the solid electrolytes is given. Solid electrolytes for solid oxide fuel cell and their fabrication techniques are discussed along with other aspects concerning solid oxide fuel cell. Applications of solid electrolytes in different areas are also presented.

1.1 Background

The substance in which ionic conduction takes place through movement of ions is called ionic conductor. Ionic conductivity is observed in those solids in which defects (vacancies) exist. Ionic conductors have always provided a fascinating interdisciplinary field of study ever since their discovery by Faraday over 200 years ago. He introduced the basic terminology of electrochemistry and classification of substances into first and second type of conductors in 1834 [1]. Solid ion conductors were technically recognized for the first time with the development of electric lightning devices. In recent years, the practical importance of solid ionic conductors has increased. Their application in batteries, fuel cells and other large and small devices has increased many fold. The ionic conductivity is a critical property of a solid electrolyte which determines the efficiency and operating temperature of electrochemical cells. In order to obtain a material that is a pure ion conductor (solid electrolyte), the level of electronic contribution to the total electrical conductivity (ionic + electronic) must be negligible. Solid electrolyte must have high ionic conductivity at the operating temperature to allow efficient transfer of ions from the cathode to anode and also a low electronic conductivity to prevent electron leakage across the cell.

1.2 Solid Electrolytes: A Classification

Solid compounds that exhibit the high ionic conductivity are termed as solid electrolytes or superionic conductors or fast ion conductors or hyperionic conductors. Solid electrolytes or superionic solids paved the way for the development of solid state electrochemistry or solid state ionics. Solid electrolytes have either mobile anions or cations, which due to their high degree of disorder are free to move throughout the

structure. The maximum ionic conductivity of these materials lies between 0.1 and 10 ohm^{-1} cm^{-1}. Thus, these materials are intermediate in between normal crystalline solids and liquid electrolytes. Different solid electrolytes can be broadly categorized as follows:

1.2.1 Crystalline Electrolytes

High ionic conductivity in some of the crystalline solid electrolyte is well recognized because of fast ionic conduction. A number of solid electrolytes under this class notably, α-AgI [2], $MbAg_4I_5$ (where M = Rb, K) [3, 4] and Na β-alumina [5, 6] display anomalously high conductivities. Their cations Ag^+ and Na^+ exhibit high conductivity in one of their ionic sublattices which is called the mobile ion sublattice, a behaviour observed at temperatures well below melting points. These materials provide an essentially rigid framework with channels along which one of the ionic species can migrate. Ion transport involves hopping from site to site along these channels. Presently, cationic and anionic crystalline solid electrolytes are readily available. A large number of fast ion conducting solids with anions and cations namely H^+, Li^+, Na^+, K^+, Ag^+, Cu^+, F^-, O^{2-} are reported. Most of the research is focused on Ag^+ and Li^+ under cationic conduction. Oxygen ion conductor (O^{2-}) is well known for its high anionic conductivity in various types of compounds like YSZ and $Bi_4V_2O_{11}$. The most important application of these materials are found in solid oxide fuel cells and oxygen gas sensors.

Ionic conductivity in some of the materials is influenced by allotropic transitions that take place with variation in temperature. For instance, pure Bi_2O_3 is stable at 730 ^oC in a face centered cubic form (fcc) known as δ - Bi_2O_3 and shows an oxygen conductivity in excess of 1 S/cm. Below 730^oC, however it reverts to monoclinic α-Bi_2O_3, which is a p-type electronic conductor. δ - Bi_2O_3 is a very disordered structure and sometimes

referred as a semi liquid. Other crystalline solid electrolytes may show a gradual increase in defect concentration with increasing temperature. These defect structure solids may acquire sufficient defect concentration at higher temperature and start behaving like fast ion conductor.

1.2.2 Glass Electrolytes

Apart from crystalline materials, the second class of electrolytes is the family of amorphous conductors. These conductors are more close to liquid electrolytes than crystalline ion conductors. Amorphous ion conducting materials have some unique properties such as isotropic properties, absence of grain boundaries, easy film formation and so on. Some excellent reviews on development of amorphous electrolytes are given by various researchers [7-9]. Recently, glass electrolyte based on quaternary system was synthesized and its impedance study revealed the characteristics similar to that of superionic solids [10]. Mechanochemically synthesized amorphous and thermally stable electrolyte $xAgI(100-x)[0.5Ag_2O+0.5MoO_3]$ showed high ionic conductivity of the order of $\sim 10^{-2}$–10^{-3} Ω^{-1} cm^{-1} at room temperature [11, 12].

1.2.3 Polymer Electrolytes

The class of polymer in which electrical transport occurs mainly due to ion carriers is called polymer electrolytes. Polymer electrolytes are the newest area of solid state ionics which has applications in electrochemical devices such as batteries and electrochromic windows. Various types of new conducting polymers have been discovered and characterized. Ion transport in polymers relies on dynamics of the polymer chains in contrast to hopping in a solid electrolyte. Binod Kumar *et al*. [13] synthesized polymer

electrolyte $LiN(SO_2CF_2CF_3)_2$ by energy milling process and obtained conductivity value of 1.5×10^{-4} S cm^{-1} at ambient temperature.

1.3 Characteristics of Solid Electrolyte

In the early stages, systematic study on ionic conductivity in solids was not done as the basic mechanism of ionic conductivity was not established because of fact that the crystal structures of the materials were not known at that time. Good electrolyte is supposed to have crystal structures with open channels, layers so as to provide pathways for easy ionic transport via hopping mechanism. High conducting electrolytes are required to fulfill the following conditions:

a) Availability of large number of free ions

b) Large number of vacancies for hopping

c) Same energies of the occupied and vacant sites

d) Three dimensional networking through open channels for the migration of ions

e) High polarizability of the anion framework

The performance of electrolytes depends upon the number of above mentioned parameters.

1.4 Properties of Various Electrolytes

Much of the research is focused for optimization of the structure to achieve high ionic conductivity of the solid electrolyte. Some materials exhibit higher ionic conductivity but they are very expensive, for example Yb_2O_3. These materials find limited applications due to cost factor. Doped ZrO_2, CeO_2 and Bi_2O_3 are considered as ideal electrolyte materials for ceramic oxygen generators and solid oxide fuel cell (SOFC) [14-17].

Among these, the electrolyte materials derived from bismuth oxide (Bi_2O_3) compositions show the highest conductivity as compared to others, particularly below 600^oC [18, 19]. Various electrolyte materials which are currently in use as a solid electrolyte in different devices are discussed below:

1.4.1 Zirconia-based Oxide Ion Conductors

In pure ZrO_2, ionic conductivity is very low because of presence of low concentration of the oxide ion vacancies and interstitial oxide ions. However, when yttria is added, the conductivity increases significantly. Yashima *et al.* [20] surveyed the phase diagrams of doped zirconia systems, including ZrO_2-Y_2O_3 [21] and ZrO_2-Sc_2O_3 [22]. Various attempts [23, 24, 25] to explain the conductivity behaviour on the basis of clusters in the first and second coordination shells and variation in their structure have been made. It was observed that the amount of dopant decreases with increasing radius of dopant ion to achieve higher conductivity. The dopant Sc^{3+} (0.81 Å), which has the closest ion radius to the host ion, Zr^{4+} (0.80 Å), shows the highest conductivity and higher doping level as compared to yttrium doping.

For electrolytes, high electrolyte strength and toughness are also desirable in addition to high ionic conductivity especially for its applications in solid oxide fuel cell. The bending strengths of zirconia-based electrolytes along with their thermal expansion coefficients are also shown in Table 1.1. ZrO_2 doped with 11 mol% Sc_2O_3 and 1 wt% Al_2O_3 appears as one of the best candidates because of its high oxide ion conductivity, phase stability and excellent mechanical properties in real SOFC conditions.

Table 1.1 Electrical conductivity, bending strength, and thermal expansion coefficient of zirconia-based electrolytes

Electrolyte	Conductivity at 1000°C (S/cm)		Bending strength (MPa)	Thermal expan. coeff. ($1/K \times 10^6$)
	As sintered	After annealing		
ZrO_2-3 mol%Y_2O_3	0.059	0.050	1200	10.8
ZrO_2-3 mol%Yb_2O_3	0.063	0.09		
ZrO_2-2.9 mo1%Sc_2O_3	0.090	0.063		
ZrO_2-8 mol%Y_2O_3	0.13	0.09	230	10.5
ZrO_2-9 mol% Y_2O_3	0.13	0.12		
ZrO_2-8 mol%Yb_2O_3	0.20	0.15		
ZrO_2-10 mol%Yb_2O_3	0.15	0.15		
ZrO_2-8 mol%Sc_2O_3	0.30	0.12	2 70	10.7
ZrO_2-l l mo1%Sc_2O_3	0.30	0.30	255	10.0
ZrO_2-11 mol%				
Sc_2O_3-l wt% $A1_20_3$	0.26	0.26	250	

1.4.2 Ceria-Based Oxide Ion Conductors

CeO_2 doped with CaO, Y_2O_3, Sm_2O_3, Gd_2O_3 and a number of other rare earth oxides have high oxygen ion conductivity. However, the ionic conductivity regime is rather narrow. Ceria-based oxide ion conductors are reported to have purely ionic conductivity at high oxygen partial pressures. However, in reducing environments, ceria based systems lose oxygen and develop electronic conductivity behavior at 800°C [26].

The conductivity of doped ceria systems depends on the kind of dopant and its concentration. Mobile oxygen vacancies are introduced by substituting Ce^{4+} with trivalent rare earth ions. In ceria based systems, the maximum conductivity is observed at 10 mol% Sm_2O_3. The conductivity of CeO_2-Ln_2O_3 (Ln = Gd, La etc.) system depends on the dopant (Ln) ionic radius. The binding energy calculated by Butler *et al.* [27] shows a close relationship to the conductivity. The dopant with low binding energy exhibits higher conductivity as indicated in table 1.2.

Table 1.2 Electrical conductivity data for CeO_2-Ln_2O_3

Electrolyte	Conductivity at 1000°C (S/cm)		Activation energy (kJ/mol)	References
	500 °C	700 °C		
CeO_2 -10 mol%Sm_2O_3	5.0×10^{-3}	4.0×10^{-2}	75	28
CeO_2 -10 mol%Gd_2O_3	3.8×10^{-3}	3.6×10^{-2}	70	29
CeO_2 -10 mol%Y_2O_3	0.21×10^{-3}	1.0×10^{-2}	95	28
CeO_2 -10 mol%CaO	1.5×10^{-3}	2.0×10^{-2}	80	29

CeO_2-Gd_2O_3 and CeO_2-Sm_2O_3 show an ionic conductivity as high as 5×10^{-3} S/cm at 500 °C corresponding to 0.2 Ω cm^2 ohmic loss for an electrolyte of 10 μm thickness.

1.4.3 Bi_2O_3-Based Oxide Ion Conductors

1.4.3.1 Electrical Properties of Bi_2O_3:

Electrolyte material such as doped bismuth oxide exhibit superior ionic conductivity over YSZ and CeO_2 based electrolytes at lower temperature [30]. Structurally, higher disorder

state is responsible for high ionic conductivity in Bi_2O_3 systems. Bi_2O_3 exhibits four polymorphs *viz.* α, β, γ and δ. The phase transition from low conducting monoclinic α-phase to high conducting δ-phase has been observed at 730 ^oC [31]. The conductivity of various phases [32] is given in table 1.3. Takahashi *et al*. [33] reported enhancement of ionic conductivity over a factor of 3 due to the oxygen ion movement during transition of low temperature α to high temperature δ-phase.

Table 1.3 Conductivity of the various phases of Bi_2O_3

Phase	Conductivity at 650^oC (Scm^{-1})
α-Bi_2O_3	3×10^{-4}
β-Bi_2O_3	2×10^{-3}
γ-Bi_2O_3	5×10^{-3}
δ-Bi_2O_3	1

Mairesse *et al.* [34] have given some factors which are responsible for the high oxygen ion conductivity in δ- phase of Bi_2O_3. These factors are as follows:

- Availibilty of oxygen vacancies in the fluorite related structures.
- Presence of $6s^2$ lone pair electrons accounting for high polarizability of the cation network consequence of oxide ion mobility.
- Capability of the Bi^{3+} to accommodate highly disordered surroundings.

1.4.3.2 Coefficient of Thermal Expansion of Bi_2O_3

The coefficient of thermal expansion is very important factor while fabricating electrochemical device. This helps to realize the life expectancy as far as other

components of the device are concerned. It will make impact on the heating and cooling characteristics of the device. A very high value of coefficient of thermal expansion (43.6 $\times 10^{-6}$/ ^{o}C) was first reported by Gattow *et al.* [35] in 1962. Subsequently, half of this value was measured by another group [38]. Typical values of cefficient of thermal expansion are given in table1.4.

Table 1.4 Thermal expansion coefficients of various phases of Bi_2O_3

Temperature (^{o}C)	Expansion coefficients (10^{-6} / ^{o}C)				References
	α	β	γ	δ	
100-200	12.2	-	-	-	35
200-400	12.4	-	-	-	35
400-575	14.2	-	-	-	35
575-675	14.8	-	-	-	35
675-750	-	-	-	43.6	35
Room temperature	-	-	-	22.6/22.5	36/37
25-730	11.0	-	-	-	38
730-825	-	23.0	-	-	38
640-25	-	-	20.0	-	38
650-500	-	-	-	24.0	38

1.5 Structural Aspects

A major goal of research in oxygen ion conducting materials is to develop new compounds having high oxygen ion conductivity at relatively low temperatures (400-800 ^{o}C). For synthesizing new conductors, attempts are made to combine the extrinsic vacancies through doping with the intrinsic vacancies already present in the structure. The provision of a low activation energy barrier for hopping between adjacent sites by using structures with a large free volume and highly polarizable ions, is the second consideration.

Above required phenomenon needs several consideration to understand it from crystal structures. These considerations are as follows:

- Crystal must contain unoccupied sites equivalent to those occupied by the lattice oxygen ions.
- Energy involved in the process of migration from one site to the unoccupied equivalent site must be low (less than 1eV)

The small barrier to migrate would be difficult to attain due to larger size of the oxygen ion with an ionic radius of 1.4 Å as compared to smaller metal ion. However, in certain very special and open crystal structures, migration of oxygen ions is easy in the electric field. It is thus clear from these initial observations that materials displaying oxygen ion conductivity must have highly disordered open crystal structures. These materials can be divided into various structural types as categorized below.

1.5.1 Fluorites Structure

Study of fluorite-structured oxides as electrolytes begins with the early investigations by Walther Nernst in 1900. The general formula of a fluorite oxide is AO_2. This structure is a face centered cubic arrangements of cations with anions occupying all the tetrahedral sites as shown in fig.1.1. The fluorite structure has a large number of octahedral interstitial voids. Oxide ion conduction is provided by oxide ion vacancies and interstitial oxide ions. Uranium dioxide (UO_2), thorium dioxide (ThO_2) and ceria (CeO_2) are the materials that readily form the fluorite structure. High temperature zirconia (ZrO_2) has the cubic fluorite structure which can be stabilized to room temperature by substitution of larger cations of lower valence like $Zr_{1-x}Ca_xO_{2-x}$ and $Zr_{1-x}Y_xO_{2-0.5x}$ (YSZ). YSZ has good high temperature mechanical properties which have been extensively covered in the

literature [39]. High temperature δ-Bi_2O_3 phase exhibits fluorite structure where three quarters of the tetrahedral interstices are randomly occupied by oxide ion.

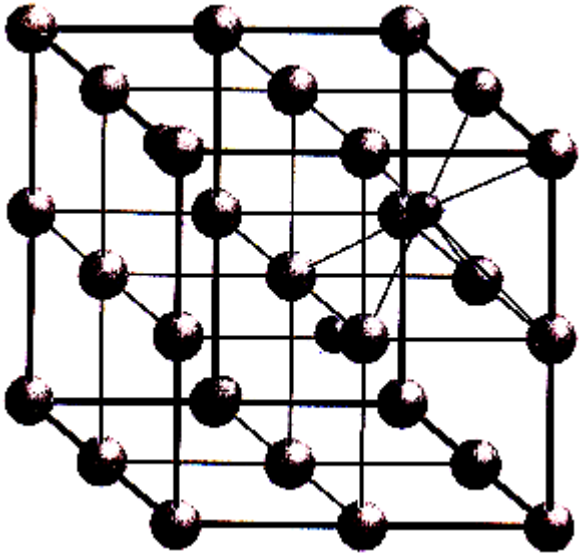

Fig.1.1 The fluorite (AO_2) structure

(small spheres represent the A *cation sites and the large one are oxygen sites)*

1.5.2 Pyrochlores Structure

Pyrochlore structure (fig.1.2) of the formula $A_2B_2O_7$ is derived from an oxygen deficient fluorite structure by an ordering of both cations and oxygen vacancies [40-44]. Moon and Tuller [45, 46] have reported such a transition in $Gd_2(Ti_{1-x}Zr_x)O_7$ with a primarily oxide ion conductivity for $x > 0.4$ but the conductivity $\sigma = 10^{-2}$ S/cm at 1000°C is not competitive with other oxide ion electrolytes. Lattice structure compounds $A_2B_2O_7$ has shown significant promise as ideal candidates for various applications such as electronic materials, solid electrolytes and heating elements. This versatility depends upon the fact that pyrochlore crystal structure allows a wide variety of ionic substitutions on both A, B sites. B element can be a transition metal with variable oxidation state. An element can be

a rare earth or an element, with inert lone pair. At the same time they satisfy other requirements such as physical stability, chemical or thermal compatibility with other materials involved in the design.

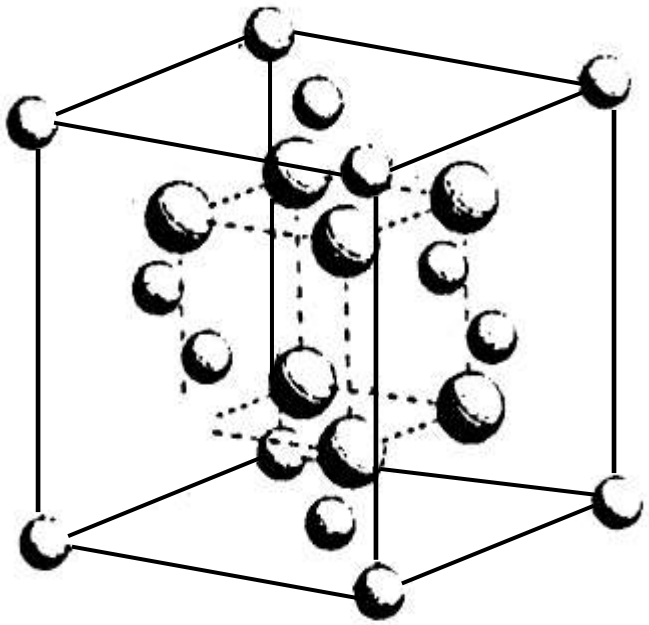

Fig. 1.2 Schematic pyrochlore arrangement, Ref. [47]

(small spheres represent the A *cation sites and the large one are oxygen sites)*

1.5.3 Pervoskites Structure

The crystal structure with ABO_3 stoichiometry is called the perovskite structure. Most striking feature of this structure is to contain large concentration of oxide ion vacancies. A typical crystal structure of perovskite based compounds is shown in fig. 1.3. A number of perovskite structures are purely oxide ion conductors, which have been used as electrolytes in the intermediate temperature range (650^oC - 800^oC). Structurally, perovskite type oxides (ABO_3) score over fluorite based oxide systems (AO_2) because

these materials offer two sites (A and B) for aliovalent doping and thus creating vacancies in the oxygen sublattice, which help the migration of oxygen ions through the lattice. In comparison to perovskite structure, doping in fluorite type oxides is limited to A site [48]. Lanthanum gallate ($LaGaO_3$) is the only material found suitable for ionic applications. Doped $La_{1-x}Sr_xGa_{1-y}Mg_yO_3$ (LSGM) were studied independently by Feng *et al.*, Huang *et al.* [49, 50] and Ishihara *et al.* [51-53]. Interestingly, LSGM exhibited higher ionic conductivity in intermediate temperature range. However, the long-term stability of the electrolyte has yet to be demonstrated and there are some concerns regarding the high creep rate of this material as compared to YSZ [54].

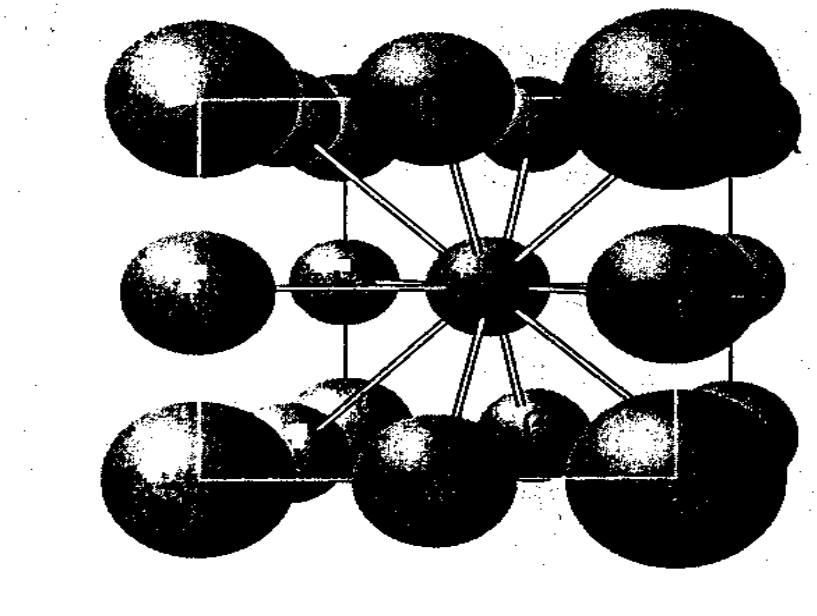

Fig. 1.3 The perovskite ABO_3 structure where large spheres represent A-cation and small are oxygen ions

1.5.5 Brownmillerite Structure

A perovskite oxide with disordered oxygen vacancy may transform to the brownmillerite structure ($A_2B_2O_5$) with an increased number of oxygen sites being vacant and in the ordered state [55]. The Brownmillerite structure is shown in figure 1.4. Such transformation has been reported in several perovskite-type oxides of LaSrCoFeO series with lower Fe content [56-58].

The Brownmillerites may be intergrown with perovskites to produce hybrid oxygen ion conducting materials [59, 60]. This structure is formed where the B cations are stable in both octahedral and tetrahedral symmetry. In this structure, oxide ion vacancies are introduced without aliovalent substitution. $Ba_2In_2O_5$, with large cation size, was investigated under this class for easy oxygen diffusion.

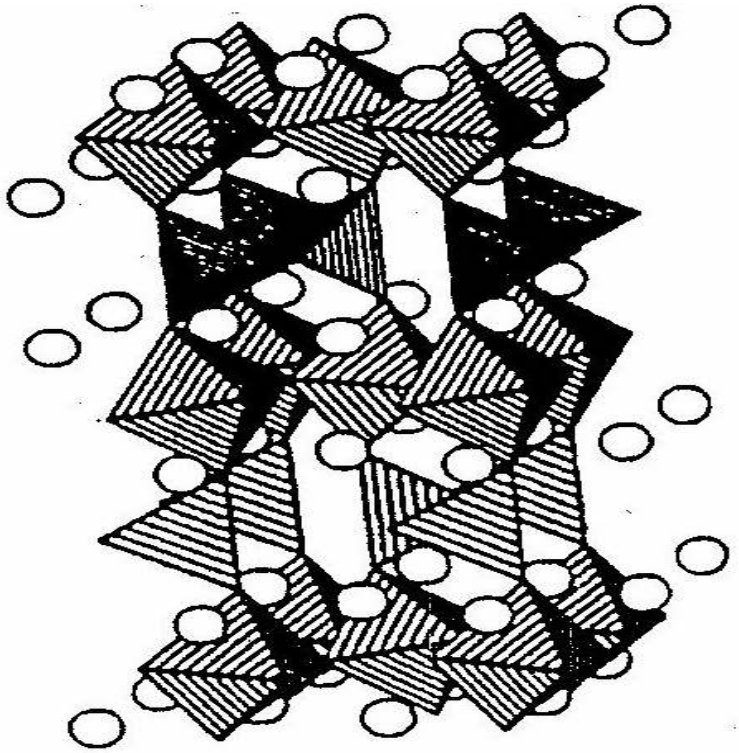

Fig 1.4 Brownmillerite structure

1.5.6 Aurivillius Structure

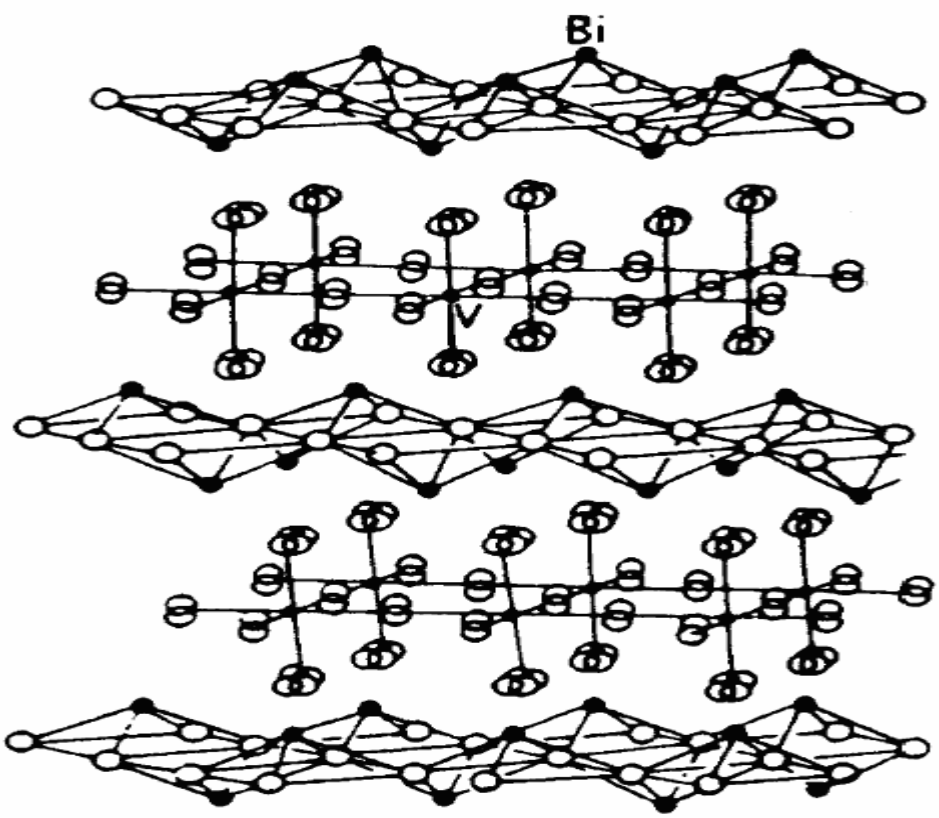

Fig.1.5 Aurivillius structure of $Bi_4V_2O_{11}$

Aurivillius structure was first reported by Aurivillius in 1949 [61-63]. However, oxide ion conductivity was first reported in 1970s by Takahashi [64, 65] and Yanovski [66]. For instance, ($Bi_2A_{n-1}M_nO_{3n+3}$) showed the Aurivillius phases [61] in which perovskite $\{A_{n-1}M_nO_{3n+1}\}^{2-}$ regions are sandwitched between sheets of $\{Bi_2O_2\}^{2+}$ which contain from n = 1 to 5 octahedral layers (fig.1.5). Oxygen vacancies in the perovskite region lead to the high conductivity reported for Bi_2WO_6 and $Bi_2VO_{5.5}$ (n=1) [67, 68]. These materials consist of an intergrowth between puckered bismuth oxide layers $(Bi_2O_2)^{2+}$ and perovskite blocks $(A_{n-1}B_nO_{3n+1})^{2-}$. The $(Bi_2O_2)^{2+}$ sheets have basal edge shared BiO_4

groups with the bismuth occupying the apex of a square pyramid and the oxygen forming the basal plane. The A and B sites can have a variety of cations (A = Na, K, Ca, Sr, Ba, Bi etc.; B = Fe, Cr, Ti, Ga, Nb, V, Mo, W etc.) [69] with the restriction that the perovskite layer and bismuth oxide layer must match to each other structurally [70].

Among the Aurivillius oxides [61-63], the family $(Bi_2O_2)^{2+}$ $(VO_{3.5})^{2-}$ is of particular interest, owing to its high ionic conductivity [71]. Abraham *et al*. [67] observed that $Bi_4V_2O_{11}$ exhibits three (α, β, γ) phases whereas room temperature α -phase has low ionic conductivity which transforms to β and γ phase at 450 and 570 ^oC respectively. The high oxygen ion conductivity of γ phase at elevated temperature is due to the disordering of the oxygen vacancies in the vanadate $(VO_{3.5})^{2-}$ layers. The fascinating conducting behaviour of γ-$Bi_4V_2O_{11}$ [67] has led to several attempts to stabilize such materials at room temperature by means of doping on vanadium site using different metallic ions. Such substitutions give rise to the so called BIMEVOX family of materials [72]. In order to increase the number of vacancies present in the vanadate layer substitution on vanadium site was adopted. However, High resolution transmission electron microscopy (HRTEM) study by Zhou *et al.* [73] has proposed the structure of $Bi_4V_2O_{11}$ to be made up of continuous and orderly but distorted pattern of Bi_2O_2 layers, suggesting the presence of oxygen vacancies in the Bi_2O_2 layers rather than the $VO_{3.5}$ layers.

1.6 Principle of Defect Formation

Solid state electrochemical systems are increasingly being considered in the areas of sensing and combustion control, energy conversion and storage and chemical processing. Example includes zirconia based auto exhaust sensors and solid oxide fuel cell, mixed ionic electronic conducting (MIEC) oxides as oxygen separation membranes and Li^+ ion

battery electrodes. In all these applications, the key element electrolyte satisfies (i) level of ionic conductivity (ii) phase, morphological and dimensional stability and (iii) thermal, mechanical and chemical compatibility. Out of these, the defects and their transport properties influence substantially .The defects can mainly be divided into two types (i) Extended defects (ii) Point defects.

Extended defects may be viewed in terms of dislocation and grain boundary. The point defects include interstitial and vacancies as shown in figure 1.6. Such defects are essential for hopping process for ions under the applied electric field. A point defect can be developed by intrinsic and / or extrinsic mechanism. Intrinsic defect is accompanied by thermal disorder in a stoichiometric compound by the generation of pairs of species to maintain stoichiometry. This may be achieved in a binary compound by a formation of (1) Schottky disorder: cation anion vacancy pairs (fig. 1.7(a) (2) Frenkel disorder: cationic or anionic interstitial vacancy pairs (fig. 1.7(b), whereas, the extrinsic defect is the result of addition of aliovalent impurity. Addition of yttria to zirconia introduces oxygen vacancies due to charge compensation effects. For every two Y^{3+} ions taking the place of Zr^{4+} ions, one oxygen vacancy is created to maintain overall charge neutrality. Substitution of Zr^{4+} with Y^{3+} causes the negative net charge in the lattice. The charge neutrality condition is maintained by forming oxygen vacancy written as follows according to Kroger – Vink notation.

$$Y_2O_3 \xrightarrow{ZrO_2} 2Y'_{zr} + 3O^x_o + V_o^{\cdot\cdot}$$

Where Y'_{zr} means Y in the Zr site with the apparent negative charge (denoted by the symbol') and $V_o^{\cdot\cdot}$ is the vacancy in the oxygen site with double positive charge ($^{\cdot\cdot}$). O^x_o means the lattice oxygen i.e. oxygen in the oxygen site with net charge of zero (^{x}).

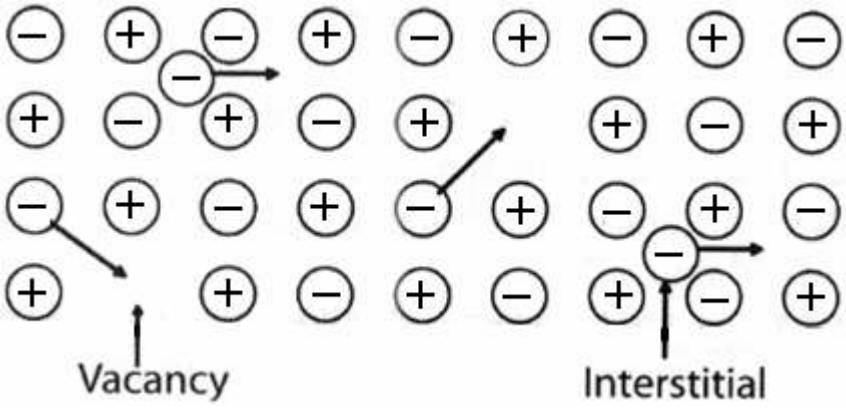

Fig. 1.6 Hopping mechanism for ionic conductivity

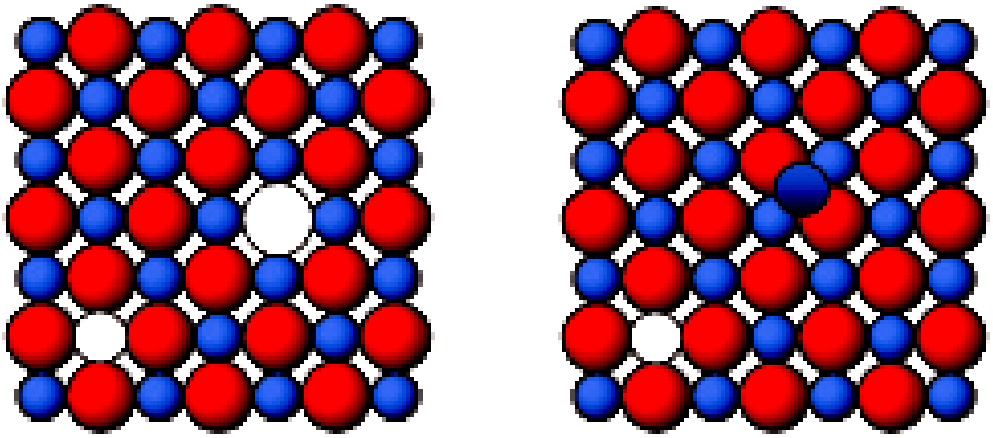

(a) (b)

Fig. 1.7 (a) Schottky defect and (b) Frenkel defect

Expression for defect concentration can be derived from thermodynamics by considering the free energy ΔG of an elemental defective crystal.

$$G = G_1 + G_2 \qquad (1.1)$$

Where $G_1 = ng$ is the work done in creating n defects and $G_2 = -TS_{config}$ is the configurational entropy. At equilibrium,

$$\frac{\partial G}{\partial n} = 0 = g\text{-}T\left[\frac{\partial S_{config}}{\partial n}\right] \tag{1.2}$$

$$S_{config} = k \ln \{N! / [(N\text{-}n)!\, n!]\} \tag{1.3}$$

In which N is the total number of lattice sites of a given type. Applying the Sterling's Approximation and solving for n results in

$$n/N = \exp(-g / kT)$$

This treatment can be readily extended to a compound by defining g_i = work to form a defect pair and noting that

$$T\frac{\partial S}{\partial n} \approx -kT\frac{n}{N}\frac{n}{N'} \tag{1.4}$$

where N and N' are the number of lattice sites on the two respective lattice and n the number of defect pairs. For schottky disorder, N and N' correspond to the cation and anion lattices while in Frenkel disorder they refer to say the cation sublattice and the cation interstitial site lattice, respectively. Again solving the appropriate form of equation 1.2 for n, one obtains

$$\frac{n}{N}\frac{n}{N'} = \exp(-g_i / kT) \tag{1.5}$$

$$n = (NN')^{1/2} \exp(-g_i / 2kT) \tag{1.6}$$

It can be inferred from above equation (1.6) that (i) at any temperature above absolute zero, disorder is thermodynamically stable due to a lowering of the free energy by the

entropy term, (ii) the higher the temperature, the higher the equilibrium defect density; defect disorder increases exponentially with temperature.

1.7 Ion Transport Mechanism

Ion transport occurs by means of activated hopping through defects (vacancy, interstitial). Figure 1.8 shows the schematic representation of variation of energy *E* with minima and maxima at A and B respectively.

All the ions in a solid vibrate with frequency ν_o due to their thermal energy. At a temperature *T*, the probability *P* (per unit time) that a given ion has vibrational energy greater than *E* for hopping can be expressed as

$$P \propto \nu_o \exp(-E/kT) \tag{1.7}$$

where *k* is Boltzmann's constant

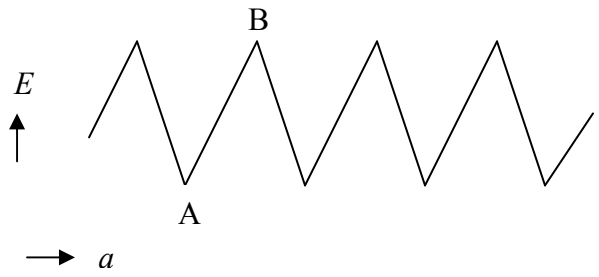

Fig. 1.8 Schematic of the energy variation with position of an ion

Ions hopping can also occur randomly in the absence of electric field amounting to no net current flow.

On the application of an electric field V, the work done in and against the electric field is equal to *Vea* in moving an ion of charge *e* through a distance *a* and corresponding net probability of migration in the two opposite direction is given as;

$$P \alpha \ \nu_o \exp\left[\frac{-(E-\frac{1}{2}Vea)}{kT}\right] - \nu_o \exp\left[\frac{-(E+\frac{1}{2}Vea)}{kT}\right] \quad (1.8)$$

By assuming eVa ‹‹ kT, the above equation reduces to

$$P \alpha \ \nu_o \, Vea \exp\left(\frac{-E}{kT}\right) \quad (1.9)$$

The mean velocity of the ions u is given by

$$u = Pa = \nu_o \, Vea^2 \exp\left(\frac{-E}{kT}\right) \quad (2.0)$$

The mobility μ, of the ion is given by

$$\mu = u/V = \nu_o \, ea^2 \exp\left(\frac{-E}{kT}\right) \quad (2.1)$$

and, the conductivity σ, is given by

$\sigma = Ne\,\mu$, N is the number of mobile ions. (2.2)

Substituting equation for μ (2.1) in to equation of σ (2.2), one can get,

$$\sigma = \nu_o \, \frac{Ne^2a^2}{gkT} \exp\left(\frac{\Delta S}{k}\right) \exp\left(\frac{-E}{kT}\right) \quad (2.3)$$

where $\exp\left(\frac{\Delta S}{k}\right)$ is a proportionality constant, ΔS is the entropy of activation and g is a geometrical factor giving the possibility of several jump directions for a given ion.

The term of proportionality constant $1/g \exp\left(\frac{\Delta S}{k}\right)$ is negligibly small as compared to the number of mobile ions for solid electrolyte.

So above equation can be generalized to following Arrhenius type equation for the solid electrolyte.

$$\sigma = \sigma_o \exp\left(-\Delta E_a / kT\right) \tag{2.4}$$

where σ_o is the pre exponential factor ($= \nu_o \frac{Ne^2a^2}{kT}$), and E_a is the activation energy.

1.8 Applications of Solid Electrolyte

The oil crisis of the early 1970s focused attention on the development of batteries and fuel cells for electric traction which is most relied on the use of solid electrolytes. In recent years, solid electrolytes have been used in various other devices based on large and small power sources [38, 74, 75]. The development of compact low power batteries for portable electronic equipment including mobile telephones, laptop computers etc. and electrochromic devices such as smart windows, which are electrochemical cells that can change their opacity by the passage of small amount of charge, are the newest area where solid electrolytes find its importance. The various applications of solid electrolytes are discussed below.

1.8.1 Solid Electrolyte Batteries

Conventional batteries with liquid electrolytes have limited life period because of the corrosion reactions between the liquid electrolyte and electrodes. Another shortcoming is the leakage of aqueous electrolyte. Moreover, their operational temperature range varies from room temperature to boiling point of liquid electrolyte. The requirement of miniaturized power source for mounting the energy source on the electronic circuit board could not be met by these aqueous electrolyte batteries. Thus the concept of solid state battery in which the electrolyte is also in a solid state besided the two electrodes attracted renewed interest. All solid state cells have many advantages such as miniaturization, long storage life, operation over wide temperature range, rugged structure, no volatilisation

and no leakage because all the cell components are solids. A solid sulphur type battery is attractive for power source in electric vehicles and electric energy storage as a part of load leveling systems.

Other types of cells which are in applications are miniature primary cells which operate at room temperature and have long life rather than a high power output. They are used in electronic watches, heart pacemakers and in military applications.

1.8.2 Solid Eelectrolyte Thermometer

Solid electrolytes are used as high temperature electrochemical thermometer. This has the advantage of working at high temperatures greater than 1000 ^{o}C due to ceramic material used for its construction. However, gas thermometry is limited to a maximum of 1000 ^{o}C due to lack of suitable material. The cell geometry of a solid electrolyte thermometer is

$$Pt / O_2 (P_1) / \text{Solid electrolyte} / O_2 (P_2) / Pt$$

The temperature can be calculated from the oxygen pressure levels P_1 and P_2.

1.8.3 Oxygen Sensors

To maximize energy output for efficient combustion process, on line monitoring of the oxygen content with minimizing partial combustion pollutants such as CO_2 and NO_x, is required. This can be made with the help of oxygen sensors. The currently used YSZ based sensors operates at high temperature over 800^{o}C while desirable operating temperature range (200^{o}C-400^{o}C) is lower for the sensors. Thus new materials are being developed [76] for its efficient working at lower temperature range.

1.8.4 Air Separators

The process of air separation is the reverse of oxygen sensors. Solid electrolytes have selectivity to only one type of charge carrier for its use in air separator. A device based upon this is used to separate oxygen from air particularly from gases, for example, oxygen free nitrogen or argon [77].

1.9 Solid Electrolytes and Solid Oxide Fuel Cells

In 1905, Haber filed the first patent on fuel cells with solid electrolyte [78]. In the last decades, solid oxide fuel cells (SOFC) have been of great interest for the next generation energy efficiency with pollution free environmental [79]. As the requirements for cheap clean electrical energy source increasing, fuel cells are becoming a viable source of power for many applications. SOFC can be categorized due to its high operational temperature (~1000 ^{o}C). Such a high operating temperature produced many unfavourable influences on the fuel cell/stack performance due to the degradation of its constitutent components and undesirable interfacial reaction among the components. Thus, reducing the operating temperature of SOFCs has been one of the key issues for the longevity of the constituent components and the SOFC system itself.

There have been two trends in research to develop intermediate or low temperature SOFCs. The first approach is to reduce the ohmic resistance of solid electrolytes by simply reducing the thickness of solid electrolytes. But this approach has some limitations because, once the thickness goes below 10 μm, an additional reduction in thickness does not contribute further to reduce the ohmic resistance. Moreover, excessively thin electrolytes drastically decrease the mechanical strength of the electrolyte.

Another approach is to develop new solid electrolyte materials, which have higher ionic conductivity being more profitable for lower temperature application. There has been lot of research to develop the suitable solid electrolyte for the application of intermediate or low temperature SOFCs [80-83].

Fuel cell efficiency depends on the properties of materials from which the cell is fabricated. One of the most critical components in the fuel cell is the solid electrolyte. The electrolyte for solid oxide fuel cell must be stable in both reducing and oxidizing environments and must have sufficiently high ionic with low electronic conductivity at cell operating temperature. In addition to this, material must be able to be formed into a thin strong film with no gas leaks. The required properties for these materials, fixed by both electrochemical constraints and high operating temperature, are the following:

- High ionic conductivity ($\geq 0.1 Scm^{-1}$ at $900^{o}C$).
- Low electronic transference number ($<10^{-3}$ at $900^{o}C$).
- Phase stability in wide range of temperature (RT - $900^{o}C$).
- Thermal expansion characteristics compatible with other cell components.
- Chemical compatibility with electrodes, sealants and interconnect materials in oxidizing and reducing atmosphere.
- Gas tightness.
- Fracture toughness (>400 MPa at room temperature).
- Moderate cost of materials and easy fabrication.

SOFC consists of solid electrolyte such as yttria-stabilized zirconia (YSZ) which acts as a oxide ions conductor from $600^{o}C$ to $1000^{o}C$. YSZ ceramic reduces oxygen atom by the electron on porous cathode surface to oxide ion which is then transported to fuel

rich porous anode where oxide ion combines with hydrogen giving up electron in the outer circuit producing electric current as shown in fig.1.9.

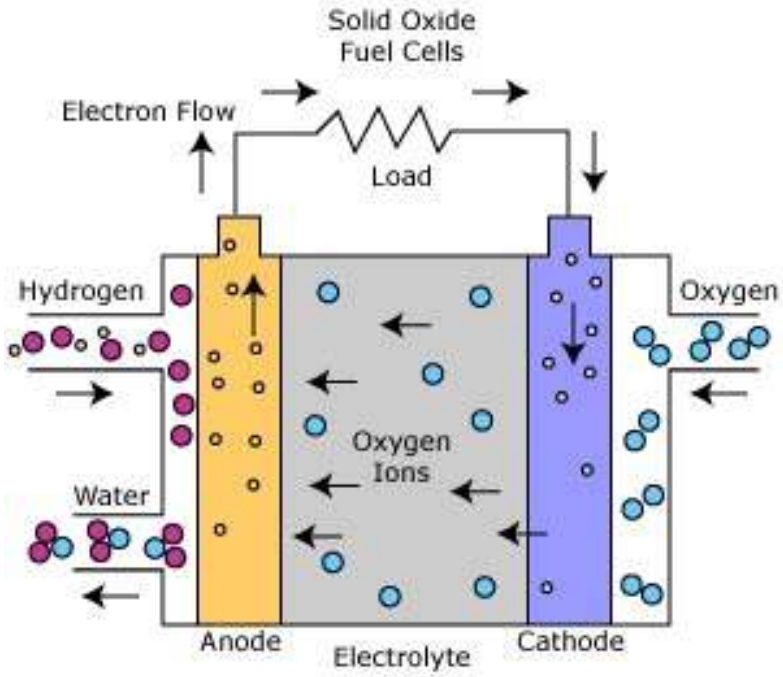

Fig.1.9 Working of solid oxide fuel cell

Solid oxide fuel cells are the most efficient devices yet invented for conversion of chemical fuels directly into electrical power. Considerable advances in theory and experiments are still being made over after 100 years of invention of its basic idea and materials by Nernst and his colleagues. On the molecular scale, collisions between hydrogen and oxygen molecules result in a reaction producing water and releasing heat whereas the bond energy of the produced water is lower than the bonding configuration of the initial hydrogen and oxygen gases. This energy difference is released as heat for combustion engines which occurs by reconfiguration of electrons in picoseconds at an intimate, subatomic scale. To produce electricity, this heat energy must be converted into

mechanical energy and then the mechanical energy must be converted into electrical energy which is potentially complex and inefficient.

1.9.1 Classification of Fuel Cells

There are five primary classes of fuel cells, identified by their electrolytes which have emerged as viable systems [84]. Each fuel cell differs in materials of construction, fabrication techniques and the system requirements, in addition to classification, by the type of electrolyte used. At present, several types of fuel cells are available in the consumer market and following five types of fuel cells are commonly employed.

(i) Polymer Electrolyte membrane fuel cell (PEMFC)

(ii) Alkanine fuel cell (AFC)

(iii) Phosphoric Acid fuel cell (PAFC)

(iv) Molten carbonate fuel cell (MCFC)

(v) Solid oxide Fuel cell (SOFC)

The summary of the all the types of fuel cell has been given in table 1.5.

Table 1.5 Comparison of fuel cell technologies

Fuel Cell Type	Common Electrolyte	Operating Temperature	System Output	Efficiency	Applications	Advantages	Disadvantages
Polymer Electrolyte Membrane (PEM)*	Solid organic polymer poly-perfluorosulfo-nic acid	50 - 100°C	<1kW – 250kW	50-60% electric	• Back-up power • Portable power • Small distributed generation •Transportation	• Solid electrolyte reduces corrosion & electrolyte management problems • Low temperature • Quick start-up	• Requires expensive catalysts • High sensitivity to fuel impurities • Low temperature waste heat
Alkaline (AFC)	Aqueous solution of potassium hydroxide soaked in a matrix	90 - 100°C	10kW – 100kW	60-70% electric	• Military • Space	• Cathode reaction faster in alkaline electrolyte so high performance	• Expensive removal of CO_2 from fuel and air streams required
Phosphoric Acid (PAFC)	Liquid phosphoric acid soaked in a matrix	150 - 200°C	50kW – 1MW (250kW module typical)	80 to 85% overall with combined heat and power(CHP (36-42% electric)	•Distributed generation	• High efficiency •Increased tolerance to impurities in hydrogen • Suitable for CHP	• Requires platinum catalysts • Low current and power • Large size/weight
Molten Carbonate (MCFC)	Liquid solution of lithium, sodium, and/or potassium carbonates, soaked in a matrix	600 - 700°C	<1kW – 1MW (250kW module typical)	85% overall with CHP (60% electric)	• Electric utility • Large distributed generation	• High efficiency • Fuel flexibility • Can use a variety of catalysts • Suitable for CHP	• High temperature speeds corrosion and breakdown of cell components • Complex electrolyte management • Slow start-up
Solid Oxide (SOFC)	Solid zirconium oxide to which a small amount of yttira is added	650 - 1000°C	5kW – 3MW	85% overall with CHP (60% electric)	• Auxiliary power • Electric utility • Large distributed generation	• High efficiency • Fuel flexibility • Can use a variety of catalysts • Solid electrolyte reduces electrolyte management problems • Suitable for CHP	• High temperature enhances corrosion and breakdown of cell components • Slow start-up

1.9.2 Electrolyte Fabrication Process for SOFC

The development of SOFCs has suffered because of the lack of good electrolyte material. The electrolyte has to meet certain requirement for its success like dense and leak tight electrolyte, correct composition of the dopant(s) into base material of electrolyte to provide enhanced ionic conductivity, sufficiently thin to reduce the ionic resistance, extended area to maximize the current density, resistance to thermal shock. Moreover it should be easily processable so as to reduce the cost.

Industrial ceramic processing has traditionally focused on the pressing of dry powders in metal dies or in rubber moulds. A stacked tubular design made by powder pressing had been demonstrated but this proved to be expensive because of diamond grinding and of high resistance due to the 500 μm thick electrolyte [85]. It was far better to move towards the advanced ceramic processes such as electrochemical vapour deposition (EVD), tape casting and extrusion (fig. 1.10) to make the required thin films of electrolyte.

EVD technique was used to make tubular substrate (~15-20 mm) for tubular cells from calcia stabilized zirconia by placing in a low pressure furnace followed by passing of zirconia chloride and ytrrium chloride along the outside of the tube, while water vapor passed down inside. This deposited a layer of yttria-doped zirconia that grows to 40 μm in thickness to form the electrolyte layer [86].

Tape casting was originally used as to make thin tape materials for Electronic applications [87] using organic solvents. A slurry of the YSZ powder with solvent and dispersing agent, for example methyl ethyl ketone mixture was ball milled for 24 hours to finely grind the particles and remove agglomerates [88]. Then a polymer and plasticizer mixture was prepared by milling polyethylene oxide and dibutylphthalate with the

solvent, mixed with the particle dispersion and followed by further ball milling. After filtering and vacuum deairing, the slurry was tape cast on a polymer film and dried for 3 hours before firing at 1300^{o}C.

Small diameter tubes have been produced by extrusion [89] to prevent the thermal shock problem. Again, these compositions were prepared by mixing zirconia powder with water and polymer like polyvinyl alcohol. Extrusion through a die gave tubes which could be as little as 2 mm in diameter and 100-200 mm in diameter and 100-200 μm in wall thickness sinterable at 1450^{o}C.

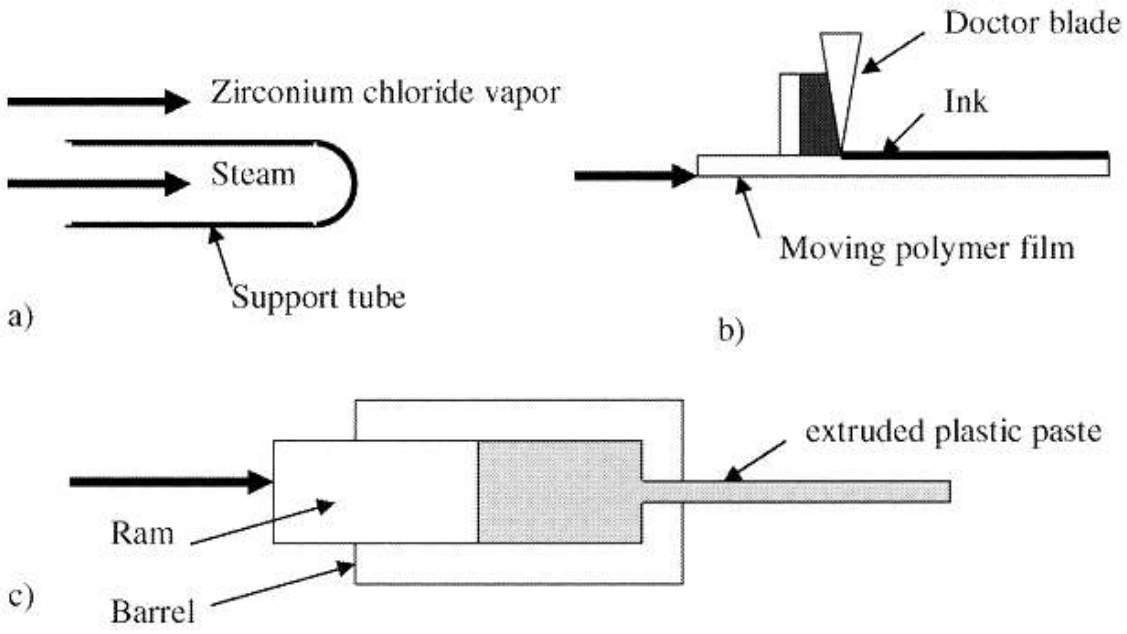

Fig. 1.10 Schematic diagram of three electrolyte fabrication processes:

(a) electrochemical vapour deposition (b) tape casting and (c) extrusion, Ref. [90]

Chapter II

LITERATURE REVIEW

Overview

In this chapter, the present status of research in the field of solid electrolytes especially bismuth vanadate based compounds is reviewed in context with other reported electrolytes. Bismuth based electrolytes are of considerable interest for several investigators because of high ionic conductivity at lower temperatures (<700^{o}C) than other electrolytes, for instance YSZ. The purpose of this chapter is to review some of the key developments in the field of oxide anionic conductors.

Solid electrolytes are materials which find their application in several devices like electrochemical cells, sensors etc. The basic property which is responsible for the development of such technology is the ionic conductivity of the material. In order to improve the ionic conductivity to have a technical product of better performance, researchers are trying hard to synthesize new compounds exhibiting higher ionic conductivity. The requirement of new product where oxide ion conductivity plays dominant role such as SOFC is increasing to save the fuel, a conventional source of energy [91]. Many researchers [92, 93] have synthesized various solid electrolytes and monitored their suitability and applicability in SOFC. In the following section, sequential development of solid electrolytes for its application in electrochemical devices have been reviewed.

Yttria stabilized zirconia (YSZ) is the most common material which have been used as a solid electrolyte in SOFC. YSZ exhibits adequate ionic conductivity in reducing and oxidizing atmosphere. The ionic conductivity of stabilized zirconia is independent of oxygen partial pressure over several orders of magnitude in a wide range of temperature [92-94]. The most commonly used stabilizing oxides or dopants are CaO, MgO, Y_2O_3, Sc_2O_3 and certain rare-earth oxides. The conductivity increases as the radius of the dopant cations approach to that of zirconium. Thus, scandia-doped zirconia shows the highest conductivity ($r_{Sc^{3+}}$ = 0.81 Å and r_{Zr}^{4+} = 0.8 Å). YSZ is the most suitable solid electrolyte in all respect at higher temperature (1000^{o}C). However, higher operating temperature (~1000^{o}C) causes degradation due to the aging effects in YSZ electrolyte.

Another oxide family involving zirconium oxide has been examined as a possible alternative to YSZ as electrolytes for SOFCs. Their general formula is $M_2Zr_2O_7$, where M

is a rare earth metal [49, 50]. Zirconium can be substituted by a transition metal such as titanium etc.

Recently, Mogensen *et al.* [94] have given a general rule to enhance the ionic conductivity which is achieved for a given oxide vacancy concentration in doped fluorite and perovskite structures. According to this rule, cubic lattice should be strains and distortion free to achieve higher ionic conductivity.

In an attempt to improve the YSZ properties, Liu *et al.* [95] recently, added ZnO as a sintering aid to promote densification of the YSZ ceramics. The densification increased the total conductivity by 120% of YSZ at 800 ^{o}C. Binod Kumar *et al*. [96] synthesized 20 wt. % nanosize Al_2O_3 doped YSZ composite membrane by tape casting process. The high conductivity of this system was attributed to space charge effect. Luo *et al.* [97] showed that as gadolinia doped ceria is added to YSZ, a gradual decrease in ionic conductivity has been noticed whereas conductivity of gadolinia doped ceria is higher than that of YSZ. Above observations clearly indicate that undoped YSZ and doped YSZ exhibit good ionic conductivity at 1000 ^{o}C. However, to reduce the working temperature of SOFCs (say 700 ^{o}C), the conductivity of YSZ related systems are not suitable due to sudden drop in conductivity because of structural change.

Doped ceria has been proposed as another potential candidate for SOFC electrolyte [98]. Ceria (CeO_2) doped with CaO, Y_2O_3 is an excellent oxygen ion conductor [99]. It shows a higher conductivity and lower conduction activation energy as compared to stabilized zirconia. Tuller *et al.* [98] and Adham *et al.* [100] excluded the use of CeO_2 based electrolytes in SOFC due to reduction of cerium cations during long operation.

Ceres power Ltd, (Crawley, UK) is developing a novel fuel cell based on doped cerium oxide to produce a robust intermediate temperature SOFC capable of operating in the temperature range of 500-600^{o}C. Electrolyte used by Ceres power Ltd. is ceria gadolinia oxide (CGO) that attains the conductivity of 10^{-2} S cm^{-1} above 500^{o}C, whilst the YSZ electrolyte has this value above 700^{o}C [101].

Lee *et al.* [102] also investigated co-doped ZrO_2 with Sc_2O_3 and CeO_2 electrolyte for better application in intermediate temperature range. This material showed much higher electrical conductivity than YSZ in the temperature range of 300-1100 ^{o}C and better long term stability than any other Sc-ZrO_2-based electrolyte.

$CaTi_{1-x}Al_xO_{3-\delta}$, $CaTi_{1-x}Mg_xO_{3-\delta}$ and $La_{1-x}Ca_xAlO_{3-\delta}$ fall under the second family of oxide conductors with a perovskite structure. Takahashi [103] found $CaTi_{1-x}Al_xO_{3-\delta}$, with x = 0.3 as one of the suitable electrolyte material for SOFC.

Steele *et al.* [104] and Vanbaelinghen *et al.* [105] have reported the third category of oxide conductors. These are CaO or SrO doped Y_2O_3, La_2O_3, Sc_2O_3 etc. The ionic conductivity of above mentioned systems are lower than YSZ at 900^{o}C except $(La_2O_3)_{0.945}(SrO)_{0.055}$ system. It has slightly higher conductivity than YSZ with relatively low activation energy (E_a = 0.55eV). Unfortunately, this material can not be used as electrolyte in SOFC since it decomposes in the presence of water vapour or carbon dioxide.

$La_{0.8}Sr_{0.2}Ga_{0.83}Mg_{0.17}O_{2.815}$ (LSGM) doped with Ni or Co in place of the Mg have been identified as a electrolyte by K. Huang *et al.* [106] which indicated that below 700^{o}C, LSGM could be good electrolyte material.

Recently, Amit Sinha *et al.* [107] prepared undoped and Ca-doped $GdAlO_3$ systems. These systems exhibited good sinteribility and achieved high experimental

density. Undoped $GdAlO_3$ exhibited a total conductivity of 1.3×10^{-3} S cm^{-1} and it can be increased up to 15% with calcium doping. The conductivity versus 1/T plots for some electrolyte materials are given in figure 2.1.

In recent years, much consideration is being given to search electrolyte materials for solid oxide fuel cell, which exhibits high ionic conductivity at intermediate temperature (700^{o}C). Above described electrolytes, in general showed low ionic conductivity below 800°C.

Hu *et al*. [108] investigated Bi_2O_3 based compositions for the intermediate temperature range. Various authors reported four polymorphs of Bi_2O_3 viz: α, β, γ and δ in the literature [7, 34]. Bi_2O_3 based systems have higher conductivity than YSZ at the same temperature [109]. In these systems, the high conductivity δ (FCC) phase can be stabilized by using various dopants such that aliovalent. Doped Bi_2O_3 has highest conductivity as compared to any other known solid electrolyte system.

However, Helfen *et al.* [110] have stabilized the electrodeposited thin film (1-2 μm) of δ–Bi_2O_3 at room temperature. The long term stability of the film was also checked by XRD of aged sample (aging time 1-year).

The stabilization of δ – Bi_2O_3 phase can be achieved at lower temperatures than its transition temperature $\alpha \rightarrow \delta$ (705^{o}C – 840^{o}C) by the substitution of bismuth with rare earth dopants such as Y, Dy or Er and their combinations with higher valency cations, such as W or Nb [112-117]. The maximum conductivity in the binary systems is observed for Er- and Y-containing phases, namely $Bi_{1-x}Er_xO_{1.5}$ ($x \approx 0.20$) and $Bi_{1-x}Y_xO_{1.5}$ ($x = 0.23$-0.25). However, both binary and ternary solid solutions with the disordered fluorite structure are metastable at temperatures below 500-600^{o}C. Moreover, these compounds undergo a slow phase transformation with time [113, 118-121]. The aging

effects on these systems also reduce the conductivity. Although such degradation can be suppressed partly by the incorporation of higher valence dopants such as Zr^{4+}, Ce^{4+}, Nb^{5+} or W^{6+} for Bi_2O_3 [119, 120, 122, 123]. However, in these systems, it is not possible to avoid phase transformation completely.

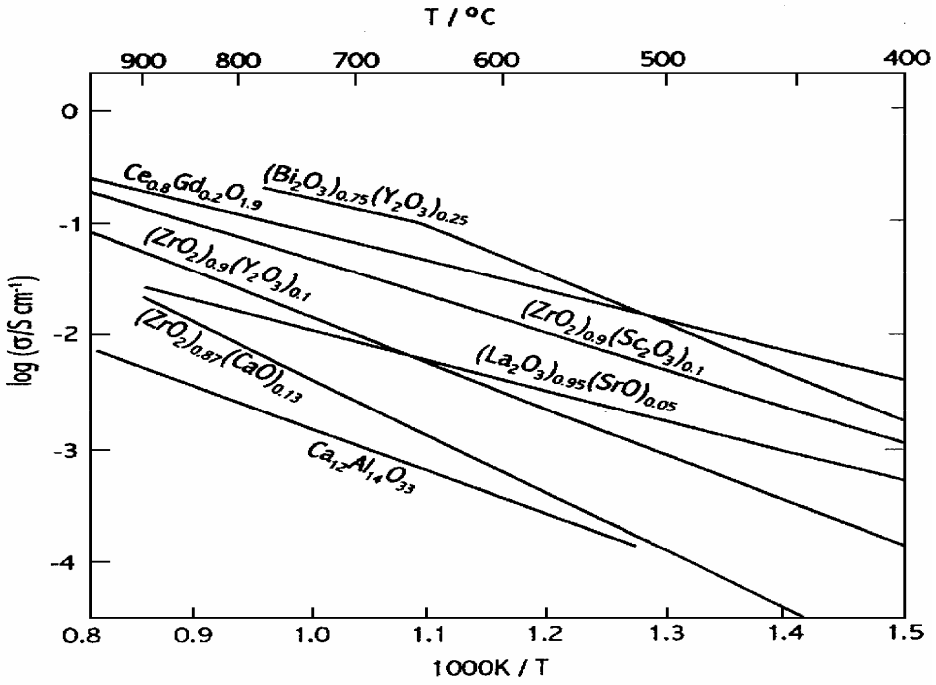

Fig. 2.1 Temperature dependence of electrical conductivity for oxide ion conductors Ref. [111]

Jiang *et al.* [117] have developed Dy_2O_3 and WO_3 doped Bi_2O_3 electrolyte that exhibits higher conductivity than 20 mol% ebria stabilized bismuth oxide (20ESB). The conductivity behaviour of these systems is given in figure 2.2. Apart from this, conductivity behaviour of several Bi_2O_3-based systems [112, 117, 124, 125] is also given in figure 2.2. The dopants were selected on the basis of their polarizability and its effect on structural stability and conductivity.

Praseodimia (Pr) and Zirconia (ZrO_2) doped Bi_2O_3 were synthesized and studied by Naumovich *et al*. [126]. However, it has been demonstrated that solid electrolytes of the system Bi_2O_3-ZrO_2-Y_2O_3 have important advantages over other systems due to higher conductivity and lower polarizability.

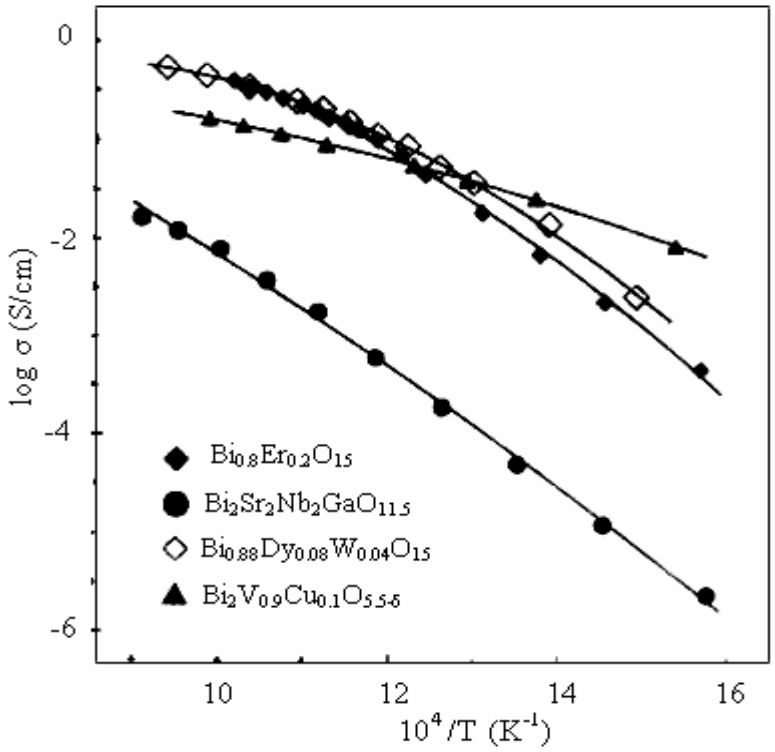

Figure 2.2 Conductivity of several Bi_2O_3-based systems Ref. [112, 117, 124, 125]

Takahashi *et al.* [127] examined the electrical conductivity, ionic transference number and phase equilibrium of Bi_2O_3-M_2O_5 (M = V, Nb and Ta).

The initial work of Debreuille-Gresse [128] for the phase equilibrium of Bi_2O_3-V_2O_5 showed a $BiVO_4$ phase. Perovskite systems also exhibit a high ionic conductivity when cations are used to form a solid solution that shows a high ionic conductivity. Lu and Steele [129] investigated ionic conductivity behaviour of $BiVO_4$ systems. Doped $BiVO_4$ systems showed good ionic conductivity at lower temperatures. The work on

$BiVO_4$ and $Bi_4V_2O_{11}$ systems has been investigated extensively by many researchers due to its attracting transport properties. This system exhibit very complicated structure. Abraham *et al*. [67] is the first who investigated the structure of $Bi_4V_2O_{11}$. According to them, $Bi_4V_2O_{11}$, consists of Bi_2O_3 layers interleaved with the pervoskite like sheets of V_2O_5 with the perovskite slab containing oxygen vacancies $V_o^{\cdot\cdot}$ responsible for the high oxide ion conductivity [67, 72]. The vanadium is in a highly distorted octahedral site. It is assumed that the numerous oxygen vacancies in the perovskite-like sheets, and shifts of the cations from their ideal positions are responsible for the high oxide ion mobility and the low activation energy in this phase**.** The schematic view of $Bi_4V_2O_{11}$ crystal structure is shown in figure 1.5. $Bi_4V_2O_{11}$ compound exhibits three structural phases (α, β and γ). The phase transition temperatures of above mentioned compound ($Bi_4V_2O_{11}$) are as follows:

1. α to β at 447^{o}C
2. β to γ at 567^{o}C
3. γ to γ' at 877^{o}C
4. liquid above 887^{o}C.

α - $Bi_4V_2O_{11}$ is indexed as face centered orthorhombic cell, with cell parameters a = 5.533 Å, b = 5.611 Å and c = 15.28 Å. β-$Bi_4V_2O_{11}$ is tetragonal cell with lattice parameters $a = b$ = 11.285 Å and c = 15.42 Å at 502^{o}C. γ - $Bi_4V_2O_{11}$ is found to be tetragonal with $a = b$ = 3.98 Å and c = 15.42 Å with space group 14/mmm [72].

Below, 567^{o}C temperature, α and β phases in $Bi_4V_2O_{11}$ systems are more ordered and has larger unit cell with the unit cell with markedly lower conductivity [72]. On the other hand, γ- phase is disordered and exhibit higher ionic conductivity than α and β phases. However, disordered γ- phase could be stabilized at room temperature by partial

substitution of various metallic ions for vanadium. These doped $Bi_4V_2O_{11}$ compounds have been collectively termed BIMEVOX and characterized by the formula $Bi_2V_{1-x}Me_xO_{11}$, where Me is the substituting metal cation and x is the molar substitution of the metal cation for vanadium. A wide range of ions have been tried to stabilize high temperature γ-phase, as shown in table 2.1 with the references.

Table 2.1 Substitution of various cation for vanadium in bismuth vanadate

Cation substitute	Ref.	Cation substitute	Ref.
Nb^{5+}	130	La^{3+}	133
Ta^{5+}	130	Y^{3+}	133
Ge^{4+}	131	Co^{3+}	134,135
Sn^{4+}	132	Cu^{2+}	130,131,136-143
Ti^{4+}	130-132	Mg^{2+}	130
Zr^{4+}	130, 132	Ni^{2+}	130,137,138
Al^{3+}	130,131,133	Pb^{2+}	132
B^{3+}	133	Zn^{2+}	131, 136
In^{3+}	133	Li^{+}	131

In the sequence of doping to stabilize high conducting γ - $Bi_4V_2O_{11}$ phase, single valent cations were also used [131, 144, 145]. However, monovalent substitution for vanadium site could not provide the desired conductivity. Therefore, monovalent doped $Bi_4V_2O_{11}$ could not be used as an electrolyte in SOFCs.

The dopants in the family of Me^{2+} has been the most widely investigated. Copper doped $Bi_4V_2O_{11}$ is the most attractive and first member of BIMEVOX family because of its very high conductivity (10^{-2} S cm^{-1} at 350°C) [146].

Abraham *et al.* [72] studied the $Bi_2V_{1-x}Cu_xO_{5.5-3x/2}$ series from x = 0 - 0.12. From $x = 0 \leq x \leq 0.07$, the sample was found to be orthorhombic and isotype with the α - $Bi_4V_2O_{11}$. However, from x = 0.07 to 0.12, the compound was observed to be highly

conducting γ - $Bi_4V_2O_{11}$ phase at room temperature. The conductivity of $Bi_2V_{0.9}Cu_{0.1}O_{5.35}$ was found to be 3×10^{-3} S cm^{-1} at 237°C.

Dygas *et al.* [140] studied the impedance of a polycrystalline sample of $Bi_2V_{0.9}Cu_{0.1}O_{5.35}$, sintered from crushed single crystals. A time dependence of conductivity was found in a limited temperature range similar to the earlier observations for single crystals. Prolonged annealing at about 425°C decreased the ionic conductivity, however, the high conductivity state was recovered when same system was heated at 550°C.

According to Simner *et al*. [147] copper-substituted bismuth vanadate ($Bi_2V_{0.9}Cu_{0.1}O_{5.35}$), known as BICUVOX, possesses high oxygen ion conductivity at 300°C. The ionic conductivity of this compound at 300°C (~1×10^{-3}S/cm) is 50 to 100 times greater than any other solid electrolyte.

In the literature, some ambiguity was reported on the dopant concentration which is necessary to stabilize the tetragonal γ - phase. According to Pernot *et al.* [138], tetragonal phase can be stabilized at 7% of Cu doping whereas Goodenough *et al.* [130] and Lee *et al*. [148] reported a higher value (15%) of the dopant to stabilize the same phase.

Doping on the desired sites in $Bi_4V_2O_{11}$ system [148, 149] is very important. In most of the cases, it is assumed that vanadium is replaced without disturbing the bismuth oxide layer. Based on Bi_2O_3-V_2O_5-MeO (Me = Co, Cu, Zn, Ca, Sr) phase diagrams, Lee *et al.* [145, 148] examined the probability of dopant occupancy in $Bi_4V_2O_{11}$ system, they concluded that the Bi↔V and Me↔Bi may also take place in addition to Me↔V substitution depending upon the substituting cation.

The similar conclusion was also drawn by Lazure *et al.* [135] for $Bi_2(V_{1-x-y}Co_xBi_yO_z)$. According to them, maximum cobalt doping (x = 0.25) was associated with a slight bismuth excess (y = 0.04) in this system. The bismuth is believed to replace the vanadium in the perovskite region and there is no indication of bismuth insertion into an interstitial site.

Reseilhuber *et al*. [142] observed the effect of grain size and processing condition on the ionic properties of BICUVOX and reported the difference in the conductivity between the large grains and small grains in the fired ceramic material.

Anne *et al.* [137] and Pernot *et al*. [138] also studied the structure and conductivity of $Bi_4V_2O_{11}$ with Cu and Ni dopants and reported that high temperature γ-phase with highest conductivity could be stabilized at room temperature. These systems showed the hystersis behaviour on the conductivity during heating and cooling. The ionic conductivity does not change very much on heating, but it observed the increasement in conductivity during cooling by more than one order of magnitude for α-phase.

The effect on conductivity of Zn and Ni substitution in $Bi_4V_2O_{11}$ was studied by P.Kurek *et al.* [150]. The conductivity values have been reported to be 1.28 x 10^{-4} S cm^{-1}, 1.19 x 10^{-4} S cm^{-1} for Zn and 3.05 x 10^{-4} S cm^{-1}, 2.78 x 10^{-4} S cm^{-1} for Ni at 227^{o}C during heating and cooling cycles respectively. Decreasing trend in conductivity with time was also observed for BIZNVOX during heating and cooling in certain temperature ranges. They explained on the basis of possible loss of vanadium during the preparation procedures which may be due to the shifting of lower V/Me ratio than actual of the formula $Bi_2Me_{0.1}V_{0.9}O_{5.35.}$

The conductivity reported for La and Al-substituted $Bi_4V_2O_{11-\delta}$ on vanadium site is 1.4×10^{-4} S cm^{-1} at 300^{o}C and 1.1×10^{-1} S cm^{-1} at 600^{o}C respectively [151]. The doping

of Cr^{3+} for V^{5+} in $Bi_4V_2O_{11}$ compound could not stabilize the γ-phase at room temperature. When the substitution of x in $Bi_4V_{2-x}Cr_xO_{11-\delta}$ is >0.05, β-phase was suppressed and $\alpha \leftrightarrow \gamma$ phase transition occurred [152]. Moreover, the conductivity also decreases drastically for this particular dopant. Substitution for V^{5+} with Fe^{3+} leads to α, β and γ- phase stabilization [152]. The stabilization of β and γ-phases depend on the amount of iron. The best value of ionic conductivity of the order of 10^{-4} S cm^{-1} at 300°C was observed in the composition range of $0.1 \leq x \leq 0.5$ [152].

Lazure *et al.* [135] reported direct $\alpha \rightarrow \gamma$ transition in heating cycle, whereas two successive $\gamma \rightarrow \beta$ and $\beta \rightarrow \alpha$ transitions occur on cooling in $Bi_2V_{0.95}Co_{0.05}O_{11-\delta}$. This result underlines the high sensitivity of these phases with respect to thermal condition.

In addition to Ge^{4+}, which has been mainly investigated for its ferroelectric characteristics [131], Ti^{4+} has been the most widely studied dopant in BIMEVOX. Goodenough *et al*. [130, 153] observed that $Bi_4V_{1.80}Ti_{0.20}O_{11}$ is most promising composition for high conductivity. Yan *et al*. [132] has reported that the ionic conductivity increases with increasing Ti concentration up to x = 0.30 in $Bi_4V_2O_{11}$. It has the higher ionic conductivity ($\sigma = 4x10^{-4}$ Scm^{-1} at 225°C) than other substitution in $Bi_4V_{2-x}M_xO_{11}$ (M^{4+}= Zr, Sn, Pb, Ti). The ionic conductivity of x = 0.20 composition at 225°C varies in the order of $\sigma_{(Ti)} > \sigma_{(Sn)} > \sigma_{(Zr)} > \sigma_{(Pb)}$ in agreement with the trend of decreasing activation energy. The ionic conductivity of γ -$Bi_4V_{1.80}Ti_{0.20}O_{11}$ and γ -$Bi_4V_{1.80}Cu_{0.20}O_{11-\delta}$ measured by Yan *et al.* [132] are comparable to those reported by Gopal Krishanan *et al*. [131] on the same composition of BIMEVOX. However, the conductivities of γ-$Bi_4V_{1.7}Ti_{0.30}O_{10.85}$ are about one order of magnitude higher than that of γ-$Bi_4V_{1.80}Cu_{0.20}O_{11-\delta}$.

They pointed out the importance of the defect pair formation on conductivities. These defect pairs are formed due to interaction between oxide ions vacancies [154].

γ - phase can also be stabilized with MnO_2 in bismuth vanadate when doping occurs on the vanadium site [155, 156]. The transference number varies from 0.67 to 0.82 when the temperature increases from 550°C to 850°C for $Bi_4V_{1.80}Mn_{0.20}O_{11-\delta}$. The conductivity data show little dependence on x and the measured values are comparable to those reported for the γ-phase [169].

Goodenough *et al.* [130] and Joubert *et al.* [157] made isovalent M^{5+} substitution such as Sb, Nb and Ta leading to the bigger domain of solid solution. This result is likely due to the equality of charge between the dopant cation and substituted (V^{5+}) cation. Antimony exhibits higher value of the ionic conductivity i.e. 10^{-2} Scm^{-1} at 320°C than niobium. The ionic conductivity values are comparable to those obtained with the best BIMEVOX (ME = Cu or Ti).

Uranium is the first substituent ($V^{5+} \leftrightarrow U^{6+}$) that allows the stabilization of γ-type compounds. Substitution of U^{6+} for V^{5+} involves a decrease of oxide ion vacancies, but as demonstrated by Lazure *et al.* [135], the BIMEVOX properties are more sensitive to the dopant ability to affect the long range ordering of the parent compound $Bi_2VO_{5.5}$ than to radius and valency state of the dopant. Thery *et al.* [158] have reported solid solution formation in $Bi_2V_{1-x}U_xO_{5.5+0.5x-y}$ in the compositional range of $0 \leq x \leq 0.06$. Ionic conductivity was measured for $Bi_2V_{1-x}U_xO_{5.5+0.5x-y}$ with x = 0.1 which are comparable with BICUVOX.10 [83] and Bi_2UO_6 [159]. For γ- BIUVOX, best properties are observed for x = 0.10. This confirms the general trend pointed out by Lazure *et al.* [160] for BIMEVOX that the maximum σ values are obtained with x values of the ME dopant content close to the lower limit of the solid solution with γ-type structure.

Goodenough *et al.* [153] tried to substitute higher valent Mo^{6+} and W^{6+} for vanadium site but could not succeed. However, Vannier *et al.* [161] showed that γ - phase could be formed up to substitution of 0.225 with high ion conductivity in the $Bi_4V_{2-x}Mo_xO_{11-\delta}$. They obtained solid solution of α-phase for $x < 0.05$ while β-phase in the range of $0.05 < x < 0.225$. Since the V^V/Mo^{VI} substitution implies to decrease the oxygen vacancies. Interestingly, conductivity remains the same throughout the composition range. Therefore, it was concluded that the predominant parameter for determining the conductivity is the structural arrangement. The number of atoms/number of vacancies ratio appears only as a second order parameter. Identical observations have frequently been reported in super ionic conductor [162]. Similar study was also carried out on an quenched sample of W-substituted bismuth vanadate by the same author [163]. This study indicates the stabilization of high conducting γ-phase.

Attempts have also been made to increase the ionic conductivity by double substitution. Vannier *et al.* [164] have attempted the double substitution either on Bi site or on the V site using a variety of dopants. Vannier *et al.* [149] introduced two kinds of atoms in vanadium site (Cu-Ni, Cu-Zn, Ni-Zn, Cu-Mo) and also performed simultaneous substitution for bismuth and vanadium sites (Bi-Pb and V-Cu, Bi-Pb and V-Mo). There was no improvement in the ionic conductivity as compared to single cation doped BICUVOX system. However, it was emphasized that such an approach could be useful to optimize other parameters such as mechanical properties or thermodynamic activity which can be determental for practical applications.

Vannier *et al.* [164] analyzed thoroughly the lead substitution on both sites of bismuth and vanadium as well as alternatively Bi and V sites with different variation of x

and y in $Bi_2V_{1-x}Pb_xO_{(11-3x/2)}$ and $Bi_{2-y}Pb_yVO_{9(11-y)/2}$ respectively. These systems showed the similarity with $Bi_4V_{1.8}Cu_{0.2}O_{11-\delta}$ system.

Goodenough *et al.* [153] also observed the comparable conductivity of $Bi_4V_{1.8}Me_{0.2}O_{11-\delta}$ (Me = Ti, Nb). The substitution of Pb, Nb for Bi and V sites in $Bi_{3.8}Pb_{0.2}V_{1.8}Nb_{0.2}O_{11-\delta}$ compound. The conductivity of Pb and Nb doped systems is comparable to that of $Bi_4V_{1.8}Cu_{0.2}O_{11-\delta}$.

Various researchers have studied the role of dopants and its effect on the conductivities using various techniques. Basically, most of the researchers emphasized that the perovskite layers in $Bi_4V_2O_{11}$ compound are responsible for high ionic conductivity due to oxygen vacancies. This hypothesis is confirmed by Aboukais *et al*. [165] using EPR and UV-visible spectroscopy to characterize the copper and vanadium environment in BICUVOX. The data were consistent with distorted oxygen octahedra around the copper with a compression of the apical oxygen. In addition, they reported that the vanadium was present predominately as V^{5+} rather than V^{4+} which is in contrast with the results reported by Delmaire *et al*. [166] about the reduction of $Bi_4V_2O_{11}$ under a hydrogen flow. The reduction of V^{5+}-V^{4+} leads to the formation of $Bi_4V_2O_{10.66}$.

The nature and reversibility of the modifications that may affect $Bi_4V_2O_{11}$ [167] and BIMEVOX [168, 169] system under reducing conditions, have also been investigated by Huve *et al*. [167]. Using high temperature TEM, with high resolution and *in situ* XRD, α - $Bi_4V_2O_{11}$ converts into a γ - type structure at 330^oC under hydrogen atmosphere. The reduction of V^{5+} to V^{4+} lead to form of a new insulator phase i.e. $Bi_2(V^{5+}_{1-x}V^{4+}_x)O_{5.5-x/2}$ with x = 0.33. From the structural point of view [170], this phase is different than γ-phase.

E. Capoen *et al.* [171] performed and confirmed an *in-situ* neutron diffraction on BIMEVOX ($Bi_4V_2O_{11}$ and $Bi_2V_{0.9}Co_{0.1}O_{5.35}$) membranes for the electrochemical reduction of these electrolytes. Under these conditions, the structure of the BIMEVOX compound was retained. However, a slight change in the unit cell parameters due to slight variation in oxygen stoichiometry was observed.

Abraham *et al.* [172] studied the conduction mechanism and solid solution formation in terms of the defect structure of the BIMEVOXes. Based upon two theoretical models, they proposed a general defect equation to form the solid solution. Basically, these models consist Equatorial Vacancy (EV) model and Apical Vaccancy (AV) model in which vacancies are assumed to be located exclusively in the bridging sites and non-bridging apical sites in the vanadate layer respectively. The solid solution limits are found to vary not only with charge of the dopant ion, but also with the coordination number of the metal dopant. In most cases it is found that the EV model yields theoretical solid solution limits close to experimental values.

Abrahams *et al*. [173] also proposed the conduction mechanism in divalent substituted BIMEVOXes system. The main theme of this model is polarizability and arrangement of the Bi $6s^2$ lone pairs, variable coordination of V in oxide systems and the large vacancy concentration in the vanadate layer. This unique combination in the BIMEVOXes enables high ionic conductivity at lower temperature than other electrolytes. This involves positional exchange of oxygen ions with vacancies in the equatorial plane of the vanadate layer.

Zhou *et al*. [73] investigated location of oxygen vacancies in the Bi_2O_2 layers by structural analysis of $Bi_4V_2O_{11}$. These results are contrary to above results which

assumed the presence of vacancies in the vanadate layer. This necessitates to reconsider commonly applied mechanism of oxide ion conductivity based on oxygen vacancies in the vanadate layer.

In addition to the well known yttria stabilized zirconia based electrolytes, that has good stability with higher ionic conductivity, there is a need to develop an electrolyte which shows higher ionic conductivity at lower temperature with less aging effect so that it can be used for longer periods. A replacement of YSZ, which has good ionic conductivity at lower temperature than YSZ would be immensely helpful to reduce material and fabrication problems with improved cell reliability during prolonged operation. Recent evidences indicate that fast oxide ion conductors seem the most promising materials for low temperature ($T < 600^{o}C$). New field of applications have emerged because of the significant reduction of operating temperatures with better properties. Doped CeO_2 undergoes large departures from stoichiometry at elevated temperatures in reducing atmospheres with parasitic electronic conductivity. The application of the Bi_2O_3 electrolytes has been seen as an alternative for solid oxide fuel cell. From this point of view, doped-Bi_2O_3 is a very interesting material and forms a vast array of solid solutions having high oxygen ion conductivity. The ionic conductivity and phase stabilization depends on the dopants and its chemical nature. A number of different dopants were examined and studied. Based on these studies, family of the BIMEVOX systems presently exhibit the most attractive properties to use an electrolyte for SOFC which can work at lower temperature. In addition to this, the transport properties of BIMEVOX exhibit other interesting features such as including anisotropic conductivity and order disorder transitions. However, even after extensive research on Bi_2O_3-based solid electrolytes, a systematic study does not exist. Moreover, a correlation among

various parameters is still required to check their suitability and applicability as an electrolyte for SOFC. The microstructural effects on the conductivity, variation in processing condition are also important aspects to use these materials as electrolyte for SOFC's applications.

In order to solve these problems, an attempt is made to achieve higher ionic conductivity by doping at V and Bi site both in BIMEVOX system. A systematic study over a wider range of composition has led to draw certain conclusion on the basis of microstructural, crystal structure and processing conditions.

Chapter III

Experimental Procedures

Overview

In this chapter, the procedure adopted to prepare samples from raw materials is described. The heat treatment cycle(s) required for synthesis of compounds is described. Finally, the procedure to prepare pellets from these synthesized compounds is also described. Various techniques which are used to characterize the samples are given. As prepared samples after sintering were characterized by X-ray diffraction (XRD), differential scanning calorimetry (DSC) / differential thermal analysis (DTA) and scanning electron microscopy (SEM). The gold sputtered pellets were used to measure a.c. conductivity.

3.1 Raw Materials

In the present study, raw materials used for preparing the samples were Bi_2O_3 (99%, Loba chemie), V_2O_5 (99%, CDH), CuO (99.99%, CDH), Ti_2O_3 (99.9%, Sigma Aldrich), Al_2O_3 (99.9%, CDH), Cr_2O_3 (99.9%, Sigma Aldrich), MnO (99%, Sigma Aldrich), Ga_2O_3 (99.995, Sigma Aldrich), As_2O_5 (99.99%, Sigma Aldrich), PbO (99%, CDH), La_2O_3 (99.9%, CDH) and Gd_2O_3 (99.9%, CDH). All these materials were used without any further purification.

3.2 Sample Preparation

For sample preparation, the following procedure was adopted:

3.2.1 Powder Preparation

Powders of following eleven different systems were prepared:

Parent System

(i) $Bi_4V_2O_{11}$

Substitution on vanadium site

(ii) $Bi_4V_{2-x}Cu_xO_{11}$

(iii) $Bi_4V_{2-x}Ti_xO_{11}$

(iv) $Bi_4V_{2-x}Al_xO_{11}$

(v) $Bi_4V_{2-x}Cr_xO_{11}$

(vi) $Bi_4V_{2-x}Mn_xO_{11}$

(vii) $Bi_4V_{2-x}Ga_xO_{11}$

(viii) $Bi_4V_{2-x}As_xO_{11}$

Substitution on bismuth site

(ix) $Bi_{4-x}Pb_xV_2O_{11}$

(x) $Bi_{4-x}La_xV_2O_{11}$

(xi) $Bi_{4-x}Gd_xV_2O_{11}$

The powders of each system were prepared by solid-state reaction technique by taking stoichiometric amounts of constituent oxides for the mentioned systems. For all the above mentioned systems, composition x = 0.1, 0.2, 0.3 and 0.4 was selected. For each system, required amount of raw materials as per the stoichiometric ratio were taken. These powders were first mixed in wet medium (acetone) using mortar pestle for an hour to break any large agglomerates. The hand ground powders are further ball milled for two hours to reduce the particle size. The ball milling was done using porcelain balls in porcelain jar (Retsch, Germany, Model S 1000). The mass to ball ratio for each system was 1**:**2 which was kept constant for each milling. The resulting mixture was dried in air, ground thoroughly to homogenize it and then calcined at 700 ^oC in silica crucibles for 12 h. in air. The calcination process was carried out in a resistance heating furnace **(**(Nutronics, India)**.** Before calcination, the furnace was calibrated by chromel alumel thermocouple and calcination was done in hot zone where fluctuation in temperature was ± 2 ^oC. The obtained agglomerated mass was ground and mixed in acetone media for half an hour. The dried powders were recalcined at 800 ^oC for 12 h.

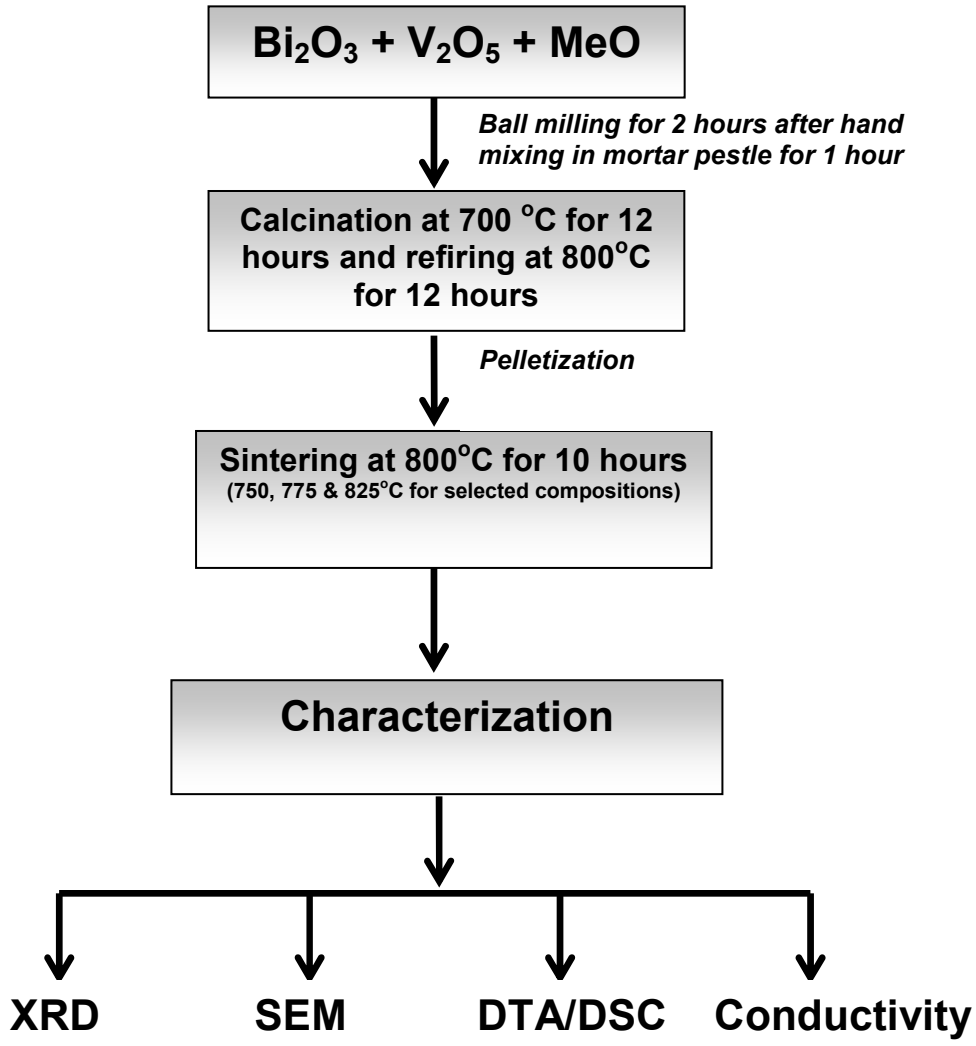

Fig. 3.1 Flow chart of the experimental procedure

3.2.2 Pellets Preparation

The calcined powders were crushed again and mixed with 10 mole percent polyvinyl alcohol (PVA). Known weight of dried powders was transferred in a die which manufactured from hardened die steel by Central Institute of Hand Tools, Jalandhar, Punjab (India). The die alongwith punch was kept below hydraulic press (Polyhedron, India; Model 5010) and a compaction pressure of 124 kg/cm^2 was applied slowly. After waiting for 1 minute, the pressure was released. Afterward the compacted mass was ejected out.

3.2.3 Sintering

The pellets obtained after compaction were sintered at 800 ^{o}C for 10 hours in air in a calibrated resistance heating furnace. Some selected samples were also sintered at different sintering temperature (750-825 ^{o}C) to optimize the processing condition for achieving better properties. The flow sheet of the experimental procedure adopted is given in figure 3.1.

3.3 Characterization of Materials

Characterization is an integral part of the study of any particular solid electrolyte. These include the understanding of polymorphism, structure determination, conductivity measurement and structure-conductivity relationship. For the analysis of above parameters, the sintered samples were characterized using X-ray diffraction (XRD), differential scanning calorimetry (DSC) / differential thermal analysis (DTA), scanning electron microscopy (SEM) and conductivity was measured by AC - impedance spectroscopy technique. The details of these techniques are given below:

3.3.1 X-Ray Diffraction

X-ray diffraction is one of the powerful techniques to obtain crystallographic information about a sample. X-ray diffraction technique was used to identify various phases and their volume fraction in the samples. X-ray powder diffractrogram was recorded at room temperature by Rigaku X-ray diffractrogram (Model Geiger flex D max IIIc) using monochromatic CuK_α radiation (λ = 1.5418 Å) at a scan speed of 5^o/minutes. Lattice parameters were calculated with the help of the diffractogram obtained for each sample using Bragg's law as describe below:

$$2d \sin \theta = n \lambda \tag{3.1}$$

where d = interplanar spacing; λ = wavelength of incident x-ray,

θ = diffraction angle, n = integer

The lattice parameters (*a, b, c*) was calculated with interplanar spacing d as follows:

$$\frac{1}{d^2} = \frac{h^2}{a^2} + \frac{k^2}{b^2} + \frac{l^2}{c^2} \quad \text{(orthorhombic)} \tag{3.2}$$

$$\frac{1}{d^2} = \frac{h^2 + k^2}{a^2} + \frac{l^2}{c^2} \quad \text{(tetragonal),} \tag{3.3}$$

where *h, k and l* are miller indices

The diffraction data of the samples was indexed using standard powder diffraction files provided by International Centre for Diffraction Data -ICDD (formerly known as JCPDS).

3.3.2 Differential Thermal Analysis (DTA) / Differential Scanning Calorimetry (DSC)

Differential thermal analysis (DTA) and differential scanning calorimetery (DSC) are two closely related methods to monitor the behaviour of sample with variation in temperature. DSC is different from DTA on the basis of output obtained from it. The term "differential" indicates the difference between the material under study and an inert reference material. The temperature of the sample and reference is same until some thermal event occurs in the sample. In this manner, the temperature can be found at which any event either absorb or release heat**.** The sample temperature either leads (if the change is exothermic) or lags behind (if the change is endothermic). These changes are attributed to phase transition, order-disorder transitions and chemical reactions.

The present samples were analyzed by both DSC and DTA techniques. The DSC analyses were carried out at a heating rate of 20^{o}C/min. in nitrogen atmosphere using DSC analyzers of Perkin Elmer (Model: Pyris Diamond) from 50 ^{o}C to 900 ^{o}C and Water (Model: SDTQ600) from room temperature to 700 ^{o}C in oxygen atmosphere. Single sample of undoped $Bi_4V_2O_{11}$ was analyzed by Mettler Toledo (Model: Star SW 9.00) at the heating rate of 10^{o}C/min. in air. The DTA measurement was done on titanium doped sample using Perkin Elmer (Model: Pyris Diamond). The sample was examined at a heating rate of 20^{o} C/min. in the temperature range of 50 ^{o}C to 800 ^{o}C in nitrogen atmosphere. Analysis of all the samples was performed by taking alumina as reference sample.

3.3.3 Scanning Electron Microscopy (SEM)

Scanning electron microscope (SEM) is an important tool for microstructural analysis. The microstructural characteristic of the sample correlate the effect of different processing condition with properties and behaviour of materials that involves their microstructural changes. The SEM provides information relating to topographical features, morphology, phase distribution, compositional differences, crystal orientation and presence of defects and their location. The strength of SEM lies in its inherent versatility due to the multiple signals generated, simple image formation process, wide magnification range and excellent depth of field. The SEM micrographs could be taken in two modes *i.e.* secondary emission and back scattered. In the present investigation secondary emission mode was used.

In the present study, scanning electron micrographs of the fractured surfaces of the samples were taken by SEM (Jeol, 840A and JSM, 6100) in order to understand the morphology of phases. Structural analyses were carried out to see the morphological features of grain formation. Grain sizes were also measured directly from the micrographs of the samples as grain size influences the ionic conductivity substantially.

3.4 Conductivity Measurement

Electrical conductivity of a material can be measured directly by imposing a dc current [174] in which voltage drop is measured across the material according to ohm's law. In case of ionic conductors, it is not so straight forward as dc voltage will cause the flow of current due to both ions and electrons. The material will become polarized as electrodes blocks the ion movement and voltage drops to zero. Four probe method [175] is employed to overcome this effect. But this method is suitable when the internal resistance

of the voltmeter is higher than the resistance between voltage probes. Further, conductivity values are measured without any additional information about grain and grain boundary contribution.

Another commonly used alternative is to impose an alternating current signal at a range of different frequencies on sample and measure the impedance. Detailed investigations of the polarization of the solid electrolyte cells by determining the complex admittance were first conducted by Bauerle in 1969 [176]. Impedance spectroscopy is essentially a non-destructive technique which can provide information that can not be obtained by other means. Impedance spectroscopy is a powerful ac measurement technique [177, 178] which has been applied quite successfully to determine a number of important characteristics such as bulk resistivity in case of single crystals and contribution of grain and grain boundary resistance in poly crystalline solid electrolytes. SOFC electrolytes are oxygen ion conductors and can therefore be studied using this technique.

For impedance measurements, a Wheatstone bridge type of apparatus is used, where the resistive and capacitative circuit elements are in series [179, 180] as shown in figure 3.2 (a) and (b) respectively. Interface between the electrode and sample electrolyte therefore adds a double-layer capacitance in series with the simple bulk resistance and with the resistance due to grain boundary effects.

Ohm's law can also be written in terms of impedance, Z, as

$$Z = V(t)/I(t) \tag{3.4}$$

where $V(t) = V_m \sin \omega t$, and

$I(t) = I_m \sin (\omega t + \varphi)$,

Since the total voltage drop across a circuit containing resistive and capacitive elements is a simple sum of the voltage drops across each element, $V = V_R + V_C$; the total impedance for such a circuit is given by Equation (3.5):

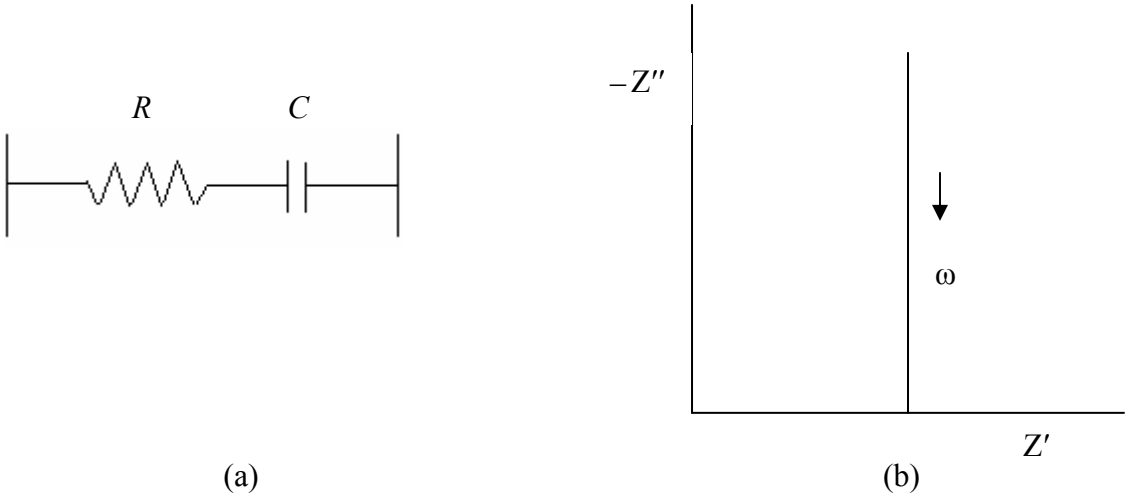

Fig. 3.2 (a) Series combination of R and C, (b) Impedance plot for the equivalent circuit

The impedance of the circuit (fig. 3.2) is given by

$$Z = R + \frac{1}{i\omega C} = R - \frac{i}{\omega C} \tag{3.5}$$

This can be separated into real and imaginary parts as:

$$Z' = R, \quad Z'' = \frac{1}{\omega C}$$

When imaginary part is plotted against the real part, the above combination gives a vertical spike in the complex Z^* plane as shown in fig 3.2 because Z' of fixed value R and Z'' decreases with increasing ω.

In the case of parallel combination of R and C, as shown in fig 3.3 (a),

$$Z = \left(\frac{1}{R} + i\omega C\right)^{-1} = \frac{R}{1+(\omega RC)^2} - R\frac{i\omega RC}{1+(\omega RC)^2} \tag{3.6}$$

The data when plotted lies in a semicircle in the complex Z^* plane, as shown in fig. 3.3 (b).

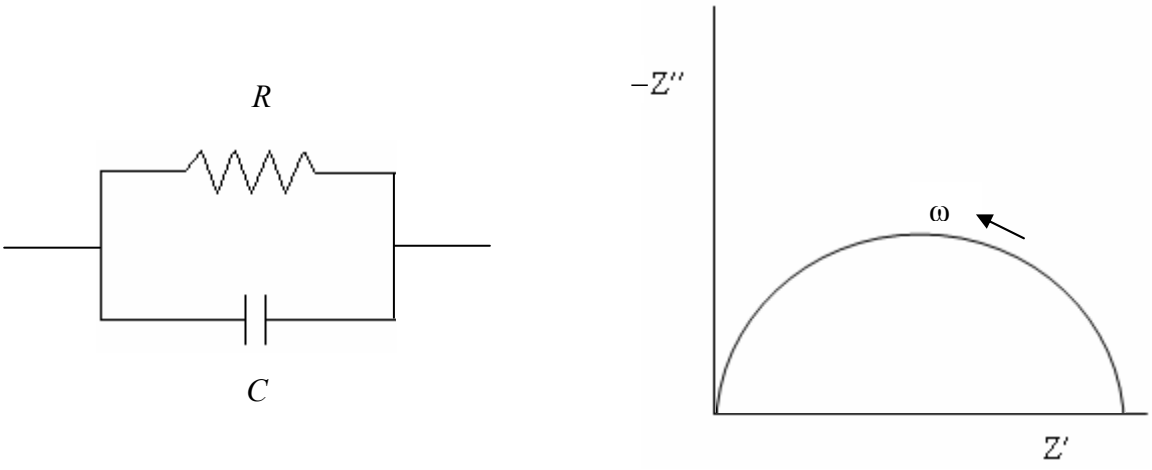

(a) (b)

Fig. 3.3 (a) Parallel combination of R and C, (b) Impedance plot

A simple equivalent circuit model that could be used to represent electrode-electrolyte system consists of three parallel *RC* circuits representing grain, grain boundaries and electrodes, connected in series. The values of the components are obtained from the intercepts of respective arcs on the *Z′* axis and the frequencies at which the arcs show a maximum height. Thus the values of resistivities can be obtained from ac measurements.

In the present study, ionic conductivity was measured by an ac impedance analyzer with multi frequency Hewlett-Packard LCR meter (Model 4274A) in the frequency range of 100 – 100 kHz. The gold sputtered (Ion sputter-JFC, model 1100) pellets were used to carry out a.c. conductivity measurement in the temperature range of 200 to 700^{o}C during cooling cycle.

3.5 Spectrophotometry

Ultraviolet visible Spectrophotometry (UV/VIS) technique was used to confirm the valence state of element.

In this technique, spectrophotometer measures the intensity of light passing through a sample (I), and compares it to the intensity of light before it passes through the sample (I_o). The ratio $\frac{I}{I_o}$ is called the *transmittance* (T), and is usually expressed as a percentage (%T). The absorbance, A, is based on the transmittance and can be calculated by using the following equation:

$$A = -\log(\%T) \tag{3.7}$$

An ultraviolet-visible spectrum is essentially a graph of light absorbance versus wavelength in a range of ultraviolet or visible regions.

The samples for the spectrophotometry characterization were dissolved in 70% hydrochloric acid. Absorption spectra of the samples in the ultraviolet visible region in the wavelength range from 190 nm to 600 nm at the scanning rate of 100 nm / minute were taken by spectrophotometer (Hitachi, model U-2800) to confirm the valance state of titanium in the desired pellet.

Chapter IV

Structural, Thermal and Ionic Conductivity of $Bi_4V_{2-x}Me_xO_{11-\delta}$

Overview

In order to decrease the operating temperature of SOFC, the $Bi_2O_3 - V_2O_5$ system has attracted much attention due to its better ionic conductivity in intermediate temperature range (500-700^oC). In this chapter, the results of $Bi_4V_2O_{11}$ (pure) and various doped $Bi_4V_2O_{11}$ samples are given. These results are obtained from X-ray diffraction (XRD) studies, ionic conductivity measurements, differential scanning calorimetery / differential thermal analysis (DSC/DTA) and scanning electron microscopy (SEM). The results obtained are discussed in the light of phase stabilization, vacancies formation, disordering, grain growth and order-disorder transformation.

4.1 Results and Discussion

In binary Bi_2O_3-V_2O_5 system, $Bi_4V_2O_{11}$ is the end member of a small solid solution domain which occurs in the range of 66.6 - 68.5 mol% Bi_2O_3 at 400 ^oC. It can be extended up to 70% of Bi_2O_3 at 860 ^oC [68]. Various other phases have also been reported in this binary system such as $BiVO_4$ [181, 182], $Bi_{3.5}V_{1.2}O_{8.25}$ [183], $Bi_4V_2O_{11}$ [69], $Bi_{23}V_2O_{44.5}$ [184] and $Bi_8V_2O_{17}$ [185]. Among these, the $Bi_4V_2O_{11}$ compound is considered as the best ionic conductor. The high ionic conductivity of this compound is ascribed due to the large number of oxygen vacancies and anion mobility. $Bi_4V_2O_{11}$ is the first member of the Aurivillius family of structures with the ideal composition $Bi_2A_{n-1}B_nO_{3n+3}$ (n = 1) [67, 68]. The structure is composed of $[Bi_2O_2]_n^{n2+}$ sheets interleaved with the perovskite layers of $[VO_{3.5}\square_{0.5}]_n^{n2-}$ (where $\square$ represents an oxygen ion vacancy). The oxygen vacancies located in the perovskite layer undergo ordering with decreasing temperature leading to form structurally distinct polymorphs, α, β and γ of $Bi_4V_2O_{11}$ systems [67]. The γ-phase has a simple tetragonal structure with the ideal symmetry of n = 1 Aurivillius structure (*I*4/mmm). The unit cells of the α- and β-phases can be indexed with orthorhombic structure. Their lattice constants can be correlated to γ-phase $6a\sqrt{2}$; $a\sqrt{2}$; c and $2a$; $\sqrt{2}a$; $\sqrt{2}c$ respectively, where a and c are the lattice constants of the tetragonal γ-phase. It is worthwhile to mention that there is some ambiguity in crystal structure of the three phases owing to twinning [67], occurrence of incommensurate supercell, disordering of oxygens and cations, [72]. It is particularly difficult to describe precisely the position of O^{2-} ion with respect to vanadium atoms in perovskite layer.

4.1.1 $Bi_4V_{2-x}Me_xO_{11-\delta}$ (x = 0)

4.1.1.1 X-ray Diffraction

The X-ray diffraction pattern of prepared sintered sample from stoichiometric amounts of Bi_2O_3 and V_2O_5 was obtained as shown in fig. 4.1.

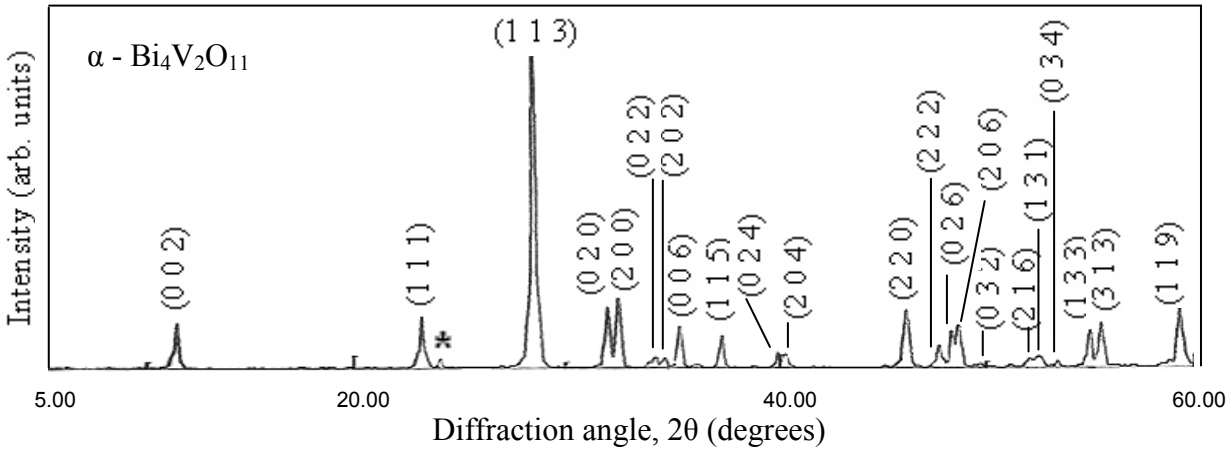

Fig.4.1 XRD pattern of $Bi_4V_2O_{11}$; (*) superlattice reflection

The compound obtained is bismuth vanadate and denoted as $Bi_4V_2O_{11}$. Analysis of XRD pattern indicated the formation of a single phase compound. The XRD pattern of undoped $Bi_4V_2O_{11}$ shows the doublets at $2\theta \approx 31^o$, 39^o, 48^o, 54^o and a very weak reflection at $2\theta \approx 24.2^o$. This weak reflection indicates the superstructure of α - phase of bismuth vanadate ($Bi_4V_2O_{11}$) [72, 186]. All other reflections could be indexed with orthorhombic - $Bi_4V_2O_{11}$ (ICDD card no. 42-0135) except this superlattice reflection [187]. The different structures of α -$Bi_4V_2O_{11}$ such as orthorhombic [76] and monoclinic [188] have been reported. The striking feature of the monoclinic pattern is the presence of a characteristic doublet at $2\theta \approx 45.5^o$ and 46.5^o which is a singlet in the orthorhombic pattern [167, 188]. As shown in figure 4.1, there is singlet at $2\theta \approx 45.5^o$ and 46.5^o which confirms that phase

is orthorhombic. It was observed that the structure of $Bi_4V_2O_{11}$ is highly sensitive to the purity of the initial ingredients [167].

The lattice parameters of the undoped $Bi_4V_2O_{11}$ sample show the close resemblance with reported values. The values of lattice parameters are as follows:

$$a = 5.52 \text{ Å} ; \quad b = 5.60 \text{ Å} ; \quad c = 15.24 \text{ Å}$$

Phase diagram studies [133, 148, 189] of Bi_2O_3 - V_2O_5 system indicated that large numbers of aliovalent cations can be doped into $Bi_4V_2O_{11}$ owing to its versatile host structure. Generally, doping process to stabilize the γ-phase leads to lower contents of oxygen in $Bi_4V_2O_{11}$ [190].

4.1.1.2 Thermal analysis

Thermal analysis of $Bi_4V_{2-x}Me_xO_{11-\delta}$ (x = 0) sample was carried out by differential scanning calorimetery (DSC) and representative plot is shown in figure 4.2.

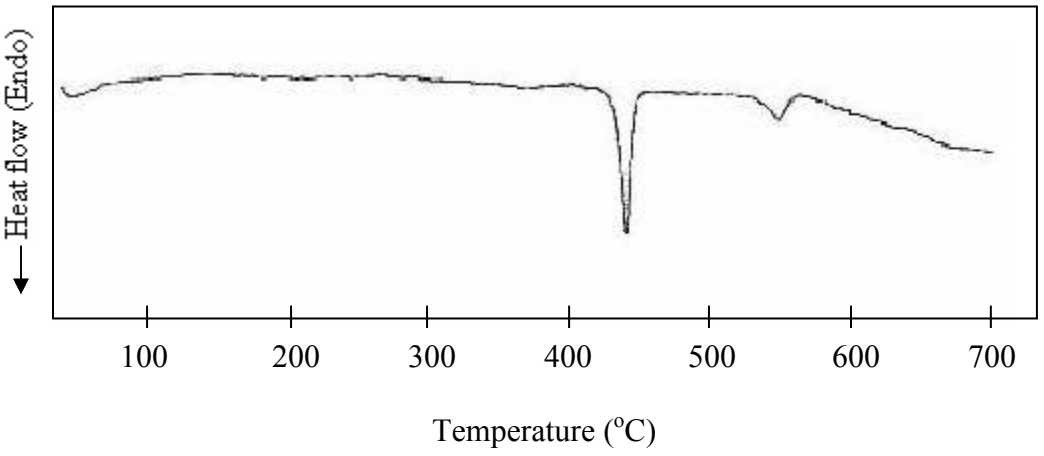

Fig. 4.2 DSC plot of $Bi_4V_2O_{11}$

The DSC plot clearly indicates two endothermic peaks at 453 and 520 °C. However, second peak is broader than first peak which means the second transition is very sluggish.

These transitions are due to α → β and β → γ phase change. Similar transitions were observed by other researcher also [124].

4.1.1.3 Electrical Conductivity

The typical impedance plots obtained by plotting imaginary part Z'' against the real part Z' at different frequencies is shown in figure 4.3.

For temperatures below 400^{o}C, the impedance spectra consisted of one semicircle as represented in figure 4.3 (a). At this temperature, contribution from the bulk and grain boundaries could not be distinguished. At the higher temperatures, an additional spike inclined at 60^{o} to the horizontal is observed at very low frequencies as shown in figure 4.3 (b) . This phenomenon is associated with the polarization of the electrode [139] and suggests that present compound is primarily an ionic conductor [189]. The total sample resistance at each temperature was determined from the intersection point of the spectrum with the real axis and converted into conductivity using the following relation:

$$\sigma = \frac{l}{RA} \tag{4.1}$$

where l is the pellet thickness and A is the pellet cross sectional area.

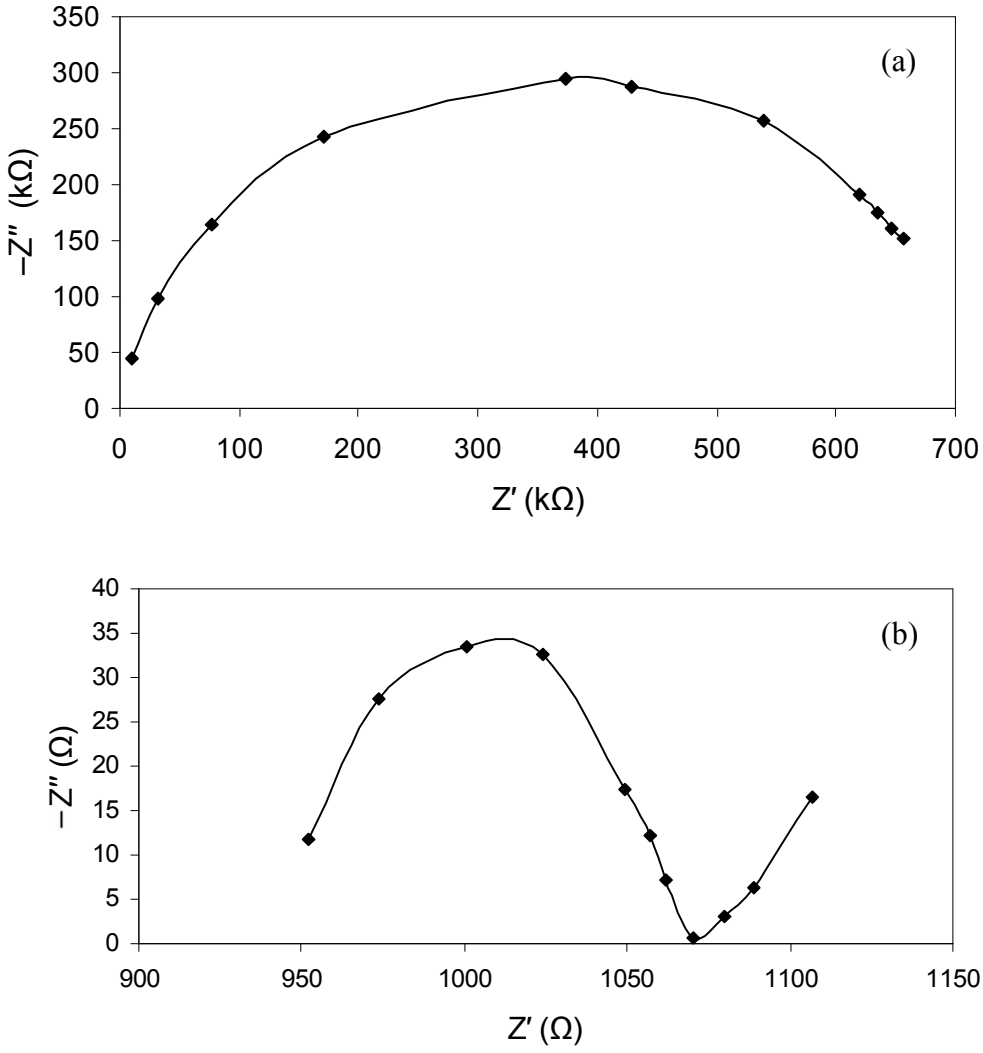

Fig. 4.3 Impedance plot of undoped $Bi_4V_2O_{11}$ at (a) 200 ^oC (b) 500 ^oC

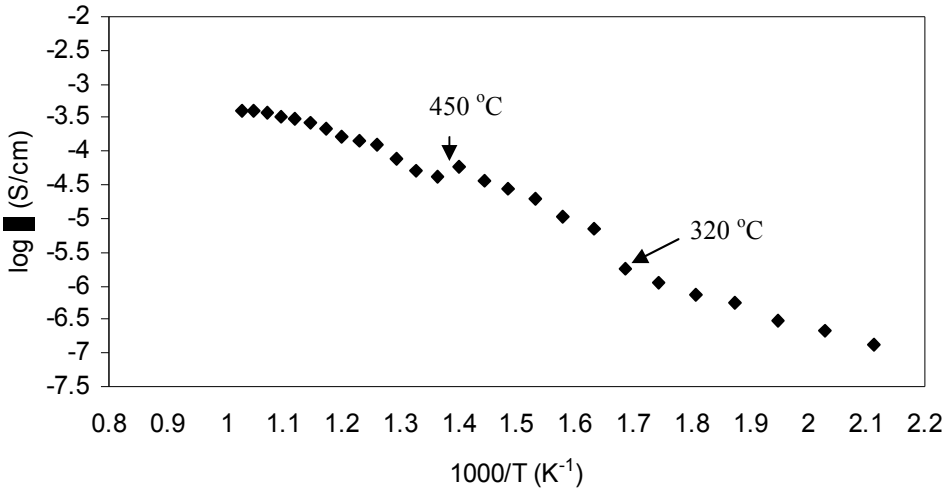

Fig. 4.4 Arrhenius plot of undoped $Bi_4V_2O_{11}$

Arrhenius plot of conductivity for undoped $Bi_4V_2O_{11}$ (fig. 4.4) clearly shows three transition regions which can be ascribed to the three principal polymorphs of $Bi_4V_2O_{11}$. The transitions are observed at 320 ^oC and 450^oC with different values of the activation energies. The large difference in the transition temperatures measured by two different techniques (DSC and conductivity) is attributed to the different measuring mode for DSC (heating) and conductivity measurement (cooling). The $Bi_4V_2O_{11}$ system showed the hystersis behavior during heating and cooling cycle [155]. The conductivity of $Bi_4V_{2-x}Me_xO_{11-\delta}$ (x = 0) sample is 1.12×10^{-6} S/cm at 300 ^oC.

4.1.2 Divalent Substitution

In this section, the results and discussion of partially substituted V^{5+} with Cu^{2+} and Mn^{2+} in $Bi_4V_2O_{11}$ compound are presented.

4.1.2.1 $Bi_4V_{2-x}Me_xO_{11-\delta}$; (Me = Cu^{2+})

4.1.2.1.1 X-ray Diffraction

X-ray diffraction analyses of the powders of the prepared samples were conducted. The XRD patterns for composition x (mol %) = 0.1, 0.2, 0.3, 0.4 are depicted in fig 4.5.

As described in section 4.1.1, superlattice reflection is also observed at $2\theta \approx 24.2^o$ with doublet peaks at $2\theta \approx 31$, 39, 48 and 54^o for x = 0.1 sample. These features characterize the orthorhombic α-polymorph of $Bi_4V_{2-x}Cu_xO_{11\ -\delta}$ for this sample [72]. However, broadening of peak at ~ 32^o as compared to undoped sample (fig.4.1) suggests the small contribution of orthorhombic β-phase in x = 0.1 sample.

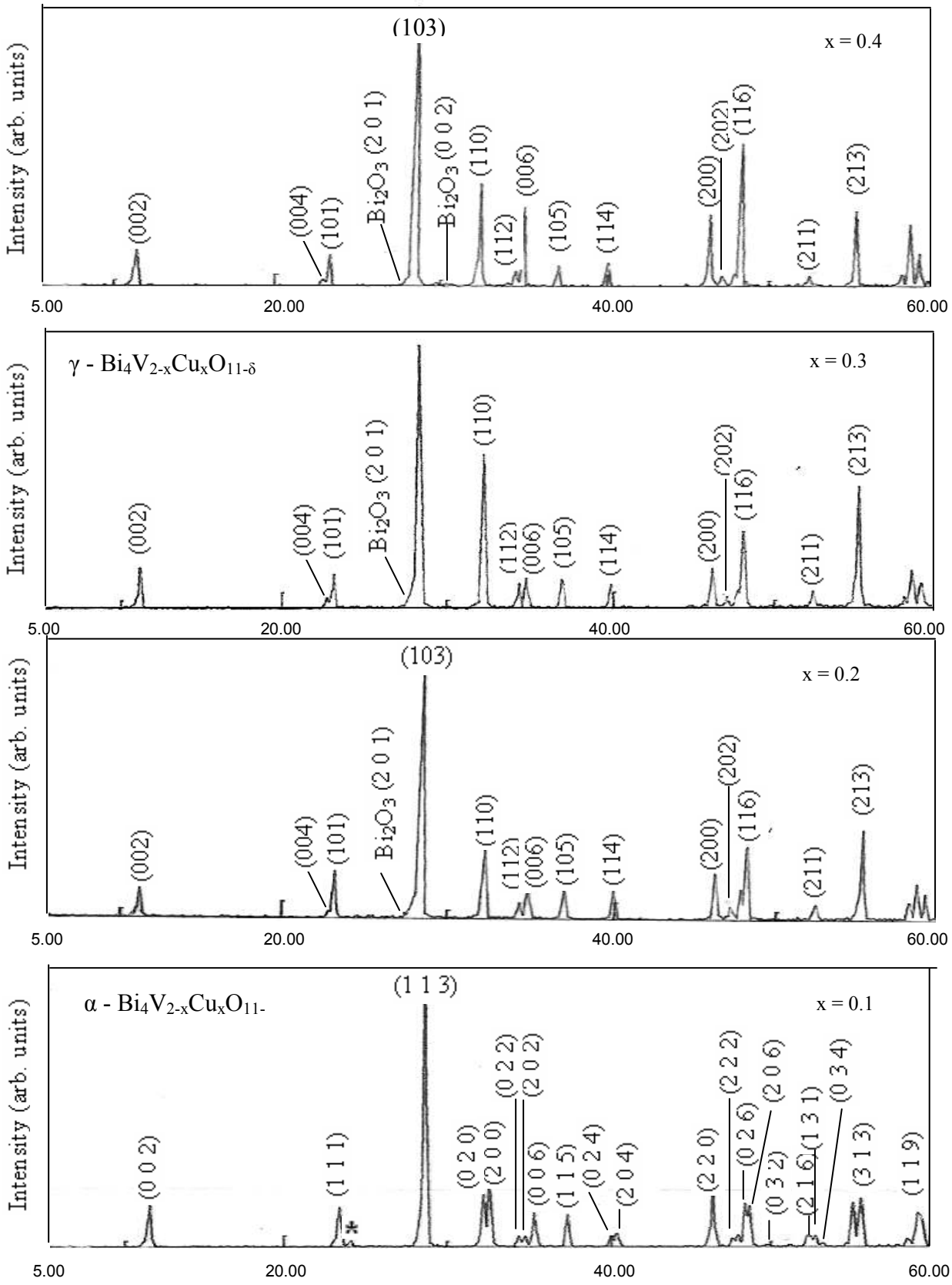

Fig. 4.5 X-ray diffraction pattern of $Bi_4V_{2-x}Cu_xO_{11-\delta}$; (*) superlattice reflection

Comparison of XRD patterns of samples of x = 0 and x = 0.1 do not show any significant change in their d- values except some peak broadening. This may be attributed to disorder enhancement with Cu-doping in x = 0.1 sample as compared to x = 0 sample.

On the other hand, no such type of behaviour of α-phase is observed for $0.2 \leq x \leq 0.4$ samples. XRD patterns of these samples are indexed with tetragonal γ-phase [138].

The peaks of γ-phase of all the systems have been indexed with ICDD card no. -44-0358. However, peak of (004) at $2\theta \approx 23^{o}$ has been indexed on matching with the substituted γ- $Bi_4V_2O_{11}$ (ICDD card no. 47-0481, 48-0273 and 48-0279). The shifting of peaks at lower diffraction angle (2θ) for x = 0.2 may further be manifestation of γ-phase stabilization at room temperature.

Apart from γ-phase, these samples ($0.2 \leq x \leq 0.4$) also exhibit the unreacted Bi_2O_3. The peaks of Bi_2O_3 are indexed with (ICDD card no. 78-1793). The volume fraction of Bi_2O_3 phase increases with increasing dopant contents. Lattice parameters of the samples have been determined from XRDs. The lattice parameters for the compositions $0.1 \leq x \leq 0.4$ are given in table 4.1. The change in *c*-direction lattice parameter from x = 0 to x = 0.1 is owing to size difference between Cu^{2+} and V^{5+} (0.72 Å, and 0.59 Å, respectively [191]) and V^{5+} may occupy the site along *c*-direction. For the samples of compositions (x = 0.2, 0.3 and 0.4) in the γ-phase region, the cell parameters did not show any trend. However, the significant increase in volume for x = 0.4 sample suggests the presence of relatively large amount of Bi_2O_3 as shown by extra peaks in XRD (fig. 4.5).

Table 4.1 Lattice parameters of $Bi_4V_{2-x}Cu_xO_{11-\delta}$

Composition	*a* (Å)	*b* (Å)	*c* (Å)	Volume (Å^3)
x = 0.1	5.51	5.60	15.28	471.48
x = 0.2	3.94	3.94	15.51	240.77
x = 0.3	3.77	3.77	15.52	220.58
x = 0.4	3.93	3.93	15.38	237.54

4.1.2.1.2 Thermal Analysis

Differential scanning calorimetry measurement (fig. 4.6) was performed on $Bi_4V_{2-x}Cu_xO_{11-\delta}$ which indicated the transitions at 479 ^oC, 483 ^oC, 520 ^oC and 531 ^oC for x = 0.1, 0.2, 0.3 and 0.4 samples respectively.

Figure 4.6 shows that phase transition temperature goes on increasing with dopant concentration. A very small exothermic peak at the temperature of ~725 ^oC for x = 0.1, 0.2, 0.3 and 0.4 samples was observed which may be assigned to unreacted Bi_2O_3 transforming to *fcc* δ-Bi_2O_3 as also confirmed by XRD. One additional peak at 764.06 ^oC and 777.85 ^oC in DSC measurement for x = 0.3 and 0.4 might be attributed to melting of Bi_2O_3. In addition to above peaks, sample x = 0.4 also exhibit one extra peak at 871 ^oC which may be assigned to melting of $Bi_4V_2O_{11}$. It is imperative to mention here that α-Bi_2O_3 at room temperature exhibit monoclinic structure and transform to δ-FCC structure at 727^oC as has been reported [192]**.**

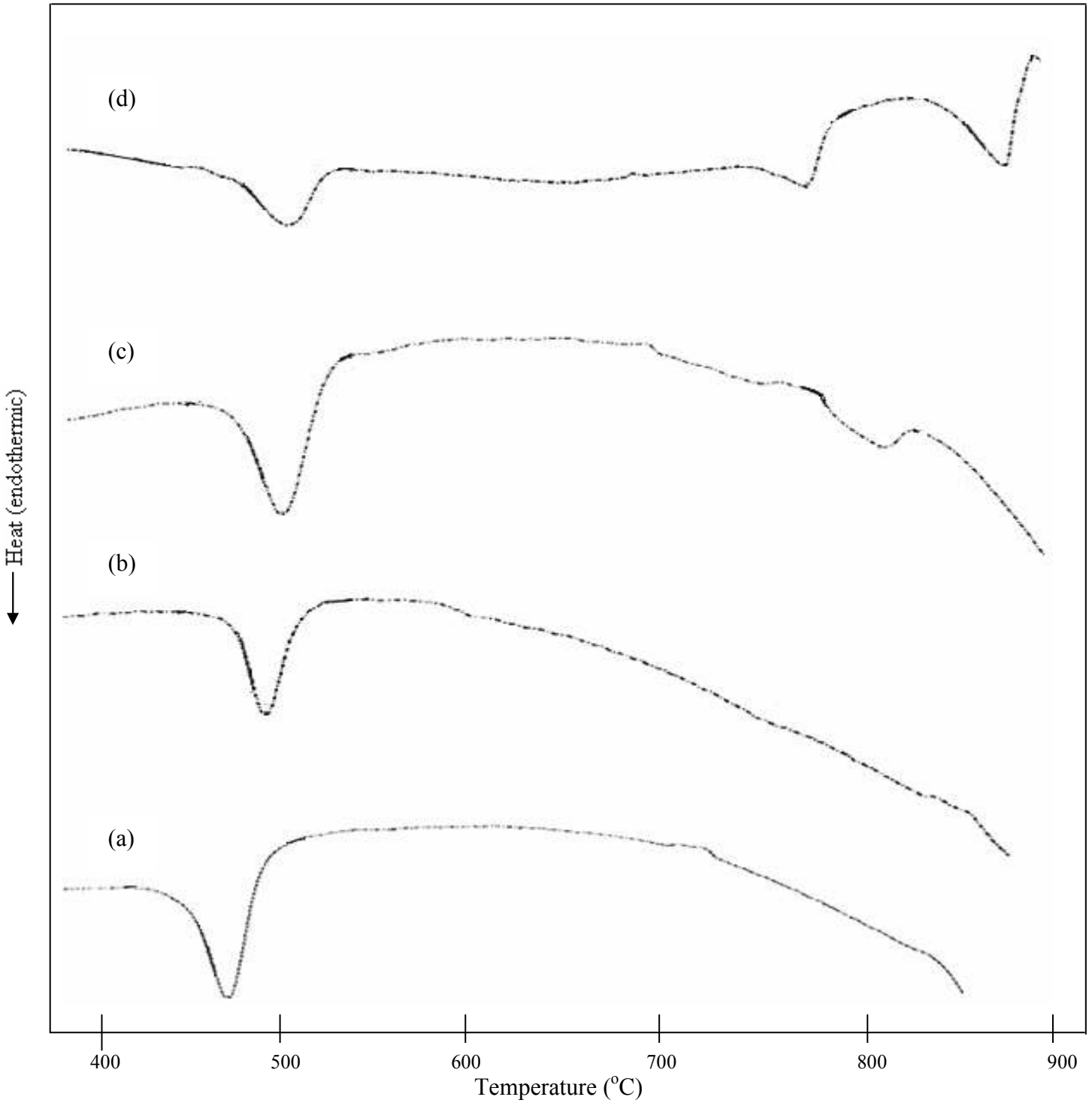

Fig.4.6 DSC plot of $Bi_4V_{2-x}Cu_xO_{11-\delta}$, (a) x = 0.1 (b) x = 0.2 (c) x = 0.3 (d) x = 0.4

4.1.2.1.3 Electrical Conductivity

Electrical conductivity was measured from the complex impedance spectra of the $Bi_4V_{2-x}Cu_xO_{11-\delta}$ (x = 0.1 to 0.4) samples. These impedance spectra were obtained by plotting imaginary part Z″ against the real part Z′ at room temperature measured at different frequencies as shown by representative graphs in figure 4.7 at 200°C. Ionic polarization phenomenon observed is shown in figure 4.8.

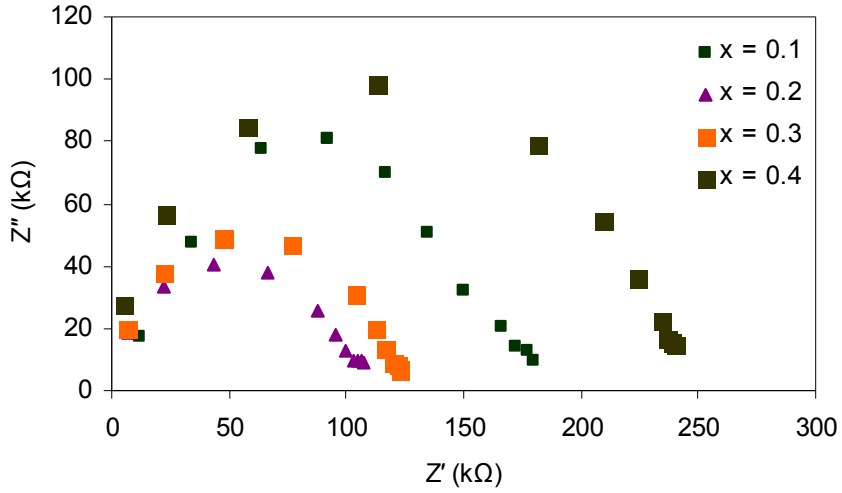

Fig. 4.7 Impedance spectra of $Bi_4V_{2-x}Cu_xO_{11-\delta}$ at 200 °C

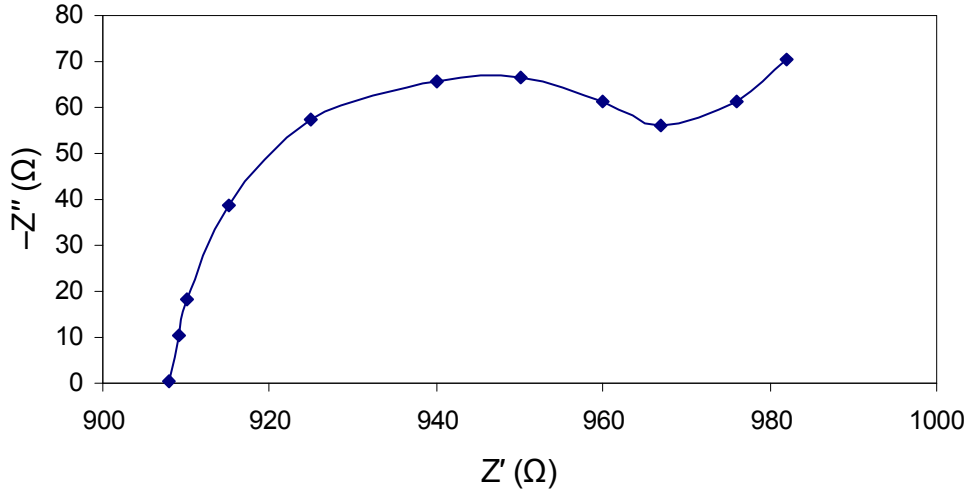

Fig. 4.8 Impedance spectra of $Bi_4V_{3.8}Cu_{0.2}O_{11-\delta}$ at 420 °C

The temperature dependence of the conductivity was studied up to 700 ^{o}C. The results of ionic conductivity measurement for α and γ-phase compositions are shown in the form of Arrhenius plots (fig. 4.9). In earlier reported work [72], γ′ polymorph associated with partial melting of $Bi_4V_2O_{11}$ is mentioned in addition to α, β and γ. However, another low temperature γ′ phase is also reported afterward [135, 138, 151].

Arrhenius plot reveals direct transition γ → γ′ for the compositions of x = 0.1, 0.2, 0.3 and 0.4 at 460 ^{o}C, 500 ^{o}C, 520 ^{o}C and 540 ^{o}C respectively with the suppressed β – phase for all the copper doped samples. However, the sample of x = 0.1 shows the γ to α transition at the temperature of 480 ^{o}C. This fact is supported by the slight change in slopes occurring for x = 0.1, 0.2, 0.3 and 0.4 at 400-600 ^{o}C [68]. The change in activation energy is attributed to a phase transition in which partially ordered oxygen vacancies become disordered. The phase transition was also confirmed by XRD studies of single crystal BICUVOX with the disappearance of incommensurate superlattice reflections corresponding approximately to 3a×3b×c unit cell at 510 ^{o}C [138].

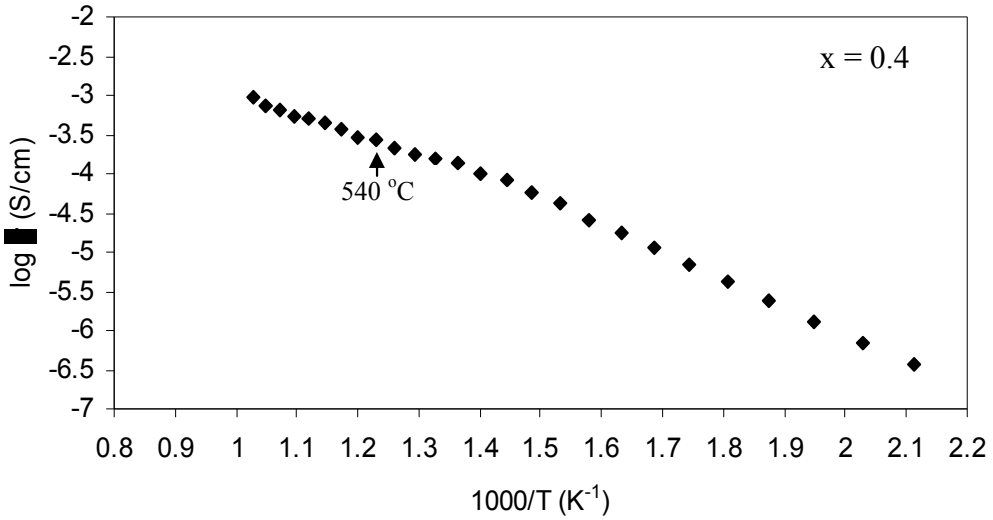

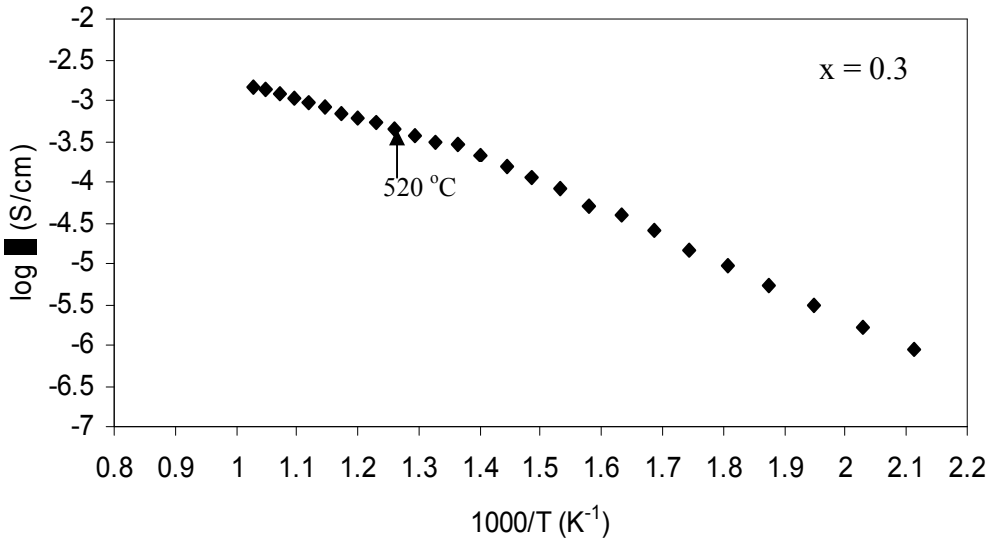

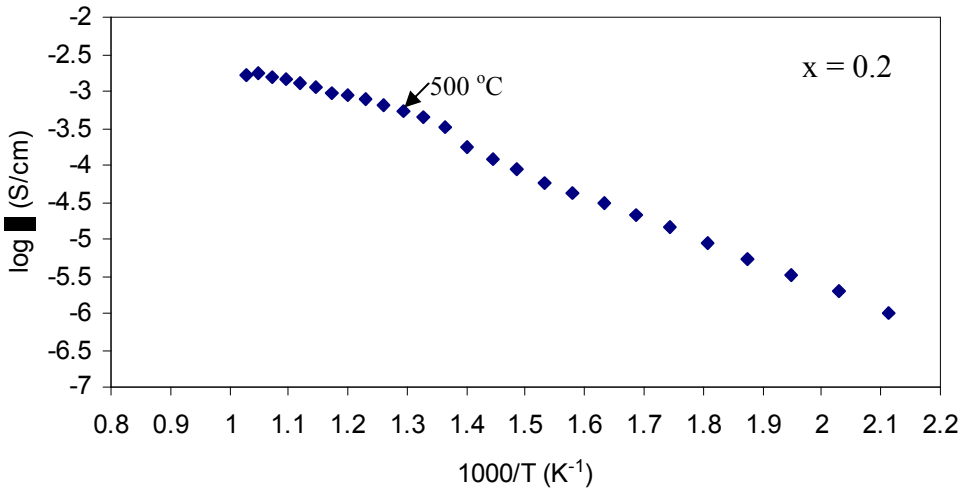

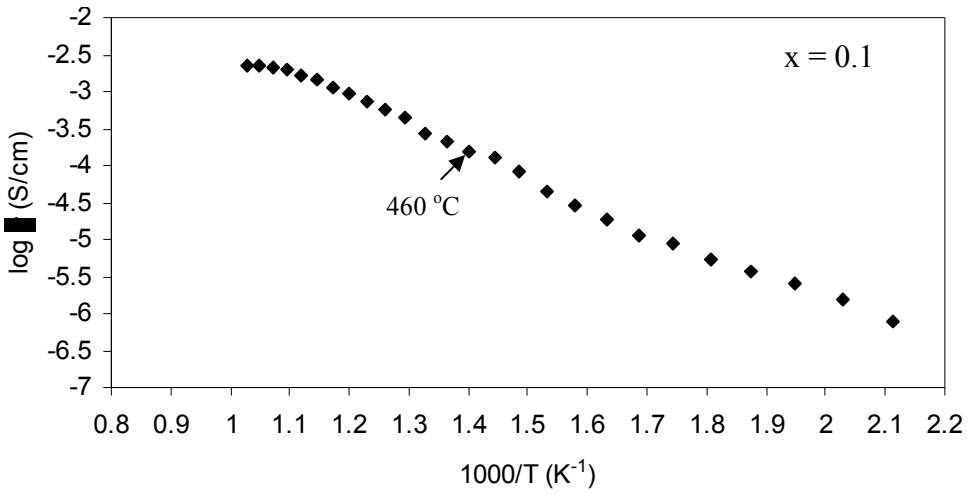

Fig.4.9 Conductivity measurement of $Bi_4V_{2-x}Cu_xO_{11-\delta}$ ($0.1 \leq x \leq 0.4$)

Other advantage of stabilizing the γ-polymorph that hystersis observed during the heating and cooling cycle disappears and conductivity data is more nearly reversible [151].

Table 4.2 Conductivity and activation energy of $Bi_4V_{2-x}Cu_xO_{11-\delta}$

Composition	σ_{300^oC} (S/cm)	E_a (eV) < 440°C	E_a (eV) >540°C
x = 0.1	8.67×10^{-6}	0.27	0.19
x = 0.2	1.42×10^{-5}	0.26	0.15
x = 0.3	1.41×10^{-5}	0.29	0.19
x = 0.4	6.73×10^{-6}	0.30	0.22

For the linear region below 440°C and above 540°C, the values of activation energy (E_a) along with ionic conductivities at 300°C for ($0 \leq x \leq 0.4$) samples are summarized in table 4.2. It can be seen that the conductivity for x = 0.1 rises to about 6.5 times the value of x = 0 sample when measured at 300 °C. The highest conductivity is observed for x = 0.2 copper substitution in the γ-phase. The conductivity value at this composition (x = 0.2) has been estimated to be 1.42×10^{-5} S/cm at 300 °C which is about an order of magnitude more than that of the value of the base compound ($Bi_4V_2O_{11}$) at 300 °C. However, at higher temperatures greater than 500 °C, the sharp increase in conductivity takes place for x = 0.1 as compared to all other samples as shown in figure 4.10. This may be attributed to presence of impurity phase for all other compositions and becomes dominant at higher temperature. This might have inhibited the movement of oxygen vacancies and hindering the hopping mechanism. However, the lower conductivity for

x = 0 can be attributed to the greater covalency in the interlayer contacts between $[Bi_2O_2]_n^{n2+}$ and $[VO_{3.5}]_n^{n2-}$ of the α-$Bi_4V_2O_{11}$.

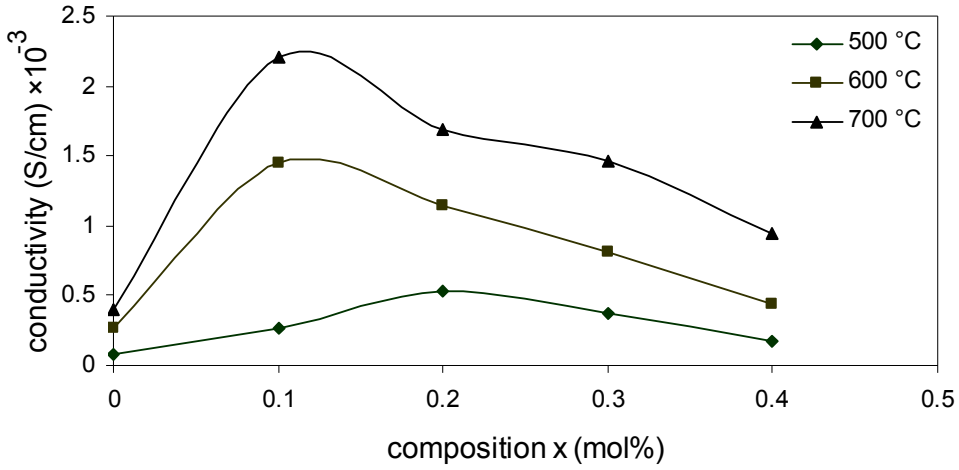

Fig.4.10 Conductivity isotherm as a function of composition (x) in $Bi_4V_{2-x}Cu_xO_{11-\delta}$, $(0 \leq x \leq 0.4)$

The decrease in overall conductivity for x = 0.4 may also be interpreted as segregation of greater amount of impurity phase of unreacted Bi_2O_3 at grain boundaries.

4.1.2.1.4 Microstructural Analysis

The microstructural study was carried out on fractured surfaces of all the samples and the micrographs are presented in figure 4.11. The SEM (scanning electron microscopy) of fractured surface of x = 0 and x = 0.1 do not show any significant change except larger grain size in case of x = 0.1 sample. On careful examination of micrographs for both the samples of compositions x = 0 and x = 0.1, one can see the interwoven wavy network (marked as arrow in the figure 4.11a, b) type of structure existing throughout the sample. Though the volume fraction of this network structure of lamellar type is more for sample x = 0 as compared to x = 0.1 but in both cases it is uniformly distributed throughout the

sample. This type of structure in ceramic compounds has been reported for piezoelectric materials [193, 194]. During sintering, the substance crystallizes above curie temperature in the cubic perovskite structure and transform into lower symmetry structure during cooling. The phase transformation leads to lattice distortion. Due to lattice distortion, thermal stresses are generated which are further reduced by the formation of domains. The domain configuration consists of 90^o and 180^o domains. Based on the different possibilities of their orientation and with variation in crystal structure, these orientations may also change. Since we are analyzing the fractured surface so instead of parallel straight lines, we are observing a parallel wavy pattern. But it is certain that the structure comprises of these parallel domains which form because of thermal lattice strain during cooling after sintering.

In contrast to these, the $0.2 \leq x \leq 0.4$ samples show totally different microstructures than $x = 0$ and $x = 0.1$ samples which is due to γ-phase stabilization. It can be seen that copper concentration $x \geq 0.2$ has greatly affected the sintering behaviour. The SEM observation of the fractured surface shows that the addition of CuO for $x = 0.2$ substitution has a strong effect on the microstructure and grain growth of $Bi_4V_2O_{11}$. The non uniform grain pattern with small grain size for $x \leq 0.1$ changed to relatively more uniform grain structure along with grain refinement. In the microstructures of samples of composition $x = 0.3$ and 0.4, the grains are very large and their size increases with doping concentration. The higher ionic conductivity for $x = 0.2$ in $Bi_4V_{2-x}Cu_xO_{11-\delta}$ is supported by the relatively more uniformity in grains pattern and size with lesser porosity as compared to $x = 0.3$ and 0.4 samples. The grain size for all the compositions is mentioned in table 4.3.

It is important to notice here that for samples containing concentration $x \geq 10\%$, there is no wavy pattern observed which might be attributed to phase transformation from α to γ.

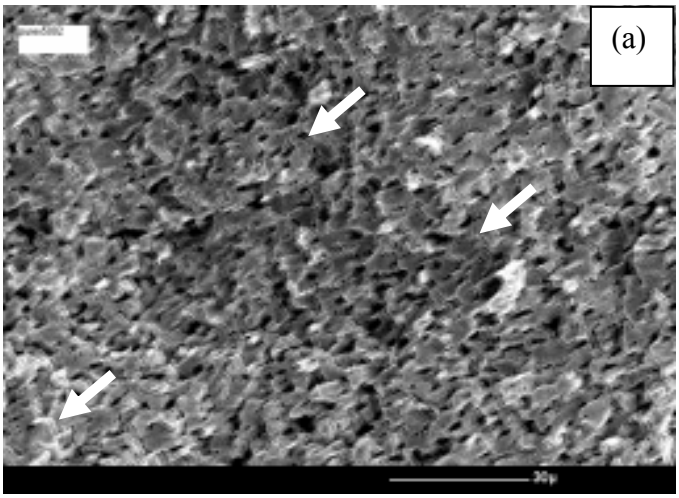

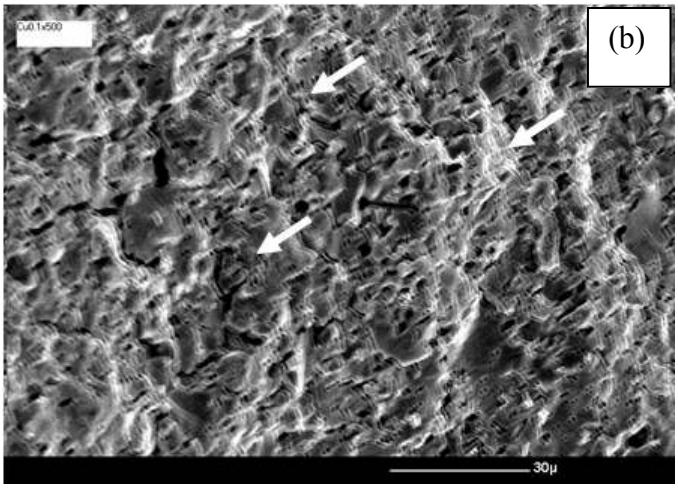

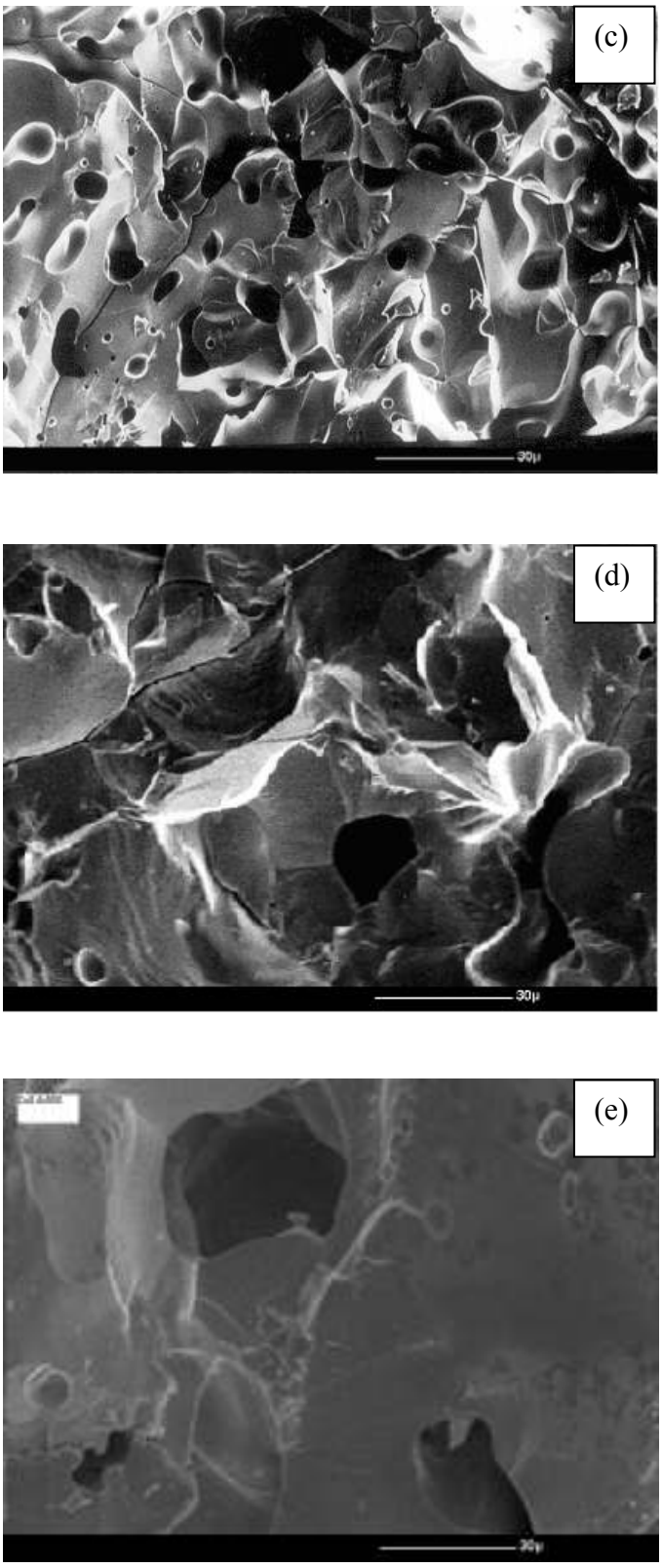

Fig. 4.11 SEM micrographs of $Bi_4V_{2-x}Cu_xO_{11-\delta}$, (a) x = 0, (b) x = 0.1, (c) x = 0.2, (d) x = 0.3, (e) x = 0.4

Table 4.3 Average grain size of $Bi_4V_{2-x}Cu_xO_{11-\delta}$ ($0 \leq x \leq 0.4$)

Composition	Grains size range (μm)
x = 0	2-6
x = 0.1	4-8
x = 0.2	10-15
x = 0.3	25-30
x = 0.4	> 30

Higher resistivity of the larger grain size may be attributed to the ordering of oxygen vacancies in these phases, which leads to a modification of the bulk response. The cracks observed in some of the micrographs may be attributed to abnormal grain growth.

4.1.2.2 $Bi_4V_{2-x}Me_xO_{11-\delta}$, ($Me = Mn^{2+}$)

4.1.2.2.1 X-ray Diffraction

The XRD analyses of the samples prepared from different stoichiometric amounts of Bi_2O_3, V_2O_5 and MnO ($Bi_4V_{2-x}Me_xO_{11-\delta}$) for the compositions of x = 0.1, 0.2, 0.3 and 0.4 were carried out. The patterns are presented in figure 4.12.

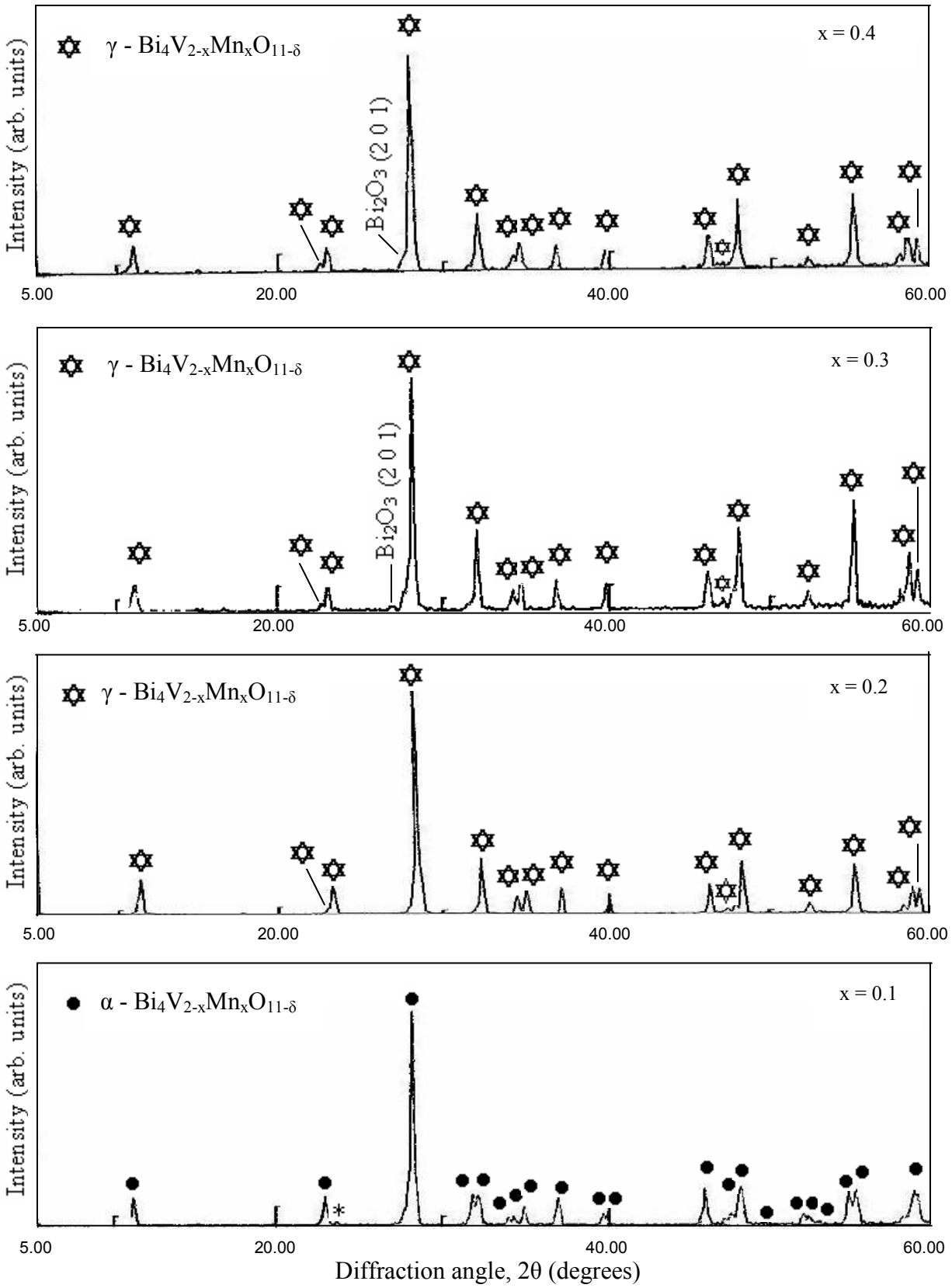

Fig.4.12 XRD patterns of $Bi_4V_{2-x}Mn_xO_{11-\delta}$, (*) superlattice reflection

The XRD pattern for composition x = 0.1 corresponds to mixed α and β -phase with weak splitting of the peak at ~ 32^{o} whereas other compositions x = 0.2, 0.3 and 0.4 are indexed with γ-phase of $Bi_4V_{2-x}Mn_xO_{11-\delta}$. The solid solution range is found to be up to x = 0.2, which is higher than copper doped system. On the other hand, the increasing concentration of dopant leads to unreacted Bi_2O_3 as shown in figure 4.12. The lattice parameters of stabilized γ- phase (table 4.4) are found to possess the trend according to dopant concentration. No significant change is observed in basal *a-b* lattice parameter. However, axial parameter *c* shows the increasing trend. It may be attributed due to size difference between dopant Mn^{2+} and V^{5+} (0.80 Å and 0.59 Å respectively [191]).

Table 4.4 The unit cell parameters of γ- $Bi_4V_{2-x}Mn_xO_{11-\delta}$

Composition	*a* (Å)	*c* (Å)	Volume (Å^3)
x = 0.2	3.91	15.37	235.38
x = 0.3	3.92	15.75	242.10
x = 0.4	3.91	15.86	243.73

4.1.2.2.2 Electrical Conductivity

The ionic conductivities, which were derived from the complex impedance plots at different temperatures, are plotted in figure 4.13 as a function of temperature in the form of log σ vs. 1/T. The conductivity behavior of the $Bi_4V_{2-x}Mn_xO_{11-\delta}$ ($0.2 \leq x \leq 0.4$) compositions show two linear regions with different activation energies in their Arrhenius plots (cooling cycle). These regions belong to $\gamma \rightarrow \gamma'$ phase transitions. In addition to this, x = 0.1 sample exhibit $\gamma \rightarrow \alpha$ transition.

The transition temperature could not show any trend as shown in figure 4.13 The anomalies in phase transition temperature can be explained on the basis of solid solution and unreacted Bi_2O_3 contents especially in x = 0.3 and 0.4 samples. The highest conductivity was observed for x = 0.2 composition followed by x = 0.3 and 0.4 samples respectively. The decreasing value of the conductivity beyond x = 0.2 sample can be explained on the basis of the solid solution formation range of the compound up to x = 0.2. This fact is supported by the increase in volume beyond x = 0.2.

Activation energy (E_a) below 400 ^oC and above 500 ^oC are calculated from Arrhenius plots of x = 0.2, 0.3 and 0.4 samples. The values of activation energy along with ionic conductivities measured at 300 ^oC are summarized in Table 4.5.

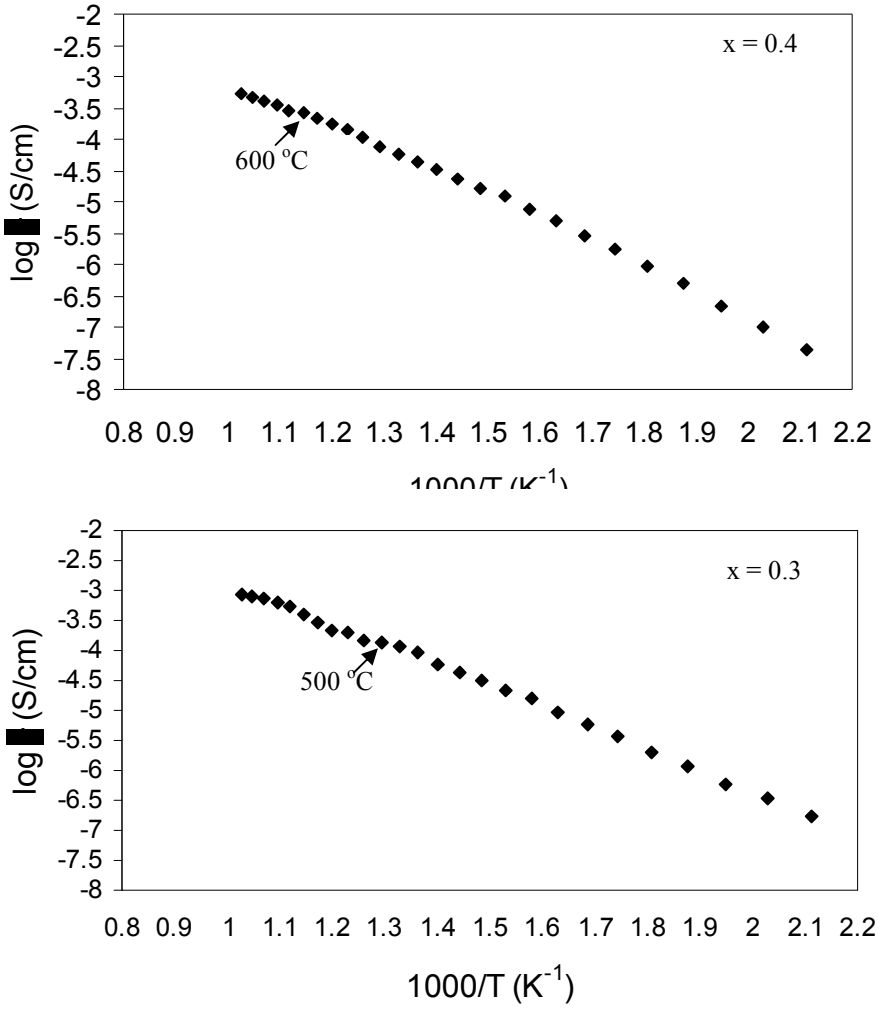

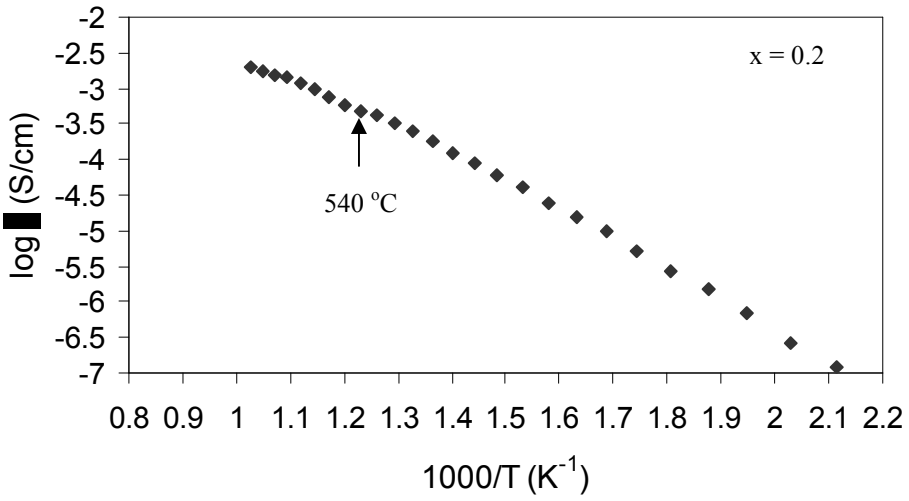

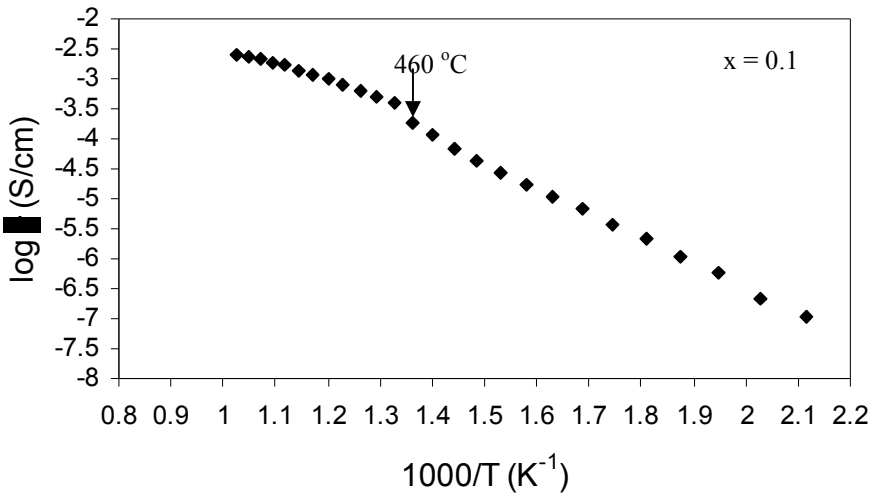

Fig. 4.13 Arrhenius plot of $Bi_4V_{2-x}Mn_xO_{11-\delta}$

The observed conductivity measurements with composition are in good agreement with the trend observed for activation energy. It is also observed from table 4.5 that conductivity value for manganese composition of x = 0.2 in the high conducting γ-phase is about 7.48 times higher than that of the base compound at 300 °C (section 4.1.1.3).

Table 4.5 Conductivity and activation energy of $Bi_4V_{2-x}Mn_xO_{11-\delta}$ (γ-phase)

Composition	$\sigma_{300\,^oC}$ (S/cm)	E_a (eV) < 400 °C	E_a (eV) >500°C
x = 0.2	5.22×10^{-6}	0.32	0.25
x = 0.3	3.68×10^{-6}	0.34	0.29
x = 0.4	1.70×10^{-6}	0.36	0.26

In the study of divalent system, γ-phase stabilization occurs at same composition of x = 0.2 with mixed α and β-phase for x = 0.1 in both of copper and manganese substitution. However, range of solid solution is higher for manganese doping. An increase of conductivity (1.69 times) is observed for copper as compared to manganese for the composition of x = 0.2 at 300 °C.

4.1.3 Trivalent Substitution

The effects of trivalent cations substitution for V^{5+} in bismuth vanadate is given in the proceeding sections.

4.1.3.1 $Bi_4V_{2-x}Me_xO_{11}$ (Me = Ti^{3+})

In earlier studies, most of the research work has been carried out with titanium (IV) substitution [161-163] on V^{5+} sites. But in the present study, Ti^{3+} was used to study the effect on phase stabilization and conductivity measurement. However, it might be possible that Ti^{3+} gets converted into Ti^{4+} (most stable state) during processing of the sample under experimental conditions. Therefore, ultraviolet spectroscopy study was undertaken to confirm the valence state of the titanium dopant.

4.1.3.1.1 Ultra-violet Spectroscopy

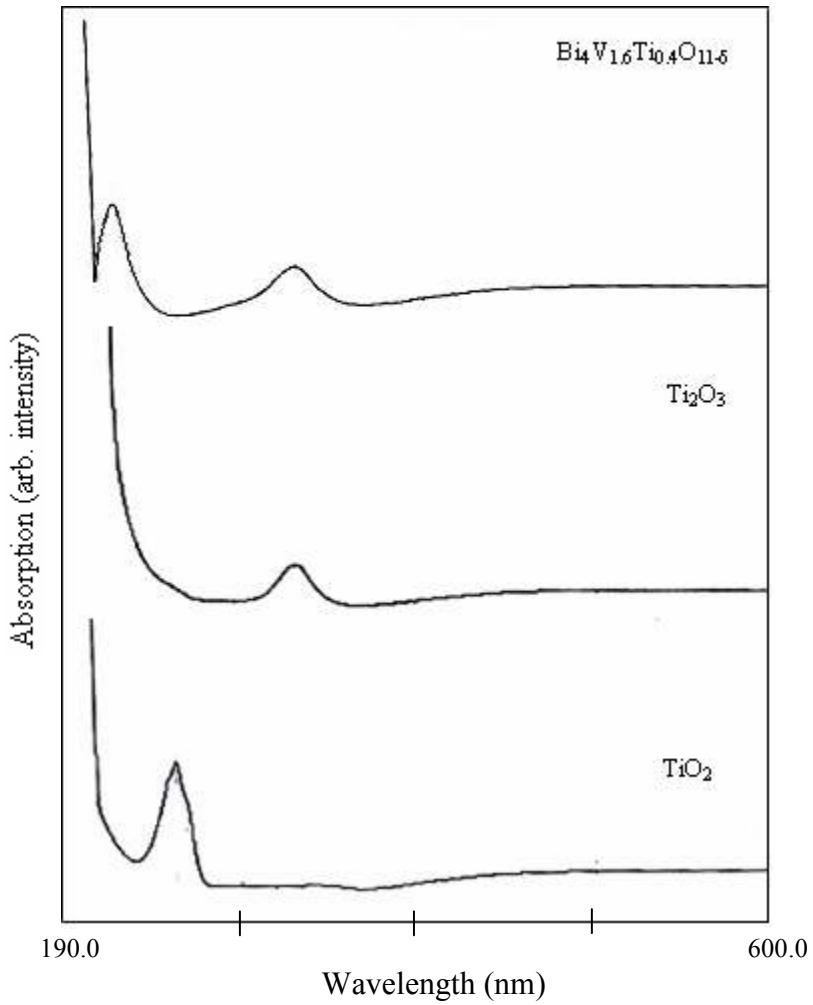

Fig. 4.14 Absorption spectra of TiO_2, Ti_2O_3 and $Bi_4V_{1.6}Ti_{0.4}O_{11-\delta}$

The ultra-violet (uv) visible spectra of Ti_2O_3, TiO_2 and $Bi_4V_{1.6}Ti_{0.4}O_{11-\delta}$ was obtained in the wavelength range from 190 nm to 600 nm and are shown in figure 4.14. The spectra of pure Ti_2O_3 indicate the absorption peak at 329 nm whereas for TiO_2 it is at 256 nm. In titanium doped bismuth vanadate, the absorption peaks exist at 329 nm and 223 nm which do not correspond to TiO_2 absorption peak rather falls exactly at peak position of Ti_2O_3. This clearly indicate that titanium remains in Ti^{3+} state in the doped bismuth

vanadate sample and is not oxidized further under high temperature oxidizing atmosphere during experimentation.

4.1.3.1.2 X-ray Diffraction

The XRD patterns of $Bi_4V_{2-x}Me_xO_{11-\delta}$ (Me = Ti^{3+}) samples are given in figure 4.15 which was indexed with representative peaks of α, β and γ-phases. The x = 0.1 sample exhibit very small reflection at $2\theta \approx 24.2^o$ diffraction angles which is attributed to superstructure of α-form. On the other hand, $Bi_4V_{2-x}Ti_xO_{11-\delta}$ (x = 0.3, 0.4) samples have been indexed which shows the presence of tetragonal (γ) phase whereas mixed phase (β and γ) was observed for x = 0.2 sample. A very weak splitting for x = 0.2 at ~ 32.9^o which corresponds to β-phase with the absence of superstructure peak at ~ 24.2^o was observed in this particular sample. From this study, one can say that mixed β and γ phase coexist for x = 0.2 sample.

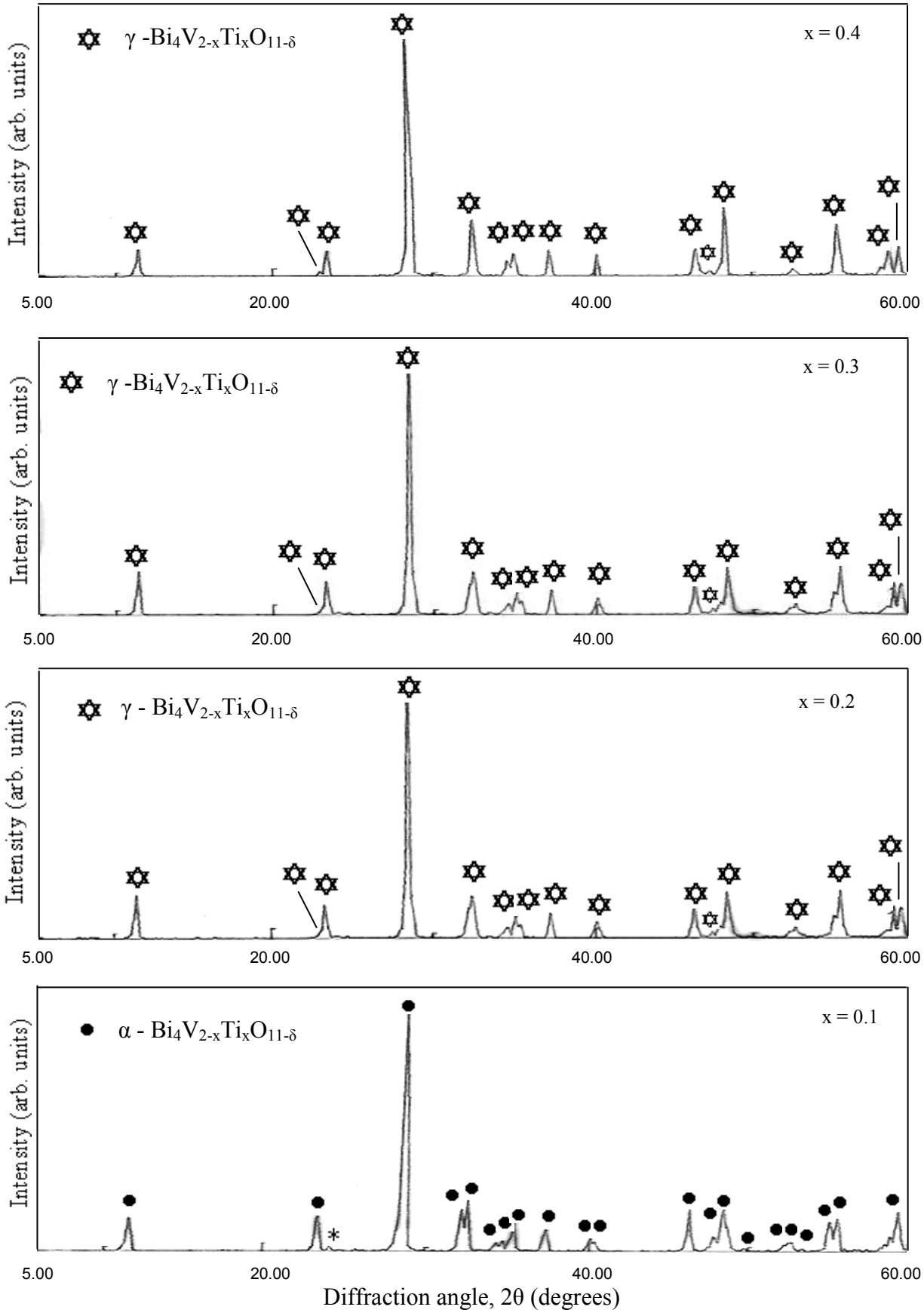

Fig. 4.15 X-ray diffraction pattern of $Bi_4V_{2-x}Ti_xO_{11-\delta}$, (*) superlattice reflection

Lattice parameters of all the compositions are derived from these XRD patterns and are given in table 4.6. XRD patterns from α (x = 0.1) to tetragonal γ-phase ($0.2 \leq x \leq 0.4$) is usually characterized by an increase in *c* parameter of the cell [158] whereas, the basal *a* –*b* lattice parameter and volume of the unit cell continue to decrease with increasing doping concentration of Ti^{3+} to V^{5+} over the studied composition range. However, the size of Ti^{3+} is larger than V^{5+}.

Basically, doping in these systems exhibit two fold effect due to quite disorderly behaviour between metal atom and oxygen positions in the perovskite layer of the substituted phases of γ- $Bi_4V_{2-x}Ti_xO_{11-\delta}$ i.e. increasing the oxygen vacancy contents in *a*-*b* basal plane, lattice parameter *c* increases due to ionic radius size difference between V^{5+} and Ti^{3+} (0.59 Å and 0.77 Å respectively [191]). On the other hand, oxygen vacancies are dominant as compared to size difference of the dopant and parent cations due to which, the unit cell volume decreases with increasing oxygen vacancies on higher dopant concentration as an increase in oxygen vacancies with x decreases the unit cell volume.

Table 4.6 Composition and lattice parameters of $Bi_4V_{2-x}Ti_xO_{11-\delta}$ ($0.1 \leq x \leq 0.4$)

Composition	*a* (Å)	*b* (Å)	*c* (Å)	Volume (Å^3)
x = 0.1	5.50	5.56	15.25	466.35
x = 0.2	3.93	3.93	15.27	235.84
x = 0.3	3.89	3.89	15.35	232.28
x = 0.4	3.86	3.86	15.57	231.98

4.1.3.1.3 Electrical Conductivity

The conductivities (σ) of the titanium doped $Bi_4V_2O_{11}$ ($Bi_4V_{2-x}Ti_xO_{11-\delta}$, $0.1 \leq x \leq 0.4$) samples were determined from complex impedance data plots as shown in representative plot for the composition x = 0.1 in figure 4.16 at 200 ^oC.

The temperature dependence of the conductivity was performed for all the compositions of x = 0.1, 0.2, 0.3 and 0.4 from 200-700 ^oC during cooling cycle. The results are plotted in log σ vs. 1/T as shown in fig. 4.17.

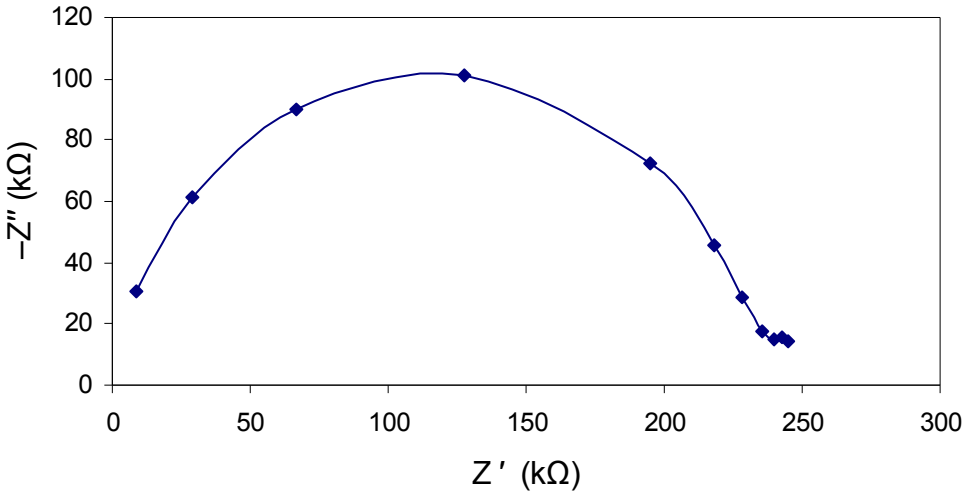

Fig. 4.16 Impedance spectrum of $Bi_4V_{2-x}Ti_xO_{11-\delta}$ (x = 0.1) at 200^oC

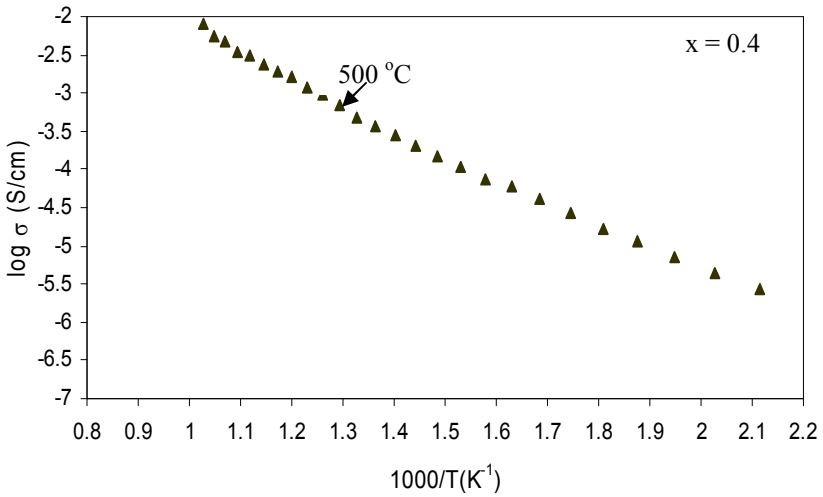

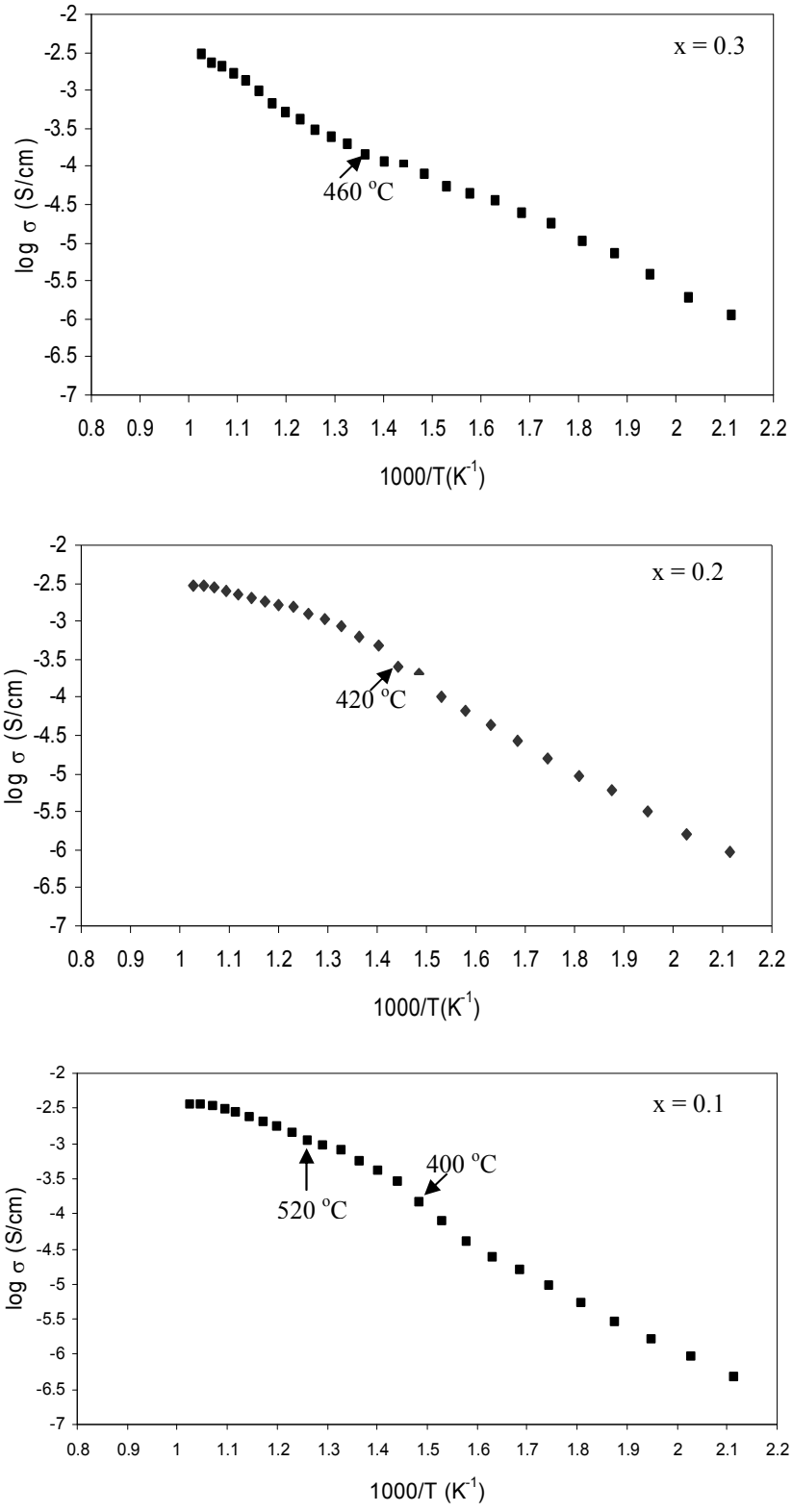

Fig. 4.17 Arrhenius plot of $Bi_4V_{2-x}Ti_xO_{11-\delta}$

In case of x = 0.2, 0.3 and 0.4 samples, the A.C. conductivity behavior is almost same except x = 0.2 sample in which higher activation energy (E_a) is observed below 300 ^oC as compared to x = 0.3 and x = 0.4 samples. This might be because of presence of both β and γ-phases. For the linear regions below 400 ^oC and above 500 ^oC, E_a values with conductivities at 300 ^oC are summarized in table 4.7.

Table 4.7 The ionic conductivity and activation energies of $Bi_4V_{2-x}Ti_xO_{11-\delta}$ ($0.1 \leq x \leq 0.4$)

Composition	σ_{300^oC} (S/cm)	E_a (eV) < 400 ^oC	E_a (eV) > 500 ^oC
x = 0.1	9.59×10^{-6}	0.33	0.20
x = 0.2	1.62×10^{-5}	0.31	0.14
x = 0.3	1.72×10^{-5}	0.25	0.36
x = 0.4	2.66×10^{-5}	0.24	0.32

For x = 0.1 (α-phase), Arrhenius plot (fig. 4.17) shows the transitions at 520 ^oC and 400 ^oC corresponding to to γ → β and β → α transition. For the composition range ($0.2 \leq x \leq 0.4$) corresponding to γ - phase indicates the phase transitions (γ → γ′) at 420 ^oC, 460 ^oC and 500 ^oC for x = 0.2, 0.3 and 0.4 respectively. The phase transition was also confirmed by DTA plot of $Bi_4V_{1.6}Ti_{0.4}O_{11-\delta}$ (fig. 4.18) which occurs at about 490 ^oC and is in good agreement with the transition in Arrhenius plot. In the Arrhenius plot, no discontinuity for x = 0.3 and 0.4 was observed, where as slight discontinuity exist for x = 0.2 which may be due to mixed phase (β and γ phase) in this sample. Generally, the discontinuity refers to β → γ phase transition in other reported BIMEVOXs [157]. This is

again a manifestation that x = 0.2 sample exhibit two phases, β and γ as observed in XRD pattern (fig.4.15). The hump observed in the ionic conductivity for x = 0.2 doping in the graph indicate that the transformation is a continuous process. Electrical measurement with the lowest and highest value of the ionic conductivity obtained for x = 0.2 and x = 0.4 respectively in the low temperature range is shown in Table 4.9. Highest ionic conductivity of $Bi_4V_{1.6}Ti_{0.4}O_{11-\delta}$ may be attributed to increase in oxygen vacancy concentration. This observation may be confirmed by the smallest volume of the composition x = 0.4 (table 4.8).

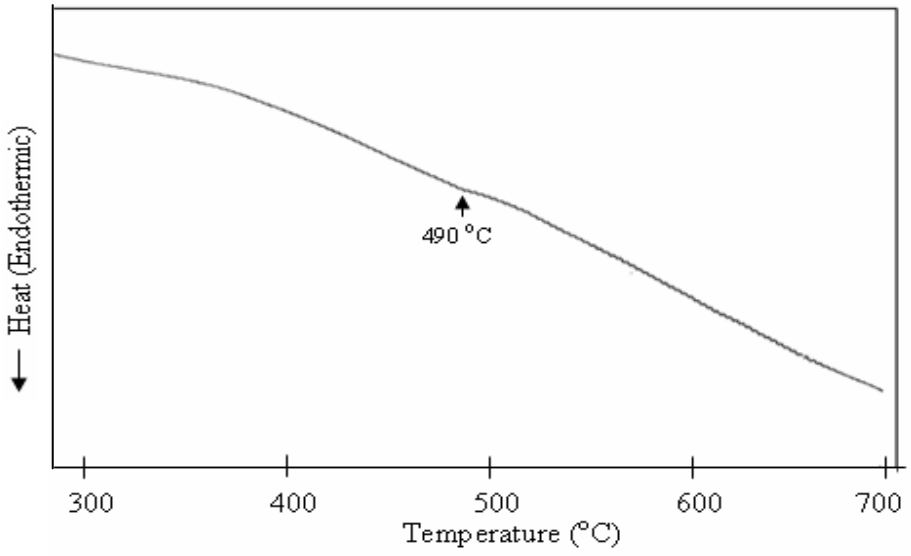

Fig. 4.18 Typical DTA plot of $Bi_4V_{1.6}Ti_{0.4}O_{11-\delta}$

It can be seen that conductivity becomes maximum at 300 ^oC (about 24 times that of the base compound $Bi_4V_2O_{11}$), for x = 0.4 ($Bi_4V_{1.6}Ti_{0.4}O_{11-\delta}$). The conductivity of $Bi_4V_{1.6}Ti_{0.4}O_{11-\delta}$ is even 1.87 times higher than the copper (divalent) substituted bismuth vanadate of highly conducting composition of x = 0.2 at 300 ^oC as given in table 4.2.

The conductivity at higher temperature is shown in figure 4.19. This represents the similar trend of conductivity at lower temperature.

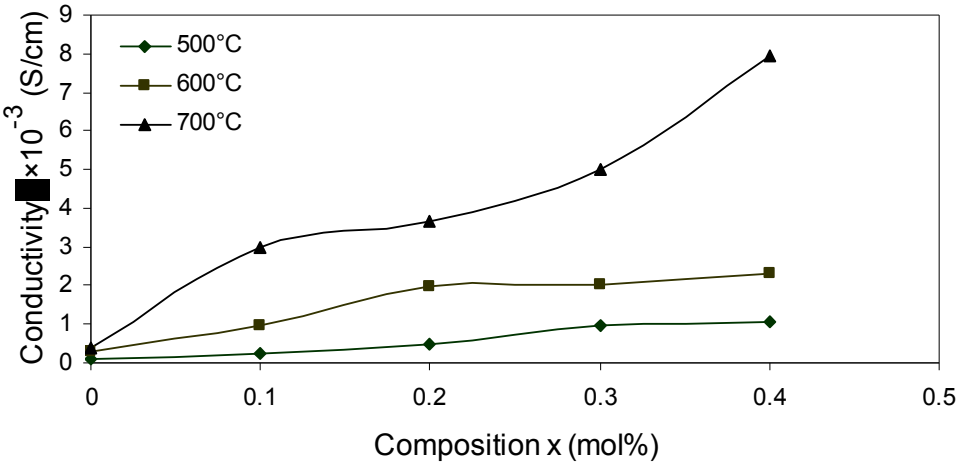

Fig. 4.19 Isothermal plot of conductivity of $Bi_4V_{2-x}Ti_xO_{11-\delta}$

The explanation for this conductivity behavior may also be accounted for the formation of defect pairs by the incorporation of guest ions of different size into the host lattice which causes a strain whose magnitude depends on a factor $f = 1 - r_h / r_g$ where r_h and r_g are the ionic radii of the host and guest ions, respectively. The net result of this strain is apparently lattice loosening which decreases the enthalpy of formation of defects. This consequently leads to generation of more number of defects contributing to conductivity enhancement. In the present system, the lattice distortion is appreciable ($f = 0.23$) causing the conductivity enhancement.

4.1.3.1.4 Microstructural Analysis

In order to get more insight about the conductivity phenomenon, we have done structural analysis of lowest and highest conducting samples of compositions x = 0.2 and 0.4. The SEM micrographs are given in figure 4.20 (a) and (b) respectively.

Doping of Ti_2O_3 leads to variation in structure. Since the typical domain structure (fig. 4.11; a, b) gets diminished in doped samples so it can be said that other phases, instead of α-phase, are being stabilized at room temperature.

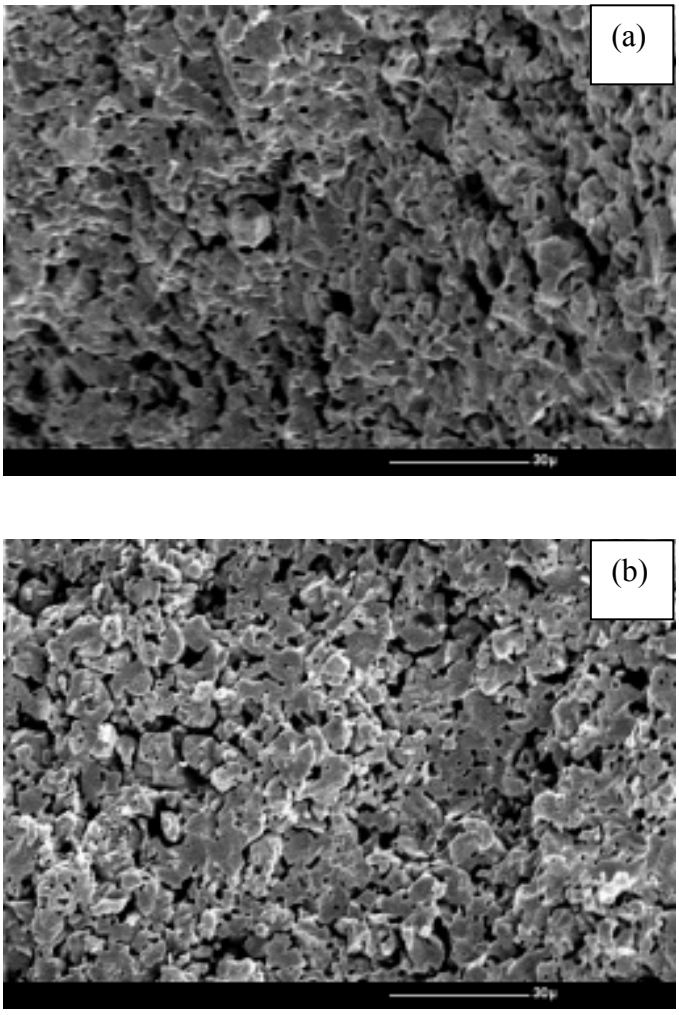

Fig. 4.20 SEM photograph of fractured surface of $Bi_4V_{2-x}Ti_xO_{11-\delta}$ (a) x = 0.2 (b) x = 0.4 sintered at 800 ^oC

Doping slowly leads to stabilization of high temperature γ-phase even at room temperature. The continuous variation in observed structure is an evidence to change in ionic conductivity of the doped samples as compared to undoped sample. In case of

doped sample of composition x = 0.2, the existing domain structure is not clear in the micrograph. However, the structure looks to be a composite type where these domain structures appear to be in transition phase (broadening in structure with little wavy pattern). This indicates that the transformation of α to γ-phase is not complete but metastable β-phase is also occuring. The X-ray analysis also confirms this phenomenon. Here in this sample of x = 0.2, parallel pattern is not completely diminished which is observed for α-phase.

In samples, where ionic conductivity is observed to be high (x = 0.4), the micrograph gives different look. Smaller grains (table 4.8) of cellular type have formed. Here no domain structure is observed as was observed for α-$Bi_4V_{2-x}Cu_xO_{11-\delta}$ (fig. 4.11; a,b). The structure seems to be single γ-phase which was confirmed by our X-ray analysis also.

In the high ionic conducting sample of x = 0.4, the structure (Fig.4.20; b) exhibits lesser amount of intergranular porosity and the pattern is relatively uniform throughout the sample as compared to x = 0.2 sample of low conductivity (Fig.4.20; a), where cluster type non-uniform pattern is observed with poor refined grains.

Table 4.8 Average grain size of $Bi_4V_{2-x}Ti_xO_{11-\delta}$ sintered at 800 ^oC

Composition	Grain size (μm)
x = 0.2	4-10
x = 0.4	6-10

4.1.3.2 Sintering at different temperatures of $Bi_4V_{1.6}Ti_{0.4}O_{11-\delta}$

Processing conditions play an important role in the formation of any compound/phase and its properties. The solid solution range [68] and phase stabilization in $Bi_4V_2O_{11}$ (α, β and γ) at room temperature be affected by the sintering temperature of samples [133]. So the sample of highest conducting composition x = 0.4 was sintered at different temperatures of 750, 775 and 825 ^oC in addition to sintering at 800 ^oC. A detailed analysis of x = 0.4 sample was carried out to understand its behaviour with variation in sintering temperature.

4.1.3.2.1 X-ray Diffraction

X-ray diffraction of the composition x = 0.4 sintered at 750, 775 and 825 ^oC was taken under similar experimental conditions. The XRD patterns of these samples are shown in figure 4.21.

On analysizing the XRD patterns of $Bi_4V_{1.6}Ti_{0.4}O_{11-\delta}$ sintered at 750 ^oC, 775 ^oC, 800 ^oC and 825 ^oC (fig. 4.21; a, b, c, d), it was observed that XRDs of samples sintered at 750, 775 ^oC and 825 ^oC indexed to γ-phase. Apart from this, XRDs of the samples sintered at 750 and 775 ^oC exhibit extra peaks. These peaks are due to unreacted Bi_2O_3 and it is more prominent in case of samples sintered at 750 ^oC. Moreover, the XRD peaks are shifted at lower diffraction angle with higher peak width in these samples. Peak broadening and shifting at lower diffraction angles are clearly manifestation of more disordering in these samples as compared to 800 ^oC heat treated sample. This is supported by the large volume of the unit cell (table 4.9) for the samples sintered at 750 and 775 ^oC.

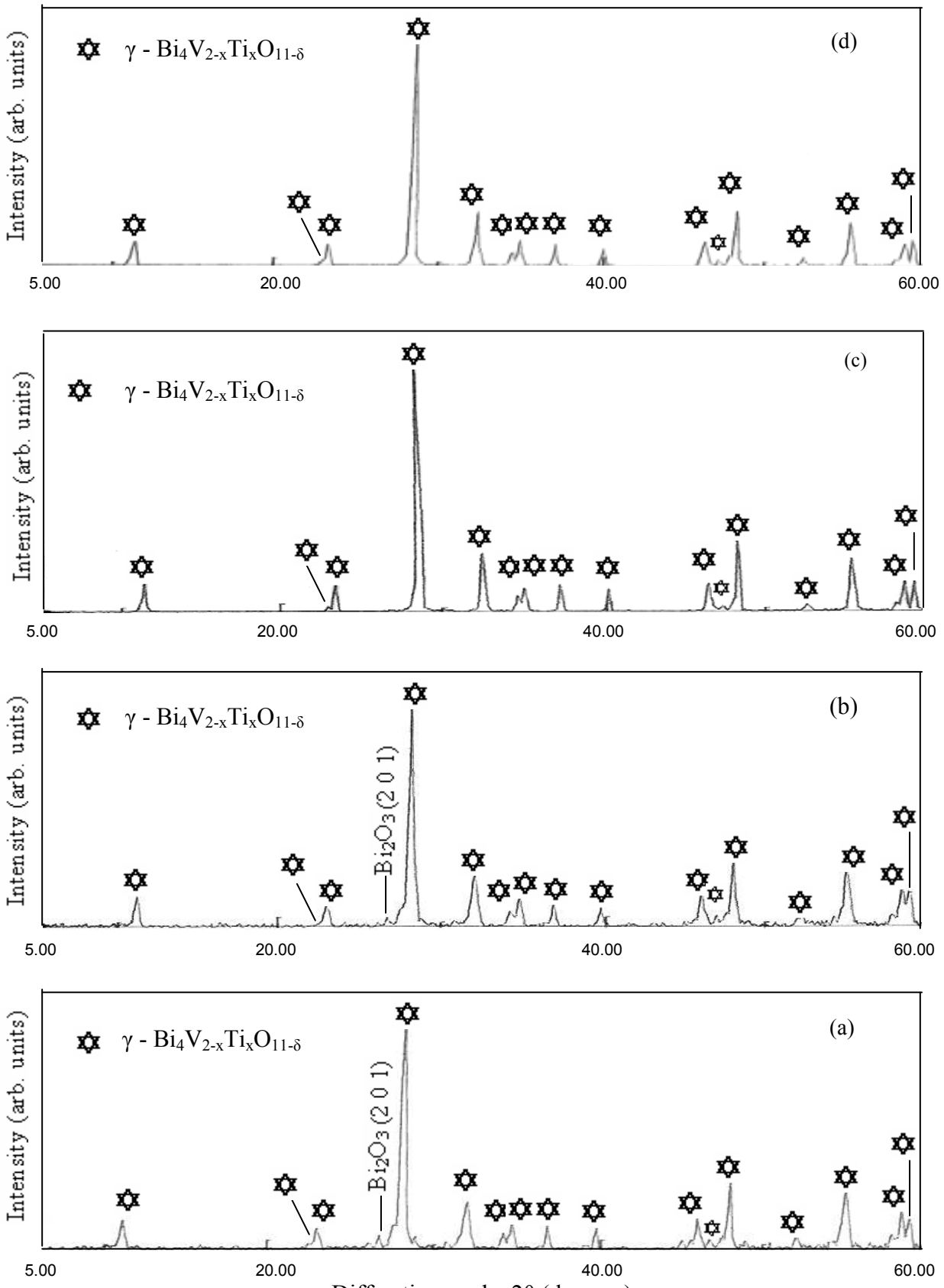

Fig. 4.21 XRD of $Bi_4V_{1.6}Ti_{0.4}O_{11-\delta}$ sintered at (a) 750 ^oC (b) 775 ^oC (c) 800 ^oC, (d) 825^oC

Table 4.9 Composition and lattice parameters of $Bi_4V_{2-x}Ti_xO_{11-\delta}$ ($0.1 \leq x \leq 0.4$)

Sintering temp.	*a* (Å)	*b* (Å)	*c* (Å)	Volume (Å^3)
750 ^oC	3.97	3.97	15.54	244.92
775 ^oC	3.97	3.97	15.52	244.61
800 ^oC	3.86	3.86	15.57	231.98
825 ^oC	3.92	3.92	15.47	237.72

4.1.3.2.2 Electrical Conductivity

The conductivity curves of different heat treated samples are plotted in the form of Arrhenius plot as shown in figure 4.22. The data do not show simple Arrhenius-type behavior with single activation energy. The curves consist of two linear segments with different activation energies (E_a), one at temperature greater than 500 ^oC and the other below 400 ^oC. In the intermediate temperature regions, a pronounced curvature is also present in the data plots at (440 ^oC), (460 ^oC) and 480 ^oC of the pellets sintered at 750, 775 and 825 ^oC respectively. For the linear regions below 400 ^oC and above 500 ^oC, E_a values along with conductivities measured at 300 ^oC are summarized in Table 4.10.

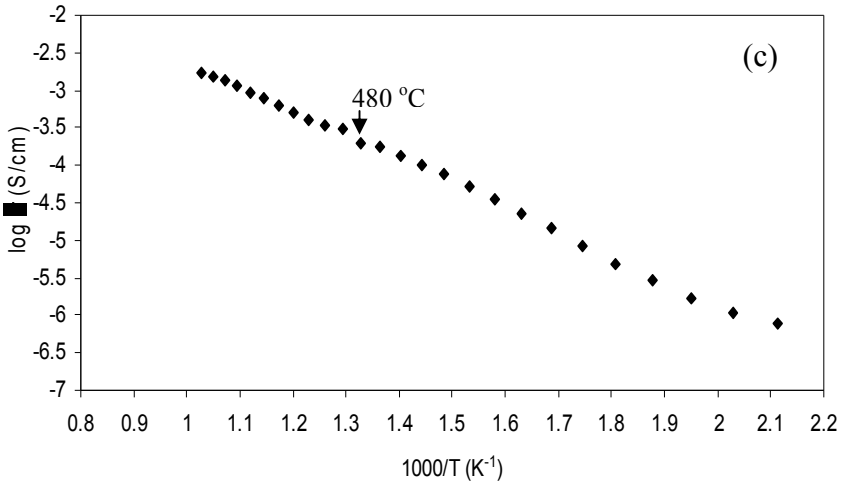

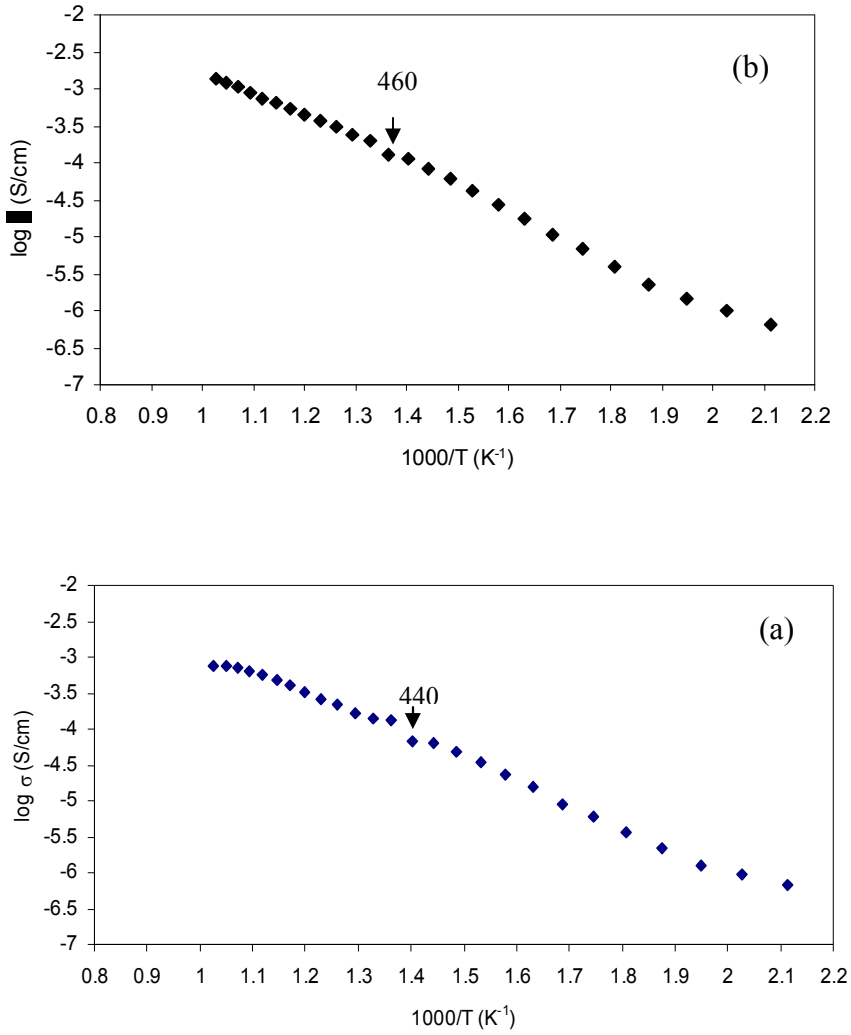

Fig. 4.22 Arrhenius plot of $Bi_4V_{1.6}Ti_{0.4}O_{11-\delta}$; (x = 0.4) at different sintering temperatures (a) 750 ^oC (b) 775 ^oC (c) 825 ^oC.

Increase of oxygen vacancies/formation of solid solution for the sample sintered at 800 and 825 ^oC provides higher conductivity of these samples than for the samples sintered at 750 and 775 ^oC.

About four times higher ionic conductivity was obtained in sample sintered at 800 ^oC as compared to sample sintered at 825 ^oC. The higher value might be attributed due to optimized size of grains and less porosity for sample sintered at 800 ^oC.

Interestingly, the volume of this particular sample is less than any other heat treated sample at various temperatures (table 4.9).

Table 4.10 Conductivity and activation energy at different sintering temperature of $Bi_4V_{2-x}Ti_xO_{11-\delta}$ (x = 0.4)

Sintering Temperature	$\sigma_{300\,^oC}$ (S/cm)	E_a (eV) < 400 °C	E_a (eV) > 500 °C
750 °C	5.99×10^{-6}	0.28	0.26
775 °C	6.82×10^{-6}	0.27	0.24
800 °C	2.66×10^{-5}	0.24	0.32
825 °C	8.42×10^{-6}	0.26	0.22

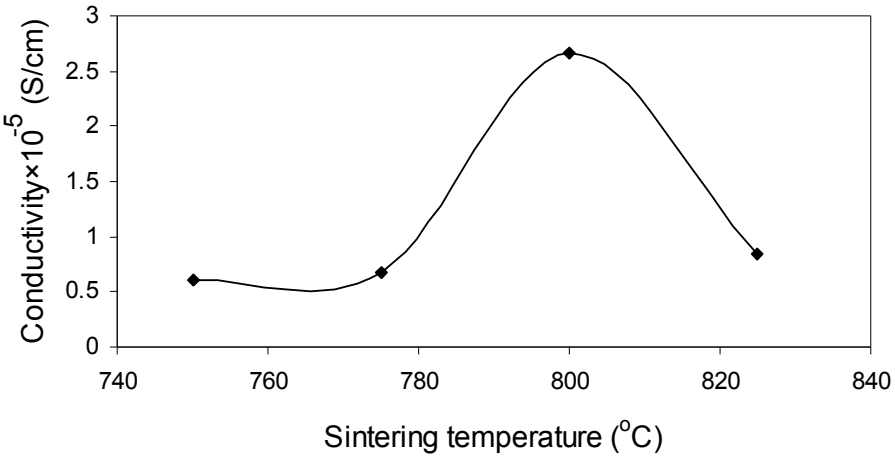

Fig. 4.23 Isothermal conductivity plot at 300 °C of $Bi_4V_{1.6}Ti_{0.4}O_{11-\delta}$ at different sintering temperatures

The conductivity trend in this system is in accordance with the creation of oxygen ion vacancies in the basal *a-b* plane. However, excess of impurity phase in case of samples sintered at 750 and 775 ^{o}C may cause the lowering of conductivity (fig. 4.23). The study of these samples clearly point out the importance of the processing condition on the properties.

4.1.3.2.3 Microstructural Analysis

Microstructural analyses on fractured surface of the samples sintered at 750, 775 and 825 ^{o}C were carried out under SEM. The micrographs are shown in figures 4.24. The SEM of the sample sintered at 750 ^{o}C has quite irregular patterns of grains with large variation in size (table 4.11). However, pattern of the samples sintered at 775 and 825 ^{o}C is giving similar look except the larger grain size observed for sample sintered at 825 ^{o}C. On comparing the microstructures of all the samples, it can be said that for higher ionic conductivity, stabilization of higher temperature γ-phase at room temperature is not the only criteria but a proper grain size along with low porosity is also an important factor to enhance the conductivity.

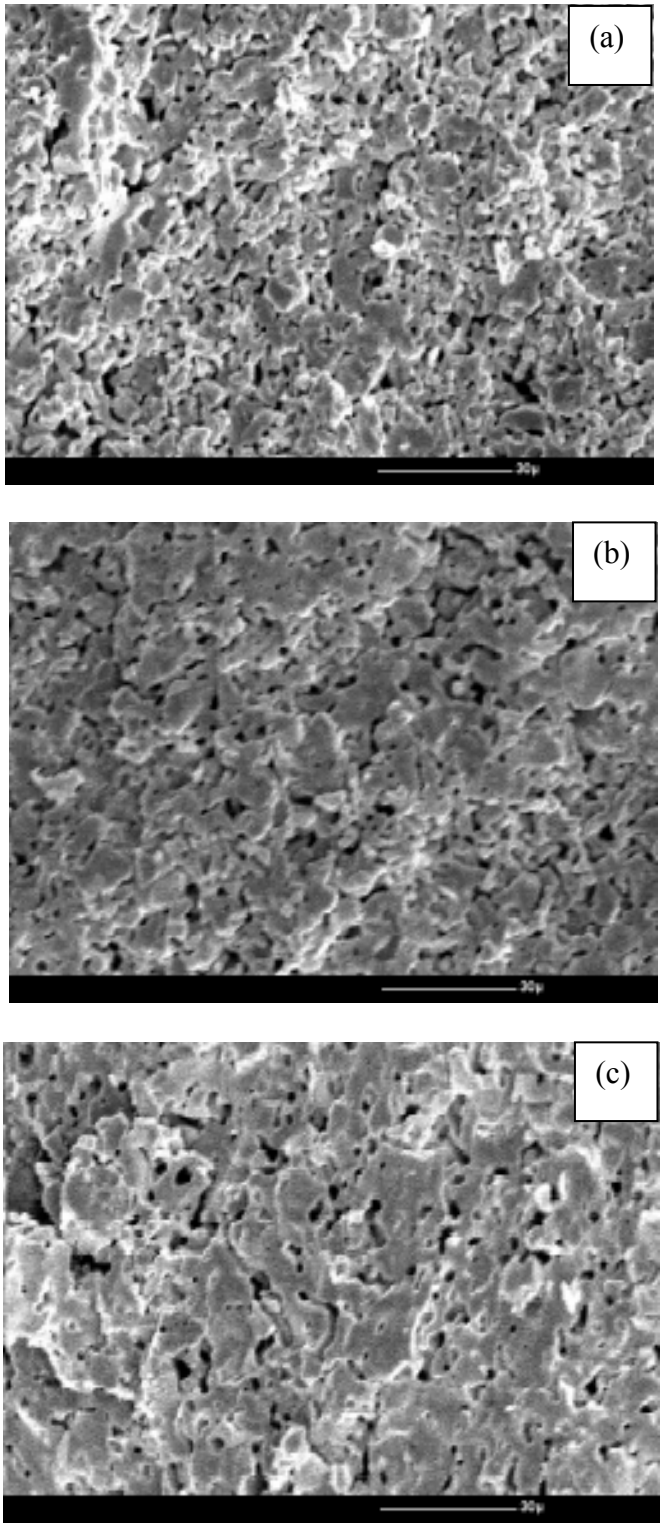

Fig. 4.24 SEM photographs of $Bi_4V_{1.6}Ti_{0.4}O_{11-\delta}$ sintered at (a) 750 ^oC (b) 775 ^oC and (c) 825 ^oC

Table 4.11 Average grain size of $Bi_4V_{1.6}Ti_{0.4}O_{11-\delta}$ at different sintering temperatures

Sintering temperature (^oC)	Grain size (μm)
750	4-10
775	8-12
800	6-10
825	15-20

4.1.3.3 $Bi_4V_{2-x}Me_xO_{11-\delta}$, (Me = Al^{3+})

4.1.3.3.1 X-ray Diffraction

The structure of Al-doped $Bi_4V_{2-x}Me_xO_{11-\delta}$ compounds for the composition x = 0.1, 0.2, 0.3, 0.4 were analyzed by X-ray diffraction study. The XRD patterns observed for $Bi_4V_{2-x}Al_xO_{11}$ ($0.1 \leq x \leq 0.4$) are shown in fig.4.25. XRD pattern of samples of x = 0.1 of $Bi_4V_{2-x}Al_xO_{11-\delta}$ characterized with the α-orthorhombic and presence of some β-phase while the room temperature unit cell is tetragonal of γ-type $Bi_4V_2O_{11}$ for x = 0.2, 0.3 and 0.4.

X-ray Powder Diffraction data confirmed that samples of $Bi_4V_{2-x}Al_xO_{11-\delta}$ of x = 0.1 and 0.2 are single phase whereas samples of compositions x = 0.3 and 0.4 show the presence of additional small intensity peaks at $2\theta \approx 25.7$ and 28^o that may be attributed to unreacted Bi_2O_3. This result is quite in disagreement with the solid solution range up to x = 0.5 by Lee *et al.* [133].

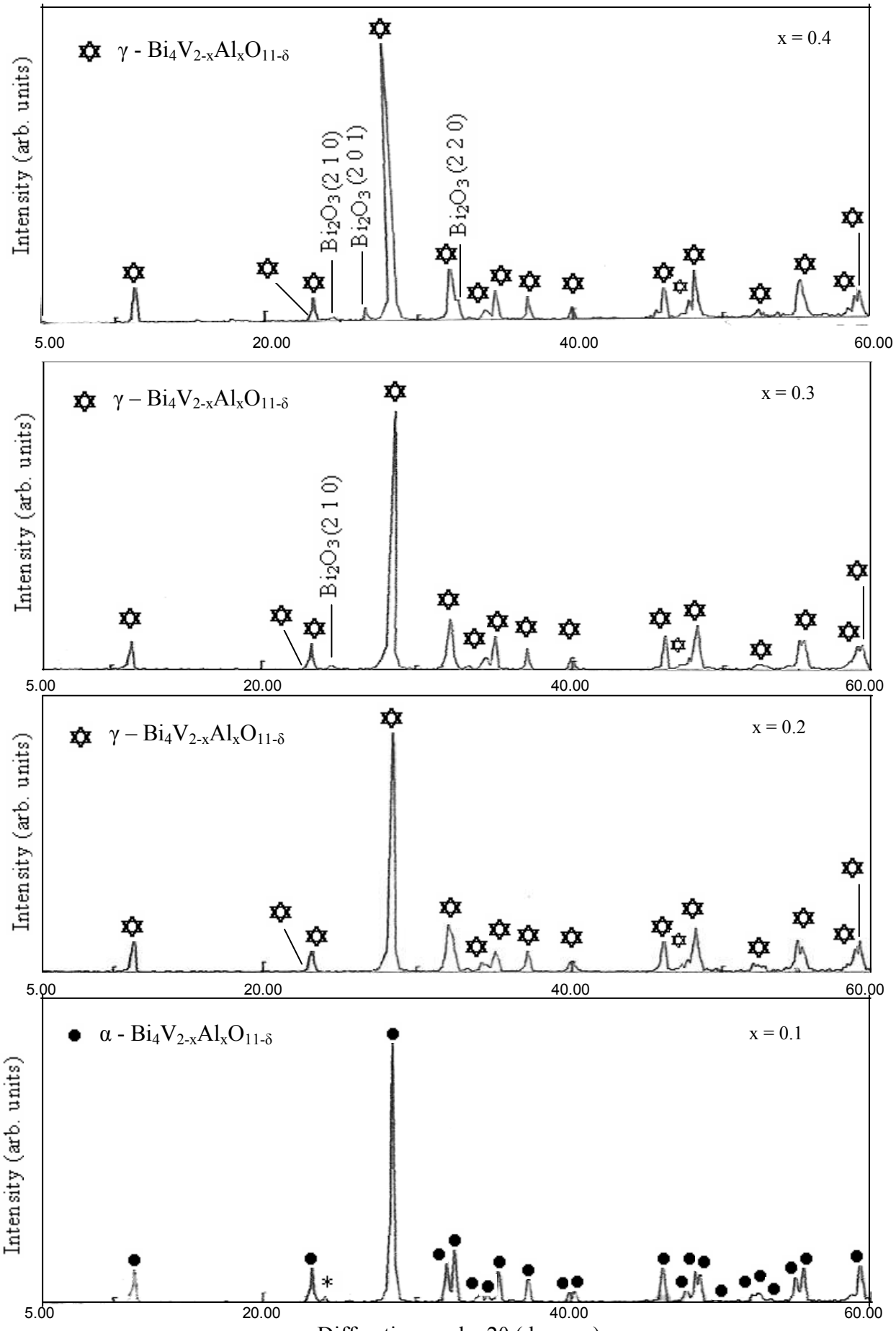

Fig. 4.25 X-ray Diffraction pattern of $Bi_4V_{2-x}Al_xO_{11-\delta}$, (*) superlattice reflection

No significant changes were observed in XRD diffraction pattern of samples of composition x = 0.2, 0.3 and 0.4. XRD patterns of $0.2 \leq x \leq 0.4$ are indexed to the γ- phase whereas other authors [131, 133] reported α-phase for value of x = 0.2.

4.1.3.3.2 Electrical Conductivity

The Arrhenius plots of $Bi_4V_{2-x}Al_xO_{11-\delta}$ for the composition x = 0.1 and 0.2, 0.3, 0.4 corresponding to α and γ- phases respectively are shown in fig.4.26. This indicates small or sharp discontinuity owing to phase transitions at 440°C, 450°C, 490°C and 460°C for x = 0.1, 0.2, 0.3 and 0.4 respectively.

The highest and lowest values of the ionic conductivity obtained with x = 0.2 and x = 0.4 respectively along with activation energy in the low temperature region are shown in Table 4.12.

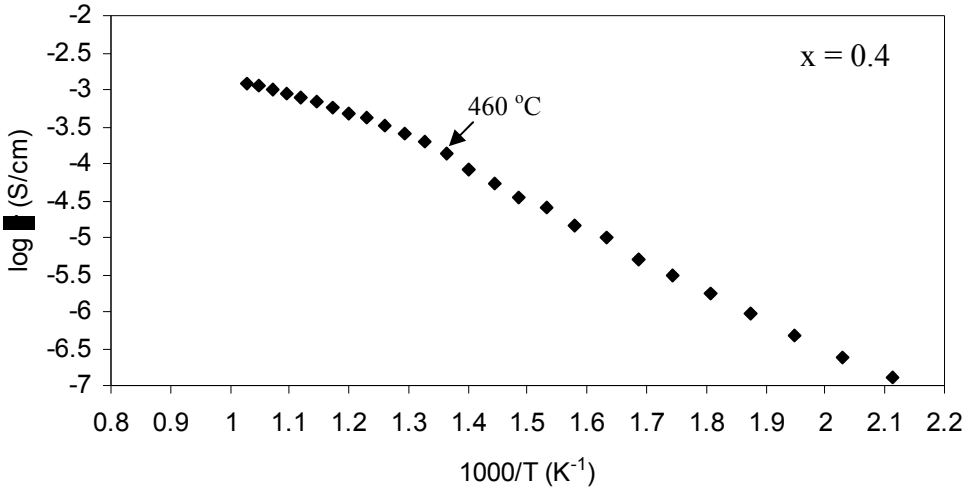

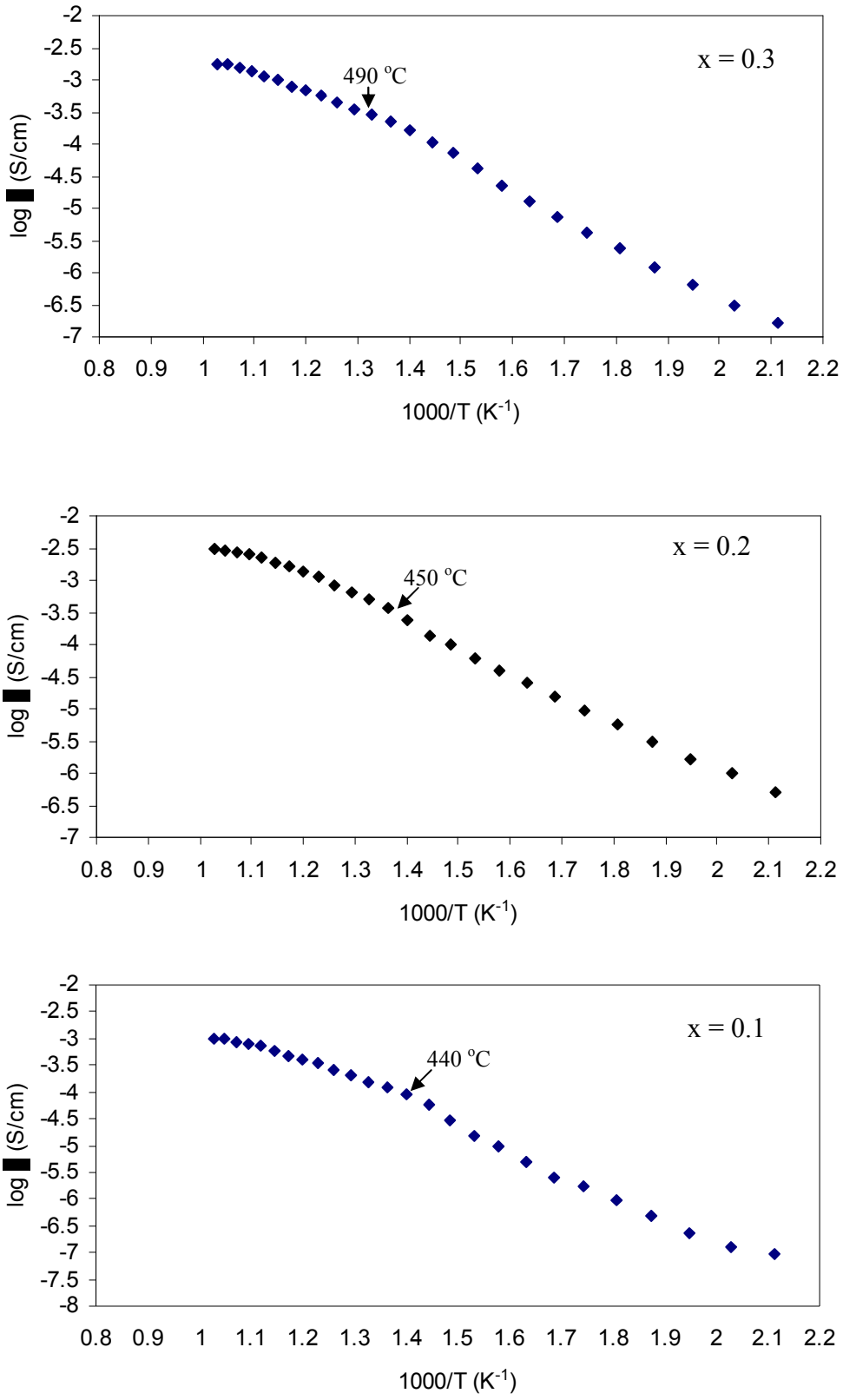

Fig.4.26 Arrhenius plot of $Bi_4V_{2-x}Al_xO_{11-\delta}$ ($0.1 \leq x \leq 0.4$)

The decrease of ionic conductivity from x = 0.2 to x = 0.4 (table 4.12) can be attributed to the formation of defect pairs. The effect of higher concentrations of vacancies is offset by the locally ordered states [195] due to presence of the impurity of Bi_2O_3 in the samples of compositions x = 0.3 and 0.4. For the x = 0.2 phase, both the vacancy concentration and the pathways for O^{2-} motion are optimized.

Table 4.12 Ionic conductivity at 300°C and activation energies of $Bi_4V_{2-x}Al_xO_{11-\delta}$

composition	σ_{300^oC} (S/cm)	E_a (eV) < 400°C
x = 0.1	1.74×10^{-6}	0.24
x = 0.2	8.38×10^{-6}	0.22
x = 0.3	4.20×10^{-6}	0.23
x = 0.4	3.02×10^{-6}	0.24

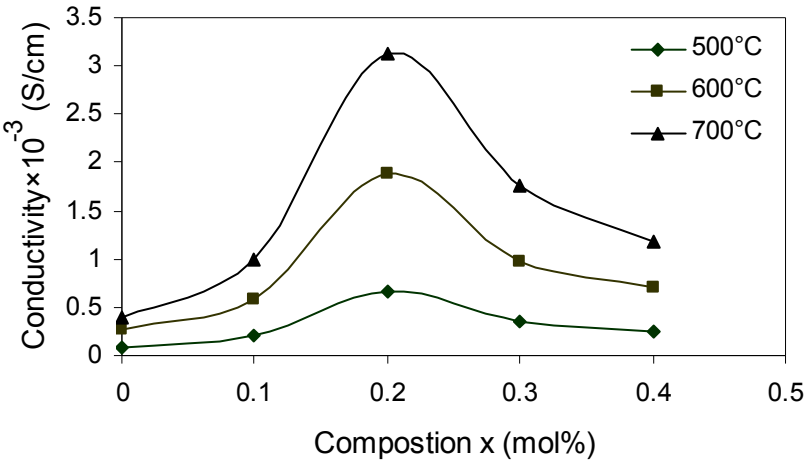

Fig. 4.27 Isothermal plot of composition dependant conductivity at different temperatures of $Bi_4V_{2-x}Al_xO_{11-\delta}$

The conductivities at higher temperatures are given in figure 4.27**,** which shows the higher conductivity for x = 0.2 as found at 300 ^{o}C.

4.1.3.3.3 Microstructural Analysis

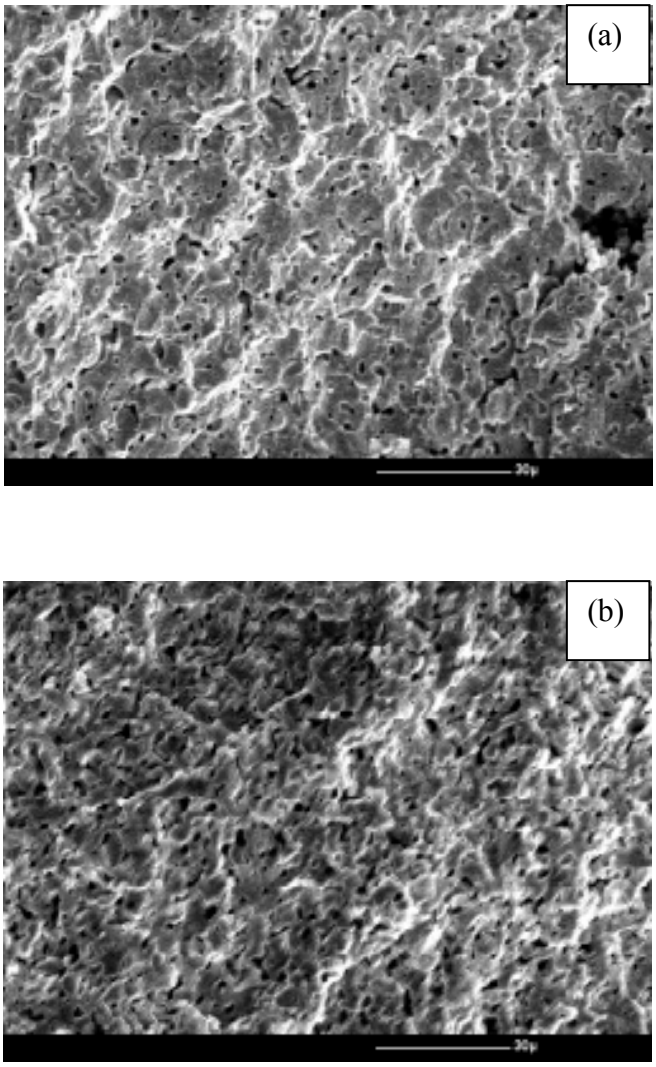

Fig.4.28. SEM photograph of fractured surface of $Bi_4V_{2-x}Al_xO_{11-\delta}$ (a) x = 0.2 (b) x = 0.4 sintered at 800 ^{o}C

Scanning electron micrographs of the fractured surface of aluminium substituted $Bi_4V_2O_{11}$ of the compositions of x = 0.2 and x = 0.4 with highest and lowest value of

conductivity, respectively are shown in fig. 4.28 (a) and (b). The grains (8-12 μm) are observed to be relatively uniform for x = 0.2 when compared to sample of x = 0.4 where non-uniform pattern is observed with size 4-8 μm. Big hole existing on the right side of the micrograph is because of material removal when the pellet for SEM study was fractured (fig.4.28a). The material is detached from this area and the pattern is uniformly distributed throughout the structure.

Another important aspect can be generated about the smaller grain size of the sample of composition x = 0.4 which is accustomed to decrease the electrical conductivity by increasing low conductive grain boundary area and consequently has higher activation energy for the conduction as well. This supports the well known fact that the transport properties of solid electrolytes at intermediate temperature are controlled mainly by the grain boundaries.

4.1.3.4 Sintering at different temperatures of $Bi_4V_{1.8}Al_{0.2}O_{11-\delta}$

Sintering at different temperatures for aluminium based bismuth vanadate for the high conducting composition x = 0.2 was also done to see its effect on phase formation /stabilization *viz.* α, β and γ and electrical conductivity. This study is also important to correlate the effect of sintering temperature with the type of dopant / substitutent cation. For this study, final sintering / reaction temperature was kept at 750 ^oC, 775 ^oC and 825 ^oC in addition to 800 ^oC which was studied above.

4.1.3.4.1 X-ray Diffraction

The XRD patterns of the samples sintered at 750, 775, 800 and 825 ^oC (fig. 4.29) has shown the contribution of β-phase at lower sintering temperatures of 750 and 775 ^oC

which is observed due to weak splitting of tetragonal (1 1 0) peak at ~ 32°. Whereas other two samples sintered at 800 and 825 °C show the complete γ-phase. It can be concluded from above analysis that phase stabilization of α, β and γ at room temperature is also dependant on sintering temperature in similar with the composition variation. The minima at 775 °C in *c*-parameter (table 4.13) also suggest the boundary between phase transition from β to γ. This result supports the work by Lee et al. [133]. Furthermore, samples sintered at 750 °C, shows the presence of additional phase of Bi_2O_3 whereas sintering temperature 800 °C is the optimum to obtain phase pure compound. However, little amount of impure phase is also noticed in the samples sintered at 775 °C.

Table 4.13 Lattice parameters of $Bi_4V_{1.8}Al_{0.2}O_{11-\delta}$ sintered at 750 °C, 775 °C, 800 °C and 825 °C

Sintering temp.	a (Å)	c (Å)	Volume (Å^3)
750 °C	3.96	15.35	244.92
775 °C	3.96	15.31	244.61
800 °C	3.96	15.36	231.98
825 °C	3.98	15.35	237.72

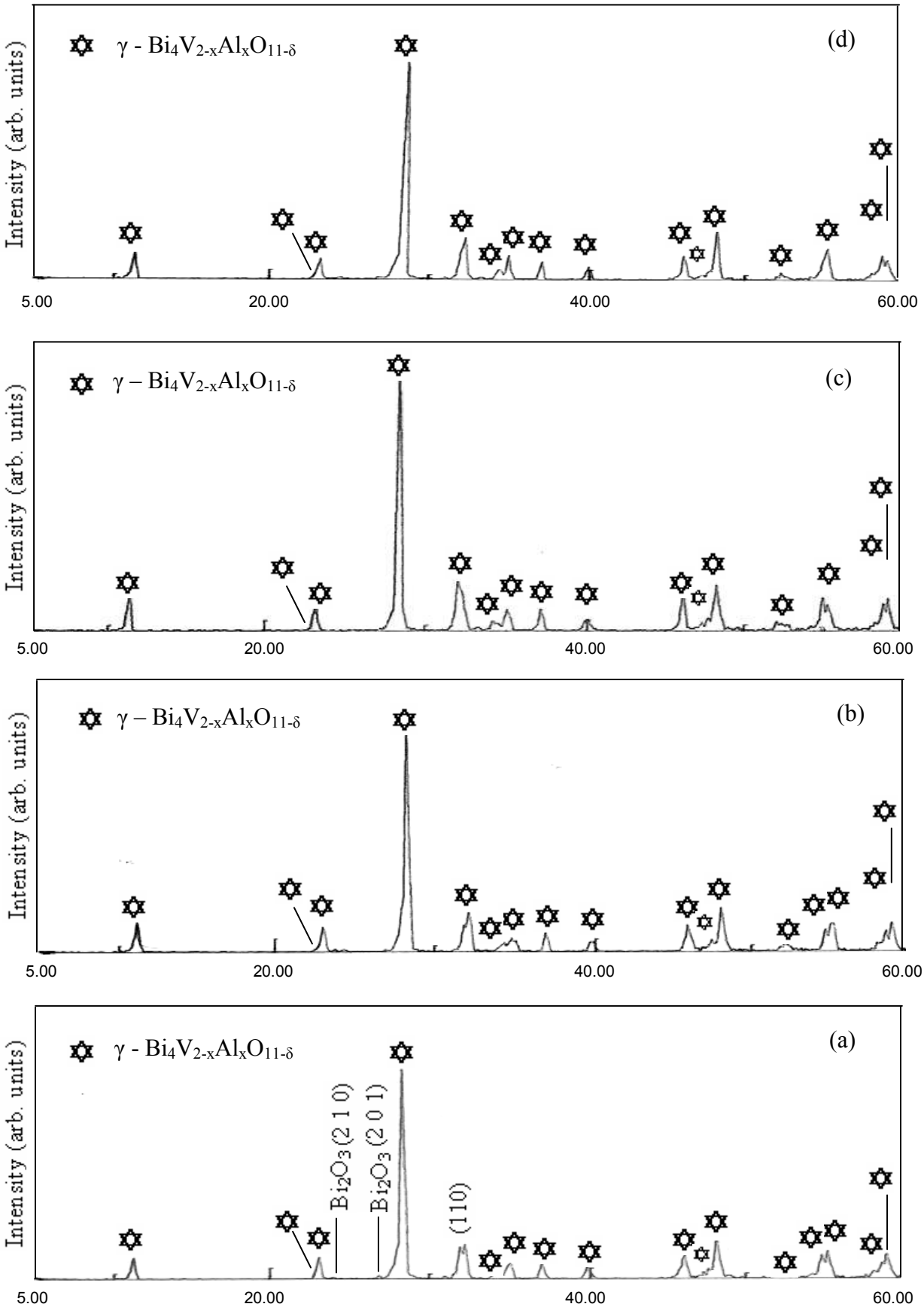

Fig. 4.29 X-ray Diffraction pattern of $Bi_4V_{1.8}Al_{0.2}O_{11-\delta}$ sintered at (a) 750 °C, (b) 775 °C, (c) 800 °C and (d) 825 °C

4.1.3.4.2 Electrical Conductivity

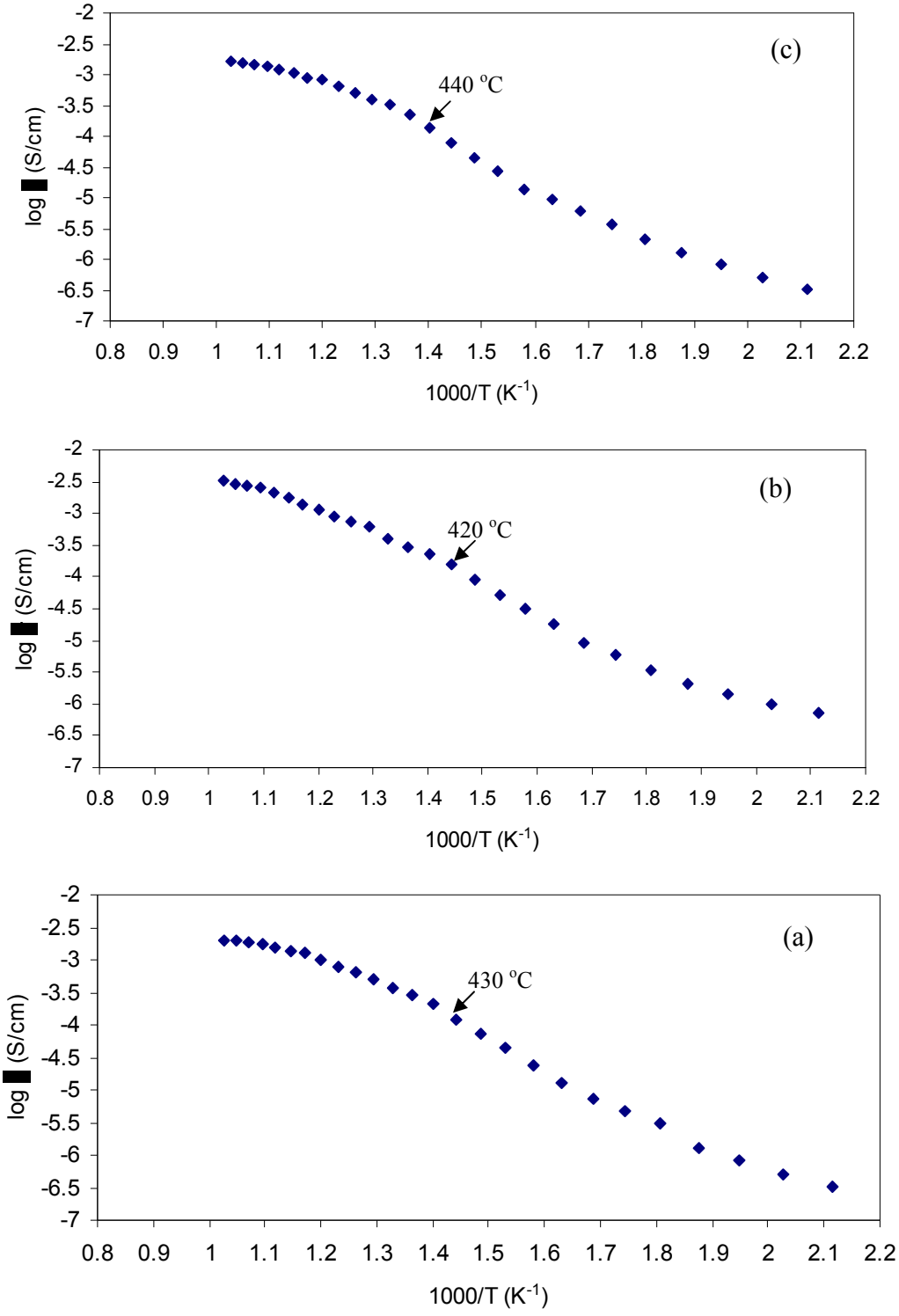

Fig. 4.30 Arrhenius plot of $Bi_4V_{2-x}Al_xO_{11-\delta}$ (x = 0.2) at different sintering temperatures

(a) 750 °C (b) 775 °C (c) 825 °C

The electrical conductivity measurement data at sintering temperatures of 750, 775 and 825 ^{o}C are presented in the form of Arrhenius plots (fig.4.30). The curves do not follow the linear behaviour. The curves consist of two linear regions. In the intermediate temperature regions, a pronounced curvature is also present in the Arrhenius plot (fig.4.30) at 430 ^{o}C, 420 ^{o}C and 440 ^{o}C of the pellets sintered at 750 ^{o}C, 775 ^{o}C and 825 ^{o}C respectively. The conductivity measured at 300 ^{o}C is summarized in table.4.14.

The highest conductivity is obtained for sample x = 0.2 sintered at 800 ^{o}C as compared to all other selected temperatures followed by 775^{o}C in the following sequence of conductivity measured at 300 ^{o}C: $\sigma_{825}<\sigma_{750}<\sigma_{775}<\sigma_{800}$. This trend is in complete agreement with the x-ray diffraction study of these samples which shows the single phase γ for sintering temperature of 800 ^{o}C.

Table 4.14 Conductivity and activation energy at different sintering temperature of $Bi_4V_{1.8}Al_{0.2}O_{11-\delta}$

Sintering Temperature	$\sigma_{300\,^{o}C}$ (S/cm)	E_a (eV) < 400 ^{o}C
750 ^{o}C	4.83×10^{-6}	0.32
775 ^{o}C	6.09×10^{-6}	0.29
800 ^{o}C	8.38×10^{-6}	0.22
825 ^{o}C	3.63×10^{-6}	0.29

The conductivity obtained for the sample of composition x = 0.2 at sintering temperature of 800 ^{o}C (fig. 4.31) is greater by 1.37 and 2.30 times of the sample sintered at 775 and 825^{o}C respectively whereas it is 2.77 times high by lowest conducting composition of x = 0.4. This suggests that conductivity is more composition dependent than sintering temperature.

However, it is low by 3.17 times as compared to titanium based compound for x = 0.4 for the sintering temperature 800 ^{o}C which supports the stacking claim of superiority of each dopant over the other.

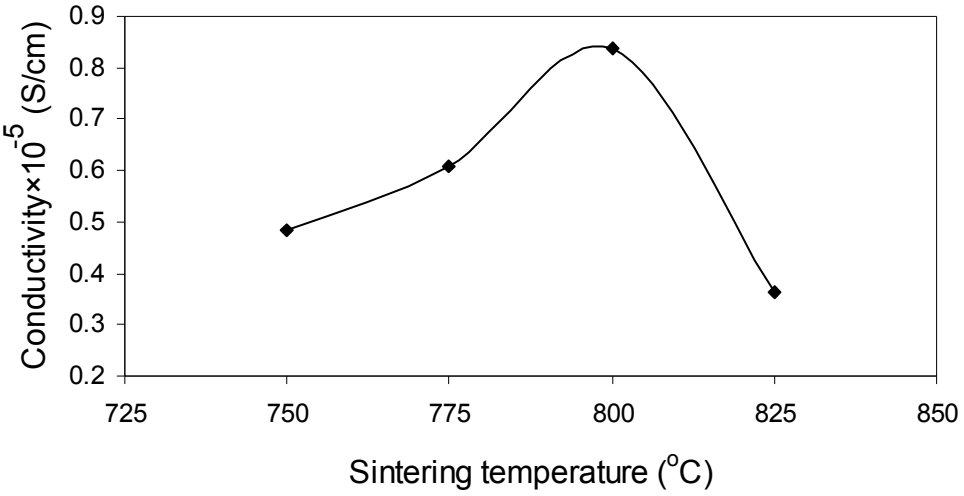

Fig. 4.31 Conductivity versus sintering temperature at 300^{o}C

4.1.3.4.3 Microstructural Analysis

Scanning electron microscopy of the fractured surfaces of the samples sintered at 750, 775 and 825 ^{o}C was carried out to correlate the variation in sintering temperature with microstructure and electrical conductivity.

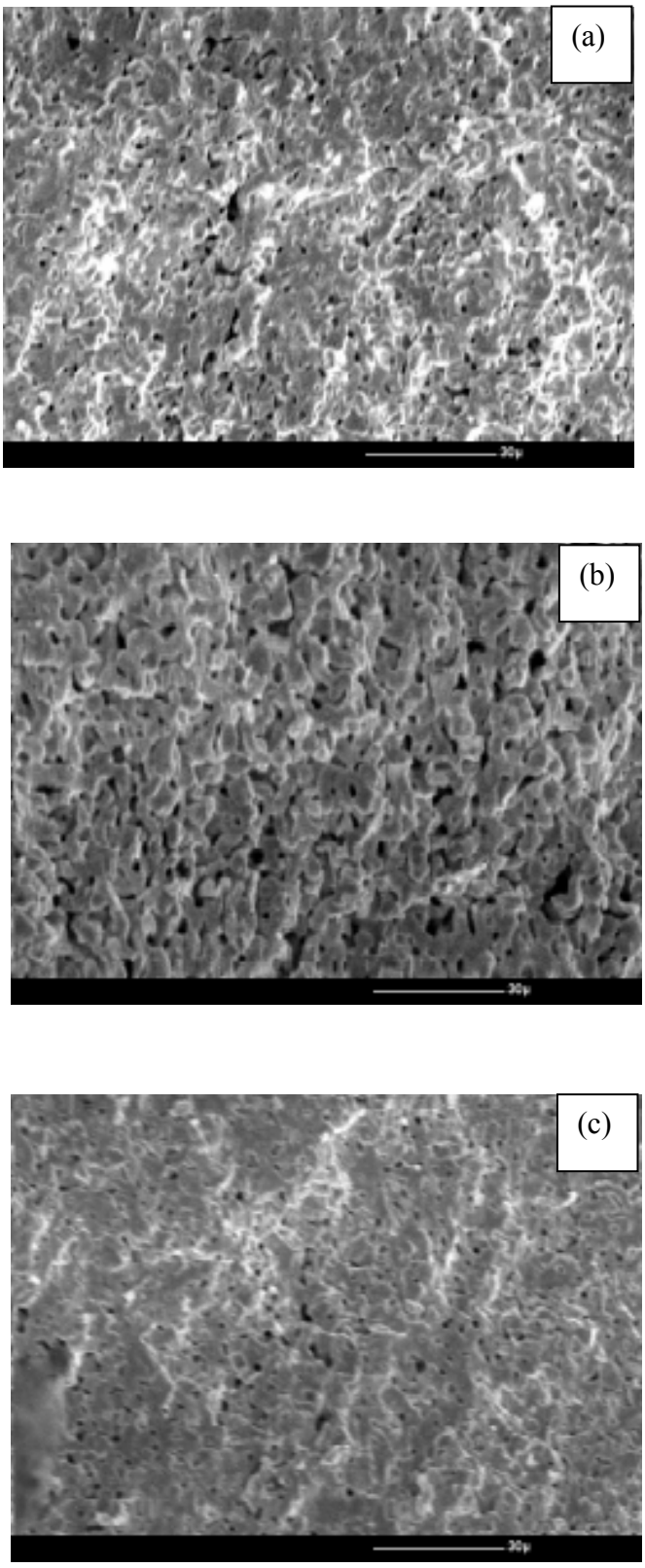

Fig. 4.32 SEM photographs of $Bi_4V_{1.8}Al_{0.2}O_{11-\delta}$ sintered at (a) 750 ^oC (b) 775 ^oC and (c) 825 ^oC

The above results of variation in conductivity are further supported by fractured surface SEM photographs of the samples at the studied temperature range as shown in figure 4.32 (a, b, c). A closer look at the micrographs clearly shows uniform distribution of grains (10-15 μm) for the samples sintered at 775 ^{o}C. The other two samples, one sintered at 750 ^{o}C shows non uniform pattern and no evidence of textured microstructure. Partial melting to the left of lower side is observed for the sample sintered at 825 ^{o}C which may be accounted for these samples exhibiting low conductivity owing to smaller conducting path.

4.1.3.5 $Bi_4V_{2-x}Me_xO_{11-\delta}$, ($Me = Cr^{3+}$)

4.1.3.5.1 X-ray Diffraction

The X-ray diffraction analyses of the powders of the sintered pellets prepared from stoichiometric amounts of Bi_2O_3, V_2O_5 and Cr_2O_3 ($Bi_4V_{2-x}Cr_xO_{11-\delta}$) for the compositions of x = 0.1, 0.2, 0.3 and 0.4 were conducted.

In the present system, the patterns corresponding to composition x = 0.1, 0.2, 0.3 and 0.4 are shown in figure 4.33. The pattern for x = 0.1 were analyzed and one can see very weak reflection at $2\theta \approx 24.2^{o}$ and splitting at $2\theta \approx 31$, 39, 48 and 54^{o} which is attributed to the superstructure of α-form. The superstructure reflection is formed due to vacancy ordering in this composition [196]. However, in samples of x = 0.2, 0.3 and 0.4, peak at 32.9^{o} has broadened suggesting the small contributon of β-phase. Formation of α-phase and solid solution has been reported for composition up to 0.5 by various authors [133, 152]. Moreover, XRD of above samples are showing very anomalous results which shows the presence of impurity of $BiVO_4$ (ICDD card no. 83-1698) with a very strong peak at ~ 28.5^{o} and another small peak at ~ 27.9^{o} in close neighbourhood of $BiVO_4$.

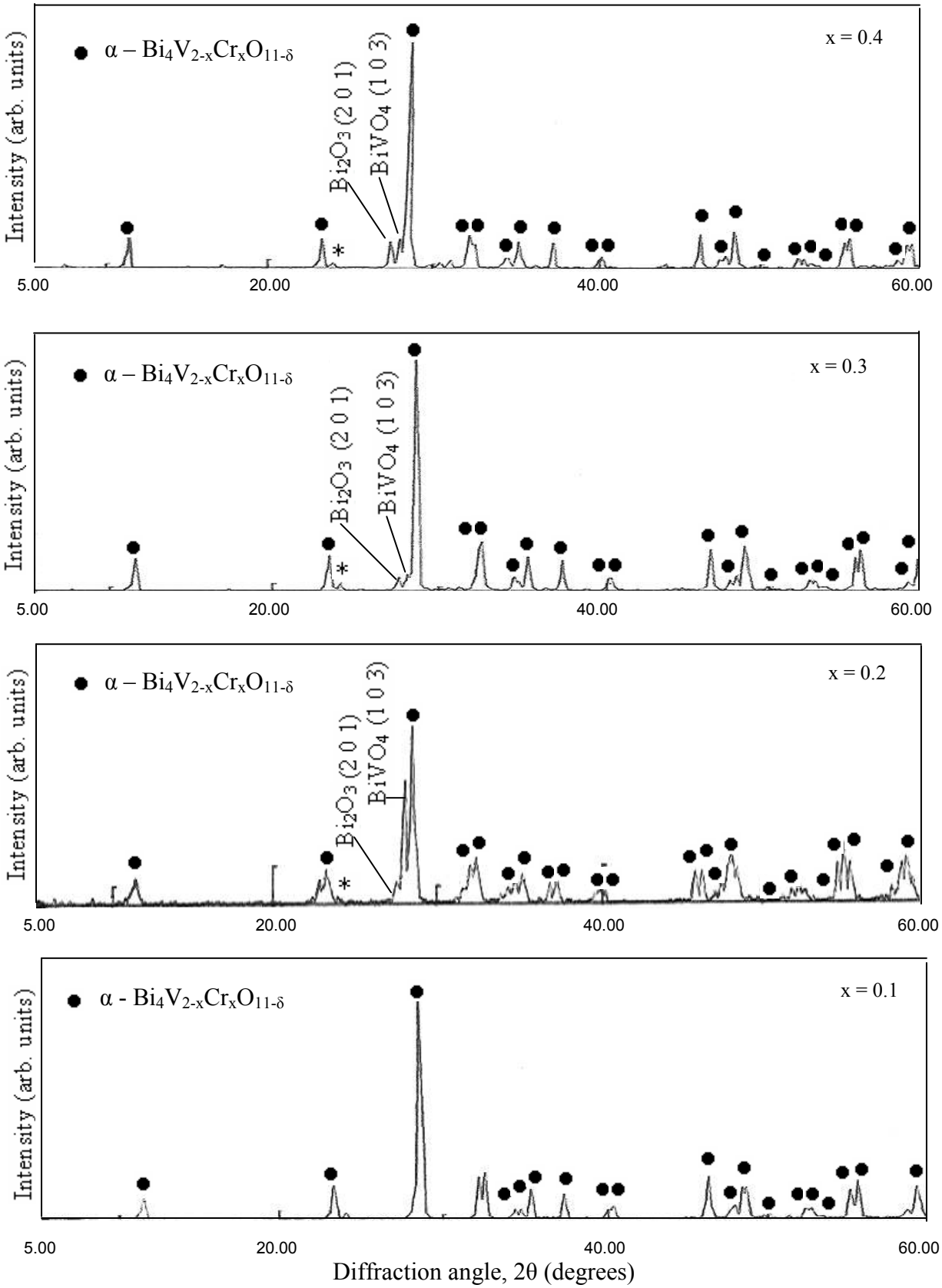

Fig. 4.33 X-ray Diffraction pattern of $Bi_4V_{2-x}Cr_xO_{11-\delta}$ (a) x = 0.1, (b) x = 0.2, (c) x = 0.3, (d) x = 0.4; (*) superlattice reflection

This is due to Bi_2O_3 for x = 0.2 and almost same trend was observed for other two samples of x = 0.3 and 0.4 but of varying peak intensities. The formation of $BiVO_4$ may be attributed to some stoichiometrical changes in the bismuth and vanadium composition during synthesis [167].

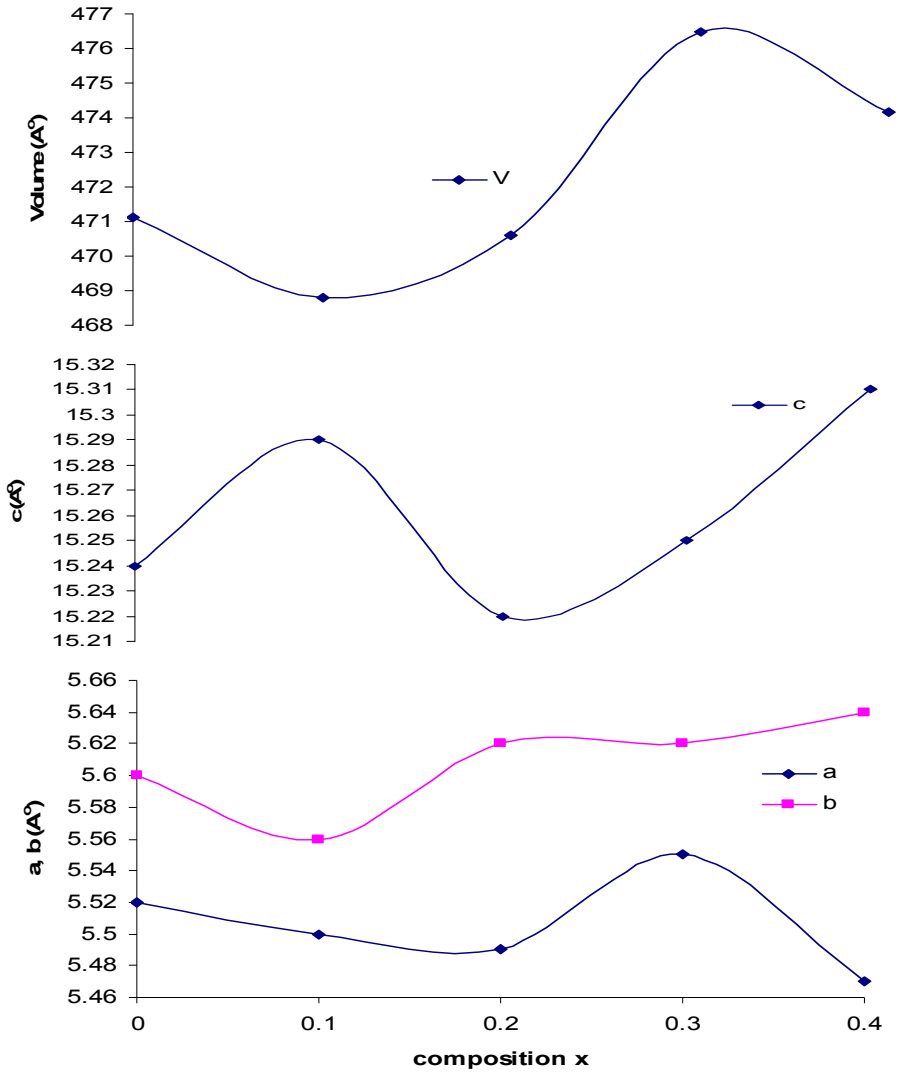

Fig. 4.34 Mean cell parameters and volume of $Bi_4V_{2-x}Cr_xO_{11-\delta}$ w.r.t. composition (x)

The variation in lattice parameter could not show any trend (fig. 4.34). However, sample x = 0.1 exhibits overall shrinkage in the unit cell. It may be attributed to the increase in oxygen vacancies and formation of solid solution, which leads to the decrease in unit cell, as indicated in figure 4.34.

4.1.3.5.2 Electrical Conductivity

The conductivity behaviour of all the Cr-doped compositions shows two linear regions with different activation energies in their Arrhenius plot - a low temperature region and a high temperature region as shown in figure 4.35. The link between these two linear regions is either in the form of a simple but distinct change in the slope at about 450-500 ^{o}C or a discontinuity around this temperature range.

The Arrhenius plots for the composition range in the BICRVOX family ($0.1 \leq x \leq 0.4$) are shown in figure 4.35. A direct $\gamma \rightarrow \alpha$ transition is observed with suppressed β-phase for ($0.1 \leq x \leq 0.4$). The phase transitions occur at 440 ^{o}C for x = 0.1, 0.4 and at 460 ^{o}C for x = 0.2, 0.3 during cooling. These transitions occur at lower temperatures than that reported by Joubart et al. [152], i.e. at around 600 ^{o}C. The discrepancy occurs possibly due to the change in processing conditions. It leads to more distortion in orthorhombic unit cell after doping bismuth vanadate with Cr^{3+}.

The values of conductivity obtained from impedance spectroscopy are in the range of those values which correspond to α-phase for all the compositions studied. Generally, ordering of the mobile sublattices results in an increase in activation energy for conduction due to ion trapping effects.

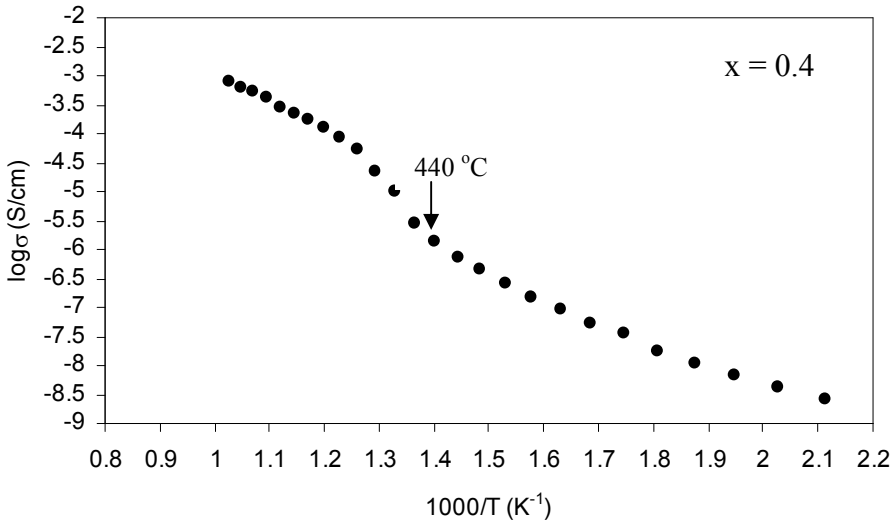
x = 0.4
440 °C
logσ (S/cm)
1000/T (K-1)

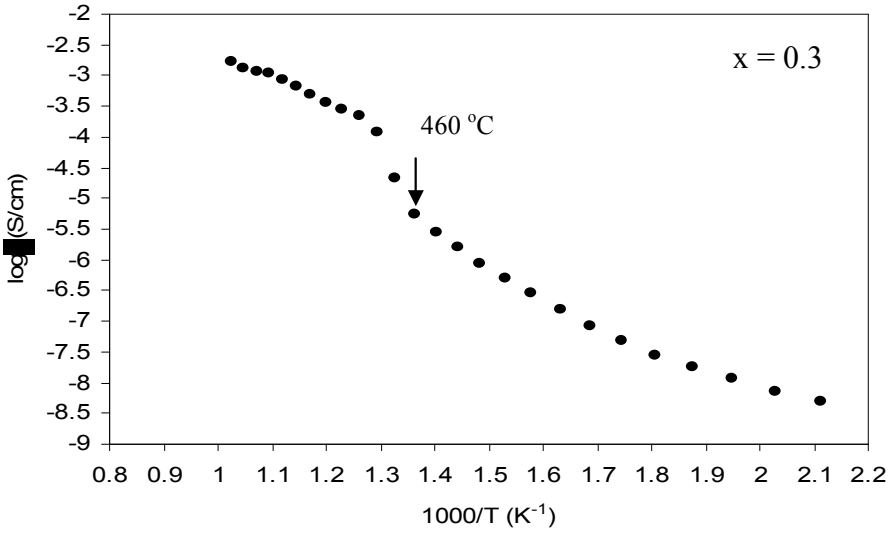
x = 0.3
460 °C
log (S/cm)
1000/T (K-1)

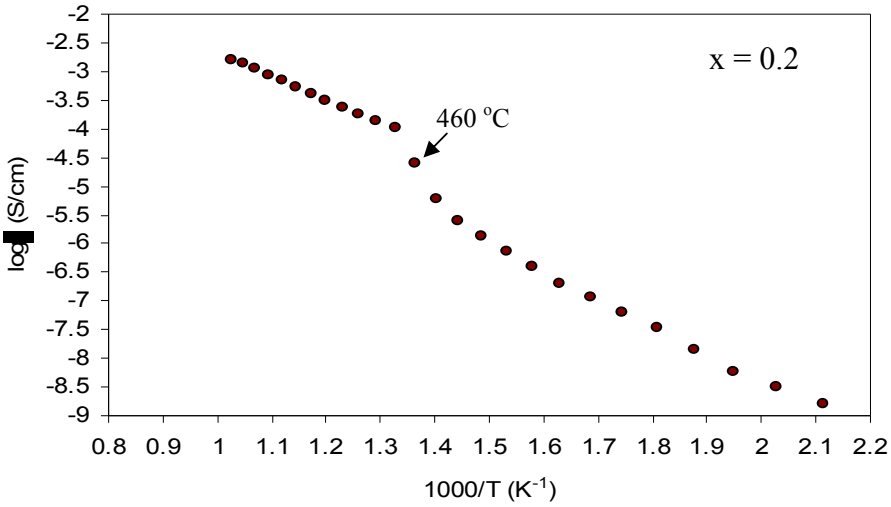
x = 0.2
460 °C
log (S/cm)
1000/T (K-1)

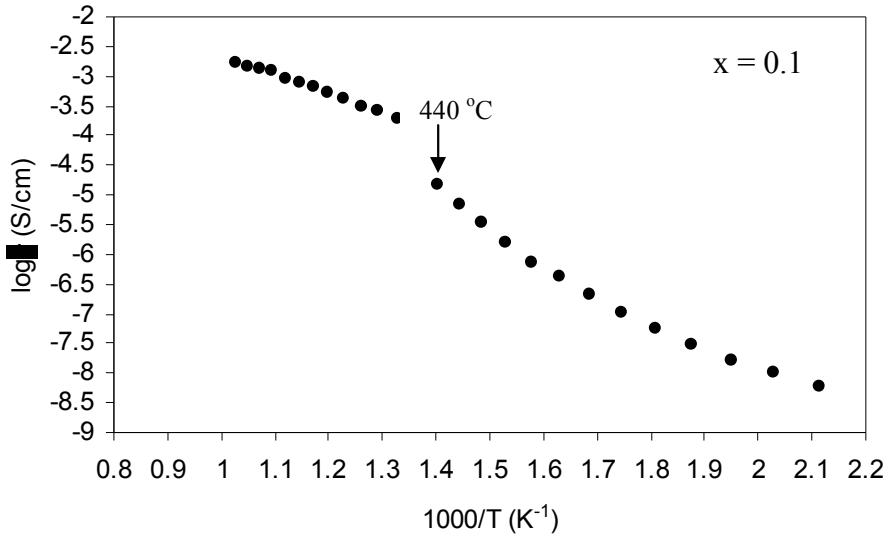

Fig. 4.35 Arrhenius plot of $Bi_4V_{2-x}Cr_xO_{11-\delta}$, $(0.1 \leq x \leq 0.4)$

High conductivity of the sample of composition x = 0.1 (table 4.15) is owing to large increase in oxygen vacancies which leads to smaller unit cell volume (fig.4.34) as compared to all other compositions. Conductivity of all the doped samples comes out to be smaller than that for the undoped α-$Bi_4V_2O_{11}$. It might be attributed to the fact that V^{5+} occupies the tetrahedral site with increasing amount of Cr^{3+} substitution.

As the percentage of doping increases, the ionic conductivity decrease. In Cr^{3+}-doped samples, the tendency for Cr^{3+} to adopt a full regular octahedral coordination and form clusters seems to be associated with the rise in the number of tetrahedrally coordinated V^{5+} in the lattice [152]. This clustering, as well as the increase in the number of unfavorable tetrahedral V^{5+} sites, may cause the poor oxide ion conductivity of Cr^{3+}-doped samples.

Table 4.15 Conductivity for different compositions of $Bi_4V_{2-x}Cr_xO_{11-\delta}$

Composition	σ_{300^oC} (S/cm)	E_a (eV) < 400°C	E_a (eV) >500°C
x = 0.1	1.08×10^{-7}	0.38	0.27
x = 0.2	6.52×10^{-8}	0.40	0.35
x = 0.3	4.83×10^{-8}	0.31	0.35
x = 0.4	3.67×10^{-8}	0.33	0.48

The decreasing order of conductivity with doping rate may also support the views of Sharma *et al*. [131] who reported that the anion vacancies alone can not determine the ionic conductivity of the material, but ionic potential may also be responsible for this phenomenon.

4.1.3.6 $Bi_4V_{2-x}Me_xO_{11-\delta}$ ($Me = Ga^{3+}$)

4.1.3.6.1 X-ray Diffraction

The X-ray diffraction of powders of sintered pellets prepared by taking appropriate amounts of Bi_2O_3, V_2O_5 and Ga_2O_3 were conducted. The patterns corresponding to compositions x = 0.1, 0.2, 0.3 and 0.4 of the $Bi_4V_{2-x}Ga_xO_{11-\delta}$ compound are shown in figure 4.36. It has been observed that the gallium composition of x = 0.1 exhibits α-phase of bismuth vanadate. On the other hand, orthorhombic β-phase of $Bi_4V_2O_{11}$ is present in the range of $0.2\leq x\leq0.4$. X-ray diffraction patterns of these samples have been indexed with the (*h k l*) values from reference [161]. Structurally, these β and γ-phases are more or less same except the splitting of tetragonal (110) peak which is at 32° along with the presence of weak superstructure peak at ~ 24.2°.

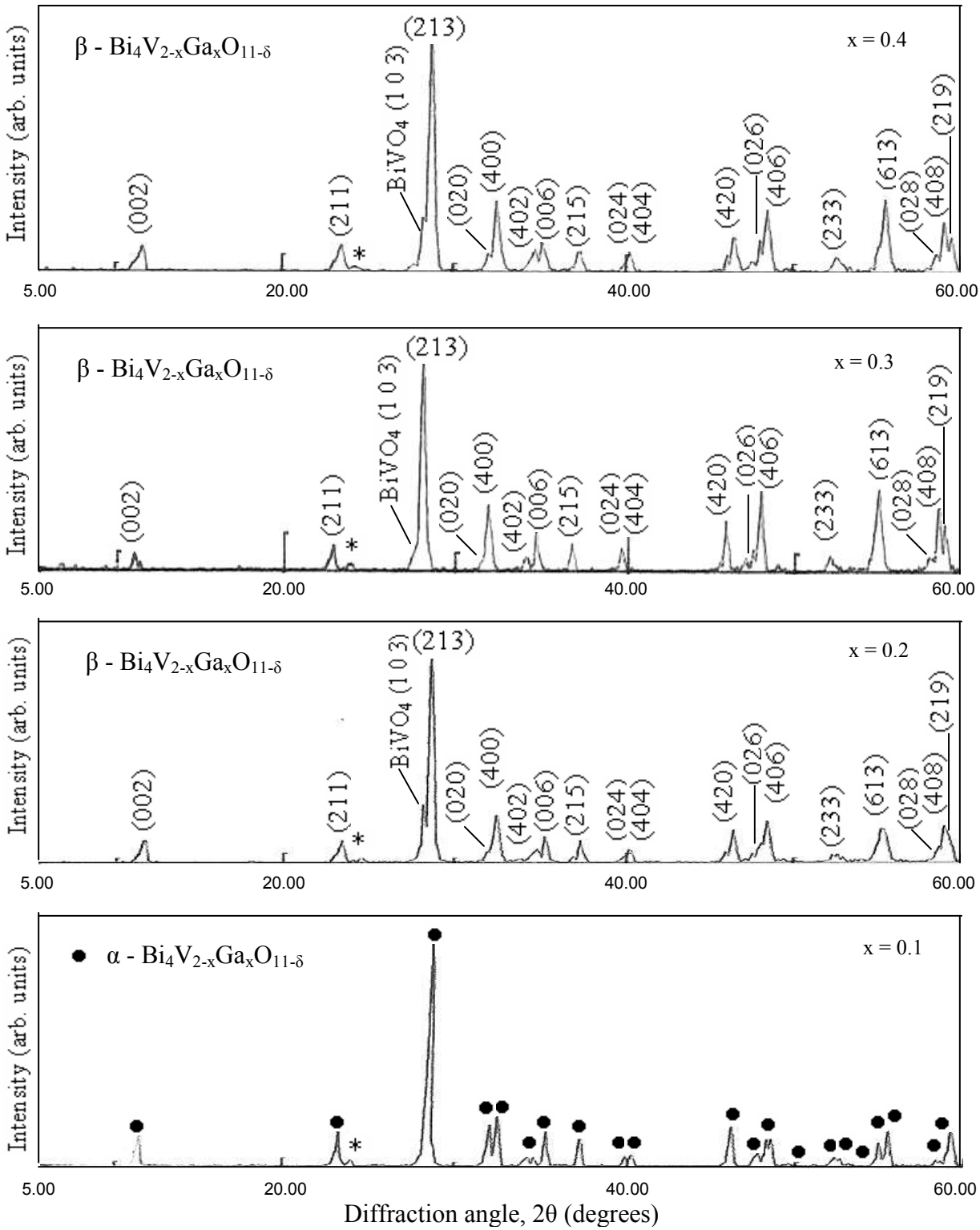

Fig. 4.36 The XRD pattern of $Bi_4V_{2-x}Ga_xO_{11-\delta}$; (*) superlattice reflection

Additional peaks of impurity phase appear when dopant percentage increased which correspond to $BiVO_4$. The splitted small peak of $BiVO_4$ in the neighborhood of highest intensity peak for x = 0.2 might be merging with highest intensity peak in sample of composition x = 0.3 and again appearing for x = 0.4.

4.1.3.6.2 Electrical Conductivity

The conductivity measurement was performed for $Bi_4V_{2-x}Ga_xO_{11-\delta}$ for the Ga^{3+} concentration of 5, 10, 15 and 20%. The conductivities were plotted as log σ vs. 1/T as shown in figure 4.37. Arrhenius plot shows two transitions for x = 0.1 (α-compound) from γ → β and β → α at 500 and 460 ^oC respectively. For higher concentration, gallium has only single transition from γ to β. These transitions are observed at 400, 420 and 440 ^oC for x = 0.2, 0.3 and 0.4 (β compound), respectively.

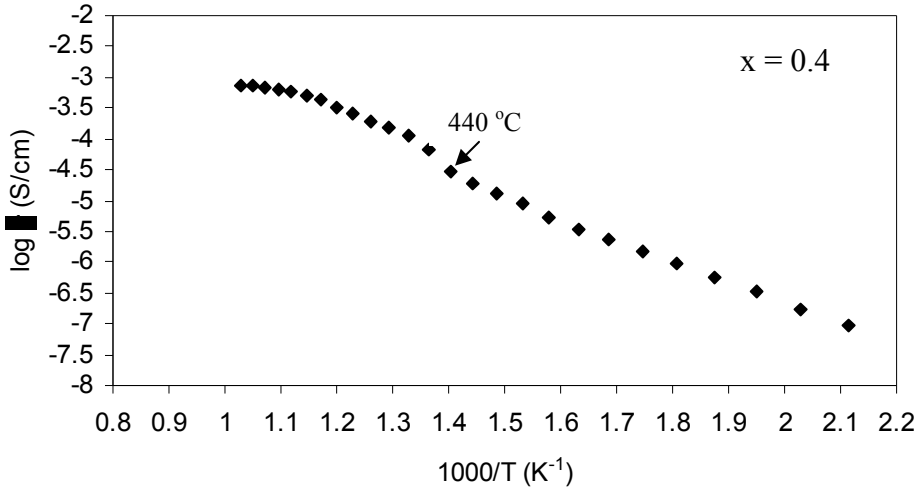

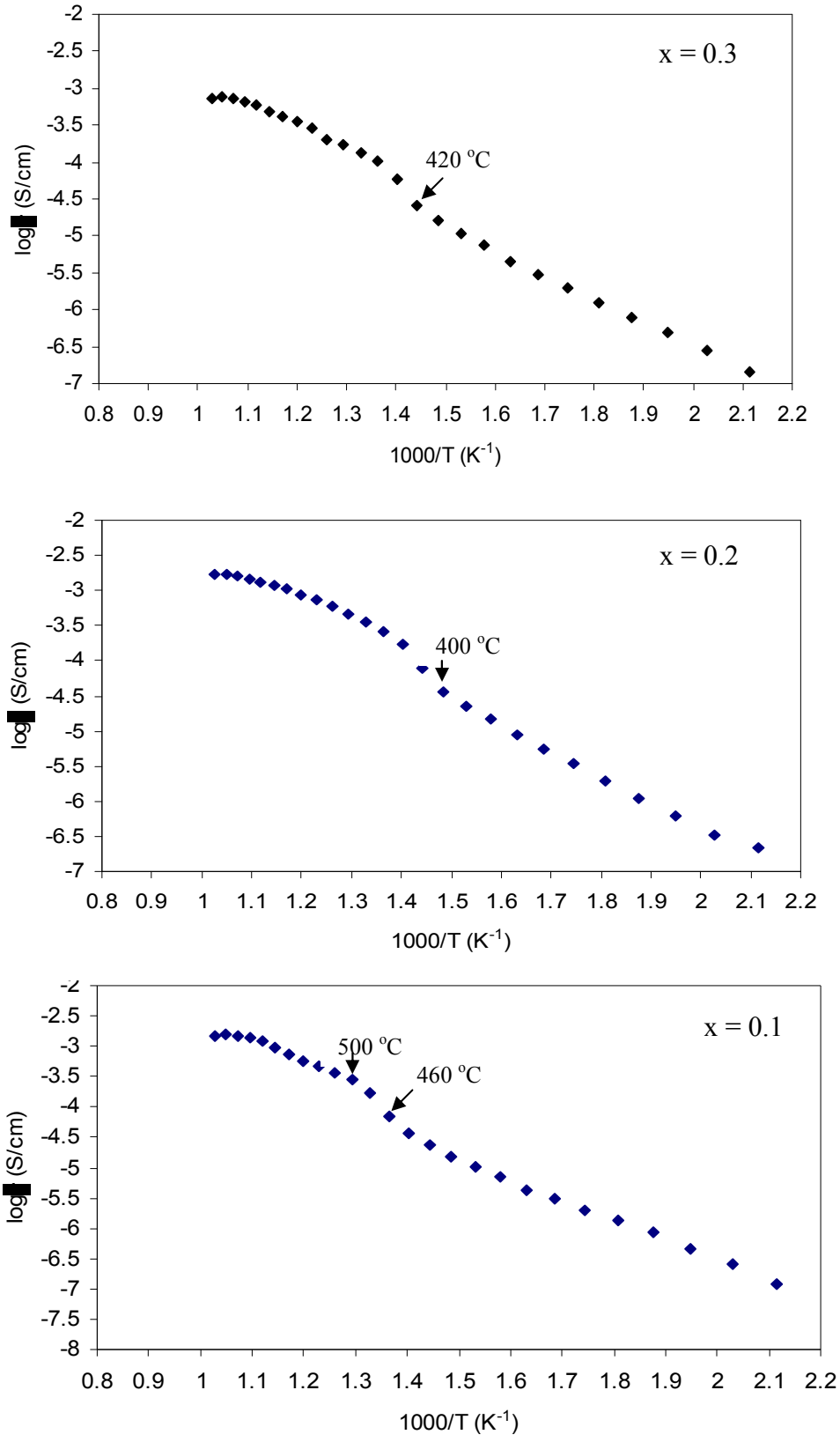

Fig. 4.37 Arrhenius plot of $Bi_4V_{2-x}Ga_xO_{11-\delta}$ ($0.1 \leq x \leq 0.4$)

Highest and lowest values of ionic conductivity was calculated at 300 ^{o}C for x = 0.2 (3.40×10^{-6} S/cm) and 0.4 (1.44×10^{-6}S/cm) respectively. Conductivity decreases beyond x = 0.2 sample due to limit of solid solution formation. The smaller values of conductivity of BIGAVOX as compared to other dopant such as Cu^{2+}, Ti^{3+} etc. could be explained on the basis of phase stabilization. In the present case, the β-phase is stabilized instead of γ-phase at room temperature.

In trivalent system, titanium substitution is done ($Bi_4V_{2-x}Ti_xO_{11-\delta}$). It was observed that pure compound (γ-phase) up to entire range of composition x = 0.4 has formed. At the same time, aluminium, chromium and gallium substitution is found to exhibit solid solution up to x = 0.1 except for x = 0.2 in case of aluminium. However, γ-phase is not stabilized for chromium ($Bi_4V_{2-x}Cr_xO_{11-\delta}$) and gallium ($Bi_4V_{2-x}Ga_xO_{11-\delta}$) based substitutions. Conductivity obtained is also highest for titanium for composition x = 0.4. SEM study revealed this fact too. Lower conductivity of chromium and gallium is characteristic of α-phase.

4.1.4 Pentavalent Substitution

The study on arsenic (As^{5+}) as pentavalent substitution on vanadium site was carried out in bismuth vanadate ($Bi_4V_2O_{11}$) under this section.

4.1.4.1 $Bi_4V_{2-x}Me_xO_{11-\delta}$ (Me = As^{5+})

4.1.4.1.1 X-ray Diffraction

Arsenic (As^{5+}) doped $Bi_4V_2O_{11}$ for the compositions x = 0.1, 0.2, 0.3 were synthesized and examined by X-ray diffraction. The patterns are presented in figure 4.38. The XRDs of all the compositions were characterized to orthorhombic α- phase of bismuth vanadate.

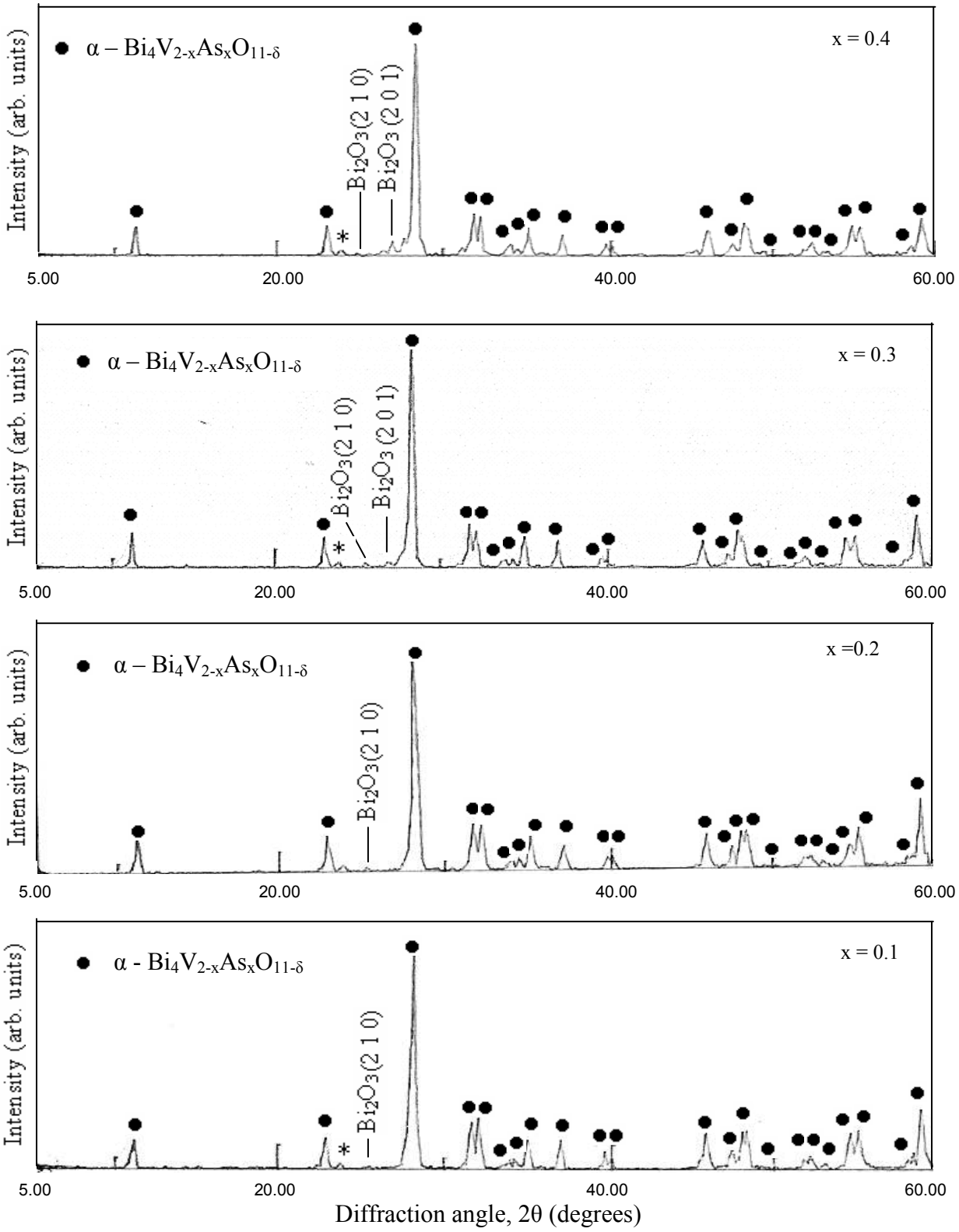

Fig. 4.38 X-ray pattern of $Bi_4V_{2-x}As_xO_{11-\delta}$ ($0.1 \leq x \leq 0.4$); (*) superlattice reflection

Sample of all the compositions exhibit the unreacted Bi_2O_3 impurity phase. The volume of unreacted phase increases with increasing concentration of dopant. This is because of the fact that there is variation in ionic radii between dopant and host cation (0.47 Å, 0.59 Å) respectively [191] which leads to disordering and interaction among the foreign and host atoms.

4.1.4.1.2 Electrical Conductivity

Arrhenius plots (fig. 4.39) show two transition regions in all the compositions x = 0.1, 0.2, 0.3 and 0.4 of α-$Bi_4V_{2-x}As_xO_{11-\delta}$ compound that correspond to γ → β and β → α regions. The transition temperatures for all the compositions are shown in table 4.16.

Table 4.16 Transition temperatures of $Bi_4V_{2-x}As_xO_{11-\delta}$

Composition	Transition temp. (γ → β)	Transition temp. (β → α)
0.1	420	280
0.2	540	380
0.3	560	360
0.4	460	380

The lowest and highest values of conductivity occurs for x = 0.4 and x = 0.2 that corresponds to 1.54×10^{-6} S/cm and 5.21×10^{-6} S/cm measured at 300 ^oC respectively. The higher value of conductivity for x = 0.2 may be attributed to higher disordering for this composition as compared to x = 0.4. Moreover, presence of unreacted separate phase of Bi_2O_3 can also decrease of conductivity for x = 0.4.

It is to be noted that higher conductivity of 10% arsenic doped α-phase is observed as compared to another two dopants (chromium and gallium) for V^{5+} in $Bi_4V_2O_{11}$ compound. It is due to $3d^{10}$ electronic configuration of As^{5+} by which there may be possibility to occupy a regular octahedral sites by oxygen atom to make the diffusion process easy and consequently improve in the conductivity values [157].

The curve corresponding to $Bi_4V_{1.9}As_{0.1}O_{11-\delta}$ is similar to those of undoped $Bi_4V_2O_{11}$ which is in good agreement with the α-type structure of $Bi_4V_2O_{11}$.

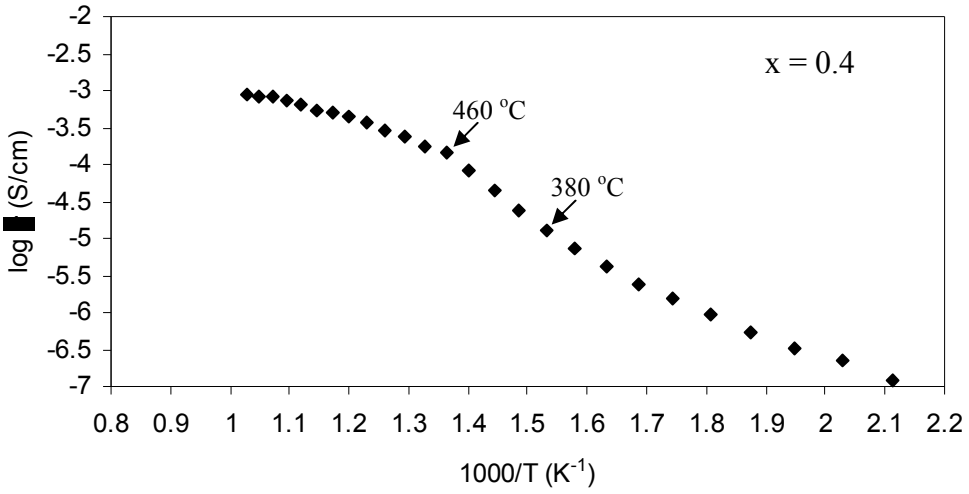

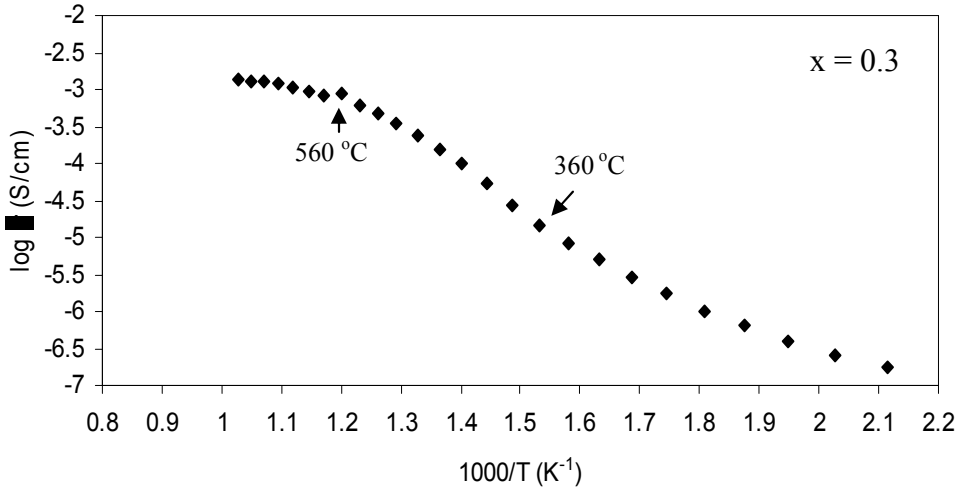

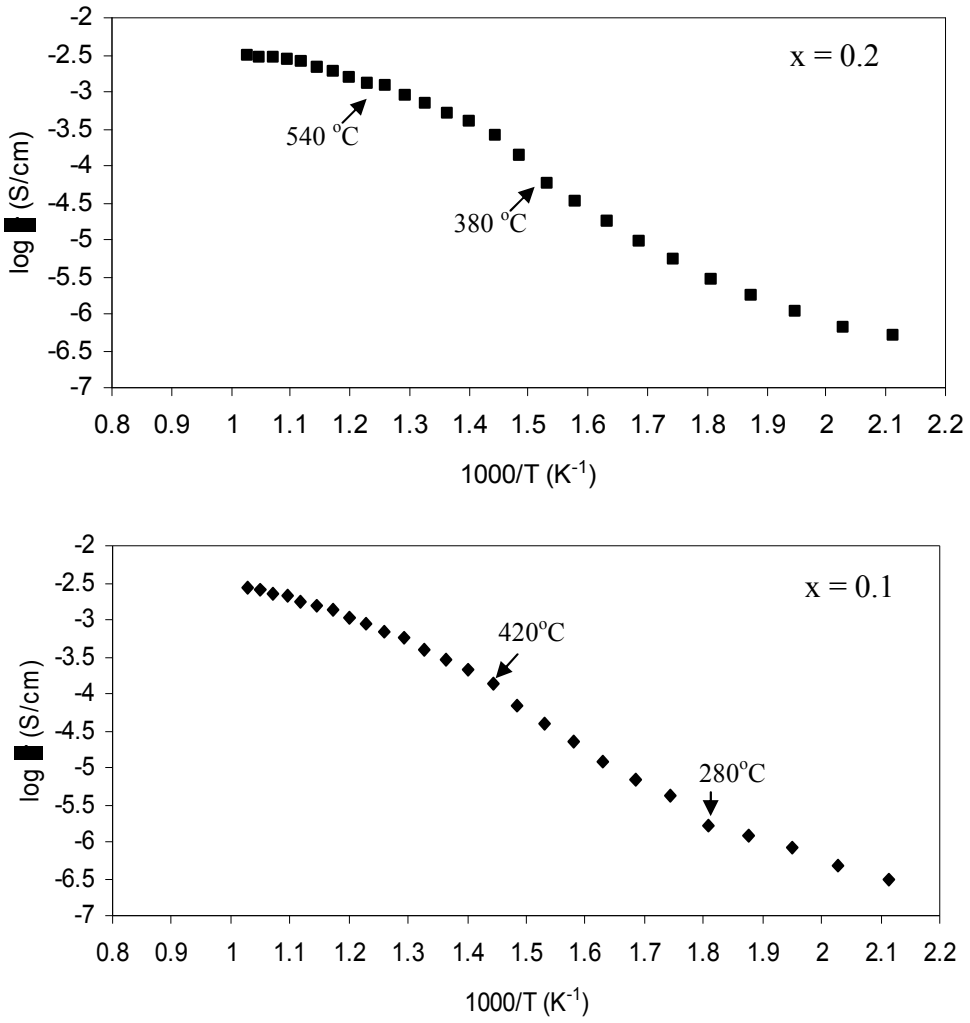

Fig. 4.39 Arrhenius plot of $Bi_4V_{2-x}As_xO_{11-\delta}$

Arsenic is the single pentavalent substitution ($Bi_4V_{2-x}As_xO_{11-\delta}$) carried out in the present study. Arsenic substitution could not stabilize the γ-phase. This is the only cation which retained the α-phase in the category of isovalent substitution up to longer range of composition. Other isovalents like Sb, Nb and Ta have stabilized the γ-phase [143].

Chapter V

Structural, Thermal and Ionic Conductivity of $Bi_{4-x}Me_xV_2O_{11-\delta}$

Overview

In the $Bi_{4-x}Me_xV_2O_{11-\delta}$ system, substitution on V as well as Bi site is possible. The work on V site substitution has been described in previous chapter. The present chapter deals with substitution on Bi site in $Bi_4V_2O_{11}$ compound. Since it is presumed that the oxygen vacancies are present in pervoskite vanadium layers so such substitution on bismuth sites is assumed to have very less effect on the ionic conductivity. These vacancies can be increased after doping of aliovalent cations. However, little work is reported on bismuth site substitution. So it is worth to study the effect of substitution on bismuth site. This chapter deals with the doping on bismuth site with three kinds of substitutents Pb^{2+}, La^{3+} and Gd^{3+} for the composition x = 0.1, 0.2, 0.3 and 0.4. This chapter further elaborates the sintering effect on selected samples and their correlation with conductivity and microstructure.

5.1 Results and Discussion

5.1.1 Divalent Substitution

Substitution of divalent lead (Pb^{2+}) on bismuth site in $Bi_4V_2O_{11}$ is undertaken in the present section.

5.1.1.1 $Bi_{4-x}Me_xV_2O_{11-\delta}$ ($Me=Pb^{2+}$)

5.1.1.1.1 X-ray Diffraction

Stoichiometric amounts corresponding to $Bi_{4-x}Me_xV_2O_{11-\delta}$ ($Me = Pb^{2+}$) for the compositions x = 0.1, 0.2, 0.3 and 0.4 were taken to prepare the sintered samples. These samples are examined by X-ray diffraction to identify the phases. The patterns for all the compositions are shown in figure 5.1. The patterns confirm the presence of superstructure peak at $2\theta \approx 24.2^o$ and characteristic doublets at $2\theta \approx 31^o$, 39^o, 48^o, 54^o which are manifestation of α-phase for $0.1 \leq x \leq 0.4$. This confirms that γ-phase is not stabilized for the lead substitution for the studied range of compositions. However, some traces of unreacted Bi_2O_3 phase appear for higher doping beyond x = 0.2. A significant increase in lattice parameter *c* also supports the observed analysis (table 5.1). Solid solution range in the present study is slightly higher than reported (x ~ 1.7) by Vannier *et al*. [164].

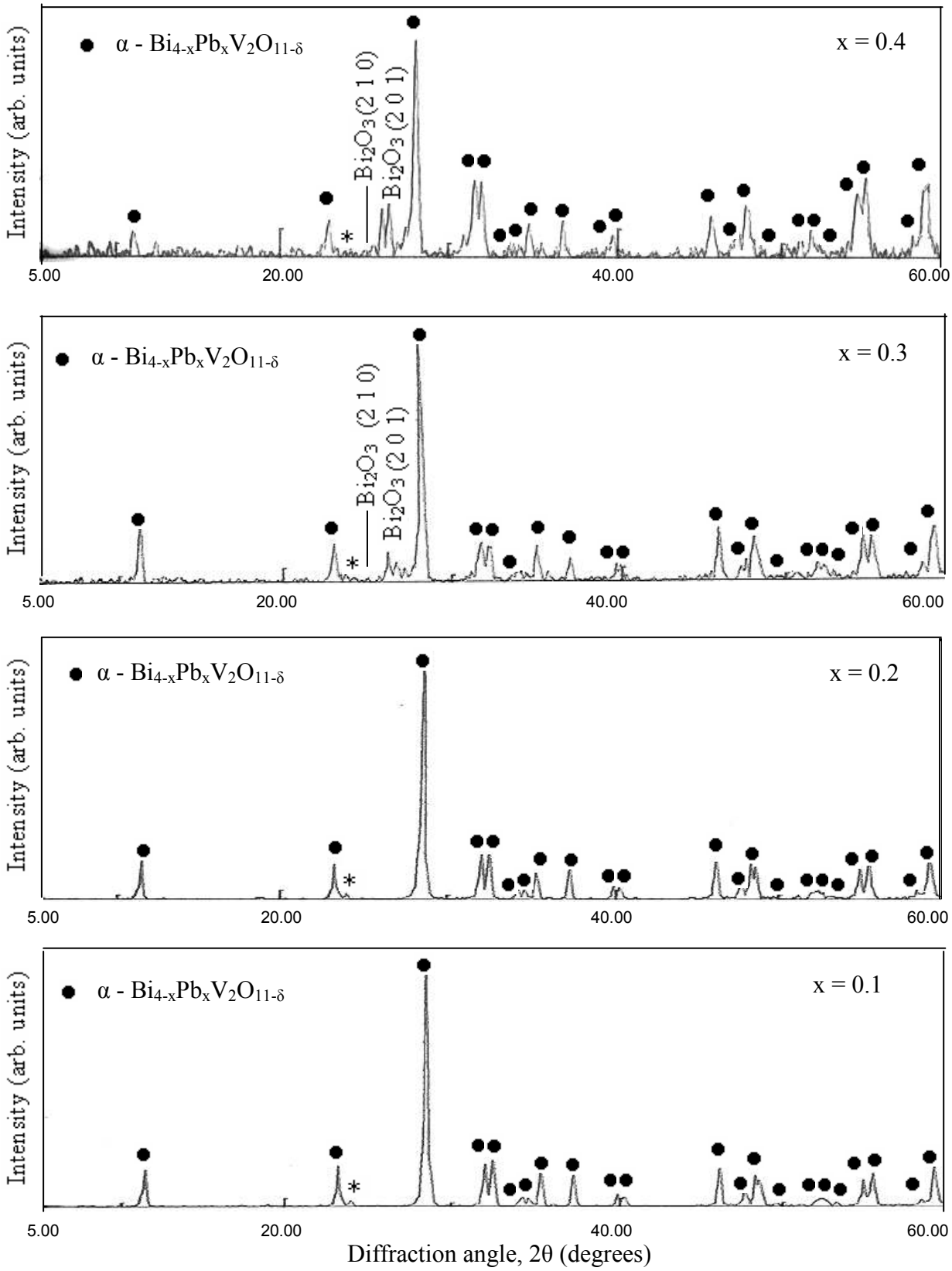

Fig. 5.1 X-ray diffraction pattern of $Bi_{4-x}Pb_xV_2O_{11-\delta}$, $(0.1 \leq x \leq 0.4)$;
(*) superlattice reflection

Table 5.1 Composition and lattice parameters of $Bi_{4-x}Pb_xV_2O_{11-\delta}$ ($0 \leq x \leq 0.4$)

Composition	*a* (Å)	*b* (Å)	*c* (Å)	Volume ($Å^3$)
x = 0	5.52	5.60	15.24	471.10
x = 0.1	5.53	5.60	15.27	471.18
x = 0.2	5.52	5.60	15.29	472.64
x = 0.3	5.56	5.64	15.49	485.74
x = 0.4	5.61	5.67	15.62	496.85

5.1.1.1.2 Electrical Conductivity

Conductivity was calculated by complex impedance data at different temperatures with respect to frequency. A typical plot is shown in figure 5.2. Conductivity increases with rise in temperature as expected and shown in Arrhenius plot (fig. 5.3). However, the conductivity does not follow the linear behavior. The discontinuity refers to transformations as reported in all other BIMEVOX compounds.

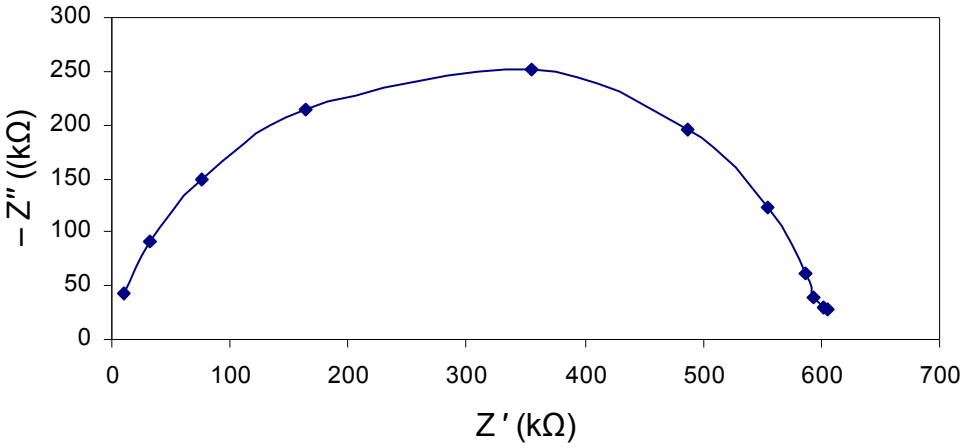

Fig.5.2 Typical impedance spectrum at 200 °C of $Bi_{4-x}Pb_xV_2O_{11-\delta}$ (x = 0.4)

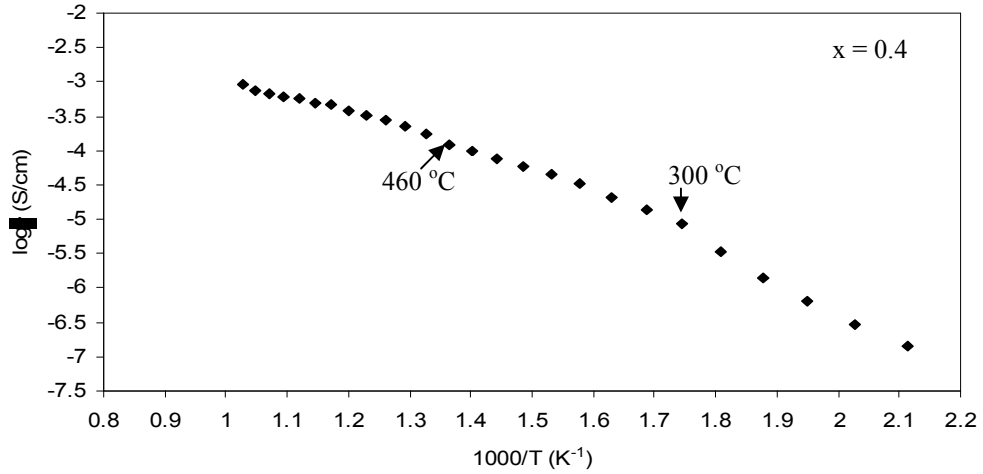
x = 0.4
460 °C
300 °C
log σ (S/cm)
1000/T (K-1)

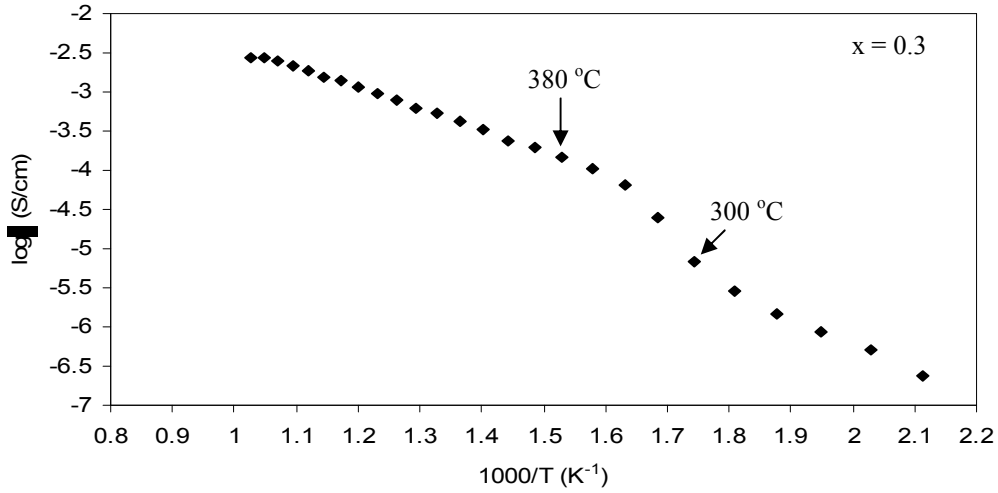
x = 0.3
380 °C
300 °C
log σ (S/cm)
1000/T (K-1)

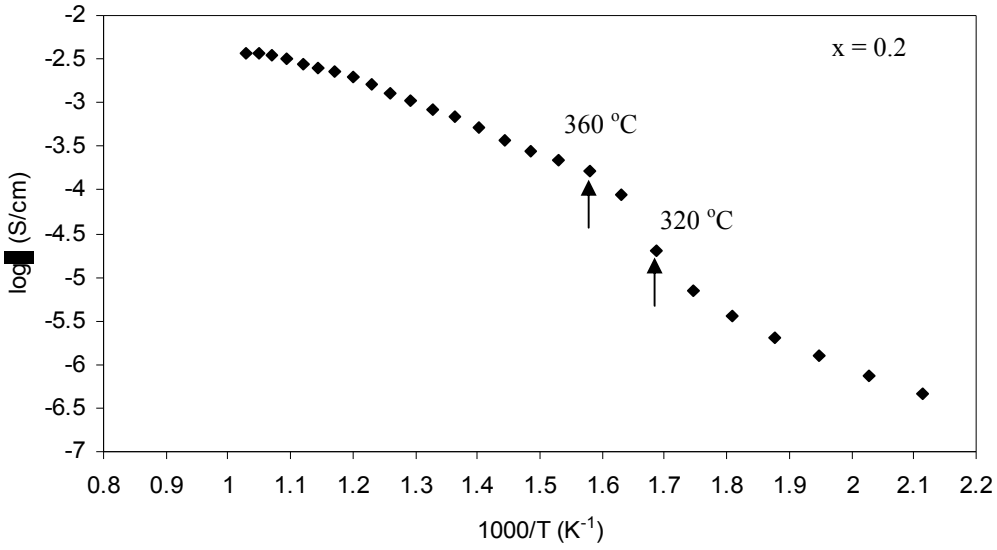
x = 0.2
360 °C
320 °C
log σ (S/cm)
1000/T (K-1)

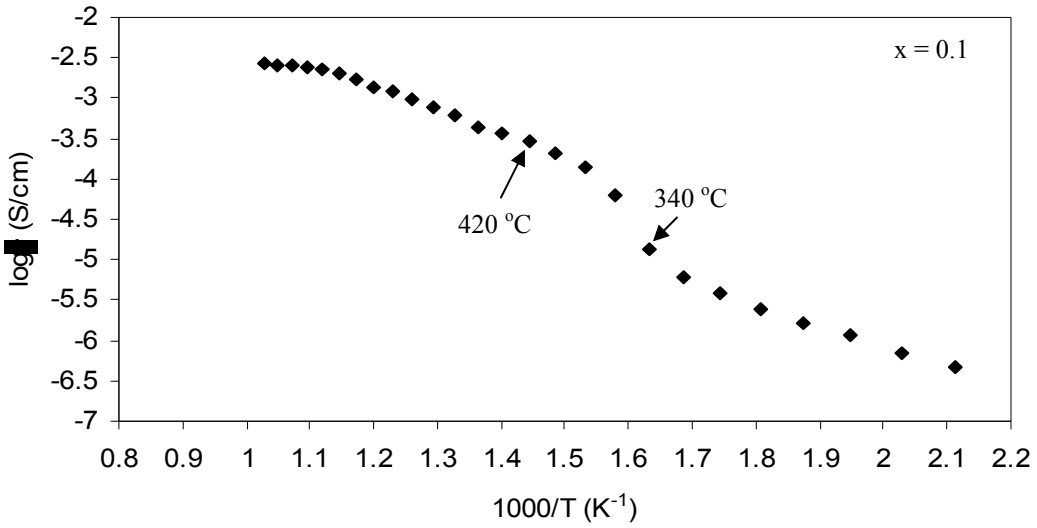

Fig. 5.3 Arrhenius plot of $Bi_{4-x}Pb_xV_2O_{11-\delta}$, $(0.1 \leq x \leq 0.4)$

Transition temperatures from $\gamma \rightarrow \beta$ and $\beta \rightarrow \alpha$ are observed for all the compositions of x = 0.1, 0.2, 0.3 and 0.4 which are presented in table 5.2. The transition $\gamma \rightarrow \beta$ and $\beta \rightarrow \alpha$ (fig. 5.3) for composition x = 0.1 are in agreement with two transition temperature range observed in the DSC measurement during cooling as reported by Vannier *et al*. [164] for the same composition and substitution.

Table 5.2 Transition temperatures of $Bi_{4-x}Pb_xV_2O_{11-\delta}$

Composition	Transition temp. (°C) ($\gamma \rightarrow \beta$)	Transition temp. (°C) ($\beta \rightarrow \alpha$)
0.1	420	340
0.2	360	320
0.3	380	300
0.4	460	300

Table 5.3 Conductivity and activation energy of $Bi_{4-x}Pb_xV_2O_{11-\delta}$, ($0.1 \leq x \leq 0.4$) at sintering temperature of 800 ^oC

Composition	σ_{200^oC} (S/cm)	E_a(eV) < 300 ^oC	E_a (eV) >500^oC
x = 0.1	4.55×10^{-7}	0.27	0.18
x = 0.2	4.72×10^{-7}	0.21	0.18
x = 0.3	2.37×10^{-7}	0.32	0.18
x = 0.4	1.40×10^{-7}	0.41	0.12

For the linear region below 300 ^oC and above 500 ^oC, the values of activation energy (E_a) along with ionic conductivities measured at 200 ^oC for x = 0.1, 0.2, 0.3 and 0.4 samples are summarized in table 5.2. The conductivity values at different temperatures are shown in figure 5.4. Conductivity at 200 ^oC is taken as reference because temperature at 300 ^oC is near or at the transition zone which could not give proper results for comparison.

The variation in ionic conductivity is in accordance with the activation energy calculated for all the compositions in the low temperature range. Moreover, the conductivity values also confirm the solid solution range for $x \leq 0.2$ as observed in XRD patterns (fig. 5.1) which shows highest conductivity in the solid solution range for x = 0.2.

The substitution of Pb^{2+} on bismuth site may likely to compensate the charge in the Bi_2O_2 layers leading to additional oxide vacancies for $x \leq 0.2$. The smaller conductivity values

of the sample of composition x = 0.3 and 0.4 may be ascribed to segregation of unreacted Bi_2O_3 at the grain boundary.

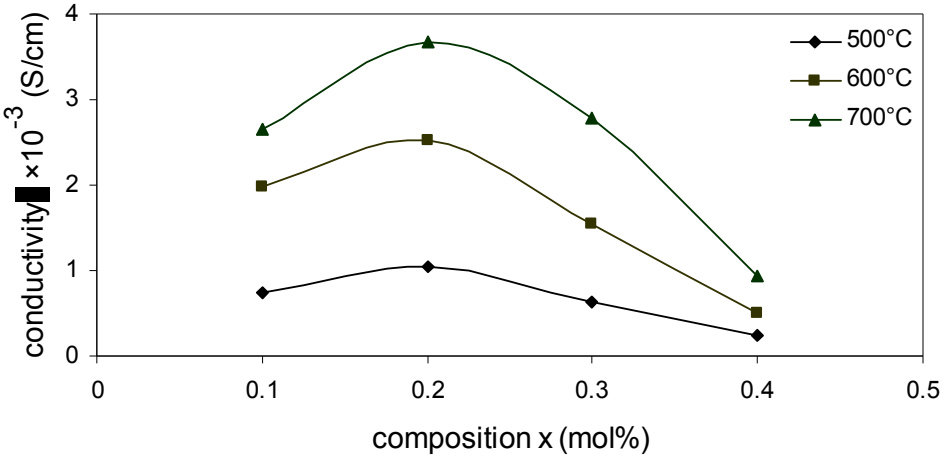

Fig. 5.4 Conductivity isotherm of $Bi_{4-x}Pb_xV_2O_{11-\delta}$, ($0.1 \leq x \leq 0.4$)

5.1.1.1.3 Microstructural Analysis

The scanning electron microscopy (SEM) of the fractured surface has been carried out for the high and low conducting samples of compositions x = 0.2 and x = 0.4 (fig. 5.5). This was done to visualize the microstructural effects on the conductivity and solid solution formation. The features show the uniform grains varying in size as given in table 5.3 for x = 0.2 sample along with some porosity. SEM of x = 0.4 shows the evidence of partial melting owing to distorted and non-uniform grain pattern as compared to x = 0.2 sample. Partial melting of the sample of x = 0.4 may be attributed to presence of Bi_2O_3 in large amount as shown in x-ray pattern (fig. 5.1; x = 0.4).

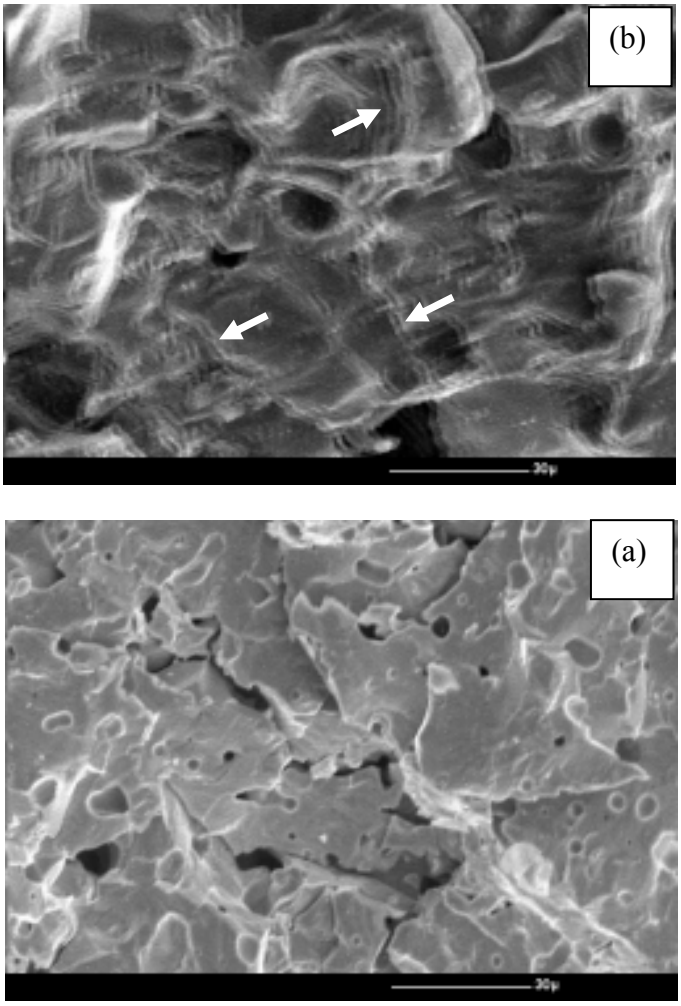

Fig. 5.5 Fractured surface SEM of $Bi_{4-x}Pb_xV_2O_{11-\delta}$ sintered at 800^oC (a) x = 0.2 (b) x =0.4

The interwoven wavy network for x=0.4 is observed throughout the sample (marked as arrow). This type of structure is a typical characteristic of lattice straining. The material possesses cubic pervoskite structure of higher symmetry at the sintering temperature which transform to lower symmetry structure during cooling. This type of phase transformation leads to lattice distortion. Due to this, thermal stresses are generated which causes the formation of domains. These domains are oriented at different angles between 90 to180° which depends upon the phase which nucleates and transforms on

cooling. These types of structures lead to either ordering or disordering of oxygen vacancies which depends upon the orientation of the domain [193, 194].

Table 5.4 Average grain size of $Bi_{4-x}Pb_xV_2O_{11-\delta}$ sintered at 800 ^oC for x = 0.2 and 0.4

Composition	Grain size (μm)
x = 0.2	25-30
x = 0.4	15-25

5.1.1.2 Sintering at different temperatures of $Bi_{1.8}Pb_{0.2}V_2O_{11-\delta}$

The study on lead (Pb^{2+}) substitution on bismuth site of $Bi_4V_2O_{11}$ was further carried out for the sample of high conducting composition x = 0.2 to see the effect of sintering temperature on the conductivity and microstructural aspects related with the conductivity. In the present study, samples were prepared under the same experimental conditions but at different sintering temperatures of 750, 775 and 825 ^oC in addition to 800 ^oC studied above.

5.1.1.2.1 X-ray diffraction

The X-ray diffraction analyses of the $Bi_{3.8}Pb_{0.2}V_2O_{11-\delta}$ samples sintered at 750, 775 and 825 ^oC also confirm the presence of α-phase of orthorhombic unit cell alongwith the characteristic superstructure peak of the above samples (fig. 5.6). XRDs of these samples sintered at 750, 775 and 825 ^oC have higher interplanar spacing 'd' values than the sample sintered at 800 ^oC. This can be inferred from the lattice parameter determination as mentioned in table 5.5.

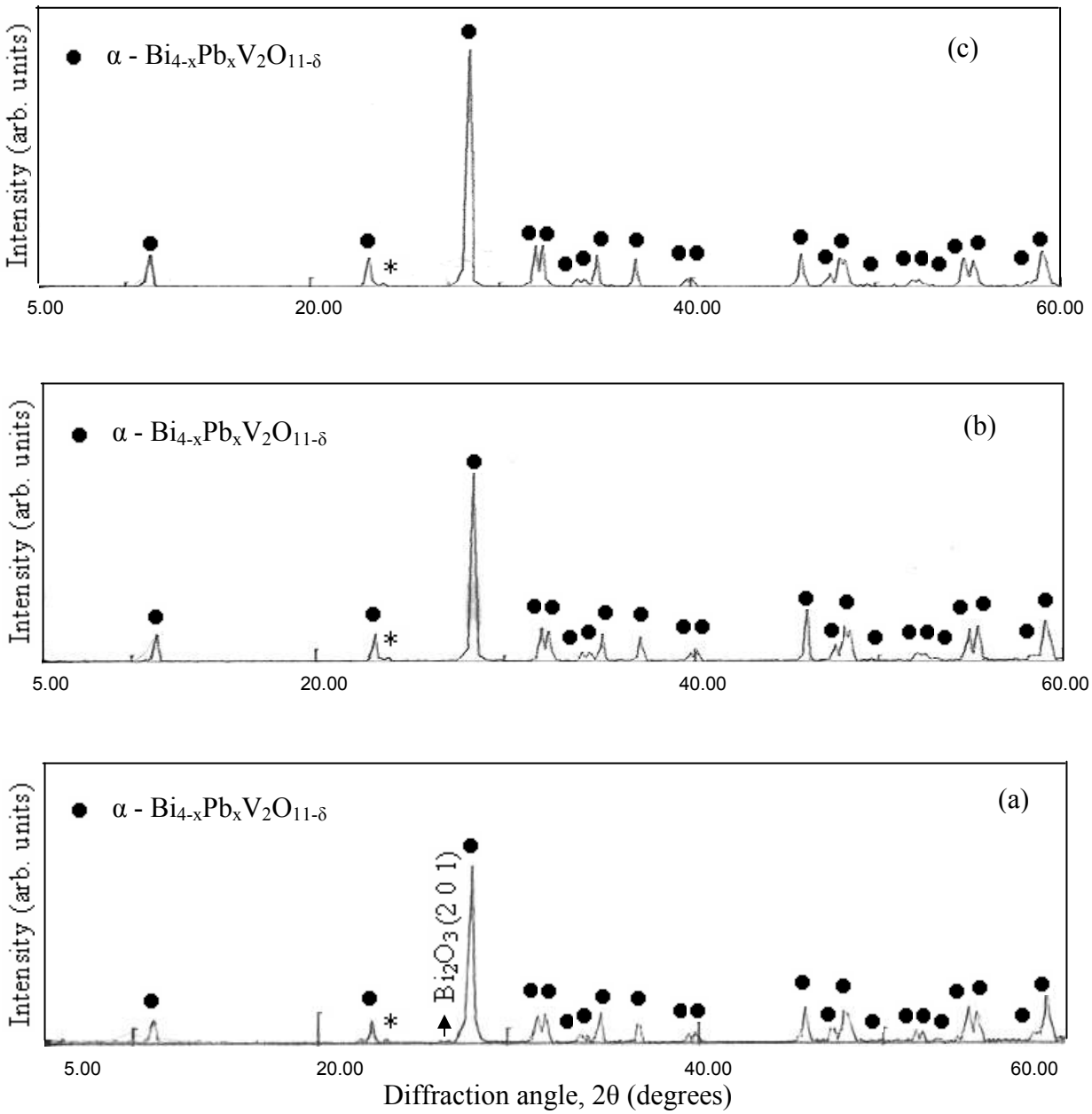

Fig. 5.6 XRD pattern of samples $Bi_{3.8}Pb_{0.2}V_2O_{11-\delta}$ sintered at (a) 750 ^oC (b) 775 ^oC (c) 825 ^oC; (*) superlattice reflection

The ordering of these samples are more as compared to sample sintered at 800 ^{o}C as can be interpreted from the larger unit cell volume for the samples sintered at 750 and 775 ^{o}C.

The pure single phase compound was obtained in the samples sintered at 775 and 825 ^{o}C and no additional phase was observed for these samples (fig. 5.6 b,c). However, sample sintered at 750 ^{o}C gives the evidence of unreacted Bi_2O_3 peak (fig 5.6a). This indicates that reaction is incomplete at temperature of 750 ^{o}C.

Table 5.5 Lattice parameters of $Bi_{3.8}Pb_{0.2}V_2O_{11-\delta}$ sintered at 750, 775, 800 and 825 ^{o}C

Sintering temperature (^{o}C)	*a* (Å)	*b* (Å)	*c* (Å)	Volume (Å^3)
750	5.55	5.61	15.39	479.17
775	5.59	5.65	15.47	488.60
800	5.52	5.60	15.29	472.64
825	5.54	5.60	15.38	477.15

5.1.1.2.2 Electrical Conductivity

The experimental data of conductivity measurement are presented in the form of Arrhenius plots in figure 5.7. Data do not show simple Arrhenius type behavior with small curvature in between temperature range of 300 ^{o}C to 500 ^{o}C.

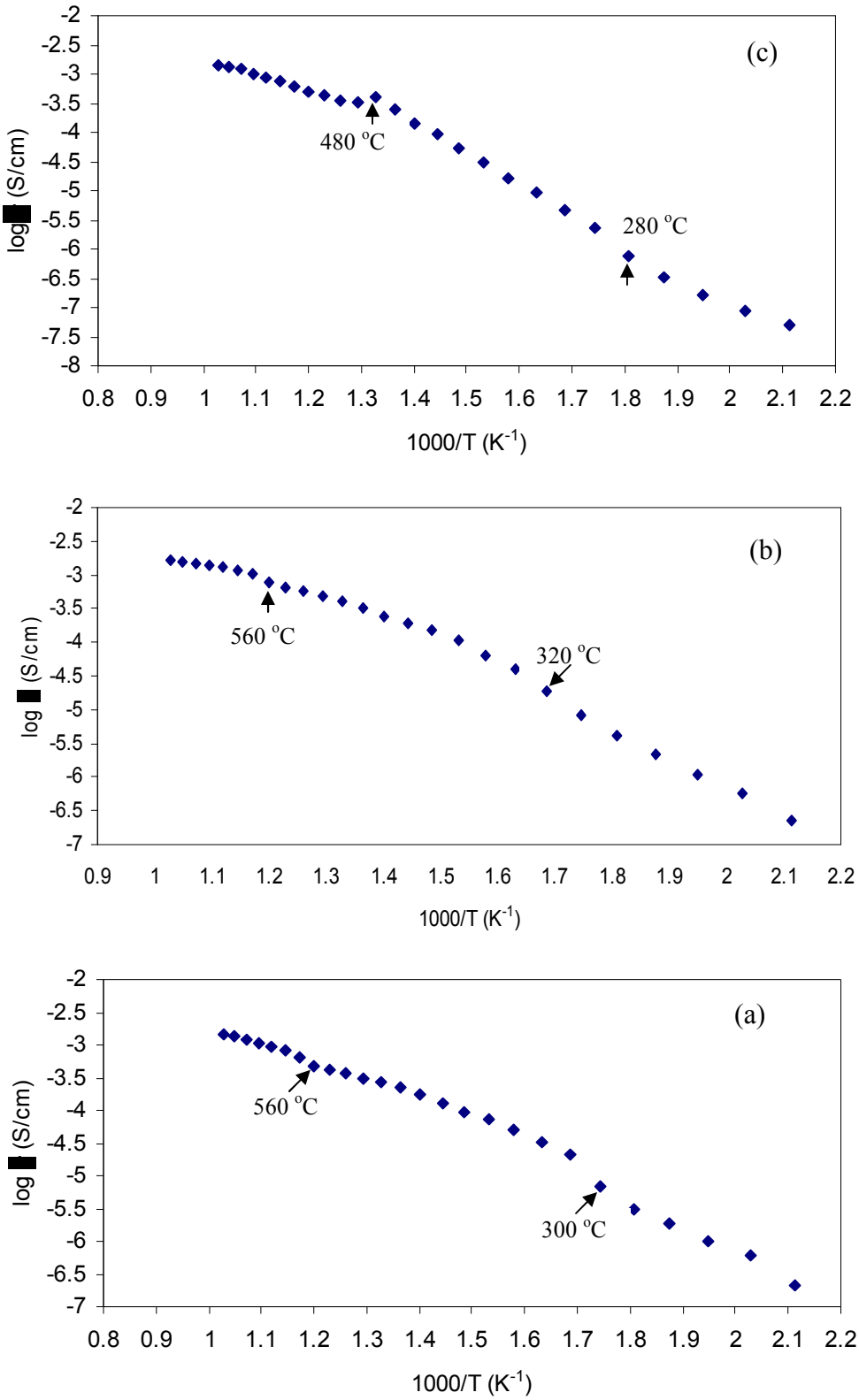

Fig. 5.7 Arrhenius plot of $Bi_{4-x}Pb_xV_2O_{11-\delta}$ (x = 0.2) at different sintering temperature, (a) 750 °C, (b) 775 °C and (c) 825 °C

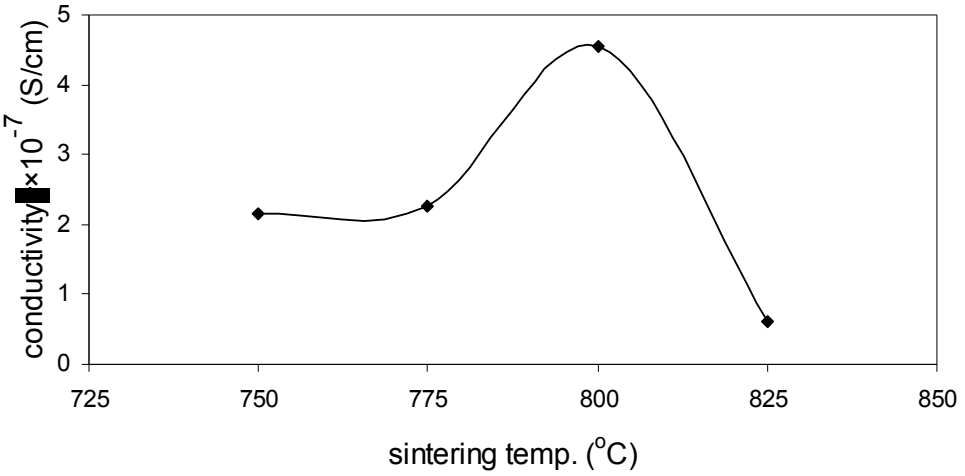

Fig. 5.8 Conductivity v/s sintering temperature of $Bi_{4-x}Pb_xV_2O_{11-\delta}$; (x = 0.2)at 200 °C

The transitions corresponding to γ → β and β → α for the samples sintered at 750, 775 and 825 °C was observed at different temperatures which are shown in figure 5.7. The conductivity values measured at 200°C are almost similar for the sample sintered at 750 and 775°C and about 3.6 times higher as compared to sample sintered at 825 °C. This result may be supported by the lattice parameters and volume (tables 5.4) in the same range for both of these samples. As shown in figure 5.8, the sintered sample at 800 °C exhibits higher conductivity than any other heat treated temperature. This sample showed the decrement in the volume due to oxygen vacancies formation and appropriate growth of the grains with small porosity.

5.1.1.2.3 Microstructural Analysis

SEM study was carried out to correlate the variation in conductivity of x = 0.2 sample sintered at 750, 775 and 825 °C temperature. The microstructure of x = 0.2 sample sintered at 750, 775 and 825 °C are given in figure 5.9.

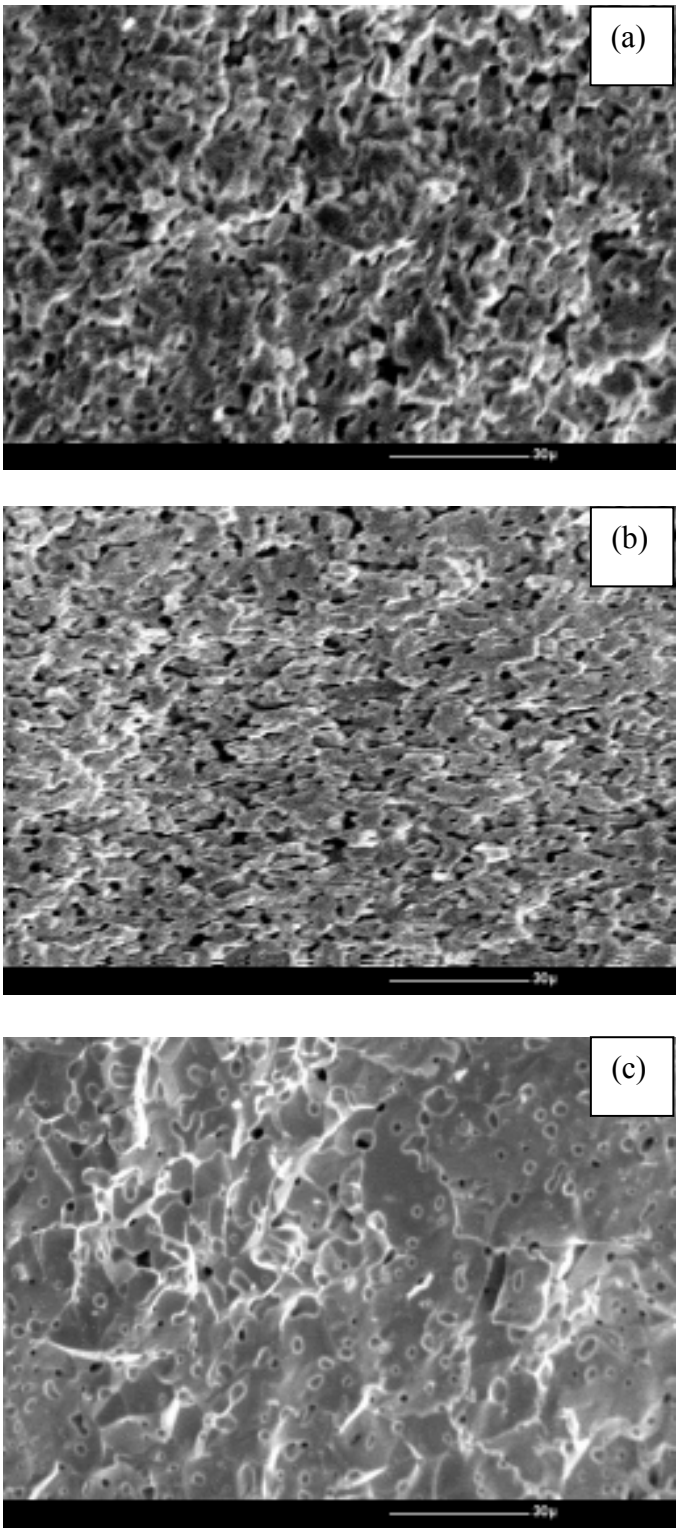

Fig. 5.9 SEM of $Bi_{4-x}Pb_xV_2O_{11-\delta}$ (x = 0.2) at different sintering temperature (a) 750 ^oC (b)775 ^oC and (c) 825 ^oC.

Grains are observed to be uniformly distributed for the sample sintered at 775 ^{o}C with average grain size of 15-20 μm (table 5.6) than the sample sintered at 750 ^{o}C. However, no uniformity is observed in grain distribution of the sample sintered at 825 ^{o}C. Partial melting of the phase is visible in micrograph of the sample sintered at 825 ^{o}C (fig.5.9c) which lowers the symmetry of α-$Bi_4V_2O_{11}$ phase in this particular sample. Due to partial melting, lower value of the conductivity is obtained as compared to the other sintered samples.

Optimum sintering temperature of 800 ^{o}C for x = 0.2 was observed to exhibit ionic conductivity measured at 200 ^{o}C which is nearly 2 times more than samples sintered at 750 and 775 ^{o}C (fig. 5.8). This value is six times higher for sample sintered at 825 ^{o}C.

A careful examination of all the micrographs of x = 0.2 samples sintered at different temperatures indicate that there is some similarities in samples sintered at 750 ^{o} C and 775 ^{o} C. The existence of aligned domain structure can be seen in all these samples though in varying amount which is not in those samples sintered at 800 ^{o} and 825 ^{o}C. This variation in structure is basic cause for variation in conductivity with variation in sintering temperature. The high conductivity observed for samples sintered at 800 ^{o} C shows uniform grain which is also there in low conductivity sample (825 ^{o} C) but amount of bubbles (island) / pores are more for 825 ^{o}C as compared to samples sintered at 800 ^{o}C which is basic cause for decrease in conductivity.

Table 5.6 Average grain size of $Bi_{4-x}Pb_xV_2O_{11-\delta}$ at different sintering temperatures

Sintering temperature (^oC)	Grain size (μm)
750	10-15
775	15-20
800	25-30
825	5-15

These samples are following the trend of conductivity as $\sigma_{0.4} < \sigma_{0.3} < \sigma_{0.1} < \sigma_{0.2}$ in terms of composition and $\sigma_{825} < \sigma_{750} < \sigma_{775} < \sigma_{800}$ in terms of sintering temperature for high conducting composition x = 0.2. Microstructural features also confirm this trend where the variation in structure is observed.

5.1.2 Trivalent Substitution

The study on the effects of trivalent substituents (La^{3+} and Gd^{3+}) was carried out in the following sections.

5.1.2.1 $Bi_{4-x}Me_xV_2O_{11-\delta}$ ($Me=La^{3+}$)

5.1.2.1.1 XRD analyses

The X-ray diffraction analysis was carried out for the sintered samples of compositions x = 0.1, 0.2, 0.3 and 0.4. XRD patterns of $Bi_{4-x}La_xV_2O_{11-\delta}$ (x = 0.1, 0.2, 0.3 and 0.4) are shown in figure 5.9. In first three compositions, superstructure peaks at ~ 24.2^o with doublets at $2\theta \approx 31^o$, 39^o, 48^o and 54^o corresponding to α phase was observed.

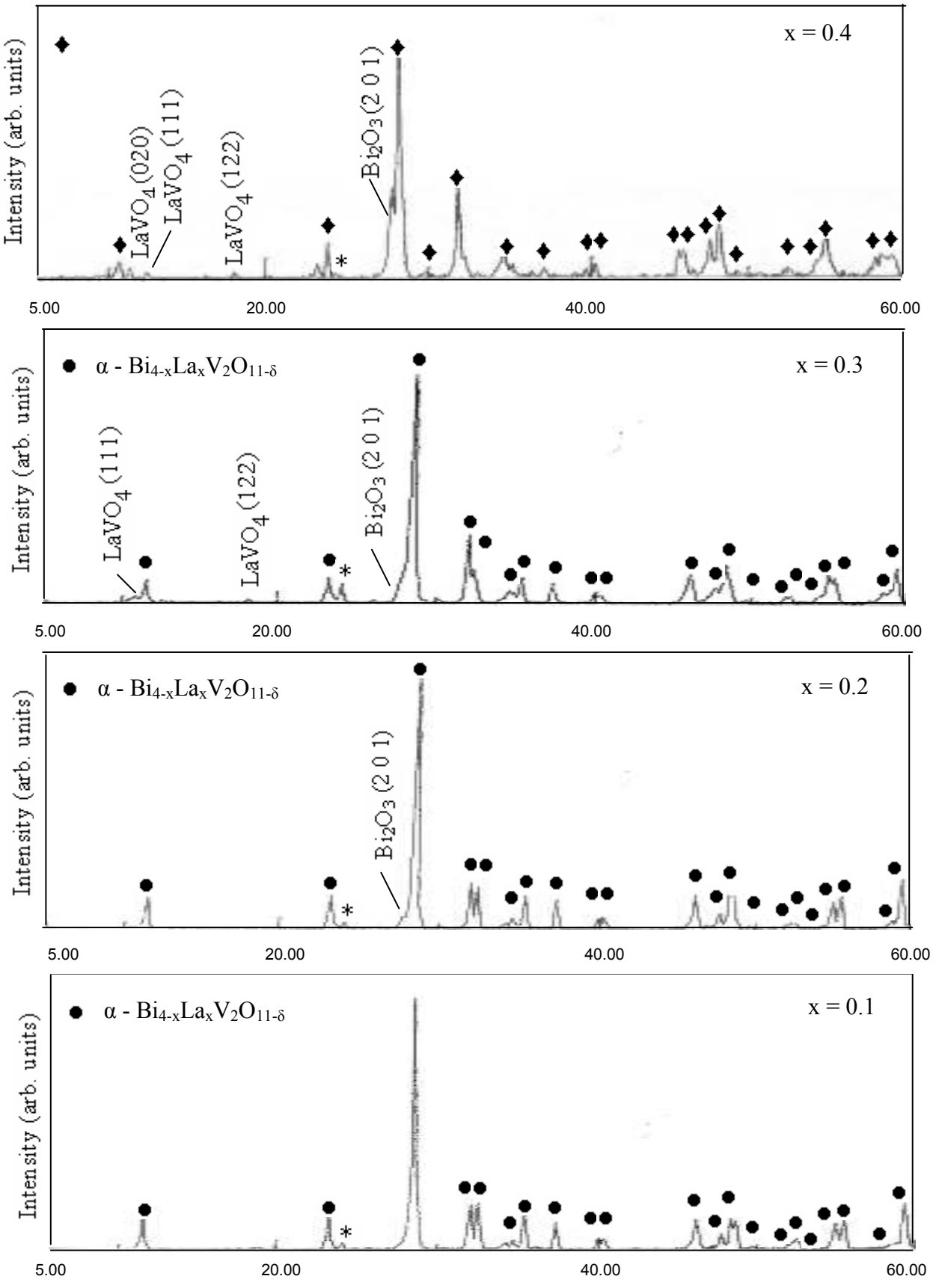

Fig. 5.10 Typical X-ray diffraction pattern of $Bi_{4-x}La_xV_2O_{11-\delta}$; (*) superlattice reflection

Sample of composition x = 0.3 exhibits small contribution of β-phase due to weak splitting of peak at ~ 32°. However, the sample of composition x = 0.4 shows β-orthorhombic phase. Some extra peaks were also observed for compositions beyond x = 0.1. The extra peaks are for unreacted Bi_2O_3. In addition to this, additional phase $LaVO_4$ (ICDD card no. 70-0216) is also present for x = 0.3 and 0.4 (fig. 5.10). Formation of this phase is also reported for the compound $Bi_{2-x}La_xV_{0.9}Cu_{0.1}O_{5.5-\delta}$ [197]. Another high intensity peak at close neighbourhood has been assigned to Bi_2O_3 and not to $BiVO_4$. Because Bi_2O_3 is likely to be present due to doping on bismuth site.

Reported work on lanthanum substituted $Bi_4V_2O_{11}$ [151, 198] indicated that La substitutes bismuth site. This also seems to be more convincing due to closer ionic radii of {La^{3+} (1.06 Å) and Bi^{3+} (0.96 Å) [191]} as compared to very small ionic radius of V^{5+} (0.59 Å).

5.1.2.1.2 Electrical Conductivity

The conductivity measured at 200 °C is given in table 5.7 for La - doped systems. Arrhenius plots for the samples x = 0.1 to 0.4 are given in figure 5.11. The lower conductivity at higher composition may be the result of segregation of insulating phase of Bi_2O_3 and $LaVO_4$. However, some contribution of electronic conductivity is also suggested in the (La, Cu) doped $Bi_2VO_{5.5}$ [197]. Oxygen ion transfer number determination [199] also suggested the decrease in oxygen ion conductivity and increase in electronic conductivity with increasing lanthanum concentration. The phase transitions for all the compositions from conductivity measurements are mentioned in table 5.8. The single transition for x = 0.4 is indicative of presence of β-phase. The transition is also confirmed by typical DSC profile (fig. 5.12) of x = 0.3 with transition at 414 and 585 °C.

The difference in transition temperature measured by the two techniques may be attributed to variation in the thermal cycle mode measurements of DSC (taken in heating mode) and conductivity (taken in cooling mode).

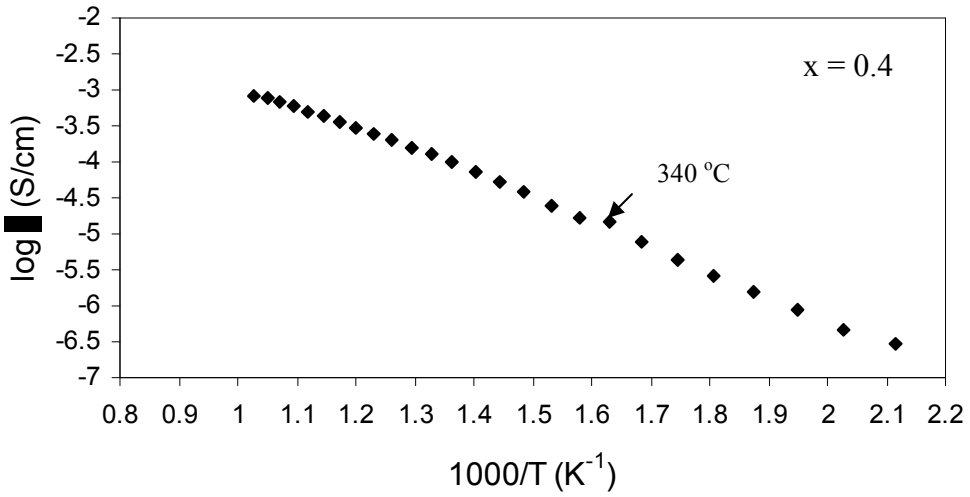

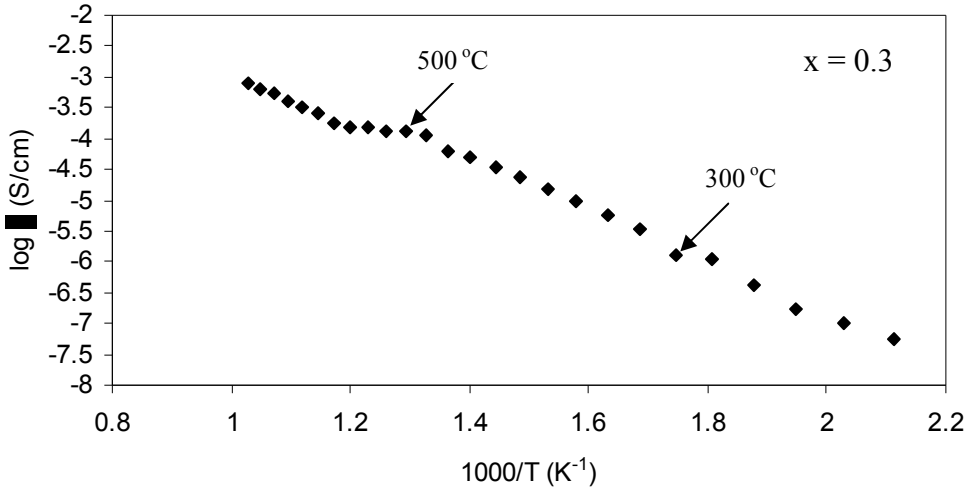

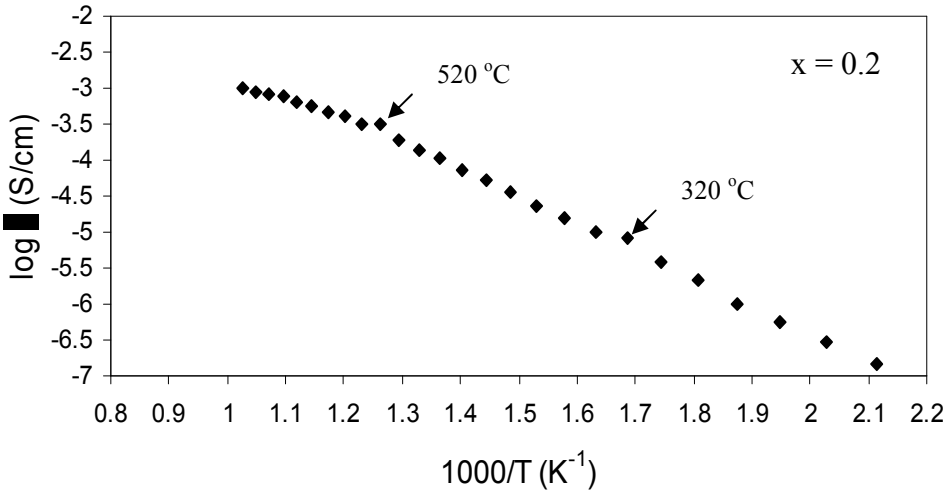

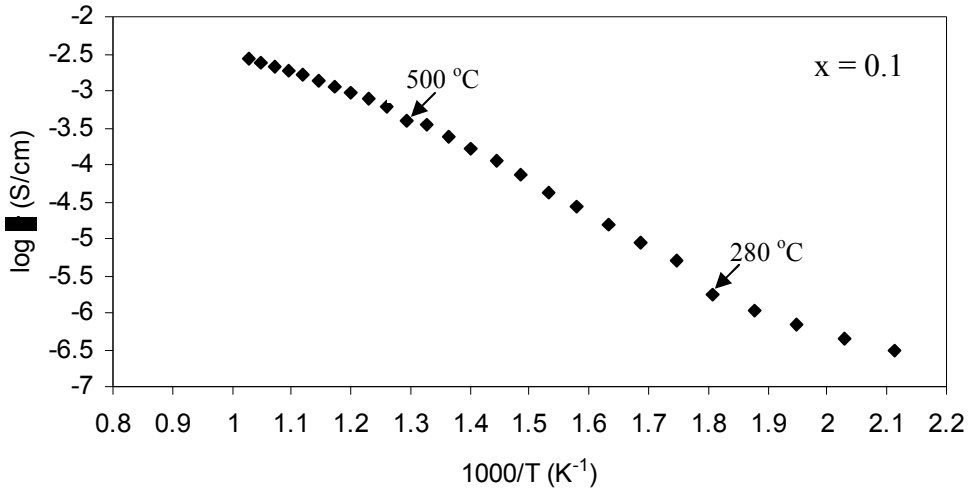

Figure 5.11 Arrhenius plot of the conductivities of the $Bi_{4-x}La_xV_2O_{11-\delta}$ ($0.1 \leq x \leq 0.4$)

Table 5.7 Conductivity and activation energy of $Bi_{4-x}La_xV_2O_{11-\delta}$, ($0.1 \leq x \leq 0.4$) samples sintered at 800 °C

Composition	σ_{200^oC} (S/cm)	E_a (eV) < 300 °C	E_a (eV) >500°C
x = 0.1	3.10×10^{-7}	0.27	0.18
x = 0.2	1.47×10^{-7}	0.33	0.23
x = 0.3	5.40×10^{-8}	0.38	0.28
x = 0.4	2.97×10^{-7}	0.28	0.24

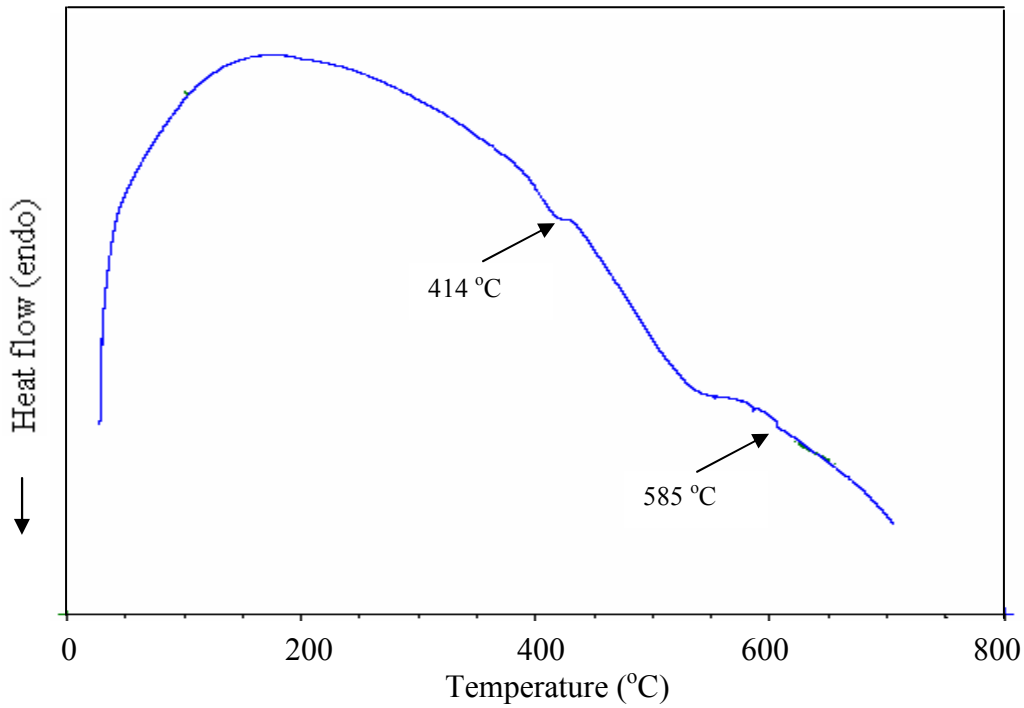

Fig. 5.12 DSC thermogram of $Bi_{4-x}La_xV_2O_{11-\delta}$ (x = 0.3)

Table 5.8 Phase transition temperatures of $Bi_{4-x}La_xV_2O_{11-\delta}$ ($0.1 \leq x \leq 0.4$) during conductivity measurement

Composition	Transition temp. ($\gamma \rightarrow \beta$)	Transition temp. ($\beta \rightarrow \alpha$)
0.1	500	280
0.2	520	320
0.3	500	300
0.4	------	340

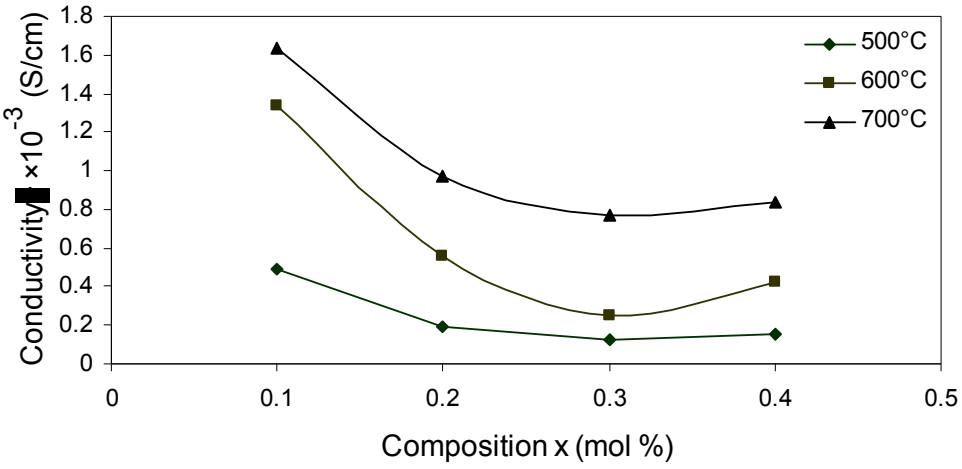

Fig. 5.13 Isothermal conductivity plot with respect to composition of $Bi_{4-x}La_xV_2O_{11-\delta}$

The conductivity at higher temperatures in the system $Bi_{4-x}La_xV_2O_{11-\delta}$ is shown in figure 5.13. .

5.1.2.1.3 Microstructural Analysis

The micrographs of fractured surface of Bi_{4-x} $La_xV_2O_{11-\delta}$ (x = 0.1) and (x = 0.3) samples corresponding to high and low conductivity are shown in figure 5.14. There is clear variation in microstructural features which reflects the variation in conductivity between low and high conducting compositions. This may be attributed to clear grain formation of size (5-8 μm) for high conducting composition x = 0.1 as compared to sample of low conducting (x = 0.3) with grain size of 2-4 μm. The grains of smaller size (table 5.9) are associated with increasing the low conducting grain boundary area where segregation of low conducting phase occurs which is responsible for low conductivity.

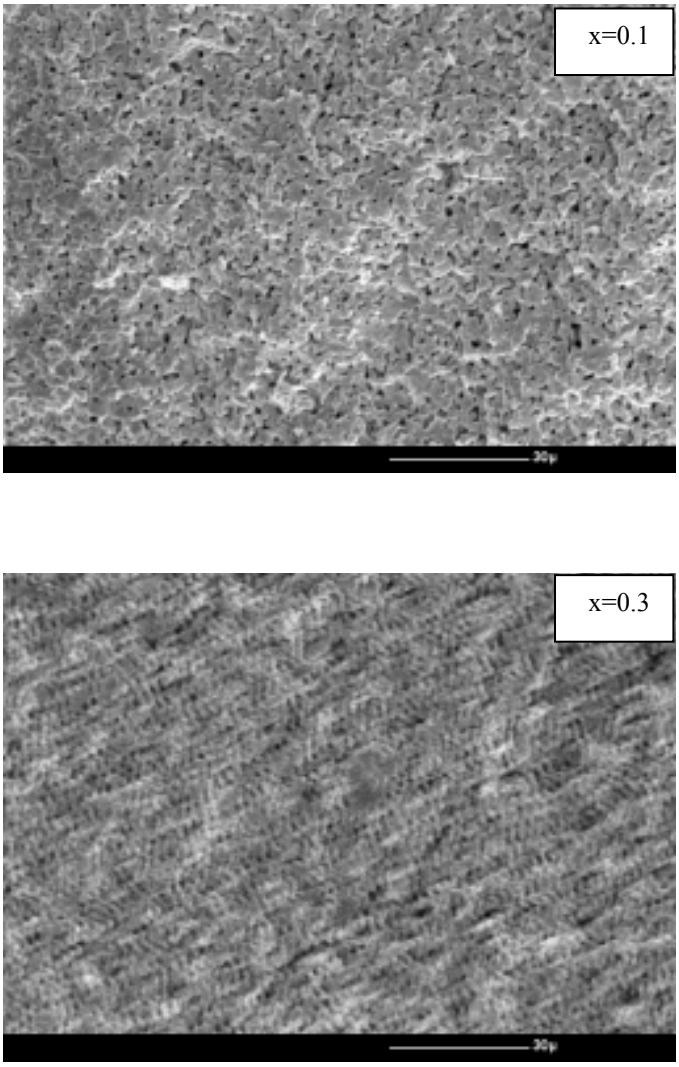

Fig. 5.14 Scanning electron micrographs of fractured surface of high (x=0.1) and low conducting (x=0.3) of $Bi_{4-x}La_xV_2O_{11-\delta}$ sintered at 800 ^oC

One typical feature observed in the micrograph here is the formation of interwoven wavy network structure of low conducting phase. The uniform appearance of this network which has not been reported in any literature is the key feature to distinguish low and high conducting samples. Depending on the occupancy of doping element, the nature of this varies. The structure forms because of lattice straining and shows the tendency for phase

separation. The strained lattice can not remain in strain condition and releases its energy by formation of domain structure as has been explained earlier also.

Table 5.9 Average grain size of $Bi_{4-x}La_xV_2O_{11-\delta}$ (x = 0.1 and 0.3) at sintering temperature of 800 ^oC

Composition	Grains size (µm)
x = 0.1	5-8
x = 0.3	2-4

5.1.2.2 Sintering at different temperatures of $Bi_{3.9}La_{0.1}V_2O_{11-\delta}$

In order to see the behaviour of high conducting phase, the sample which exhibit higher conductivity (x = 0.1) has been sintered at different temperatures to optimize the sintering conditions. The analysis is presented below.

XRD patterns of the samples sintered at 750, 775 and 825 ^oC of $Bi_{3.9}La_{0.1}V_2O_{11-\delta}$ are presented in figure 5.15. All the samples exhibit similar characteristics (α-phase) as observed for the sample sintered at 800 ^oC. Negligible peak shift was observed for the samples sintered at 750 and 775 ^oC which may be attributed to additional impurity phase of Bi_2O_3 present in these samples, whereas sample sintered at 825 ^oC is single phase compound.

Lattice parameters have been determined from XRDs of the La-doped samples which are shown in table 5.10. The lower values of lattice parameters for the samples sintered at 800 and 825 ^oC indicate the formation of single phase compound at these temperatures.

5.1.2.2.1 X-ray Diffraction

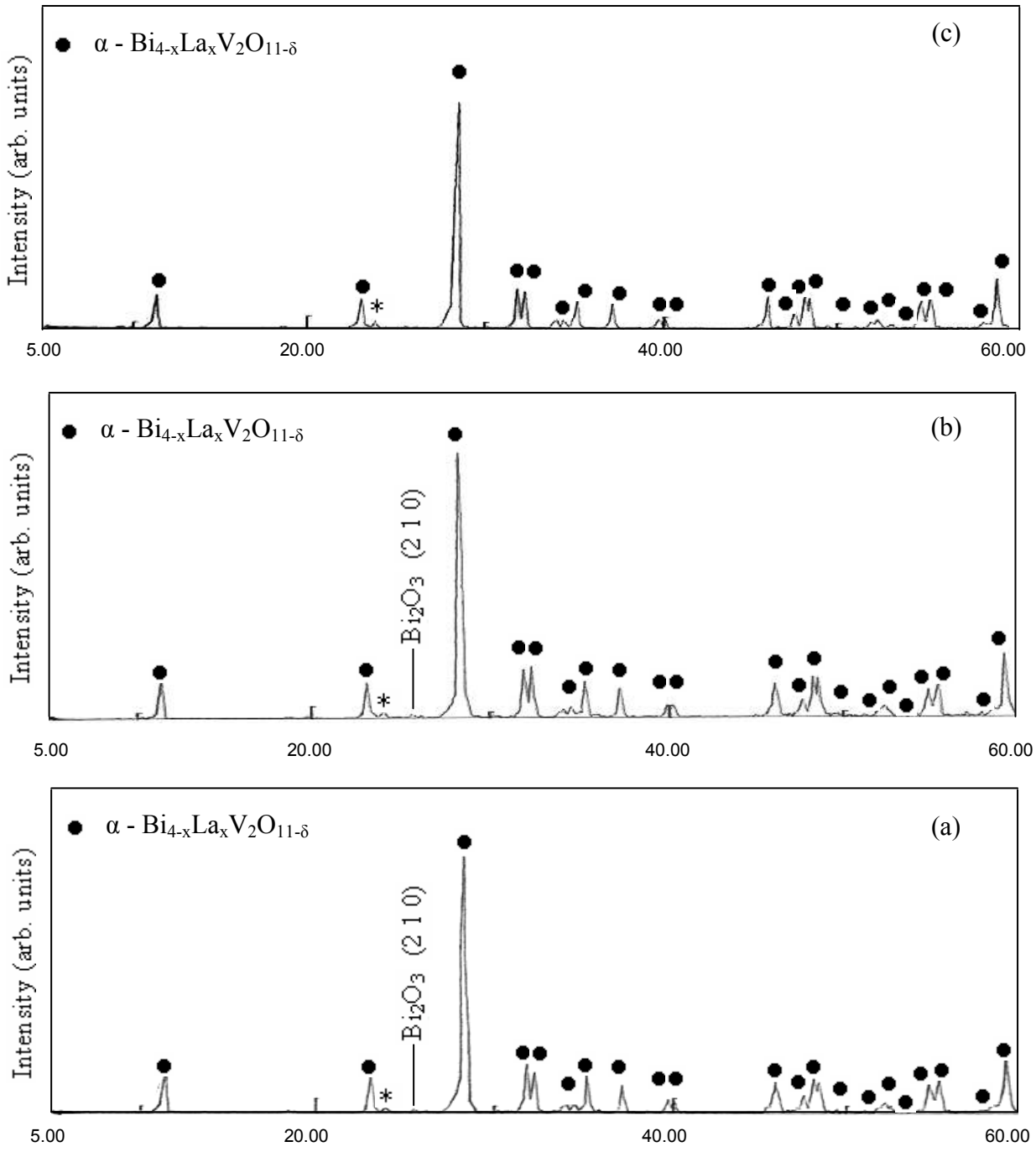

Fig. 5.15 XRD pattern of samples $Bi_{3.9}La_{0.1}V_2O_{11-\delta}$ sintered at (a) 750 ^oC (b) 775 ^oC (c) 825 ^oC; (*) superlattice reflection

Table 5.10 Lattice parameters of $Bi_{3.9}La_{0.1}V_2O_{11-\delta}$ at different sintering temperature

Sintering temp.(°C)	*a* (Å)	*b* (Å)	*c* (Å)	Volume (Å^3)
750	5.56	5.63	15.37	481.12
775	5.54	5.61	15.33	476.45
800	5.52	5.60	15.26	471.17
825	5.52	5.63	15.39	478.28

5.1.2.2.2 Electical Conductivity

The conductivity measured for samples sintered at different temperatures in addition to 800 °C for high conducting composition is presented in figure 5.16 in the form of Arrhenius plots. The transition from β → α for samples sintered at 750 °C, 775 °C and 825 °C was observed to be at 340 °C, 320 °C and 320 °C respectively. Other slope changes for these samples were also observed which corresponds to γ → β at 500 °C, 560 °C and 560 °C for all the samples.

The conductivity measured at 200 °C for sample x = 0.1 sintered at 800 °C provides higher value of conductivity (table 5.11) which is 45.85 times as compared to the sample sintered at 825 °C; the lowest conducting sample.

This fact clearly indicates that conductivity is more sensitive to the sintering temperatures than composition.

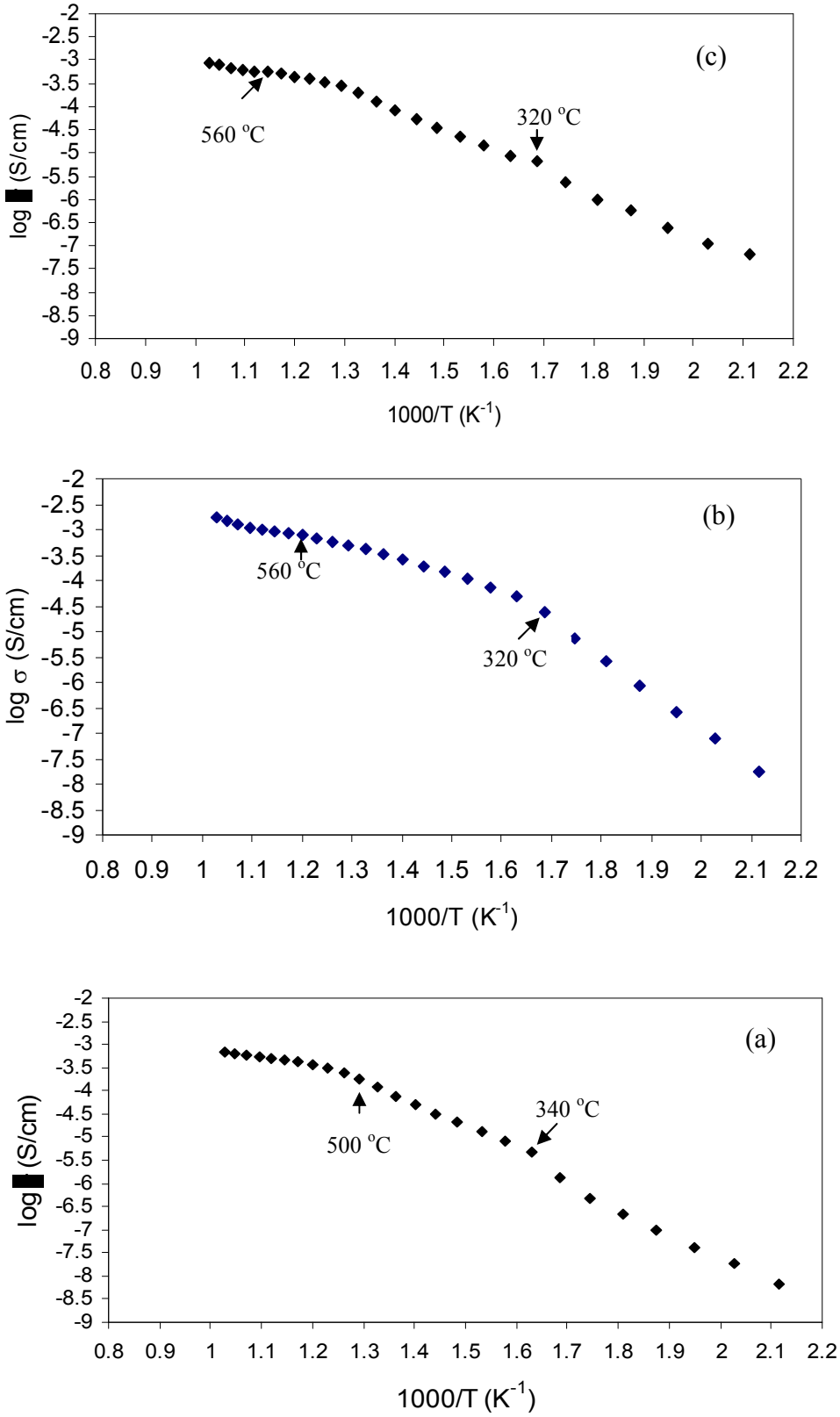

Fig. 5.16 Arrhenius plot of $Bi_{3.9}La_{0.1}V_2O_{11-\delta}$ at different sintering temperatures (a) 750 °C, (b) 775 °C (c) 825 °C

Table 5.11 Conductivity and activation energy of $Bi_{4-x}La_xV_2O_{11-\delta}$, (x = 0.1) at different sintering temperatures

Sintering Temperature (^oC)	σ_{200^oC} (S/cm)	E_a (eV) < 300 ^oC	E_a (eV) >500^oC
750	6.35×10^{-8}	0.36	0.15
775	1.76×10^{-8}	0.61	0.17
800	3.10×10^{-7}	0.27	0.18
825	6.76×10^{-9}	0.43	0.17

5.1.2.2.3 Microstructural Analysis

In order to assess the conductivity behaviour, microstructural study was carried out for the highest conducting sample (x = 0.1) sintered at 750, 775 and 825 ^oC. The SEMs of these samples are presented in figure 5.17.

The average grain size of samples sintered at 750, 775 and 825 ^oC is given in table 5.12. The lowest grain size of the sample sintered at 825 ^oC is ascribed to low conductivity which may provide higher contribution of grain boundary resistance. This fact is in agreement with the general behaviour of solid electrolyte at intermediate temperature where conductivity is governed mainly by the grain boundary.

The sintering feature for sample sintered at 800 (x = 0.3) and 825 ^oC (x = 0.1) gives similar morphological features. However, the interwoven network structure is more fine for sample sintered at 800 ^oC as compared to 825 ^oC. This transition has already been discussed for other compositions.

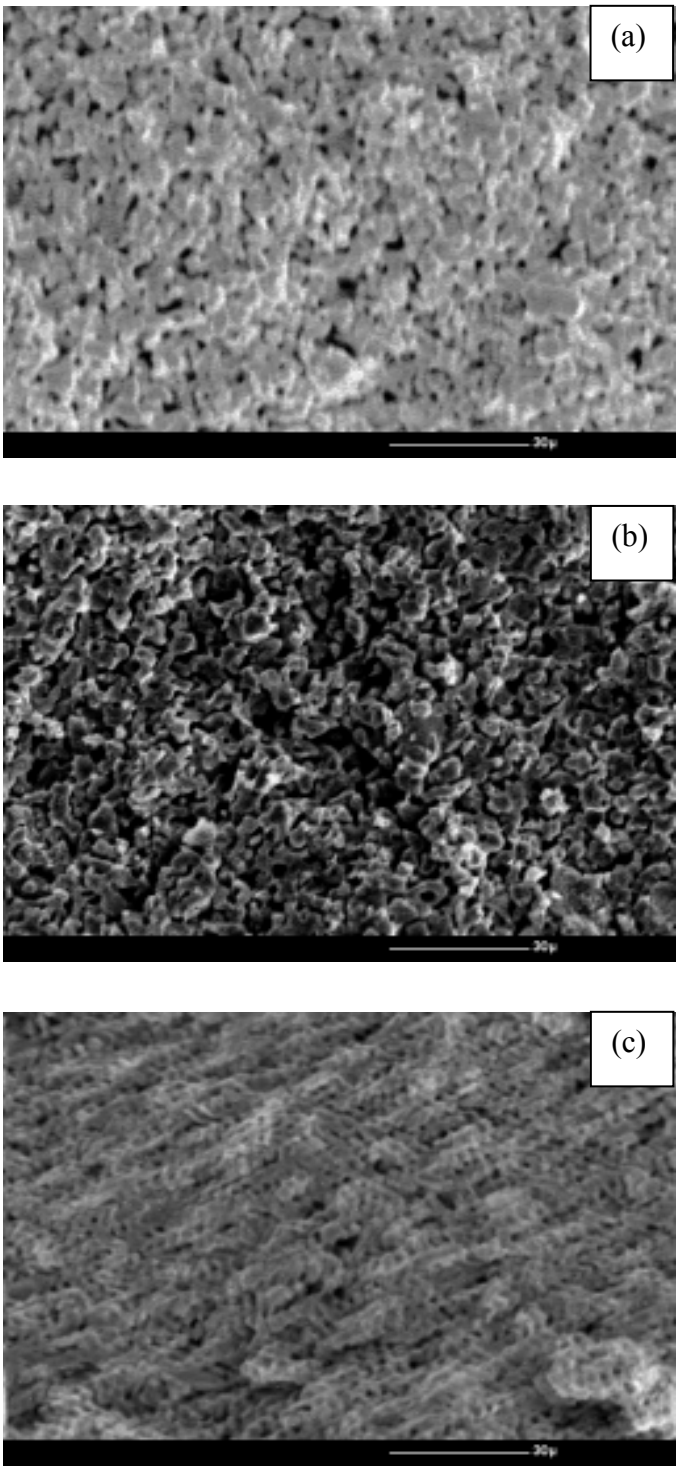

Fig. 5.17 SEM of fractured surfaces of $Bi_{3.9}La_{0.1}V_2O_{11-\delta}$ sintered at (a) 750 ^oC, (b) 775 ^oC (c) 825 ^oC

Table 5.12 Average grain size of $Bi_{3.9}La_{0.1}V_2O_{11-\delta}$ at different sintering temperatures

Sintering temperature (^oC)	Grain size (μm)
750	6-10
775	4-8
800	5-8
825	2-5

5.1.2.3 $Bi_{4-x}Me_xV_2O_{11-\delta}$ ($Me=Gd^{3+}$)

5.1.2.3.1 X-ray Diffraction

X-ray diffraction patterns were obtained for the powders of the sintered pellets prepared from stoichiometric amounts of Bi_2O_3, V_2O_5 and Gd_2O_3 corresponding to $Bi_{4-x}Gd_xV_2O_{11-\delta}$. The XRD patterns for the composition $0.1 \leq x \leq 0.4$ in the step of 0.1 are shown in figure 5.18. Patterns corresponding to first three composition x = 0.1 to 0.3 observed to be orthorhombic α-phase with doublets at $2\theta \approx 31^o$, 39^o, 48^o, 54^o along with a very weak reflection at $2\theta \approx 24.2^o$. The sample of x = 0.3 is at the phase domain of α and β. On the other hand, x = 0.4 sample exhibits only β-orthorhombic phase.

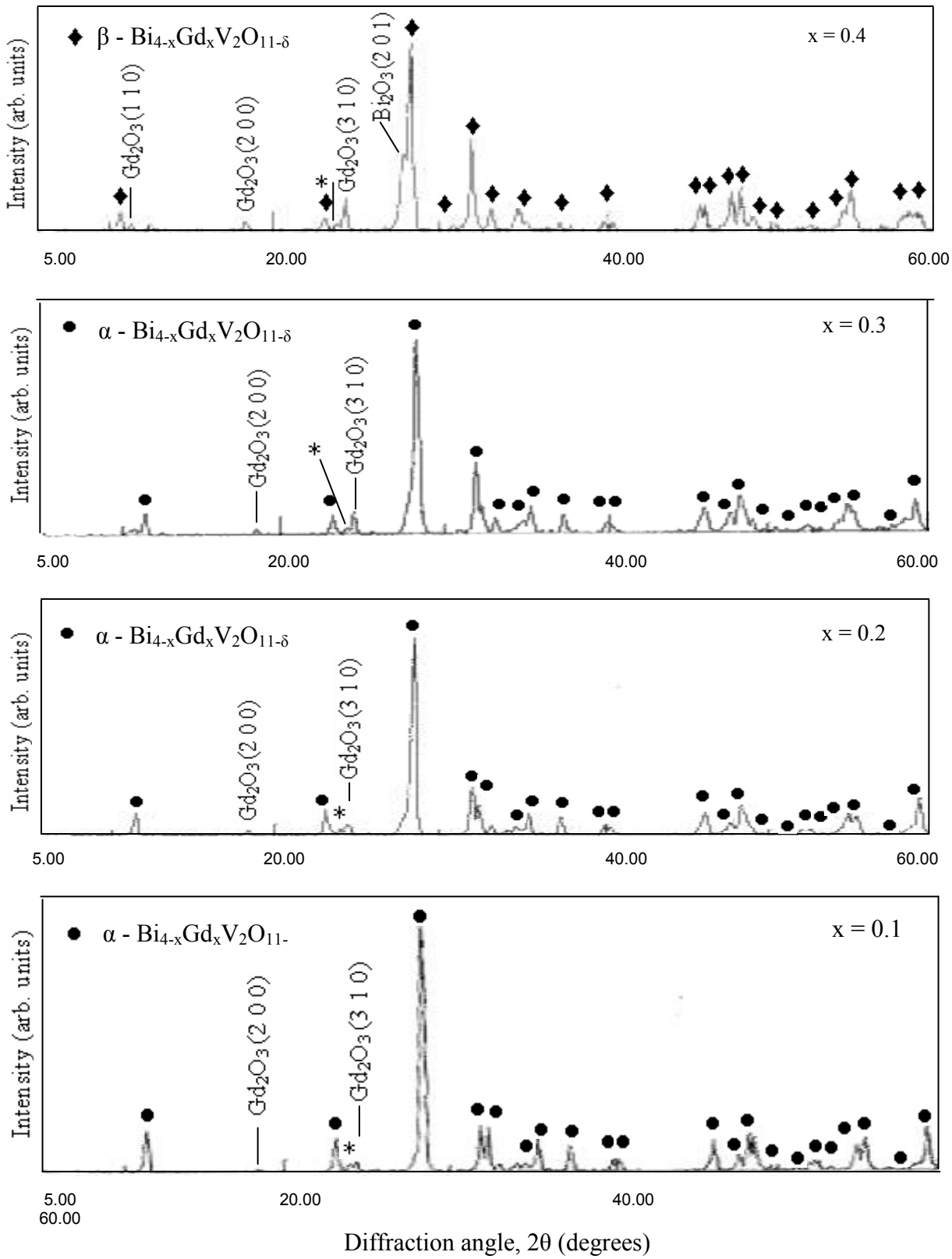

Fig. 5.18 X-ray diffraction pattern of $Bi_{4-x}Gd_xV_2O_{11-\delta}$ for x = 0.1, 0.2, 0.3 and 0.4;

(*) superlattice reflection

The solid solution was not obtained in the entire studied composition range (but possibly may occur for $x < 0.1$, though the lower range is not studied) with presence of some impurity peaks which are indexed as Gd_2O_3 (ICDD card no. 76-0155) for all the compositions but some additional peaks of Bi_2O_3 are also observed only for the composition of $x = 0.4$. The unreacted Gd_2O_3 impurity contents are increasing with doping rate.

Chadwick *et al*. [200] demonstrated that Gd^{3+} in $Bi_2V_{0.90}Gd_{0.10}O_{5.5-\delta}$ predominantly occupy bismuth sites due to comparable ionic radii of Gd^{3+} (0.94 Å) and Bi^{3+}(0.96 Å).

5.1.2.3.2 Electrical Conductivity

The conductivities of the samples of compositions $x = 0.1$, 0.2, 0.3 and 0.4 have been measured and shown in figure 5.19. Double transitions from $\gamma \rightarrow \beta$ and $\beta \rightarrow \alpha$ are shown in the Arrhenius plots of each composition (fig. 5.19). The single transition corresponding to $\gamma \rightarrow \alpha$ was observed to be at 420 ^oC for $x = 0.4$.

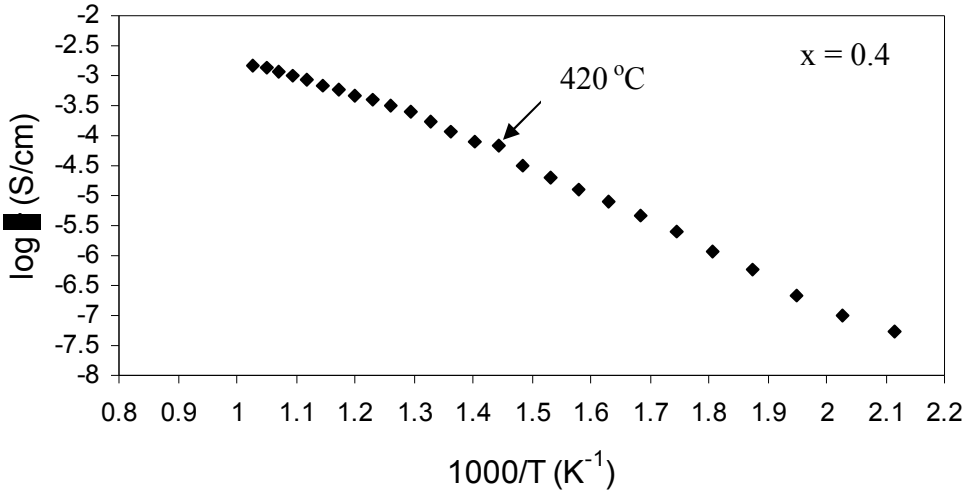

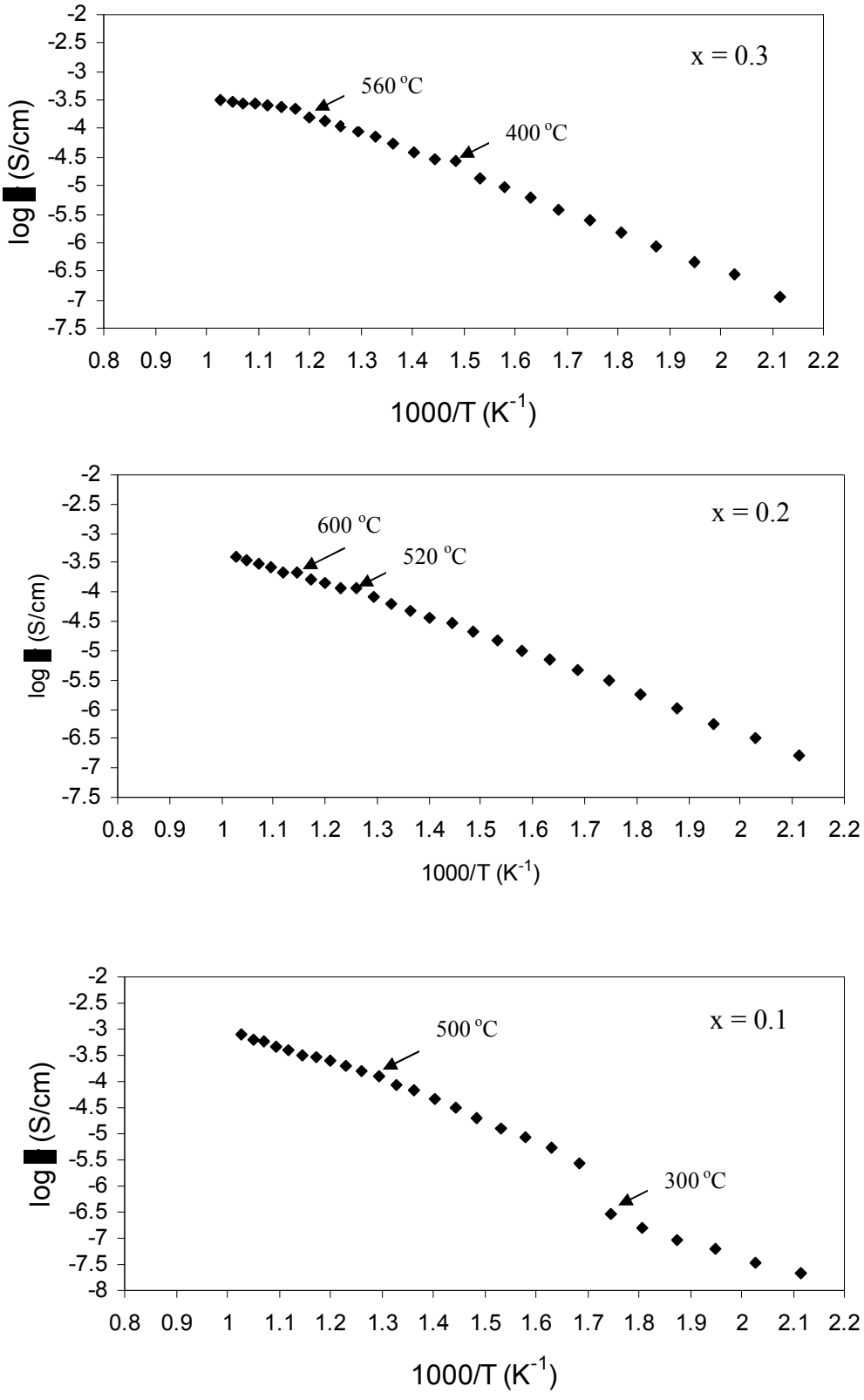

Figure 5.19 Arrhenius plot of the conductivities of $Bi_{4-x}Gd_xV_2O_{11-\delta}$ (0.1, 0.2, 0.3 and 0.4)

The highest and lowest values of conductivity is observed for x = 0.2 (2.21×10^{-7} S/cm) and 0.4 (1.69×10^{-7} S/cm) respectively at 200 ^{o}C.

The decrease in conductivity may be caused by the segregation of insulating phase Gd_2O_3 along grain boundaries which blocks the ions movement. The decrease in conductivity may be correlated to decrease in coefficient of thermal expansion at higher Gd^{3+} contents on the basis of ionic transport theory [201]. According to this theory, mobility of point defects causes the relationship between the two.

Bismuth site substitution in $Bi_4V_2O_{11-\delta}$ by divalent cations showed the better performance with lead Pb^{2+} as compared to La^{3+} and Gd^{3+} (trivalent) substitution. Lead substitution shows higher solid solution range as compared to lanthanum (La^{3+}) and gadolinium (Gd^{3+}) systems. Surprisingly, γ-phase could not be stabilized in all the three substitutions. However, La^{3+} and Gd^{3+} both exhibit β-phase at room temperature for higher composition of x = 0.4 alongwith impurity phases (Gd_2O_3, Bi_2O_3). Conductivity is also higher for $Bi_{3.8}Pb_{0.2}V_2O_{11-\delta}$ compound in the solid solution range. SEM study clearly indicates that the optimum size of grains is very crucial to achieve higher electrical conductivity in these samples.

Chapter VI

Conclusions and scope of the future work

6.1 Conclusions

The study of bismuth based electrolyte, in the present thesis, was undertaken to establish its potential applications in solid oxide fuel cell. The performance of solid oxide fuel cell depends primarily on ionic conductivity of electrolyte so there has been a continuous upsurge to develop electrolytes with higher ionic conductivity at lower temperature. Though yttria stabilized zirconia has been used as a base electrolyte in solid oxide fuel cell. However below 1000 ^{o}C, its ionic conductivity decreases drastically. Therefore, new electrolytes which have good ionic conductivity in the temperature range of (500-800 ^{o}C) are required to make cost effective SOFC. Based on this, the dissertation work was carried out on doped and undoped bismuth vanadate based electrolytes for different compositions. The possibility to enhance the ionic conductivity was explored. In order to address the above issue, the selected electrolytes for study were divided into two categories. In the first one, the dopants were substituted for vanadium site and the second category deals with the bismuth site substitution in bismuth vanadate. The extensive studies have been carried out on these systems by the various researchers. However, the effects of processing conditions on the microstructure and its correlation with ionic conductivity are less emphasized in the literature. The fact that oxide ion vacancies increase with concentration of lower valence dopants on vanadium and bismuth sites was exploited for the selection of large composition range in the present study. However, presence of additional phase(s) played a significant role on the conductivity values.

The systems of $Bi_4V_{2-x}Cu_xO_{11-\delta}$ (fig. 4.5), $Bi_4V_{2-x}Mn_xO_{11-\delta}$ (fig. 4.12), $Bi_4V_{2-x}Ti_xO_{11-\delta}$ (fig.4.15) and $Bi_4V_{2-x}Al_xO_{11-\delta}$ (fig. 4.25) were stabilized with γ – phase for $x \geq 0.2$. Other systems in the class of vanadium site substitution of $Bi_4V_{2-x}Cr_xO_{11-\delta}$ (fig. 4.33) $Bi_4V_{2-x}Ga_xO_{11-\delta}$ (fig. 4.36) and $Bi_4V_{2-x}As_xO_{11-\delta}$ (fig. 4.38) could not show the γ-phase stabilization at room temperature. In case of titanium doping the formation of solution was extended up to x = 0.4 whereas in other samples it is x=0.2. The common unreacted impurity phase of Bi_2O_3 was observed when dopant concentration exceeds the solid solution range. $BiVO_4$ phase other than Bi_2O_3 phase was also present, particularly in $Bi_4V_{2-x}Cr_xO_{11-\delta}$ (fig. 4.33) and $Bi_4V_{2-x}Ga_xO_{11-\delta}$ (fig. 4.36) systems. This is attributed to change in the stoichiometrical ratio of Bi : V from two to less than two. Based on the present study, some samples, which showed good ionic conductivity, were selected to investigate the effect of different sintering temperature. In all the cases, either they exhibit the beta phase or unreacted Bi_2O_3.

The compounds of $Bi_{4-x}Pb_xV_2O_{11-\delta}$ (fig. 5.1), $Bi_{4-x}La_xV_2O_{11}$ (fig. 5.10) and $Bi_{4-x}Gd_xV_2O_{11}$ (fig. 5.18) could not show γ – phase stabilization at room temperature for all the compositions studied for these systems. Lead (Pb^{2+}) doping on bismuth site in $Bi_{4-x}Me_xV_2O_{11-\delta}$ shows the α-phase formation for all the composition up to x = 0.4 as observed from figure 5.1. In contrast, trivalent lanthanum and gadolinium substitution show the similar structural variations up to x=0.3. However, for x = 0.4 sample with lanthanum and gadolinium showed the β phase stabilization. (fig. 5.10 and 5.18)

The conductivity of pure $Bi_4V_2O_{11}$ was observed to be 1.12×10^{-6} at 300 ^oC (section 4.1.1.3). The highest conductivity was observed in titanium doped $Bi_4V_{2-x}Ti_xO_{11-\delta}$ for x = 0.4. In this system the value of conductivity observed is 24 times more than undoped sample at 300 ^oC as shown in table 4.7. This situation demonstrates that $Bi_4V_{2-x}Ti_xO_{11-\delta}$ system has

superior effect over other doped systems. Microstructural features also support the highest conductivity of the titanium doped $Bi_4V_2O_{11}$ due to the optimum grain size (6-10 μm) which might be responsible for higher conductivity in this system (fig. 4.20). The lowest conductivity was obtained in trivalent chromium doped $Bi_4V_{2-x}Cr_xO_{11-\delta}$ system. The samples of $Bi_4V_{1.6}Ti_{0.4}O_{11-\delta}$ and $Bi_4V_{1.8}Al_{0.2}O_{11-\delta}$ were further investigated to study the effect of sintering temperature. These samples were sintered at 750, 775 and 825 ^oC. The conductivity of $Bi_4V_{2-x}Ti_xO_{11-\delta}$ and $Bi_4V_{2-x}Al_xO_{11-\delta}$ systems sintered at 800 ^oC was higher than all other sintering temperatures. The highest conducting $Bi_4V_{2-x}Ti_xO_{11-\delta}$ system follows the conductivity order as $\sigma_{0.4} > \sigma_{0.3} > \sigma_{0.2} > \sigma_{0.1}$ in terms of composition and $\sigma_{800^oC} > \sigma_{825^oC} > \sigma_{775^oC} > \sigma_{750^oC}$ in terms of sintering temperature.

On the other hand, the doping for Bi sites in bismuth vanadate exhibited the highest conductivity value = 4.7×10^{-7} S/cm at 200 ^oC in $Bi_{4-x}Pb_xV_2O_{11-\delta}$. The conductivity measured at 300 ^oC of $Bi_{4-x}Pb_xV_2O_{11-\delta}$ for x = 0.2 is higher by a factor 6.38 than the undoped $Bi_4V_2O_{11-\delta}$ compound. However, the ionic conductivity values measured at 300 ^oC of Pb^{2+} doped system are 4 times lower than titanium doped sample on vanadium site. The highest ionic conductivity for $Bi_{4-x}Pb_xV_2O_{11-\delta}$ compound among all other substitutents on bismuth site owes to the presence of $6s^2$ lone pair and chemical nature similar to bismuth.

The lead and lanthanum doped systems were further heat treated at different temperature to see the effect of sintering temperature. The systems exhibited the following trend in conductivity as $\sigma_{800^oC} > \sigma_{775^oC} > \sigma_{750^oC} > \sigma_{825^oC}$. The lowest ionic conductivity was observed when sample sintered at 825 ^oC. The micrographs of this particular system indicated the partial melting at 825 ^oC. Partial melting might be responsible to decrease the ionic conductivity.

Analyses based on the X-ray diffraction and ionic conductivity measurements, a correlation among ionic conductivity, metal ion substitution and sintering temperature may be established and categorized as follows:

(i) Partial substitution of various dopants where solid solution are formed up to x = 0.4, the ionic conductivity follows the sequence with respect to sintering temperature as $\sigma_{800} > \sigma_{825} > \sigma_{775} > \sigma_{750}$.

(ii) On the other hand, if the metal ion substitution are forming the solid solution up to composition x = 0.2, the conductivity varies in the following order $\sigma_{800} > \sigma_{775} > \sigma_{750} > \sigma_{825}$.

However, the conductivity maxima in both cases exist at sintering temperature of 800 ^{o}C. Lowest conductivity in case (ii) for the sample sintered at 825 ^{o}C may be ascribed due to reduction in melting point in presence of additional Bi_2O_3 phase.

(iii) The sample sintered at 800 ^{o}C of $Bi_4V_{1.6}Ti_{0.4}O_{11-\delta}$ is found to consist of cellular type uniform and well developed grains (fig. 4.20) of size 6-10 μm (table 4.8) whose shape and size changes with sintering temperatures and composition (fig. 4.24). These microstructural aspects support the highest conductivity observed in the $Bi_4V_{2-x}Ti_xO_{11-\delta}$. The weaker refined grains are observed in the aluminium based compound $Bi_4V_{2-x}Al_xO_{11-\delta}$ (fig. 4.28) for the high conducting composition x = 0.2 sintered at 800 ^{o}C as compared to well refined grains of $Bi_4V_{1.6}Ti_{0.4}O_{11-\delta}$ (fig. 4.20). These morphological differences of the microstructure and size of the grains supports the higher conductivity of the system $Bi_4V_{2-x}Ti_xO_{11-\delta}$ (x = 0.4) as compared to $Bi_4V_{2-x}Al_xO_{11-\delta}$ (x = 0.2).

(iv) The uniform and well refined grain formation of size 25-30 μm for lead substitution on bismuth site in $Bi_{4-x}Me_xV_2O_{11-\delta}$ for composition x = 0.2 enhanced the ionic conductivity as compared to the poor resolved grains in x = 0.4 sample of the same system. The smaller grains observed for sintering temperatures at 750, 775 and 825 ^oC (table 5.6) further establish the fact that grain size plays an important role to contribute in ionic conductivity. The lower limit of grain size (2-4 μm) was found in $Bi_{3.7}La_{0.3}V_2O_{11-\delta}$ sample. This sample showed the lowest conductivity (fig. 5.14 and 5.17) among all other systems sintered at different temperature.

(v) The unexpected reduction in conductivity of order of 2 of the bismuth vanadate based electrolytes in the present study as compared to reported one (1×10^{-3} S/cm) at 300 ^oC may be attributed to the two possible causes; the first could be the relatively high porosity in the present samples secondly, the formation of a narrow range of the solid solution.

6.2 Scope of the future work

After analyzing the data presented in the thesis, the following suggestions are recommended for further investigation:

(i) The sample preparation plays an important role to improve the ionic conductivity. Therefore preparative conditions are required to be controlled.

(ii) X-ray mapping of the systems under study can further provide the details of additional phase(s) present for the complete information.

(iii) High temperature X-ray diffraction analyses along with high resolution transmission microscopy (HRTEM) studies are required to establish the layer responsible for higher conductivity in these systems (V_2O_5) or (Bi_2O_3). Also, this study is necessary to provide the clear insight of α, β and γ-phases ranges.

(iv) Determination of carrier mobility and carrier concentration both at room temperature and as a function of temperature by some suitable method should be devised for enhancement of ionic conductivity by doping and/or formation of new compound based on bismuth vanadate.

(v) The performance of the developed electrolytes should be tested in actual configuration for solid oxide fuel cell.

(vi) Defect chemistry pertaining to determine quantitatively the oxygen vacancies can provide the direct theoretical mechanism for the increase in conductivity with particular dopant.

(vii) Fitting of the impedance data to calculate the contribution from bulk and grain boundary could be well correlated with SEM study.

(viii) The effect of particle size on ionic conductivity determination can play an important role on conductivity enhancement.

(ix) Structural analysis of the $Bi_{4-x}Me_xV_2O_{11-\delta}$ may provide detailed analysis of bismuth site substitution.

(x) Higher doping in $Bi_{4-x}Me_xV_2O_{11-\delta}$ needs to be investigated for γ-phase stabilization.

(xi) In present study, we observed that above the solid solution range, in both sides substitution irrespective to dopant size, Bi_2O_3 was found as an unreacted phase

besides $Bi_4V_2O_{11-\delta}$ phase. The reason for this can be studied to establish the fact that whether pervoskite layer is responsible or bismuth layer for high ionic conductivity in these systems.

References:

[1] Faraday M (1833) Experimental-Untersuchungen uber Elektrizitat, IV. Reihe. Uber ein neues Gesetz der Elektrizitatsleitung. In: Oettingen AJ von (ed) Ostwalds Klassiker der exakten Naturewissenschaften, Nr 86, Leipzig 1897, pp 39-55 and Note 9 of the Editor

[2] T. Takahashi, K. Kuwabara and O. Yamamoto, J. of Electrochem. Soc., 116 (1959) 357.

[3] J.N. Bradley and P.D. Greene, Trans. Faraday Soc., 62 (1966) 2069.

[4] B.B. Owens and G.R. Argue, Science, 157 (1967) 2453.

[5] M. Wittingham and R. Huggins, J. Chem. Phys., 54 (1971) 414.

[6] J. Wang, M. Gaffari and S. Choi, J. Chem. Phys., 63 (1975) 772.

[7] D. Ravaine and J.L. Souquet in: P. Hagenmuller and W. Van. Gool (Eds.), Solid Electrolytes, Academic Press, New York, 1978. p.277.

[8] J.L. Souquet, Solid State Ionics, 5 (1981) 77.

[9] H.L. Tuller, in: H.L. Tuller and M. Balkanski (Eds.), Science and Technology of Fast Ion Conductors, NATO – ASI Series, Ser B199, Plenum, New York, 1989. p.51

[10] K.P. Padmasree, D.K. Kanchan, A.R. Kulkarni, Solid State Ionics, 177 (2006) 475.

[11] A. Dalvi and K. Shahi, J. Physics and Chemistry of Solids, 64 (2003) 813

[12] A. Dalvi and K. Shahi, Solid State Ionics, 159 (2003) 369.

[13] J. S. Thokchom, C. Chen, K.M. Abraham and Binod Kumar, Solid State Ionics, 176 (2005) 1887.

[14] A.V. Virkar, J. Electrochem. Soc.138 (1991) 1481.

[15] F.M.B. Marques and L.M. Navarro, Solid State Ionics, 90 (1996) 183.

[16] K.R. Sridhar and B.T. Vaniman, Solid State Ionics, 93 (1997) 321.

[17] Y. Mishima, H. Mitsuyasu, M. Ohtaki and K. Eguchi, J. Electrochem. Soc., 145 (1998) 1004.

[18] T. Takahashi, T. Esaka and H. Iwahara, J. of Appl. Electrochem, 7 (1977) 299.

[19] B. C. H. Stelle, in "High Conductivity Solid Ionic Conductors, ed. T. Takahashi, World Scientific, Singapore (1989).

[20] M Yashima. M. Kakihana and M Yoshimura, Solid State Ionics, 86/88 (1996) 1131.

[21] R. A. Miller, J. L. Smialek and R. G. Garlik, in *Science and Technology* of *Zirconia,* eds. A. H. Heuer and L. W. Hobbs, Advances in Ceramics, vol. 3, American Ceramics Society, Columbus, OH, 19 8 1, p. 24 1.

[22] R. Ruh, H. J. Garnett, R. F. Donagala and V. A. Patel, J. Am. Ceram. Soc., 60 (1977) 399

[23] W. W. Baker and O. Knop , Proc. Br. Ceram. Soc., 19 (1 9 71) 15.

[24] D. K. Hohnlce, in *Fast Ion Transport in Solid,* eds. P. Vashista, J. N. Mundy and G. I.C. Shenoy, NorthHolland, Amsterdam, 1968, p. 669.

[25] R. E. Carter and W. L. Roth, in *Electromotive Force Measurements in High Temperature Systems,* ed. C. B. Alcoclr, IMM, London, 1968, p. 653.

[26] H.L. Tuller and A.S. Nowick, J. Electrochem. Soc., 126 (1979) 209.

[27] V. Butler, C. R. A. Catlow, B. E. F. Fender and J. H. Harding, Solid State Ionics, 8 (1983) 109.

[28] T. Kudo and Y. Obayashi, Electrochem. Soc., 123 (1976) 419.

[29] M. Mogensen, N. M. Sammes and G. A. Tompsett, Solid State Ionics, 129 (2000) 63.

[30] S. J. Skinner and J. A. Kilner, Materials Today (31-37), March, 2003.

[31] C.N.R. Rao, G.V. Subba Rao and S. Ramdas, Phase transformations and electrical properties of bismuth sesquioxide, Journal of Physical Chemistry, , 73 (1969) 672.

[32] A. Laarif and F. Theobald, The lone pair concept and the conductivity of bismuth oxides Bi_2O_3, Solid State Ionics, 21 (1986) 183.

[33] T. Takahashi, H. Iwahara and Y. Nagai, High oxide ion conduction in sintered bismuth oxide, calcium oxide or lanthanum oxide, Journal of Applied Electrochemistry, 2 (1972) 97.

[34] G. Mairesse In Fast ion transport in solids, eds. B. Scrosati, Kluver Amsterdam, 1993, p. 271.

[35] G. Gattow and H. Schroder, Die Kritallsttruker der hochtemperaturemodifikation von wismut (III) – oxide (δ-Bi2O3, Zeitschrift fur Anorganishe und Allgemeine Chemie, 318 (1962) 176.

[36] D.A. Mac Danaill and P.W.M. Jacobs, On the lattice parameter of some sesquioxides with the fluorite structure, journal of Solid State Chemistry, 84 (1990) 183.

[37] K. Koto, K. Suda, N. Ishizawa and . Maeda, Oxide ion motion in bismuth sesquioxide (δ-Bi_2O_3). Solid State Ionics, 72 (1994) 79.

[38] E.M. Levin and R. S.Roth, Polymorphism of bismuth sesquixide. II. Effect of oxide additions on the polymorphism of Bi_2O_3, Journal of Research of the National Bureau of Standards-A, 68A (1964) 189.

[39] S.TerauchiH.Takizawa,T.Endo,S.Uchida,T.Terui and M. Shimada, Mat.Letts, 23 (1995) 273.

[40] T. Van Dijk, K. J. De Vries, A. J. Burggraaf, Phys. Stat. Sol. (b) 101 (1980) 765.

[41] T. Van Dijk, K. J. De Vries, A. J. Burggraaf, Phys. Stat. Sol. (b) 58 (1980) 115.

[42] T. Fournier, J. Y. Nots, J. Muller, J. C. Joubert, Solid State Ionics 15 (1985) 71.

[43] P.K. Moon, H. L. Tuller, Solid State Ionics 28-30 (1988) 470.

[44] P. K. Moon, H. L. Tuller, in "Proceedings of the First International Symposium on Solid Oxide Fuel Cells, S. C. Singhal (ed.) The Electrochemical Society, Inc., Pennington, New Jersy, Vol. 89-11 (1989) p. 30-40.

[45] Moon P.K., Tuller H.L. Solid State Ionics 28-3 (1988) 470.

[46] Moon P.K., Tuller H.L. Mater. Res. Soc. Proc. 135 (1989) 149.

[47] A.Q. Pham, M. Puri, J.C. Di Carlo, A.J. Jacobson, J. Solid State Ionics, 72 (1994) 309.

[48] K.W. Browall, O. Muller, R.H. Doremus, Mater. Res. Bull. 11 (1976) 1075.

[49] Feng, M. and Goodenough, J. B. Eur. J. Solid State Inorg. Chem., 31 (1994) 663.

[50] Huang, K. Q. et al, J. Elecrochem. Soc. 144 (1997) 3620.

[51] Ishihara, T., et al, J. Am. Chem. Soc. 116 (1994) 3801.

[52] Ishihara, T., et al, Solid State Ionics 86-88 (1996) 197.

[53] Ishihara, T., et al, J. Elecrochem. Soc., 145 (1994) 3177.

[54] J. Wolfenstine,P.Huang and A.Petric,Solid State Ionics 118 (1999) 257.

[55] L.M.Liu, T.H.Lee, Y.L.Qui, Y.L.Yang and A.J.Jacobson, Mater.Res.Bull. 31 (1996) 29.

[56] V.V. Vashook, M.V. Zinkevich, Yu.G. Zonov, Solid state ionics 116 (1999)129.

[57] S. Stimmer, Solid state ionics 130 (2000) 71.

[58] L.V. Kokhanovskii , Inorg. Mater. 37 (2001)730.

[59] Goodenough, J. B.; Ruiz-Diaz, J. E.; Zhen, Y. S. *Solid State Ionics 44* (1990) 44.

[60] Thomas, J. K.; Krause, W. E.; zur Loye, H.-C. *Solid State Ionics*; Nazri, G.-A., Tarascon, J.-M. and Armand, M., Ed.; Mater. Res. Soc.: Boston, MA, 1992; Vol. 293, pp 307.

[61] Aurivillius B., Ark Kemi. 1 (1949) 463.

[62] Aurivillius B., Ark Kemi., 1 (1949) 499.

[63] Aurivillius B., Ark Kemi., 2 (1949) 519.

[64] T. Takahashi and H. Iwahara, J. of Appl. Electrochem, 3 (1973) 65.

[65] T. Takahashi, T. Esaka and H. Iwahara, J. of Appl. Electrochem, 7 (1977) 31.

[66] V.K. Yanovskii, V.I. Voronokova, Y.E. Roginskaya and Y.N. Venevtsev, Soviet Physics, Solid State Engl. Transl., 24 (1982)1603.

[67] Abraham, F.; Debreuille-Gresse, M. F.; Mairesse, G.; Nowogrocki, G. *Solid State Ionics 28-30* (1988) 529.

[68] Lee, C. K.; Sinclair, D. C.; West, A. R. Solid State Ionics *62* (1993) 193.

[69] B. Frit and J.P. Mercurio, J. Alloys Comp. 188 (1992) 27.

[70] T. Kikuchi, Mater. Res. Bull. 14 (1979) 1561.

[71] K.R. Kendall, C. Navas, J.K. Thomas and H.C. Zur Loye, Chem. Mater., 8 (1996) 642.

[72] F. Abraham, J.C.Boivin, G.Mairesse and G.Nowogrocki, Solid State Ionics, 40/41 (1990) 934.

[73] W. Zhou, D.A. Jefferson, H. He, J. Yuan and D.J. Smith, Philosphical Magazine Letters, 75 (1997) 105.

[74] T. Kudo, A. Hammou and J. Guindet, in "The CRC Handbook of Solid State Electrochemistry", edited by P. J. Gellings and H. J. M. Bouwmeester (CRC Press, Boca Raton, 1997) p. 407. in "The CRC Handbook of Solid State Electrochemistry", edited by P. J. Gellings and H. J. M. Bouwmeester (CRC Press, Boca Raton, 1997) p. 195.

[75] B. Zhu, J. Mater. Sci. Lett. 17 (1998) 1287.

[76] Hagenmuller, P. ; Laskar, A. L. and Chandra, S., Eds. Superionic Solids and Solid Electrolytes; Academic Press: New York, 1989, pp 679-704.

[77] Erickson, D.C., U.S. Patent No. 4,132,766, 1979.

[78] Haber F (1907) Verfahren zur Erzeugung von eleckrischer Energie aus Kohle und gasformigen Brennstoffen. Oster Pat 27 743, filed 5.8.1905.

[79] N.Q. Minh, T. Takahashi, Science and Technology of Ceramic Fuel Cells, Elsevier, Amsterdam, 1995.

[80] H.L. Tuller, in: O Toft Sorensen (Ed.), Nonstoichiometric Oxides, Academic Press, New York, 1981, 271-335.

[81] R.N. Bluementhal, F.S. Brugner, J.E. Garnier, J. Electrochem. Soc. 120 (1973) 1230.

[82] P. Huang, A. Petric, J. Electrochem. Soc. 143 (1996) 1644.

[83] T. Ishihara, H. Matsuda, Y. Takita, Solid State Ionics 79 (1995) 147.

[84] EG & G Services Parsons, Inc., Science Applications International Corporation, "Fuel Cell Handbook Fifth edition", National Energy Technology Laboratory, October 2000.

[85] D.H. Archer, L. Elikan and R.L. Zahradnik in Hydrocarbon Fuel Cell Technologies, ed. B.S. Baker, Academic Press, New York, 1965, p. 51

[86] U.B. Pal and S.C. Singhal, J. of Electrochem. Soc., 137(1990) 2937-2941.

[87] C. Bagger, Improved production methods for YSZ electrolyte and Ni-YSZ Anode for SOFC, in 1992 Fuel Cell Seminar Abstracts, Tucson, AZ, 1992.

[88] K. Kendall, Powder Technology, 58 (1989) 151.

[89] K. Kendall, in: International Forum on Fine Ceramics, Japan Fine Ceramics Centre, Nagoya, 1992, p. 143-148.

[90] S.C. Singhal and K. Kendall, in "High Temperature Solid Oxide Fuel Cell: Fundamentals, Design and Application" (Elsevier Advanced Technology, Oxford, 2003).

[91] H.L. Tuller In: H. Tuller, J. Schoonman and I. Riess (Eds.), Oxygen Ion and Mixed Conductors and their Technological Applications. Kluwer (NATO ASI series), Dordrecht, 2000, p. 245.

[92] Advances in Ceramics, Vol. 3, Science and Technology of Zirconia, Edited by A.H. Heuer and L.W. Hobbs, American Ceramic Society, Columbus, OH, 1981.

[93] Advances in Ceramics, Vol. 24, Science and Technology of Zirconia III, Edited by S. Somiya, N. Yamamoto and.H. Yanagida, American Ceramic Society, Westerville, OH, 1988.

[94] M. Mogensen, D. Lybye, N. Bonanos, P.V. Hendriksen and F.W. Poulsen, Solid State Ionics 174 (2004) 279.

[95] Y. Liu and L.E. Lao, *Solid State Ionics*, 177 (2006) 159.

[96] Binod Kumar, J.S. Thokchom, J. Am. Ceram. Soc. 19 (2008) 1175.

[97] J. Luo, R.J. Ball and R. Stevens, Journal of Materials Science, 39 (2004) 235.

[98] H.L. Tuller and A.S. Nowick, J. Electrochem. Soc., 122 (1975) 255.

[99] R.N. Bluementhal, F.S. Brugner and J.E. Garnier, J. Electrochem. Soc., 120 (1973) 1230.

[100] K.El. Adham, A. Hammou, J. Chim. Phys. 79 (1982) 633.

[101] N.P. Brandon, A. Blake, D. Corcoran, D. Cumming, A. Duckett, K.El-Koury, D. Haigh, C. Kidd, R. Leah, G. Lewis, C. Mathews, N. Maynard, N. Oishi, T. McColm, R. Trezona, A. Selcuk, M. Schmidt, L. Verdugo, Journal of Fuel Cell Science and Technology, Vol. 1 (2004) 61-65.

[102] D.S. Lee, W.S. Kim, S.H. Choi, J. Kim, H.W. Lee and J.H. Lee, *Solid State Ionics*, 176 (2005) 33.

[103] T. Takahashi and H. Iwahara, in: Research in Effective Use of Energy, sp. Publ. of the Ministry of Education Science and Culture of Japan, Vol. 3 (1982) 727-734.

[104] B. C. H. Stelle, B.E. Powell, P.M.R. Moody, Proc. Brit., Ceramic Society, 10 (1968) 87.

[105] F. Vanbaelinghen, A. Pelloux, C. Deportes, J. Appl. Electrochem. 6 (1976) 67.

[106] K. Huang, J. Wan, J.B. Goodenough, Journal of Materials Science 36 (2001) 1093.

[107] A. Sinha, B.P. Sharma and P. Gopalan, *Electrochimica Acta* 51 (2006) 1184.

[108] K. Hu, C. Chen, D. Peng, G. Meng, Solid State Ionics, 28/30 (1988) 566.

[109] M. Miyayama, T. Nishi and H. Yanagida, Journal of Materials Science, 22 (1987) 2624.

[110] A. Helfen, S. Merkourakis, G. Wang, M.G. Walls, E. Roy, K.Yu. Zhang, Y. Leprince-Wang, Solid State Ionics, 176 (2005) 629.

[111] R. Mark Ormerod, Chem. Soc. Rev., 32 (2003) 17

[112] N.M. Sammes, G.A. Tompsett, H. Nafe and F. Aldinger, J. Eur. Ceram. Soc. 19 (1999) 1801.

[113] A.A. Yaremchenko, V.V. Kharton, E.N. Naumovich, A.A. Tonoyan and V.V. Samokhval, J. Solid State Electrochem., 2 (1998) 308.

[114] V.V. Kharton, E.N. Naumovich, A.A. Yaremchenko and F.M.B. Marques, J. Solid State Electrochem., 5 (2001) 160.

[115] P.Shuk, H.D.Wiemhofer, U.Guth, W.Gopel and M.Greenblatt, *Solid State Ionics*, 89 (1996) 179.

[116] T. Takahashi, H. Iwahara, and T. Arao, J.Appl.Electrochem. 5 (1975) 187.

[117] N. Jiang, E.D. Wachsman and S. Jung, Solid State Ionics 150 (2002) 347.

[118] H. Kruidhof, H.J.M. Bouwmeester, K.J.de. Vries, P.J. Gellings and A.J. Burggraaf, Solid State Ionics 50 (1992) 181.

[119] K.-Z. Fung, J. Chen and A.V. Virkar, J. Am. Ceram. Soc. 76 (1993) 2403.

[120] A. Watanabe, Solid State Ionics 86-88 (1996) 1427.

[121] S. Boypati, E.D. Wachsman, N. Jiang, Solid State Ionics 140 (2001) 149.

[122] Y. Mizutani, M. Tamura, M. Kawai and O. Yamamoto, Solid State Ionics 72 (1994) 271.

[123] K. Huang, M. Feng and J.B. Goodenough, Solid State Ionics 89 (1996) 17.

[124] A.A. Yaremchenko, V.V. Kharton, E.N. Naumovich, and F.M.B. Marques, J. Electroceram.., 4 (2000) 235.

[125] K.R. Kendall, J.K. Thomas and H.C. zur Loye, Solid State Ionics, 70/71 (1994) 221.

[126] E.N. Naumovich, V.V. Kharton, V.V. Samokhval and A.V. Kovalevsky, Solid State Ionics, 93 (1997) 95.

[127] T. Takahashi, H. Iwahara, and T. Esaka, J. of Electrochemistry Society, 124 (1977) 1563.

[128] M.F. Debreuille-Gresse, M.F., Ph.D. Thesis, University of Lille, (1986).

[129] T. Lu and B.C.H. Steele, Solid State Ionics, 21 (1986) 339.

[130] J.B. Goodenough, A. Manthiram, M. Paranthaman and Y.S.Zhen," Mat. Sci. Engg., B12 (1992) 357.

[131] V. Sharma, A.K. Shukla and J. Gopalakrishanan, Solid State Ionics 68 (1992) 359.

[132] J. Yan and M. Greenblatt, Solid State Ionics 81 (1995) 225.

[133] C.K. Lee, B. H. Bay and A.R.West, J. Mat. Chem., 6 (1996) 331.

[134] F. Krok, W. Bogusz, W. Jakubowski, "Solid State Ionics" 70-71 (1994) 211.

[135] S. Lazure, R.N. Vannier, G. Nowogrocki, G. Mairesse, C. Muller, M. Anne and P. Strobel, J. Mater. Chem. 5(9) (1995) 1395.

[136] T.Iharada, A.Hammouche, J. Fouletier, M. Kleitz., J.C.Boivin and G.Mairesse, Solid state Ionics 48 (1991) 257.

[137] M.Anne, M.Bacmann, E. Pernot, F.Abraham, G.Mairesse and P.Stroble, PhysicaB, 180-81 (1992) 621.

[138] E.Pernot, M.Anne, M.Bacmann, P.stroble, J. Fouletier, R.N. Vannier, G.Mairesse, F.Abraham, and G. Nowogrocki, Solid State Ionics 70-71 (1994) 259.

[139] J.R.Dygas, F.Krok, W. Bogusz, P. Kurek, K. Reiselhuber and M.W.Brietter, "Solid State Ionics" 70-71 (1994) 239.

[140] J.R.Dygas, P.Kurek, and M.W.Brietter, Electrochim. Acta , 40 (1995) 1545.

[141] P.Kurek, J.R.Dygas and M.W.Brietter, J.Electrochem., 378 (1994) 77.

[142] K. Reiselhuber, G. Dorner and M.W.Brietter, Electrochimica.Acta, 38(7) (1995) 969.

[143] F. Krok, W. Bogusz, P.Kurek, M. Wasiucionek, W. Jakubowski and J.R.Dygas, Mat. Sci. Engg. B21 (1993) 70.

[144] C.J. Watson, A. coats, D.C. Sinclair, J. Mater. Chem. 7-10 (1997) 2091.

[145] C.K. Lee, A. coats and A.R. West, Powder Diffraction, 12 (1997) 245.

[146] J.C. Boivin, R.N. Vannier, G.Mairesse, F.Abraham, and G. Nowogrocki, ISSI Lett. 3-4 (1992) 3.

[147] S.P.Simner, D.S. Sandoval, J.D. Mackenzie and B. Dunn, J. Am. Ceram. Soc. 80 (1997) 2563.

[148] C.K. Lee, G.S. Lim and A.R. West, J. Mater. Chem. 4 (1994) 1441.

[149] R.N. Vannier, G.Mairesse, F.Abraham, and G. Nowogrocki, Solid State Ionics 70/71 (1994) 248.

[150] P.Kurek, and M.W.Brietter Solid State Ionics 86-88 (1996) 131.

[151] C.K. Lee and A.R. West, .Solid State Ionics, 86-88 (1996) 235.

[152] O. Joubert, M Ganne, R.N. Vannier and, G. Mairesse, Solid State Ionics, 83 (1996) 199.

[153] J.B. Goodenough, A. Manthiram, M. Paranthaman and Y.S.Zhen, Solid State Ionics, 52 (1992) 105.

[154] J.A. Kilner and B.C.H. Steele, in: Nonstoichiometric Oxides, ed. O.T. Sorensen (Academic Press, New York, 1981), p. 233.

[155] Y.L.Yang, L. Qin, W.T.A. Harrison, R. Christofersen and A.J. Jacobson, J. Mater.Chem 7 (1997) 243.

[156] Y.L.Yang, L. Qin and A.J. Jacobson, J. Mater.Chem 7 (1997) 937.

[157] O. Joubert, A. Jouanneaux, M Ganne, R.N. Vannier and, G. Mairesse, Solid State Ionics 73 (1994) 309.

[158] O.Thery, R.N. Vannier and F.Abraham, Solid State Ionics 90 (1996) 105.

[159] N. Bonanos Mat. Res. Bull 24 (1989) 1531.

[160] S. Lazure, C. Vernochet, R.N. Vannier, G. Nowogrocki and G. Mairesse, Paper 4-3P313, 10th International Conference on Solid State Ionics, Singapore (1995).

[161] R.N. Vannier, G.Mairesse, F.Abraham, and G. Nowogrocki, Journal of Solid State Chemistry, 103 (1993) 441.

[162] P. Hagenmuller and W. Van Gool, “Solid Electrolytes”, Academic Press, New York/San Francisco/London (1978).

[163] R.N. Vannier, G. Mairesse, F. Abraham, and G. Nowogrocki, Solid State Ionics, 80 (1995) 11.

[164] R.N. Vannier, G. Mairesse, G. Nowogrocki, F.Abraham and J.C. Boivin, Solid State Ionics, 53-56 (1992) 713.

[165] A. Aboukais, F. Delmaire, M. Rigole, R. Hubaut, G. Mairesse, Chem. Mater., 5 (1993) 1819.

[166] F. Delmaire, M. Rigole, E.A. Zhilinskaya, A. Aboukais, R. Hubaut and G. Mairesse, Phys. Chem. Chem. Phys., 2 (2000) 4477.

[167] M. Huve, R.N. Vannier, G. Nowogrocki, G. Mairesse and G. Van Tendeloo, J. Mater. Chem., 6 (1995) 1339.

[168] S. Lazure, Thesis, 1996, Lille, France.

[169] C. Vernochet, Thesis, 1997, Lille, France.

[170] O. Joubert, A. Jouanneaux, M Ganne, M. Tournoux, Mater. Res. Bull., 27 (1992) 1235.

[171] E. Capoen, M.C. Steil, N. Tancret, G. Nowogrocki, J.C. Boivin, G. Mairesse, R.N. Vannier, M. Anne, O. Isnard, *Solid State Ionics*, 175 (2004) 419.

[172] I. Abrahmas and F. Krok, J. Mater. Chem. 12 (2002) 3351.

[173] I. Abrahmas and F. Krok, *Solid State Ionics*, 157 (2003) 139.

[174] CRC Handbook of Solid State Chemistry, Eds. P.J. Gellings and H.J.M. Boumeester (CRC Press Inc., USA, 1997)

[175] G.J. Dudley and B.C.H. Steele, J. Solid State Chem., 21 (1977) 1.

[176] J.E. Bauerle, J. Phys. Chem. Solids, 30 (1969) 2657.

[177] D.W. Marquardt, J. Soc. Indst. Appl. Math., 11 (1963) 431.

[178] B.A. Boukamp, Solid State Ionics, 20 (1986) 31.

[179] A. R. West, *Solid State Chemistry and Its Applications*; John Wiley and Sons: New York, 1984, p 482-489.

[180] Macdonald, J. R. *Impedance Spectroscopy: Emphasizing Solid Materials and Systems*; John Wiley & Sons: New York, 1987.

[181] M.M. Qurashi, W.H. Barnes, Amer, Mineralogist, 38 (1953) 489.

[182] D.E. Cox, A.R. Moodenbaugh, A.W. Sleight, H.Y. Chen, NBS Special Publication, 567 (1980) 189.

[183] A. Watanable, J. Solid State Chem., 161 (2001) 410.

[184] A. Watanable, Y. Kitarni, Solid State Ionics, 113-115 (1998) 601.

[185] ICDD Powder Diffraction File, PDF-2, ICDD, Pennsylvania, USA, 1998, Card 44-171.

[186] R.N. Vannier, G. Mairesse, F. Abraham, G. Nowogrocki, E.Pernot, M.Anne, M.Bacmann, P.stroble and J. Fouletier,, Solid State Ionics, 78 (1995) 183.

[187] S.N. Achary, M.D. Mathews, S.J. Patwe and A.K. Tyagi, J. Materials Science Letters 18 (1999) 355.

[188] O. Joubert, A. Jouanneaux and M Ganne, Mater. Res. Bull., 29 (1994) 175.

[189] C.K. Lee, M.P. Tan and A.R. West, J. Mater. Chem. 4 (1994) 525.

[190] E. Garcia, M. Arribas and J.M. Ganzalez-Calbet, J. of Mater. Chem., 11 (2001) 2320.

[191] J.A. Dean, Lange's Handbook of Chemistry, Thirteenth Edition 1985 (Mc Graw-Hill co.), p.3-126.

[192] A.A. Yaremchenko, V.V. Kharton, E.N. Naumovich and A.A. Tonoyan, Stability of δ-Bi_2O_3 based solid electrolytes, Materials Research Bulletin, 35 (2000) 515.

[193] B. Jaffe, W.R. Cooke and H. Jaffe, Piezoelectric Ceramics, Academic press, 1971.

[194] Y. Xu, Ferroelectric Materials and Their Applications, North Holloand, 1991.

[195] M. Greenblatt, *Ionic Conductors, Encyclopedia of Inorganic Chemistry,* 33 (1994) 1584.

[196] K. V. R. Prasad, G. N. Subbanna and K. B. R. Varma, The Bulletin of the Bismuth Institute*,* 67, (1994) 3.

[197] A.A. Yaremchenko, M. Avdeev, V.V. Kharton, A.V. Kovalevsky, E.N. Naumovich and F.M.B. Marques, Materials Chemistry and Physics, 77 (2002) 552.

[198] C.K. Lee and C.S. Ong, Solid State Ionics, 117 (1999) 301.

[199] A.A. Yaremchenko, V.V. Kharton, E.N. Naumovich and V.V. Samokhval, Solid State Ionics, 111 (1998) 227.

[200] A.V. Chadwick,, C. Colli, C. Maltese, G. Marrison, I. Abrahams and A. Bush, Solid State Ionics, 119 (1999) 79.

[201] V.N. Chebotin, Physical Chemistry of Solids, Khimiya, Moscow, 1982 (in Russian).

List of Publications

1. Synthesis and Characterization of Bismuth Vanadate Electrolyte Material with Aluminium Doping for SOFC Application, Ravi Kant, K.Singh and O.P.Pandey, International Journal of Hydrogen Energy 33 (2008) 455.

2. Microstructural and Electrical Behavior of $Bi_4V_{2-x}Cu_x O_{11-\delta}$; ($0 \leq x \leq 0.4$), Ravi Kant, K.Singh and O.P.Pandey, Ceramics International (in press) 2007.

3. Effect of Cr^{3+} Substitution for V^{5+} in Bismuth Vanadate Solid Electrolyte, Ravi Kant, K.Singh and O.P.Pandey, Transactions of Indian Ceramic Society (in press) 2008.

4. Effect of Ti^{3+} Substitution for V^{5+} in Bismuth Vanadate Solid Electrolytes, Ravi Kant, K.Singh and O.P.Pandey (Communicated to Materials Research Bulletin) 2008.

5. Structural, Thermal and Conductivity Behaviour of $Bi_{4-x}M_xV_2O_{11}$ (M=La, Gd; $0 \leq x \leq 0.4$), Deepti, Ravikant, M.L.Singla and K.Singh, (Communicated to Current Applied Physics) 2008.

6. Electrical, Thermal and Microstructural Studies of BIPBVOX; ($0 \leq x \leq 0.4$), Ravi Kant, K.Singh and O.P.Pandey (Communicated to Solid State Ionics) 2008.

List of Papers presented in conference (International/National)

1. Preparation and Conductivity Measurement of Bismuth based Electrolyte for SOFC Application, Ravi Kant, K. Singh and O.P. Pandey, Proc. on National Conference on Materials & Related Technologies, page 49-53 (2003).

2. Low Temperature Ionic Conductivity of Bismuth Vanadate, Ravi Kant, Kulvir Singh and O.P.Pandey, Proc. on International Conference Inorganic materials: recent advances, Narosa Publishing House, Delhi, India, page 121-124 (2004).

3. Ionic Conductivity of Cu-substituted $Bi_4V_2O_{11}$ Compounds, Ravi Kant, K.Singh and O.P.Pandey, Proc. on National conference on Advances in Condensed Matter Physics, page 288-293 (2005).

4. Synthesis and Characterization of Bismuth Vanadate Electrolyte Material with Aluminium Doping for SOFC Application, Ravi Kant, K.Singh and O.P.Pandey, International Workshop on Hydrogen Energy: Production, Storage and Application, (2006).

5. Synthesis and Conductivity Measurement of Titanium-Doped Bismuth Vanadate Solid Electrolyte, Ravi Kant, K.Singh and O.P.Pandey, National Conference of Emerging Trends in Engineering Materials, (2007).